



Universiteit
Leiden
The Netherlands

The optimization and scale-up of the electrochemical reduction of CO₂ to formate

Philips, M.F.

Citation

Philips, M. F. (2023, November 8). *The optimization and scale-up of the electrochemical reduction of CO₂ to formate*. Retrieved from <https://hdl.handle.net/1887/3656164>

Version: Publisher's Version

License: [Licence agreement concerning inclusion of doctoral thesis in the Institutional Repository of the University of Leiden](#)

Downloaded from: <https://hdl.handle.net/1887/3656164>

Note: To cite this publication please use the final published version (if applicable).

The Optimization and Scale-Up of the Electrochemical Reduction of CO₂ to Formate

Proefschrift

ter verkrijging van
de graad van doctor aan de Universiteit Leiden,
op gezag van rector magnificus prof.dr.ir. H. Bijl,
volgens besluit van het college voor promoties
te verdedigen op woensdag 8 november 2023
klokke 10:00 uur
door

Matthew Philips
geboren te Mount Holly, New Jersey, United States of America
in 1990

Promotores:

Prof. Dr. M.T.M. Koper

Prof. Dr. G.J.M. Gruter (Universiteit van Amsterdam, Avantium)

Co-promotor:

Dr. K.J.P. Schouten (Teijin Aramid)

Promotiecommissie:

Prof. Dr. M. Ubbink

Prof. Dr. E. Bouwman

Dr. D.G.H. Hetterscheid

Prof. Dr. E.L.V. Goetheer (TU Delft)

Dr. M.C. Figueiredo (TU Eindhoven)

This work was supported by the European Commission under contract 722614 (Innovative training network Elcorel).

ISBN: 978-94-6483-526-7

Printed by Ridderprint

Table of Contents

Chapter 1: Introduction	1
Why Produce Formate?	3
Why Use a Gas Diffusion Electrode?	5
Why Use the Design of Experiments?	7
Why Use DFT Simulations?	9
Summary of Chapters	9
References	11
Chapter 2: The Gas Diffusion Electrode	19
The Limiting Current of GDEs	21
Influential Characteristics	21
The Gas Diffusion Layer	22
The Catalyst Layer	30
Outlook and Recommendations	37
References	39
Chapter 3: Production of Gas Diffusion Layers with Tunable Characteristics	43
Introduction	44
Experimental	45
Results and Discussion	49
Conclusions	57
References	59
Chapter 4: Electrochemical CO ₂ Reduction on Gas Diffusion Electrodes: Catalyst Layer Optimization Through a Design of Experiment Approach	63
Introduction	64
Experimental Methods	65
Results	69
Discussion	72
Conclusions	76
References	79
Chapter 5: Custom Multipurpose Electrochemical Cell Design and Scale-Up	81
Introduction	82
Experimental	83
Results and Discussion	88
Conclusions	90

References.....	92
Chapter 6: A Density Functional Theory Study on Surface Poisoning of Indium-Bismuth Electrodes	94
Introduction.....	95
Results and Discussion	95
Conclusions.....	101
References.....	102
Chapter 7: Outlook.....	106
Future Lab Scale Development.....	107
Future Scale-up Development.....	109
References.....	110
Appendix A.....	112
Appendix B	136
Appendix C	150
Appendix D.....	162
Appendix E	166
Appendix F.....	173
Summary	185
Samenvatting.....	187
Curriculum Vitae	189
List of Publications:	190
Acknowledgments.....	191

Chapter 1

Introduction¹

¹ This chapter is based on Philips, M. F.; Gruter, G.-J. M.; Koper, M. T. M.; Schouten, K. J. P. Optimizing the Electrochemical Reduction of CO₂ to Formate: A State-of-the-Art Analysis. ACS Sustain. Chem. Eng. 2020, 8 (41), 15430–15444, DOI 10.1021/acssuschemeng.0c05215.

Climate change has been gaining attention over the last several years, and it is generally attributed to the “greenhouse effect”: global temperatures increase as a result of a changing atmosphere that retains more heat from the sun.¹ These changes in the atmosphere are caused by various gasses, also known as greenhouse gases. Carbon dioxide is considered one of the worst greenhouse gases, even though it appears naturally in the atmosphere. This is because its increase in concentration due to human activity accounts for about half of the observed effect of rising global temperatures.²

Ways to lower the concentration of CO₂ in the atmosphere include capturing it from the atmosphere, changing process schemes to avoid emitting it, or converting the CO₂ generated from existing processes. Changing process schemes to avoid emitting CO₂ can be complicated and could be very expensive.³ On the other hand, capturing and storing CO₂ (without utilization) is not a circular solution.⁴ Directly converting CO₂, however, does not have these limitations and should be considered the best solution to reducing the amount of CO₂ in our atmosphere. However, the conversion of CO₂ comes with several challenges because it is a thermodynamic end state of every organic compound. Thus, it is difficult to economically convert CO₂ to chemicals with conventional catalysis due to the required high temperatures and pressures.⁵ Electrocatalysis, on the other hand, appears to be more attractive as the reaction takes place at ambient conditions.

One major limitation in the electrocatalytic reduction of CO₂ is the mass transfer of CO₂ to the catalyst surface due to the limited solubility of CO₂ in aqueous electrolytes at ambient pressure and temperature (33mM at 1 atm and 25°C).⁶ The solubility of CO₂ can be increased by either lowering the temperature or increasing the pressure, which is shown to slightly improve an electrode’s performance.^{7,8} Alternatively, gas diffusion electrodes (GDEs) achieve high reaction rates and efficiencies even at ambient conditions. Thus, there is enormous potential for their use in electrochemical CO₂ reduction.

GDEs have been developed and used in fuel cells, electrolyzers, air batteries, and photocatalytic reactions.^{9–14} These electrochemical devices use GDEs to enhance the mass transfer of the reactants to increase the rate at which they can efficiently operate. A GDE consists of two main layers: the gas diffusion layer (GDL) and the catalyst layer. Both layers can strongly influence the electrochemical performance of the GDE. These layers should be considered in more detail to understand how a GDE enhances mass transfer.

This first chapter contains relevant background information for statistics, electrochemistry, and density functional theory (DFT). Furthermore, this first chapter provides an extensive analysis of other work performed on the electrochemical reduction reaction (ERR) of CO₂ to formate. Moreover, this chapter seeks to explain: why formate is one of the most viable products to produce from CO₂, why the GDE is the best-known technology to produce formate electrochemically, why the experimental work in Chapters 3 and 4 uses the Design of Experiments (DOE) approach, how data from a DOE is analyzed, and why DFT is a useful tool for electrochemical development work. Finally, a summary of the chapters in this thesis is provided in the last section of this chapter.

Why Produce Formate?

Figure 1.1 shows several electrochemical reduction products of CO_2 for aqueous and organic electrolytes. Blue arrows connect the products formed in aqueous electrolytes, while orange arrows connect those formed in organic electrolytes. The number of transferred electrons increases from right to left. Additionally, formate salts can be converted non-electrochemically to oxalate salts in a thermal reaction (represented by the black dashed arrow).¹⁵

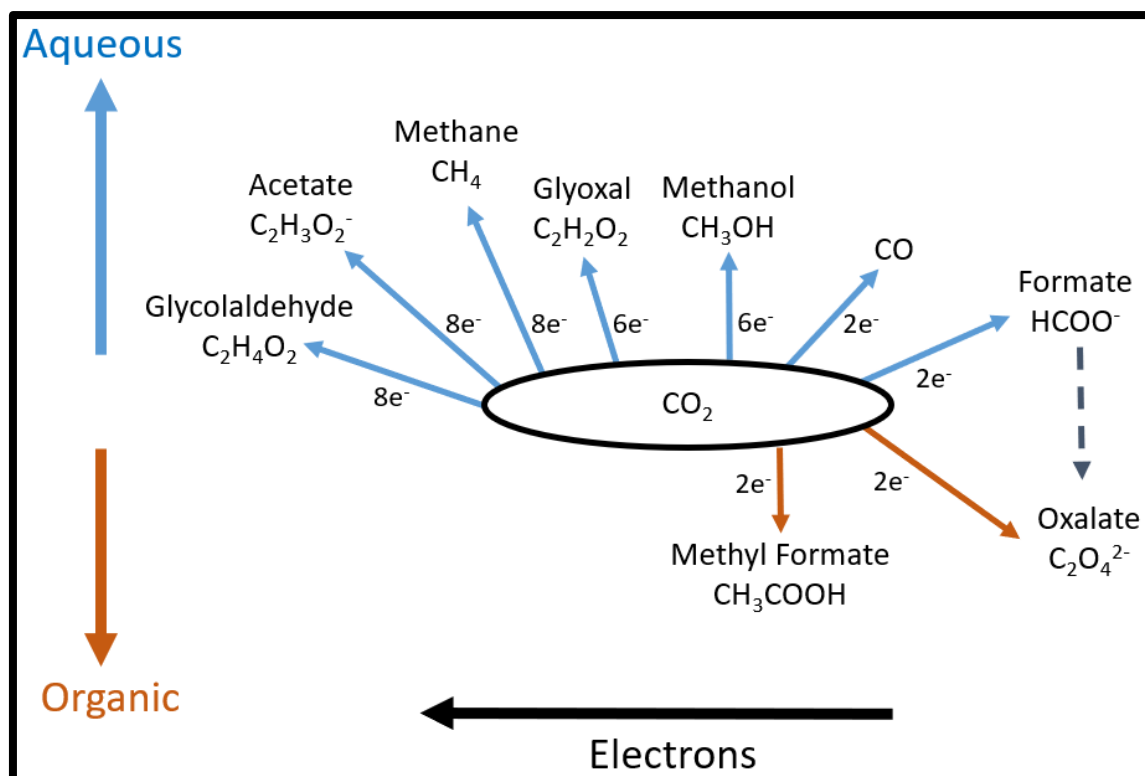


Figure 1.1 Electrochemical Reduction Products of CO_2

The key performance indicators (KPIs) that drive the economics should first be understood to determine which product in Figure 1.1 is the best to pursue and why a GDE is the best technology for this electrochemical reaction. Two of the most considerable process economic considerations are the capital investment (equipment) and the energy costs required to produce an amount of product. The number of electrochemical reactors (cells) for a given product production rate estimates the capital cost.

The number of cells required is an appropriate metric to estimate the capital cost because electrochemical cells begin to be stacked for parallel operation after a maximum size is reached (an adjustment factor may be necessary to adjust for more complex cell costs). Although other equipment costs can have scaling factors less than 1, the total capital cost of a process still increases with increasing cells.¹⁶ The number of cells required is directly proportional to the total cell active area, which can be calculated using Equation 1.1,

$$A_{total} = \frac{PPR * n * F}{CD * CE * MW * 3.6} \quad (1.1)$$

where PPR is the product production rate in kg/hr, n is the number of electrons transferred for the reaction (dimensionless), F is Faraday's constant in C/mol, CD is the current density in A/m², CE is the current efficiency for the desired product (percentage), MW is the molecular weight of the desired product in g/mol, and 3.6 is the conversion factor of $\frac{kg*s}{g*hr}$.

The energy consumption per mass of product is calculated using Equation 1.2,

$$\frac{kW*hr}{tonne} = \frac{V_{Cell} * I}{Production\ rate} = \frac{V_{Cell}*n*F}{MW*CE*3.6} \quad (1.2)$$

where V_{cell} is the whole-cell potential, and I is the total applied current. Equations 1.1 and 1.2 show that a system's energy and capital costs decrease when it operates with a high CE , targets a product with a high molecular weight, and uses few electrons in the reaction. Therefore, it is essential to select a product with a high molecular weight to the number of transferred electrons ratio. Table 1.1 shows this ratio for CO₂ electrochemical reduction products up to 8 electrons.

Table 1.1 Molecular weight to number of electrons ratio for CO₂ electrochemical reduction products

Product	MW	e ⁻	MW/e ⁻
Oxalate	88.02	2	44
Formate	46.03	2	23
CO	28.01	2	14
Glyoxal	58.04	6	9.7
Methanol	32.04	6	5.3
Methane	16.04	8	2
Acetate	60.052	8	7.5
Glycolaldehyde	60.052	8	7.5

Oxalate has the highest ratio of molecular weight to the number of transferred electrons. Unfortunately, oxalate production occurs in organic electrolytes, which leads to many technological challenges, such as membrane instability and the additional cost of the electrolyte.¹⁷ Advances in membrane technology or catalysts that form oxalate in aqueous conditions are required before considering oxalate as a viable product. Formate, however, has the second-highest ratio and is produced in aqueous electrolytes. Its ratio is over 1.5x the ratio for CO and more than double the ratio of the other reduction products. Additionally, formate can be thermally converted to oxalate, as previously discussed, and then further converted to various higher-value chemicals.¹⁸ Therefore, formate is one of the most economically viable products from CO₂ reduction, which agrees with several recent reviews.^{19–22}

Only the CE can influence both the capital and energy costs now that formate is selected as the target product. Additionally, maximizing the operating current density (CD) reduces capital costs while minimizing the cell potential (V_{cell}) lowers energy costs. Therefore, the current density, current efficiency, and cell potential are the top KPIs for electrochemical reactions. Figure 1.2 summarizes the KPIs for capital and energy costs for electrochemical cells.

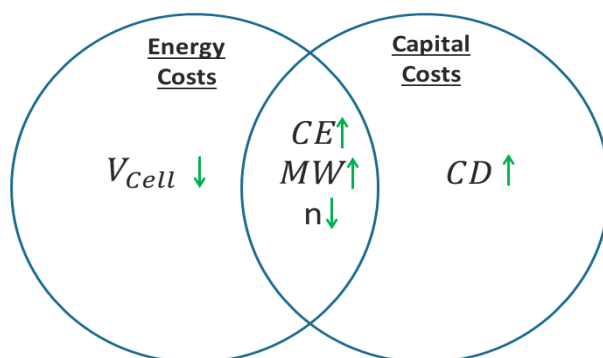


Figure 1.2. Venn Diagram of KPIs for optimizing capital and energy costs of electrochemical cells²³

One final consideration is the scalability of the reaction. For example, if the hydrostatic head is not manageable at a larger electrode size for GDEs due to the limitations of a gas diffusion layer or a cell design, then the GDE could become flooded, resulting in a decrease in performance as the cell size increases. This situation could severely limit the size of a single cell and thus drastically increase the capital cost for the process. Therefore, generally speaking, to realize an electrochemical technology at a commercial scale, a high current efficiency should be achievable at high current densities and low cell potentials without dependency on the electrode size.

The data collected for determining the best technology for this reaction consists of 554 experimental data points from 65 scientific publications and patents. These publications use various catalysts, electrode types, cell types, electrode areas, electrolytes, and separators. All of these varying factors influence the KPIs mentioned above. Unfortunately, the whole-cell potential data is scarcely reported, making insights into reducing energy costs very difficult. However, as displayed in Equation 1.2, a percentage change in CE will have the same impact as the same percentage change in cell potential (i.e., if current efficiency is doubled, the cell potential can also double without the energy costs increasing). For these reasons, this chapter compares various electrode types/cell configurations based on current efficiencies, current densities, and scale.

Why Use a Gas Diffusion Electrode?

We encountered four types of electrode/cell configurations in the literature and patents reviewed: 2D electrodes, 3D electrodes, trickle flow, and GDEs.

- The 2D electrode types include wires, rods, flat plates, and single meshes. These electrodes are typically used in H-cell experiments.
- The 3D electrode types include packed areas with granules, beads, shot, meshes, etc.
- Trickle bed flow is distinguished from a 3D electrode by having a mixed feed flow (CO₂ and electrolyte) through the electrode.
- GDEs are porous electrodes that feed CO₂ through the structure directly to the catalyst.

A comparison of the current efficiency towards formate of these electrode configurations as applied current increases is shown in Figure 1.3. The applied current includes the scale of the reaction (i.e., as cells become larger, more current must be applied to stay in the same current density range). Due to the wide range of operating currents, the x-axis is plotted on a log scale.

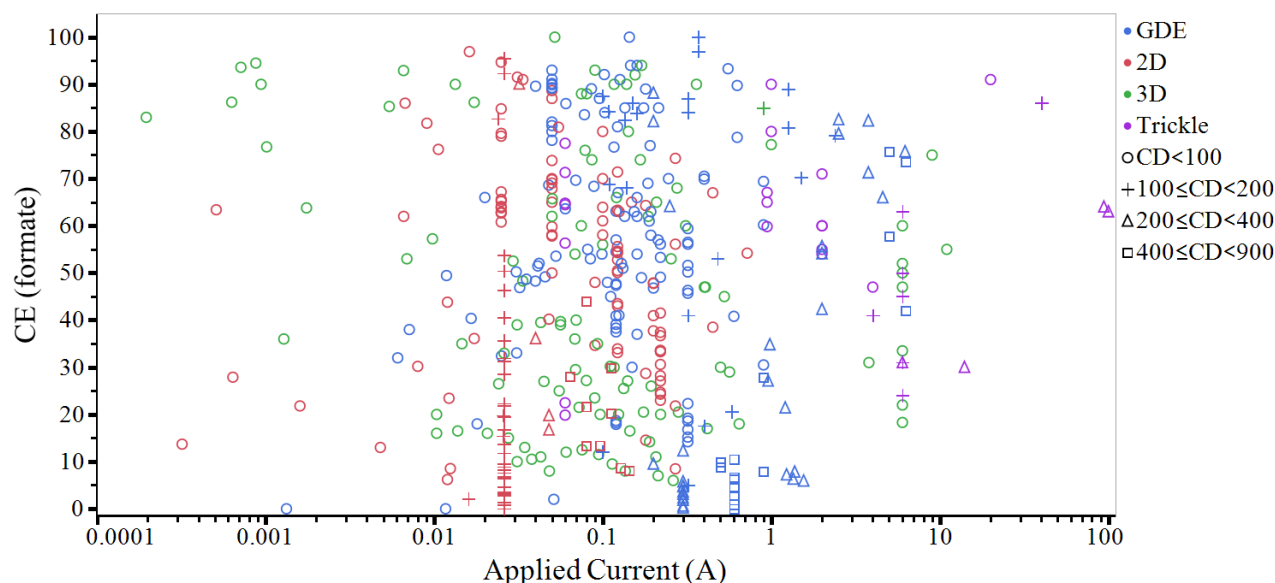


Figure 1.3. Current efficiency vs. applied current. Reported current density in mA/cm² 27,8,32–41,24,42–51,25,52–61,26,62–71,27,72–81,28,82–86,29–31

Different colors represent the four different electrode types, while different symbols distinguish four different current density (CD) ranges. Over 35 metals were used as a catalyst and reported formate production. However, tin, lead, indium, and copper catalysts make up over 85% of the data in Figure 1.3. Although the intrinsic activity of catalysts can influence the performances shown in Figure 1.3, we believe there is sufficient data across the different electrode types to assess the best electrode type.

Figure 1.3 shows that 2D electrodes rarely get over 90% current efficiency, and the maximum current efficiency achieved by these 2D electrodes appears to decrease as the operating current increases. Similarly, 3D electrode reactors appear to drop in current efficiency as the applied current increases. Additionally, both of these electrode types are rarely operated above 100 mA/cm². Trickle flow reactors can achieve similar current efficiencies as GDEs; however, the current density is only about one-third of GDEs. The best performance for trickle flow reactors is described in a patent from Oloman et al.⁸¹ where they use a 340 cm² trickle flow reactor that operates with Sn granules at current densities ranging from about 59 to 294 mA/cm². However, Figure 1.3 shows that the current efficiency drops to just above 60% at the maximum current density tested.

The 2D, 3D, and trickle electrode types become limited by mass transfer at higher current densities, which is why 2D and 3D types are not seen frequently operating over 100 mA/cm² and why the current efficiency of the trickle flow electrodes decreases as current densities are increased. The mass transfer of dissolved CO₂ in the bulk electrolyte to the surface of the electrode is the limiting factor for these electrode types (i.e., the reactant cannot reach the reaction site as fast as the reaction site can convert it). Promoting turbulent flow in these cells

(using flow distributors, a zero-gap, flow-through design, or trickle flow) would increase the mass transfer of CO₂ to the reaction surface. Although this does not seem to help substantially, Kaczur et al.⁸⁶ (similarly to Oloman et al.⁸¹) report decreasing current efficiencies with increasing current densities using a zero-gap, flow-through design. They report current efficiencies up to 100% at a current density of 56 mA/cm² but see the efficiency drop to 54 - 63% at a current density of about 95 mA/cm². GDEs, however, can drastically enhance mass transfer, which allows them to efficiently operate at current densities higher than 100 mA/cm².

Figure 1.3 shows that GDEs are consistently performing better than 2D and 3D or trickle flow electrode types. Not only are GDEs more efficient throughout the entire current range, but they are also capable of operating at higher current densities. However, GDEs appear to have a wide range of performance. Larger current densities and different catalysts can explain some of this variation, but 2 data sets use similar conditions and achieve different results. Kopljar et al.⁷⁴ report a current efficiency of up to 89% using a Sn GDE at a current density of 50 mA/cm² and an active area of 12.56 cm² using a 0.1 M potassium bicarbonate and potassium hydroxide electrolyte. Comparatively, Castillo et al.³⁶ report a current efficiency of only 40.8% using a Sn GDE at a current density of 50 mA/cm² and an active area of 10 cm² using a 0.45 M potassium bicarbonate and 0.5 M potassium chloride electrolyte. Although different electrolytes are used, the complexity of GDEs is most likely the main contributor to these stark differences in performance.

Further analysis of the layers that make up a GDE is required to understand better how GDEs are outperforming other electrodes. The gas diffusion layer (GDL) and the catalyst layer play unique roles in allowing a GDE to achieve better performance. Chapter 2 will explain the theory and design of these layers and how a GDE is able to outperform the other electrode types for this reaction. But first, helpful background information relevant to the third and fourth chapters in this thesis is presented.

Why Use the Design of Experiments?

DOEs have been rare in published academic work; most publications utilize a one-factor-at-a-time (OFAT) approach. This traditional way of experimenting uses a lot of resources to obtain information (relative to a DOE approach) and can lead to discovering local optimums rather than global optimums. On the other hand, a DOE methodically generates experiments to cover a given factor space completely, ensuring the discovery of global optimums.

Several types of designs can be used when planning a DOE and should be selected based on the experiment's main objective. In general, there are screening and optimization designs. Screening designs are typically used when there are many factors (large factor space), and the objective of the experiments is to reduce the number of factors by determining which are the most influential toward the measured response. Chapter 3 uses a screening DOE to identify which of the 11 production factors influences each of the six measured characteristics the most.

Optimization designs are typically either full factorials or response surface designs (RSDs). Full factorial designs vary each factor at a specified number of levels such that all possible combinations are run. So, three-level full factorial designs lead to a 3^k number of experiments

required to perform where k is the number of factors. Thus, these designs become exponentially more expensive to run with an increasing factor space. RSDs, on the other hand, are also three-level designs; however, not every combination of factors is run. RSDs are still more efficient and economical than the three-level full factorial design.⁸⁷ Regardless of the initial chosen design, the analysis of the results can use the same method. The results from DOEs in this thesis use multiple linear regression (MLR) for analysis.

DOE Analysis Background: Multiple Linear Regression

This background information on statistics will be most useful when considering the experiments in Chapters 3 and 4. These Chapters use a DOE for researching the GDL, catalyst layer, and GDE. Multiple Linear Regression (MLR) is frequently used to generate models for responses affected by several factors. The models generated from MLR are in the form of Equation 1.3:

$$y = b_1X_1 + b_2X_2 + b_3X_3 + \cdots + b_nX_n \quad (1.3)$$

where b_n is the model term coefficient, X_n is the factor variable, which can be a multiplicative combination of two factors (for interactions) or a squared factor (to model curvature), and y is the measured response. In our studies, typical factors are synthesis parameters such as the catalyst loading on the electrode or the amount of binder used in the catalyst layer. A typical response variable would be a characteristic of a material that is being formulated (such as the conductivity of the material) or a performance indicator of a process step, such as the current efficiency or cell potential. Numerous terms (i.e., b_nX_n) can be included in an MLR model, as seen in Equation 1.3. This can lead to overfitting when the number of parameters in the model is not limited by a model selection method. The Bayesian Information Criterion (BIC) and the Akaike Information Criterion (AIC) are two common information criteria that score candidate models to help prevent overfitting.^{88,89} The BIC and AIC scoring methods essentially impose a penalty on models with a larger number of parameters. Chapters 3 and 4 use these two criteria for selecting two models for each response studied. The final model selection between the two models generated from these criteria is discussed on a case-by-case basis.

The term coefficients (b_n) in the selected model indicate the average change in response for every unit increase of the respective term. These coefficients, however, are affected by the scale of the factor (i.e., if one factor is in milli-units and the other is in kilo-units, there would be six orders of magnitude difference between the two predicted coefficients). Consequently, comparing these coefficients can lead to biased conclusions. However, fitting a model to scaled factors (making the range between the factors two and mean equal to zero) results in coefficients that can be equally compared and allows for concluding which factors are affecting the response the most.⁹⁰

Sorting the model terms in the selected GDL characteristic models based on the coefficients of the scaled factors shows which parameters are influencing the response the greatest.⁹¹ Additionally, t-tests are used to determine with a certain level of confidence (often 95%) which coefficients are statistically significant. The null hypothesis of the t-tests performed is that the term coefficient is zero. P-values are calculated for each coefficient and used to determine if

the null hypothesis should be accepted or rejected. The null hypothesis is rejected when the p-value is less than 0.05 (for 95% confidence). In other words, when the calculated p-value is below a chosen threshold limit, the respective parameter coefficient is concluded to be non-zero or statistically significant.

The robustness of this methodology is discussed in Appendix F. A DOE is generated to explore a preset relationship between four factors. We then simulate random error of the measured value at three different percentage levels (20%, 10%, and 5%). Twenty simulations are generated for each percentage level. Models are then generated using the AIC and BIC as stopping rules for each simulation of responses (120 models for 60 total simulations). The terms and magnitude of their scaled parameter estimates are compared for each stopping rule at each level of simulated error. When the simulated variation is 10% or less, all models generated by both methods contained all of the terms found in the control models. Additionally, when the simulated variation is 10% or less, the top five influential terms in all models matched the control model (although not always in order of the magnitude of the scaled coefficients). At 20% simulated variation, there becomes a risk of missing an influential variable or falsely detecting a highly influential effect. Nevertheless, these models still successfully identify a majority of highly influential factors.

Why Use DFT Simulations?

As technology advances and computational power expands, the time to accurately model complex systems will decrease. This can allow for powerful predictions to be made with a reduction in material costs (i.e., chemicals, electrocatalysts, experimental time). Although there are still many advancements to be made to reach this point, DFT has been very useful in today's world at helping explain the "why" behind many phenomena. For example, DFT has shed light on why copper is able to produce C_{2+} products.⁹² Additionally, it has been used to show that CO/H₂ competition can be tuned on Pd rich In catalysts.⁹³ In Chapter 6 of this thesis, DFT is employed to determine if impurities found in an industrial CO₂ stream could be potential poisons to the InBi catalyst used in Chapters 4 and 5.

Summary of Chapters

The content of this thesis aims to optimize the electrochemical reduction of CO₂ towards formate reaction using a GDE. Chapter 2 begins with discussing the theory of a GDE. The role of the gas diffusion layer and catalyst layer are discussed, and work that has been performed for this reaction is reviewed.

It is important to be able to separate and change the characteristics of both layers in a GDE for the overall optimization. The catalyst layer characteristics are relatively easy to change compared to the GDL characteristics. In Chapter 3, a patented method for producing gas diffusion layers is explored using a DOE to determine the range in various characteristics that can be achieved from this production method. This work yielded 26 GDLs with varying

characteristics that could be used in future studies to help identify significant interactions between the catalyst layer and the GDL.

Chapter 4 focuses on optimizing the overall GDE by utilizing another DOE. Two GDLs with varying characteristics from Chapter 3 are tested with various catalyst layers to determine which factors and interactions affect the performance of the gas diffusion electrode (GDE) the most. The work in Chapter 4 was performed at a 10 cm^2 scale and discovered a GDE formulation that achieved 99.4% CE at $400\text{mA}/\text{cm}^2$ for two hours of operation. We wanted to demonstrate the results from Chapter 4 could be scaled up, so a custom 200 cm^2 cell was designed and fabricated for this purpose. Chapter 5 reviews this cell design and demonstrates the best-performing experiment of Chapter 4 at this larger scale.

As this technology further matures and reaches commercialization, the source of CO_2 will eventually have to change from a gas cylinder to a point source. Consequently, the impurities present in the CO_2 feed from these various sources can be different and in higher concentrations than in a gas cylinder used in a research lab. In Chapter 6, we use DFT to help predict if any impurities found in an industrial CO_2 waste stream have the potential to poison the InBi catalyst used in this thesis.

References

- (1) Schneider, S. H. The Greenhouse Effect: Science and Policy. *Science* (80-.). **1989**, *243* (4892), 771–781, DOI 10.1126/science.243.4892.771.
- (2) Rodhe, H. A Comparison of the Contribution of Various Gases to the Greenhouse Effect. *Science* (80-.). **1990**, *248* (4960), 1217–1219, DOI 10.1126/science.248.4960.1217.
- (3) Gillingham, K.; Stock, J. H. The Cost of Reducing Greenhouse Gas Emissions. *J. Econ. Perspect.* **2018**, *32* (4), 53–72, DOI 10.1257/jep.32.4.53.
- (4) Keijer, T.; Bakker, V.; Slootweg, J. C. Circular Chemistry to Enable a Circular Economy. *Nat. Chem.* **2019**, *11* (3), 190–195, DOI 10.1038/s41557-019-0226-9.
- (5) Takht Ravanchi, M.; Sahebdehfar, S. Carbon Dioxide Capture and Utilization in Petrochemical Industry: Potentials and Challenges. *Appl. Petrochemical Res.* **2014**, *4* (1), 63–77, DOI 10.1007/s13203-014-0050-5.
- (6) Dodds, W. S.; Stutzman, L. F.; Sollami, B. J. Carbon Dioxide Solubility in Water. *Ind. Eng. Chem. Chem. Eng. Data Ser.* **1956**, *1* (1), 92–95, DOI 10.1021/i460001a018.
- (7) Innocent, B.; Liaigre, D.; Pasquier, D.; Ropital, F.; Léger, J.-M.; Kokoh, K. B. Electro-Reduction of Carbon Dioxide to Formate on Lead Electrode in Aqueous Medium. *J. Appl. Electrochem.* **2009**, *39* (2), 227–232, DOI 10.1007/s10800-008-9658-4.
- (8) Hara, K. Electrochemical Reduction of CO₂ on a Cu Electrode under High Pressure. *J. Electrochem. Soc.* **1994**, *141* (8), 2097, DOI 10.1149/1.2055067.
- (9) Kolyagin, G. A.; Vasil'eva, I. S.; Kornienko, V. L. Effect of the Composition of Gas-Diffusion Carbon Black Electrodes on Electrosynthesis of Hydrogen Peroxide from Atmospheric Oxygen. *Russ. J. Appl. Chem.* **2008**, *81* (6), 983–987, DOI 10.1134/S1070427208060116.
- (10) Monteiro, M. C. O.; Philips, M. F.; Schouten, K. J. P.; Koper, M. T. M. Efficiency and Selectivity of CO₂ Reduction to CO on Gold Gas Diffusion Electrodes in Acidic Media. *Nat. Commun.* **2021**, *12* (1), 4943, DOI 10.1038/s41467-021-24936-6.
- (11) Maja, M.; Orecchia, C.; Strano, M.; Tosco, P.; Vanni, M. Effect of Structure of the Electrical Performance of Gas Diffusion Electrodes for Metal Air Batteries. *Electrochim. Acta* **2000**, *46* (2–3), 423–432, DOI 10.1016/S0013-4686(00)00601-0.
- (12) Wang, P.; Zhao, J.; Shi, R.; Zhang, X.; Guo, X.; Dai, Q.; Zhang, T. Efficient Photocatalytic Aerobic Oxidation of Bisphenol A via Gas-Liquid-Solid Triphase Interfaces. *Mater. Today Energy* **2022**, *23*, 100908, DOI 10.1016/j.mtener.2021.100908.

- (13) Shi, R.; Wang, Z.; Zhao, Y.; Waterhouse, G. I. N.; Li, Z.; Zhang, B.; Sun, Z.; Xia, C.; Wang, H.; Zhang, T. Room-Temperature Electrochemical Acetylene Reduction to Ethylene with High Conversion and Selectivity. *Nat. Catal.* **2021**, 4 (7), 565–574, DOI 10.1038/s41929-021-00640-y.
- (14) Pozio, A.; Cemmi, A.; Carewska, M.; Paoletti, C.; Zaza, F. Characterization of Gas Diffusion Electrodes for Polymer Electrolyte Fuel Cells. *J. Fuel Cell Sci. Technol.* **2010**, 7 (4), 041003, DOI 10.1115/1.3119061.
- (15) Schuler, E.; Ermolich, P. A.; Shiju, N. R.; Gruter, G. J. M. Monomers from CO₂: Superbases as Catalysts for Formate-to-Oxalate Coupling. *ChemSusChem* **2021**, n/a (n/a), DOI 10.1002/cssc.202002725.
- (16) Morgan, E. R.; Manwell, J. F.; McGowan, J. G. Opportunities for Economies of Scale with Alkaline Electrolyzers. *Int. J. Hydrogen Energy* **2013**, 38 (36), 15903–15909, DOI 10.1016/j.ijhydene.2013.08.116.
- (17) Jones, J.-P.; Prakash, G. K. S.; Olah, G. A. Electrochemical CO₂ Reduction: Recent Advances and Current Trends. *Isr. J. Chem.* **2014**, 54 (10), 1451–1466, DOI 10.1002/ijch.201400081.
- (18) Schuler, E.; Demetriou, M.; Shiju, N. R.; Gruter, G. M. Towards Sustainable Oxalic Acid from CO₂ and Biomass. *ChemSusChem* **2021**, 14 (18), 3636–3664, DOI 10.1002/cssc.202101272.
- (19) Durst, J.; Rudnev, A.; Dutta, A.; Fu, Y.; Herranz, J.; Kaliginedi, V.; Kuzume, A.; Permyakova, A. A.; Paratcha, Y.; Broekmann, P.; Schmidt, T. J. Electrochemical CO₂ Reduction – A Critical View on Fundamentals, Materials and Applications. *Chim. Int. J. Chem.* **2015**, 69 (12), 769–776, DOI 10.2533/chimia.2015.769.
- (20) Oloman, C.; Li, H. Electrochemical Processing of Carbon Dioxide. *ChemSusChem* **2008**, 1 (5), 385–391, DOI 10.1002/cssc.200800015.
- (21) Martín, A. J.; Larrazábal, G. O.; Pérez-Ramírez, J. Towards Sustainable Fuels and Chemicals through the Electrochemical Reduction of CO₂: Lessons from Water Electrolysis. *Green Chem.* **2015**, 17 (12), 5114–5130, DOI 10.1039/C5GC01893E.
- (22) Verma, S.; Kim, B.; Jhong, H.-R. “Molly”; Ma, S.; Kenis, P. J. A. A Gross-Margin Model for Defining Technoeconomic Benchmarks in the Electroreduction of CO₂. *ChemSusChem* **2016**, 9 (15), 1972–1979, DOI 10.1002/cssc.201600394.
- (23) Venn Diagram. In *The SAGE Encyclopedia of Social Science Research Methods*; Sage Publications, Inc.: 2455 Teller Road, Thousand Oaks California 91320 United States of America, DOI 10.4135/9781412950589.n1074.

- (24) Bitar, Z.; Fecant, A.; Trela-Baudot, E.; Chardon-Noblat, S.; Pasquier, D. Electrocatalytic Reduction of Carbon Dioxide on Indium Coated Gas Diffusion Electrodes—Comparison with Indium Foil. *Appl. Catal. B Environ.* **2016**, *189*, 172–180, DOI 10.1016/j.apcatb.2016.02.041.
- (25) Wang, Q.; Dong, H.; Yu, H. Fabrication of a Novel Tin Gas Diffusion Electrode for Electrochemical Reduction of Carbon Dioxide to Formic Acid. *RSC Adv.* **2014**, *4* (104), 59970–59976, DOI 10.1039/C4RA10775F.
- (26) Kopljär, D.; Inan, A.; Vindayer, P.; Wagner, N.; Klemm, E. Electrochemical Reduction of CO₂ to Formate at High Current Density Using Gas Diffusion Electrodes. *J. Appl. Electrochem.* **2014**, *44* (10), 1107–1116, DOI 10.1007/s10800-014-0731-x.
- (27) Whipple, D. T.; Finke, E. C.; Kenis, P. J. A. Microfluidic Reactor for the Electrochemical Reduction of Carbon Dioxide: The Effect of PH. *Electrochem. Solid-State Lett.* **2010**, *13* (9), B109, DOI 10.1149/1.3456590.
- (28) Hara, K. High Efficiency Electrochemical Reduction of Carbon Dioxide under High Pressure on a Gas Diffusion Electrode Containing Pt Catalysts. *J. Electrochem. Soc.* **1995**, *142* (4), L57, DOI 10.1149/1.2044182.
- (29) Li, A.; Wang, H.; Han, J.; Liu, L. Preparation of a Pb Loaded Gas Diffusion Electrode and Its Application to CO₂ Electroreduction. *Front. Chem. Sci. Eng.* **2012**, *6* (4), 381–388, DOI 10.1007/s11705-012-1216-2.
- (30) Mahmood, M. N.; Masheder, D.; Harty, C. J. Use of Gas-Diffusion Electrodes for High-Rate Electrochemical Reduction of Carbon Dioxide. I. Reduction at Lead, Indium- and Tin-Impregnated Electrodes. *J. Appl. Electrochem.* **1987**, *17* (6), 1159–1170, DOI 10.1007/BF01023599.
- (31) Prakash, G. K. S.; Viva, F. A.; Olah, G. A. Electrochemical Reduction of CO₂ over Sn-Nafion® Coated Electrode for a Fuel-Cell-like Device. *J. Power Sources* **2013**, *223*, 68–73, DOI 10.1016/j.jpowsour.2012.09.036.
- (32) Köleli, F.; Atilan, T.; Palamut, N.; Gizir, A. M.; Aydin, R.; Hamann, C. H. Electrochemical Reduction of CO₂ at Pb- and Sn-Electrodes in a Fixed-Bed Reactor in Aqueous K₂CO₃ and KHCO₃ Media. *J. Appl. Electrochem.* **2003**, *33* (5), 447–450, DOI 10.1023/A:1024471513136.
- (33) Subramanian, K.; Asokan, K.; Jeevarathinam, D.; Chandrasekaran, M. Electrochemical Membrane Reactor for the Reduction of Carbondioxide to Formate. *J. Appl. Electrochem.* **2007**, *37* (2), 255–260, DOI 10.1007/s10800-006-9252-6.
- (34) Machunda, R. L.; Ju, H.; Lee, J. Electrocatalytic Reduction of CO₂ Gas at Sn Based Gas Diffusion Electrode. *Curr. Appl. Phys.* **2011**, *11* (4), 986–988, DOI 10.1016/j.cap.2011.01.003.
- (35) Köleli, F.; Balun, D. Reduction of CO₂ under High Pressure and High Temperature on

- Pb-Granule Electrodes in a Fixed-Bed Reactor in Aqueous Medium. *Appl. Catal. A Gen.* **2004**, 274 (1–2), 237–242, DOI 10.1016/j.apcata.2004.07.006.
- (36) Del Castillo, A.; Alvarez-Guerra, M.; Irabien, A. Continuous Electroreduction of CO₂ to Formate Using Sn Gas Diffusion Electrodes. *AIChE J.* **2014**, 60 (10), 3557–3564, DOI 10.1002/aic.14544.
- (37) Hara, K.; Kudo, A.; Sakata, T. Electrochemical Reduction of Carbon Dioxide under High Pressure on Various Electrodes in an Aqueous Electrolyte. *J. Electroanal. Chem.* **1995**, 391 (1–2), 141–147, DOI 10.1016/0022-0728(95)03935-A.
- (38) Azuma, M. Electrochemical Reduction of Carbon Dioxide on Various Metal Electrodes in Low-Temperature Aqueous KHCO₃ Media. *J. Electrochem. Soc.* **1990**, 137 (6), 1772, DOI 10.1149/1.2086796.
- (39) Azuma, M.; Hashimoto, K.; Watanabe, M.; Sakata, T. Electrochemical Reduction of Carbon Dioxide to Higher Hydrocarbons in a KHCO₃ Aqueous Solution. *J. Electroanal. Chem. Interfacial Electrochem.* **1990**, 294 (1–2), 299–303, DOI 10.1016/0022-0728(90)87154-C.
- (40) Alvarez-Guerra, M.; Quintanilla, S.; Irabien, A. Conversion of Carbon Dioxide into Formate Using a Continuous Electrochemical Reduction Process in a Lead Cathode. *Chem. Eng. J.* **2012**, 207–208, 278–284, DOI 10.1016/j.ccej.2012.06.099.
- (41) Alvarez-Guerra, M.; Del Castillo, A.; Irabien, A. Continuous Electrochemical Reduction of Carbon Dioxide into Formate Using a Tin Cathode: Comparison with Lead Cathode. *Chem. Eng. Res. Des.* **2014**, 92 (4), 692–701, DOI 10.1016/j.cherd.2013.11.002.
- (42) Irtem, E.; Andreu, T.; Parra, A.; Hernández-Alonso, M. D.; García-Rodríguez, S.; Riesco-García, J. M.; Penelas-Pérez, G.; Morante, J. R. Low-Energy Formate Production from CO₂ Electroreduction Using Electrodeposited Tin on GDE. *J. Mater. Chem. A* **2016**, 4 (35), 13582–13588, DOI 10.1039/C6TA04432H.
- (43) Li, H.; Oloman, C. Development of a Continuous Reactor for the Electro-Reduction of Carbon Dioxide to Formate – Part 2: Scale-Up. *J. Appl. Electrochem.* **2007**, 37 (10), 1107–1117, DOI 10.1007/s10800-007-9371-8.
- (44) Fu, Y.; Li, Y.; Zhang, X.; Liu, Y.; Qiao, J.; Zhang, J.; Wilkinson, D. P. Novel Hierarchical SnO₂ Microsphere Catalyst Coated on Gas Diffusion Electrode for Enhancing Energy Efficiency of CO₂ Reduction to Formate Fuel. *Appl. Energy* **2016**, 175, 536–544, DOI 10.1016/j.apenergy.2016.03.115.
- (45) Tapan, N. A. CO₂ Electroreduction on P4VP Modified Copper Deposited Gas Diffusion Layer Electrode: PH Effect. *Mater. Renew. Sustain. Energy* **2016**, 5 (4), 19, DOI 10.1007/s40243-016-0082-0.
- (46) Zhang, Q.; Li, Y.; Hou, X. fan; Jung, J.; Qiao, J. Formate Fuel Production from the

- Electroreduction of CO₂ on Nanostructured SnO_x Coated on Gas Diffusion Electrode. *ECS Trans.* **2017**, *80* (9), 159–164, DOI 10.1149/08009.0159ecst.
- (47) Su, P.; Xu, W.; Qiu, Y.; Zhang, T.; Li, X.; Zhang, H. Ultrathin Bismuth Nanosheets as a Highly Efficient CO₂ Reduction Electrocatalyst. *ChemSusChem* **2018**, *11* (5), 848–853, DOI 10.1002/cssc.201702229.
- (48) Choi, S. Y.; Jeong, S. K.; Kim, H. J.; Baek, I.-H.; Park, K. T. Electrochemical Reduction of Carbon Dioxide to Formate on Tin–Lead Alloys. *ACS Sustain. Chem. Eng.* **2016**, *4* (3), 1311–1318, DOI 10.1021/acssuschemeng.5b01336.
- (49) Fu, Y.; Li, Y.; Zhang, X.; Liu, Y.; Zhou, X.; Qiao, J. Electrochemical CO₂ Reduction to Formic Acid on Crystalline SnO₂ Nanosphere Catalyst with High Selectivity and Stability. *Chinese J. Catal.* **2016**, *37* (7), 1081–1088, DOI 10.1016/S1872-2067(15)61048-8.
- (50) Zhang, S.; Kang, P.; Meyer, T. J. Nanostructured Tin Catalysts for Selective Electrochemical Reduction of Carbon Dioxide to Formate. *J. Am. Chem. Soc.* **2014**, *136* (5), 1734–1737, DOI 10.1021/ja4113885.
- (51) Zhang, Y.; Zhang, X.; Bond, A. M.; Zhang, J. Identification of a New Substrate Effect That Enhances the Electrocatalytic Activity of Dendritic Tin in CO₂ Reduction. *Phys. Chem. Chem. Phys.* **2018**, *20* (8), 5936–5941, DOI 10.1039/C7CP07723H.
- (52) Yadav, V. S. K.; Noh, Y.; Han, H.; Kim, W. B. Synthesis of Sn Catalysts by Solar Electro-Deposition Method for Electrochemical CO₂ Reduction Reaction to HCOOH. *Catal. Today* **2018**, *303*, 276–281, DOI 10.1016/j.cattod.2017.09.015.
- (53) Zhang, X.; Lei, T.; Liu, Y.; Qiao, J. Enhancing CO₂ Electrolysis to Formate on Facilely Synthesized Bi Catalysts at Low Overpotential. *Appl. Catal. B Environ.* **2017**, *218*, 46–50, DOI 10.1016/j.apcatb.2017.06.032.
- (54) Zhao, C.; Wang, J. Electrochemical Reduction of CO₂ to Formate in Aqueous Solution Using Electro-Deposited Sn Catalysts. *Chem. Eng. J.* **2016**, *293*, 161–170, DOI 10.1016/j.cej.2016.02.084.
- (55) Chen, Z.; Wang, N.; Yao, S.; Liu, L. The Flaky Cd Film on Cu Plate Substrate: An Active and Efficient Electrode for Electrochemical Reduction of CO₂ to Formate. *J. CO₂ Util.* **2017**, *22*, 191–196, DOI 10.1016/j.jcou.2017.09.023.
- (56) Lei, T.; Zhang, X.; Jung, J.; Cai, Y.; Hou, X.; Zhang, Q.; Qiao, J. Continuous Electroreduction of Carbon Dioxide to Formate on Tin Nanoelectrode Using Alkaline Membrane Cell Configuration in Aqueous Medium. *Catal. Today* **2018**, *318*, 32–38, DOI 10.1016/j.cattod.2017.10.003.
- (57) Li, Q.; Wang, Z.; Zhang, M.; Hou, P.; Kang, P. Nitrogen Doped Tin Oxide Nanostructured Catalysts for Selective Electrochemical Reduction of Carbon Dioxide to

- Formate. *J. Energy Chem.* **2017**, 26 (5), 825–829, DOI 10.1016/j.jechem.2017.08.010.
- (58) Qin, B.; Wang, H.; Peng, F.; Yu, H.; Cao, Y. Effect of the Surface Roughness of Copper Substrate on Three-Dimensional Tin Electrode for Electrochemical Reduction of CO₂ into HCOOH. *J. CO₂ Util.* **2017**, 21, 219–223, DOI 10.1016/j.jcou.2017.07.012.
- (59) Xia, Z.; Freeman, M.; Zhang, D.; Yang, B.; Lei, L.; Li, Z.; Hou, Y. Highly Selective Electrochemical Conversion of CO₂ to HCOOH on Dendritic Indium Foams. *ChemElectroChem* **2018**, 5 (2), 253–259, DOI 10.1002/celec.201700935.
- (60) Lv, W.; Bei, J.; Zhang, R.; Wang, W.; Kong, F.; Wang, L.; Wang, W. Bi₂O₂CO₃ Nanosheets as Electrocatalysts for Selective Reduction of CO₂ to Formate at Low Overpotential. *ACS Omega* **2017**, 2 (6), 2561–2567, DOI 10.1021/acsomega.7b00437.
- (61) Moore, C. E.; Gyenge, E. L. Tuning the Composition of Electrodeposited Bimetallic Tin-Lead Catalysts for Enhanced Activity and Durability in Carbon Dioxide Electroreduction to Formate. *ChemSusChem* **2017**, 10 (17), 3512–3519, DOI 10.1002/cssc.201700761.
- (62) Huan, T. N.; Simon, P.; Rousse, G.; Génois, I.; Artero, V.; Fontecave, M. Porous Dendritic Copper: An Electrocatalyst for Highly Selective CO₂ Reduction to Formate in Water/Ionic Liquid Electrolyte. *Chem. Sci.* **2017**, 8 (1), 742–747, DOI 10.1039/C6SC03194C.
- (63) Rabiee, A.; Nematollahi, D. Electrochemical Reduction of CO₂ to Formate Ion Using Nanocubic Mesoporous In(OH)₃/Carbon Black System. *Mater. Chem. Phys.* **2017**, 193, 109–116, DOI 10.1016/j.matchemphys.2017.02.016.
- (64) Bertin, E.; Garbarino, S.; Roy, C.; Kazemi, S.; Guay, D. Selective Electroreduction of CO₂ to Formate on Bi and Oxide-Derived Bi Films. *J. CO₂ Util.* **2017**, 19, 276–283, DOI 10.1016/j.jcou.2017.04.006.
- (65) Bashir, S.; Hossain, S. S.; Rahman, S. ur; Ahmed, S.; Amir Al-Ahmed; Hossain, M. M. Electrocatalytic Reduction of Carbon Dioxide on SnO₂/MWCNT in Aqueous Electrolyte Solution. *J. CO₂ Util.* **2016**, 16, 346–353, DOI 10.1016/j.jcou.2016.09.002.
- (66) Jiang, H.; Zhao, Y.; Wang, L.; Kong, Y.; Li, F.; Li, P. Electrochemical CO₂ Reduction to Formate on Tin Cathode: Influence of Anode Materials. *J. CO₂ Util.* **2018**, 26, 408–414, DOI 10.1016/j.jcou.2018.05.029.
- (67) Proietto, F.; Schiavo, B.; Galia, A.; Scialdone, O. Electrochemical Conversion of CO₂ to HCOOH at Tin Cathode in a Pressurized Undivided Filter-Press Cell. *Electrochim. Acta* **2018**, 277, 30–40, DOI 10.1016/j.electacta.2018.04.159.
- (68) Hu, H.; Tang, Y.; Hu, Q.; Wan, P.; Dai, L.; Yang, X. J. In-Situ Grown Nanoporous Zn-Cu Catalysts on Brass Foils for Enhanced Electrochemical Reduction of Carbon Dioxide. *Appl. Surf. Sci.* **2018**, 445, 281–286, DOI 10.1016/j.apsusc.2018.03.146.

- (69) Yang, G.; Yu, Z.; Zhang, J.; Liang, Z. A Highly Efficient Flower-like Cobalt Catalyst for Electroreduction of Carbon Dioxide. *Chinese J. Catal.* **2018**, *39* (5), 914–919, DOI 10.1016/S1872-2067(18)63021-9.
- (70) Shin, W.; Oh, S. Y.; Kim, S. K.; Kwon, K. N.; Yu, C. H.; Kim, G. G. Amalgam Electrode, Producing Method Thereof, and Method of Electrochemical Reduction of Carbon Dioxide Using the Same. US 2016/0032470 A1, 2016.
- (71) Shin, W.; Park, M. J. Method and Device for Electrochemical Reduction of Carbon Dioxide. WO/2016/052985, 2016.
- (72) Zhang, S.; Kang, P.; Meyer, T. J. Nanotin Catalysts for Electrochemical Reduction of Carbon Dioxide to Formate. US 2016/0097136A1, 2016.
- (73) Park, T. T.; Jeong, S. K.; Kim, H. J.; Kang, S. P.; Youn, M. H. Method and Apparatus for Preparing Reduction Product of Carbon Dioxide by Electrochemically Reducing Carbon Dioxide. US 2018 / 0202056 A1, 2018.
- (74) Kopljar, D.; Wagner, N.; Klemm, E. Transferring Electrochemical CO₂ Reduction from Semi-Batch into Continuous Operation Mode Using Gas Diffusion Electrodes. *Chem. Eng. Technol.* **2016**, *39* (11), 2042–2050, DOI 10.1002/ceat.201600198.
- (75) Ikeda, S.; Ito, K.; Noda, H.; Rusop, M.; Soga, T. Electrochemical Reduction Of Carbon Dioxide Using Gas Diffusion Electrodes Loaded With Fine Catalysts. In *AIP Conference Proceedings*; AIP, 2009; pp 108–113, DOI 10.1063/1.3160110.
- (76) Hara, K.; Sakata, T. Large Current Density CO₂ Reduction under High Pressure Using Gas Diffusion Electrodes. *Bull. Chem. Soc. Jpn.* **1997**, *70* (3), 571–576, DOI 10.1246/bcsj.70.571.
- (77) Del Castillo, A.; Alvarez-Guerra, M.; Solla-Gullón, J.; Sáez, A.; Montiel, V.; Irabien, A. Sn Nanoparticles on Gas Diffusion Electrodes: Synthesis, Characterization and Use for Continuous CO₂ Electroreduction to Formate. *J. CO₂ Util.* **2017**, *18*, 222–228, DOI 10.1016/j.jcou.2017.01.021.
- (78) Hara, K. Electrocatalytic Formation of CH₄ from CO₂ on a Pt Gas Diffusion Electrode. *J. Electrochem. Soc.* **1997**, *144* (2), 539, DOI 10.1149/1.1837445.
- (79) Narayanan, S. R.; Haines, B.; Soler, J.; Valdez, T. I. Electrochemical Conversion of Carbon Dioxide to Formate in Alkaline Polymer Electrolyte Membrane Cells. *J. Electrochem. Soc.* **2011**, *158* (2), A167, DOI 10.1149/1.3526312.
- (80) Lee, W.; Kim, Y. E.; Youn, M. H.; Jeong, S. K.; Park, K. T. Catholyte-Free Electrocatalytic CO₂ Reduction to Formate. *Angew. Chemie* **2018**, *130* (23), 6999–7003, DOI 10.1002/ange.201803501.
- (81) Oloman, C.; Li, H. Continuous Co-Current Electrochemical Reduction of Carbon

- Dioxide. US 2016/0068974A1, 2016.
- (82) Oloman, C. Process for the Conversion of Carbon Dioxide to Formic Acid. WO 2015/143560 A1, 2015.
- (83) Shin, W.; Park, M. Amalgam Electrode, Method for Manufacturing the Same, and Method for Electrochemical Reduction of Carbon Dioxide Using the Same. US 2016/0298247 A1, 2016.
- (84) Sen, S.; Skinn, B.; Hall, T.; Inman, M.; Taylor, E. J.; Brushett, F. R. Pulsed Electrodeposition of Tin Electrocatalysts onto Gas Diffusion Layers for Carbon Dioxide Reduction to Formate. *MRS Adv.* **2017**, 2 (8), 451–458, DOI 10.1557/adv.2016.652.
- (85) Li, H.; Oloman, C. The Electro-Reduction of Carbon Dioxide in a Continuous Reactor. *J. Appl. Electrochem.* **2005**, 35 (10), 955–965, DOI 10.1007/s10800-005-7173-4.
- (86) Kaczur, J. J.; Kramer, T. J.; Keyshar, K.; Majsztrik, P.; Twardowski, Z. Process and High Surface Area Electrodes for the Electrochemical Reduction of Carbon Dioxide. US 8,858,777 B2, 2014.
- (87) SAS Institute Inc. *JMPTM 14 Design of Experiments Guide*; Cary, NC, 2018.
- (88) Claeskens, G.; Hjort, N. L. *Model Selection and Model Averaging*; 2006.
- (89) Klimberg, R.; McCullough, B. D. *Fundamentals of Predictive Analytics with JMP*; Cary, NC, 2013.
- (90) SAS Institute Inc. *JMPTM 14 Fitting Linear Models*; Cary, NC, 2018.
- (91) Thompson, J. Design and Analysis in Chemical Research; Tranter, R. L., Ed.; 2000; pp 85–110.
- (92) Dattila, F.; García-Muelas, R.; López, N. Active and Selective Ensembles in Oxide-Derived Copper Catalysts for CO₂ Reduction. *ACS Energy Lett.* **2020**, 5 (10), 3176–3184, DOI 10.1021/acsenergylett.0c01777.
- (93) Pavesi, D.; Dattila, F.; Van de Poll, R. C. J.; Anastasiadou, D.; García-Muelas, R.; Figueiredo, M.; Gruter, G.-J. M.; López, N.; Koper, M. T. M.; Schouten, K. J. P. Modulation of the Selectivity of CO₂ to CO Electroreduction in Palladium Rich Palladium-Indium Nanoparticles. *J. Catal.* **2021**, 402, 229–237, DOI 10.1016/j.jcat.2021.08.021.

Chapter 2

The Gas Diffusion Electrode²

² This chapter is based on Philips, M. F.; Gruter, G.-J. M.; Koper, M. T. M.; Schouten, K. J. P. Optimizing the Electrochemical Reduction of CO₂ to Formate: A State-of-the-Art Analysis. ACS Sustain. Chem. Eng. 2020, 8 (41), 15430–15444, DOI 10.1021/acssuschemeng.0c05215.

As discussed in Chapter 1, a GDE is the superior technology for the electrochemical reduction of CO_2 to formate. The mass transfer of CO_2 to the catalyst surface limits the reaction rates that pure metal electrodes are able to achieve. A GDE, however, enhances the mass transfer of gaseous reactants to an electrocatalyst allowing for higher reaction rates, or current densities, to be attained. This chapter seeks to explain how a GDE is structured and how it can create an environment that significantly increases the mass transfer of CO_2 to the electrocatalyst.

The GDE consists of a gas diffusion layer (GDL) and a catalyst layer. The GDL consists of a porous conductive material such as carbon felt or a woven carbon structure, which also acts as a current collector and can have a microporous layer (MPL) that is typically made from carbon and polytetrafluoro ethylene (PTFE). Figure 2.1a shows these layers of a GDE.

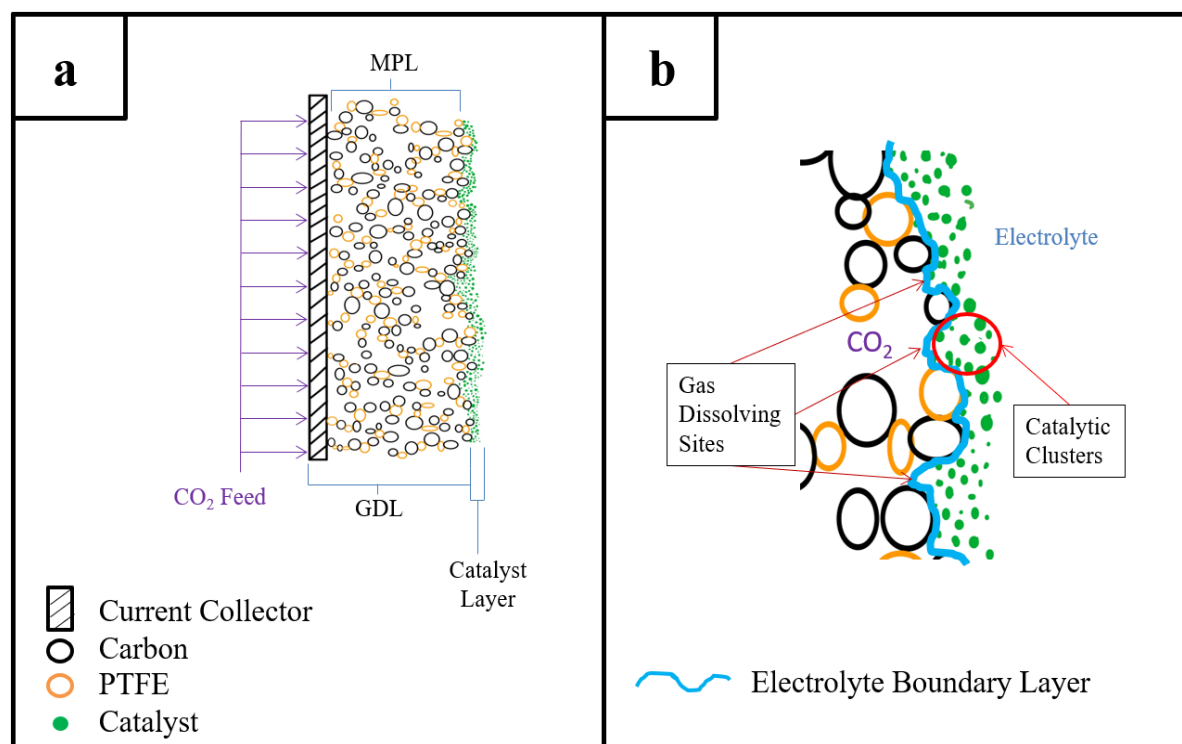


Figure 2.1. GDE layers (a) and the three-phase boundary (b)

There is common agreement that the GDE functions by maintaining three-phase boundaries with the reacting gas, liquid electrolyte, and catalyst particles.¹⁻⁵ These three-phase boundaries, shown in Figure 2.1b, are why gas diffusion electrodes outperform the other electrode types by achieving more favorable mass transfer. All of the other electrodes discussed in the previous section are limited by mass transfer related to the low solubility of CO_2 in water (about 33mM at room temperature).⁶ However, a well-synthesized GDE can drastically enhance mass transfer by creating a three-phase boundary. Thus, a GDE will not be limited at the same current density as a pure metal electrode.

The Limiting Current of GDEs

Motoo et al.⁷ explain the function of the three-phase boundary for fuel cells in four steps:

1. the supply of reactant gas to the gas chamber side of the GDL
2. the diffusion of reactant gas through the GDL to gas-dissolving sites
3. the diffusion of dissolved gas from gas-dissolving areas to catalytic sites (Figure 2.1b)
4. the reaction at catalytic sites

They further state that the limiting current of a GDE for fuel cells is determined by one of these four steps and mention that increasing the amount of gas dissolving sites should lead to a better-performing electrode. Li et al.² have obtained similar results for CO₂ electrochemical reduction. They mention that increasing the number of three-phase interfaces, or gas-dissolving sites, should promote higher reaction rates.

An additional consideration for GDEs in CO₂ reduction to formate is the diffusion of product away from the reaction site. Wang et al.⁸ have reported product accumulation in GDEs reacting CO₂ to formate. If the formate does not diffuse away as fast as it is generated, and it is not consumed (e.g., by another chemical in the electrolyte), then there will be local accumulation around the reaction sites. This could then lead to a decrease in performance and eventual electrode failure.

Influential Characteristics

The characteristics of the two layers of the GDE will influence the electrochemical performance of the electrode. The GDL's function is to maximize the number of gas diffusion sites that supply reactant gas and have a high conductivity to ensure uniform current distribution throughout the structure. The catalyst layer's function is to convert the dissolved reactant gas by having enough active surface area near the gas dissolving sites. Figure 2.2 lists several characteristics of these two layers that can influence the electrode performance in the form of a fishbone diagram.

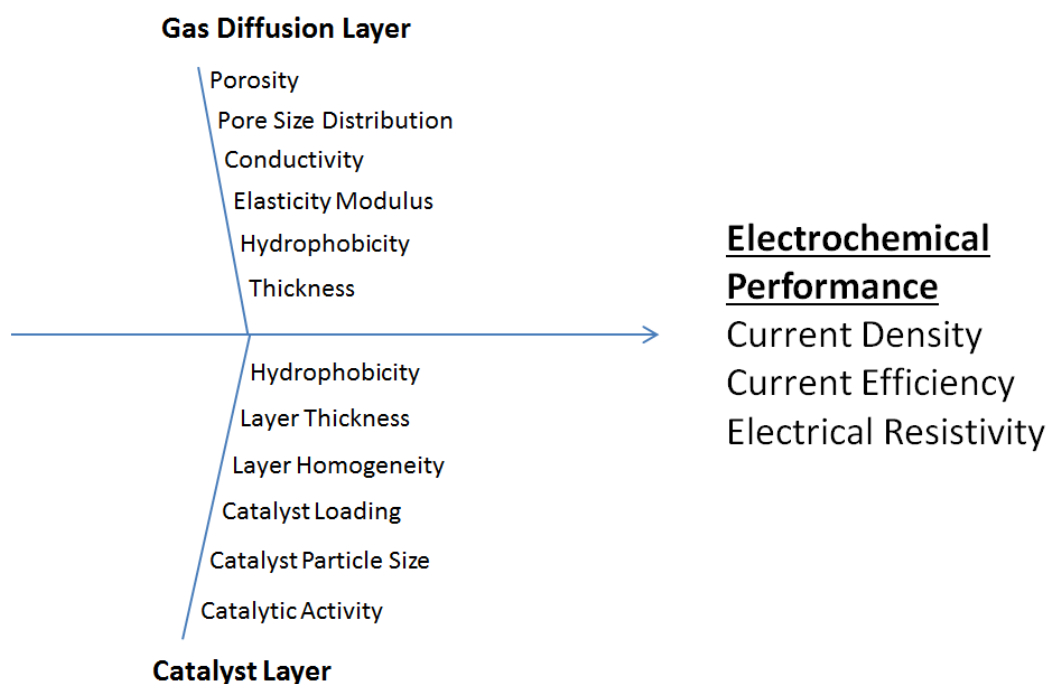


Figure 2.2. Fishbone diagram of factors influencing the electrochemical performance of GDEs

The characteristics of each layer should be fully tunable so that optimum GDEs can be identified; however, there is a lack of research reporting on how to tune some of these characteristics. A more detailed analysis of these characteristics for both layers is discussed in the following sections, starting with the GDL.

The Gas Diffusion Layer

Purpose of the GDL

The GDL has four prominent roles. It must conduct electrons to the catalyst layer^{7,9}, be mechanically stable¹⁰, supply reactant feed to the catalyst^{1,7}, and maintain the three-phase boundary by keeping water at the catalyst layer to prevent flooding^{1,7}. The GDE is ineffective if any of these conditions are not met. Furthermore, the ideal GDL should provide a high number of gas-dissolving sites when combined with the catalyst layer.^{2,7} Therefore, the characteristics of a GDL will strongly impact the performance of the complete electrode. Many factors can influence the characteristics of a GDL. Figure 2.3 displays these factors.

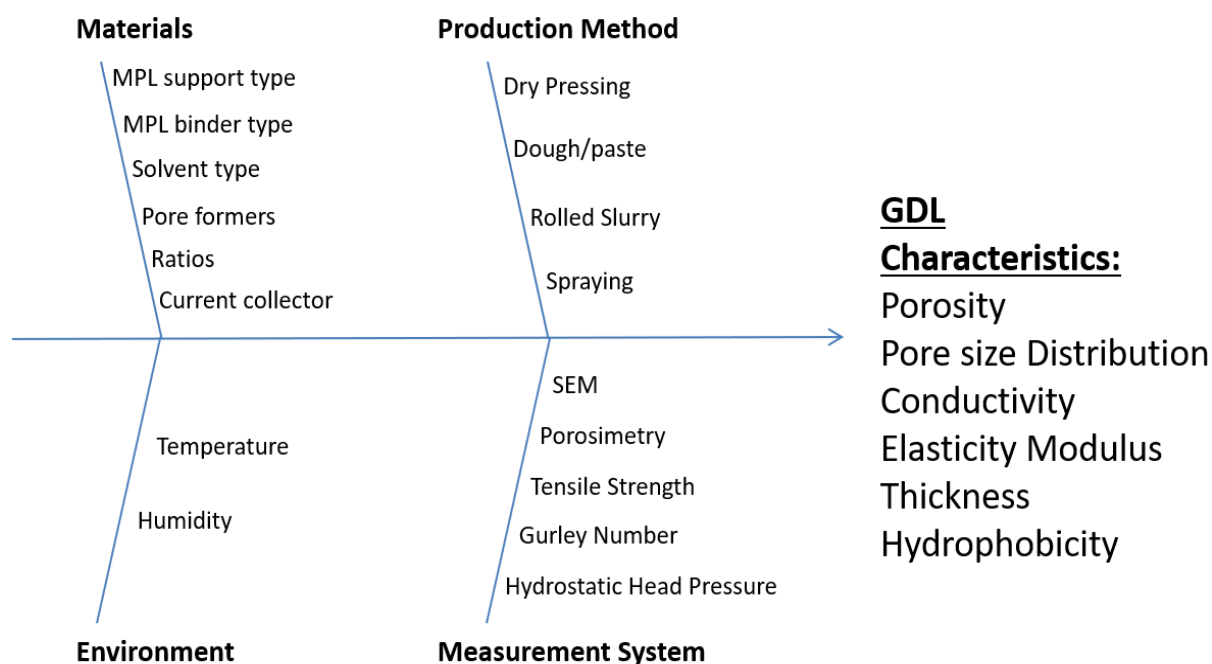


Figure 2.3. Fishbone diagram of factors in GDL production that can influence GDL characteristics

The materials used in the production, the production method, the measurement system used to quantify a characteristic, and environmental factors (such as humidity, room temperature, etc.) can all influence the reported GDL characteristics. The measurement system is also an essential consideration because it can affect which factor is observed to have an effect on the characteristic being studied. If there is a high measurement error from how a sample is taken and/or measured, then a specific factor can be deemed insignificant. Conversely, if the measurement system had a lower error, the factor may have been deemed significant. Knowing which characteristics of a GDL are most important and how to quantify them is not straightforward. Hence, we start by looking at what has been done in GDL research across various fields.

GDL Characteristics and Measurement Systems

The use of GDEs in the field of CO₂ reduction is limited; however, GDLs are used in other electrochemical fields that can still be relevant to CO₂ reduction. A lot of characterization research has been performed on GDLs for use in polymer electrolyte membrane fuel cells (PEMFC), oxygen electrodes (such as oxygen depolarized cathodes), and GDLs used in alkaline fuel cells. Although these fields are different, and the desired characteristics for the GDLs may differ, the characteristics of interest should still be the same. The various characteristics studied and the methods used for characterization across six fields of GDLs are shown in Table 2.1 and further discussed next.

Table 2.1 Common GDL Characterization Methods^{1–4,11–20}

GDL Characteristic	Method
Composition	TGA DTA
Conductivity	Contact Resistance
Electrolyte Absorption	Weighing
Hydrophobicity	Wetting
Optical/ Morphological	SEM TEM
Permeability	Diffusion Volume Darcy's Law Gas Perm. Coeff. Gurley densometer Capillary Flow Porometer
Porosity	SEM Hg Porosimetry KOH Porosimetry EIS
Surface Composition	XPS
Thickness	Calipers SEM

Porosity and Pore Size Distribution

Porosity and optical/morphological characterization are performed the most for the GDL. Maja et al.¹⁷ and Uchida et al.²⁰ determined that the pore size distribution in a GDL influences the performance of the electrode for metal-air batteries and PEMFCs, respectively. Kong et al.¹⁹ concluded that the pore size distribution is more important than the total porosity in affecting the cell performance of fuel cells.

Various methods are used to measure porosity. Hg porosimetry is most frequently used to characterize the porosity of the GDL. KOH porosimetry, scanning electron microscopy (SEM), and electrochemical impedance spectroscopy (EIS) have also been used to characterize the porosity of structures. SEM seems to be a method prone to significant errors if the structures made are not uniform, as the number of pores to characterize in a 10cm² structure would be impractical to image with SEM. Furthermore, SEM does not give any information on the pore size distribution or the internal pores in the structure. Hg porosimetry could also be prone to measurement errors if a structure is not uniform; however, combining various sections of a structure in one sample with this method could reduce this error.²¹ Combining a visual

microscopy method with Hg porosimetry could confirm the uniformity of a structure and increase confidence in the porosity measurement.

Gas Permeability

The gas permeability of the GDL is the second most studied characteristic of 12 studies found on GDLs, and there is no common way of measuring this characteristic. Tseng et al.¹⁴ used a capillary flow porometer to measure gas permeability, while Pozio et al.¹ used a Gurley densometer, which has ISO-certified methods. Both studies found that gas permeability increased with increasing PTFE concentrations used in GDL synthesis. The other publications measuring permeability seem to use their own method to estimate the value, which causes difficulty in comparing results. Furthermore, the porosity of the GDL should highly influence the permeability of the structure and could be a more important characteristic to use for these structures than gas permeability.

Conductivity, Composition, and Hydrophobicity

The conductivity, hydrophobicity, and composition of the GDL are less studied than the other characteristics. Pozio et al.¹ measured the conductivity of the GDLs by contact resistance and estimated the total composition of commercial GDLs by thermogravimetric analysis - differential thermal analysis (TGA - DTA) measurements. Schulze et al.³ used X-ray photoelectron spectroscopy (XPS) to measure the surface composition of the GDL and studied the hydrophobicity of the structures by wetting with liquid water and water vapor. Maja et al.¹⁷ measured the electrolyte absorption in the GDL by weighing the structure before and after operating in a flow cell. They discovered that excessive electrode wettability leads to degradation of the cathode performance. However, this method to determine electrolyte absorption could lead to large variations if used for electrolyte-wetted GDEs, and the process of drying the wetted layer is not optimized.

Surprisingly, the hydrophobicity of this layer is not more frequently studied. Electrolyte contact angle could be a more helpful measurement for hydrophobicity since it is a quantitative rather than qualitative measurement; however, no studies on GDLs were found that use this technique. Furthermore, no studies were found that look into the resistance of this layer to hydrostatic head. These two factors should play a significant role in preventing flooding and maintaining structural stability as it is scaled up.

GDL Characteristics Outlook

These studies performed on the characterization of GDLs attempt to link the structural characteristics to electrochemical performance, but only one study was found that investigates how production factors influence GDL characteristics. Moussallem et al.¹⁶ studied GDLs for oxygen depolarized cathodes. They found that variations in the temperature between 100-160 °C when hot pressing their electrodes led to a more stable performance of their electrode. They also found the sintering temperature did not affect the performance of the electrodes when between 280 and 380 °C. Finally, they determined that the porosity of their electrode almost linearly decreased with their applied pressure, although this only affected performance when

below a certain porosity. This study, however, did not consider the effect of different material types, which could also influence the findings. We next consider the materials commonly used in GDL production methods before discussing the methods used to produce GDLs for the CO₂ to formate reaction.

GDL Materials

There are five common categories of materials used to synthesize a GDL (see Figure 2.1): support and binder of the MPL, solvent, pore former, and current collector. An overview of the materials used in the GDL production methods found in the literature and the production method type and intended field of application can be found in Table 2.2. The following paragraphs will discuss the effect of carbon, binder, solvent, pore former, and current collector on the GDL.

Table 2.2. GDL Synthesis Method Summary^{1-4,8,11,15-17,19,22-27}

Reference	Method Type	Field of Use	Additional Materials	Current Collector	Carbon Type	Binder Type	Solvent Type
15	Dry Pressing Approach	CO ₂ Reduction	Graphite	SGL, Sigracet GDL 35BC	Acetylene Black	PTFE suspension (TF 9207Z, Dyneon)	N/A
18	Slurry Rolled	CO ₂ Reduction	Na ₂ SO ₄	Foamed Nickel	Acetylene Black	PTFE emulsion	Ethanol
19	Wet Paste	CO ₂ Reduction	N/A	Ni mesh	Vulcan XC-72	Fluon, GP1, ICI	Water
65	Dry Deposition	CO ₂ Reduction	N/A	N/A	Acetylene Black	PTFE suspension (TF 9207Z, Dyneon™)	N/A
68	Spraying	CO ₂ Reduction	N/A	Toray Paper, TGP-90	Vulcan XC-72R	N/A	N/A
78	Spraying	PEMFC	Nafion™ 5% solution	Toray Paper, TGP-90	Super-P™ Carbon Black	PTFE suspension (TF 5033, Hoechst)	2-propanol
79	Dry Coating	PEMFC	N/A	N/A	Vulcan XC-72	PTFE suspension (TF 2053, Hoechst)	N/A
80	Dough Rolled & Hot Press	Generic	Petrol	Carbon Cloth	SH100 & XC-72R	PTFE suspension	Petrol
83	Mixed into paste then rolled	CO ₂ Reduction	N/A	N/A	Carbon Black	PTFE suspension	Ethanol
86	Mixed into paste then rolled	Oxygen Electrode	Graphite	Stainless Steel Screen	Activated Carbon	PTFE dispersion (Polyflon, Daikin)	N/A
90	Spraying	Oxygen Electrode	Non-ionic Surfactant (Triton-X 100)	Nickel Mesh	N/A	PTFE suspension (TF 5035R, Dyneon™)	Water
91	Single Pass Wet Fabrication	Metal Air Batteries	N/A	N/A	Varied	PTFE	Alcohol
93	Mixed into paste then rolled	PEMFC	LiCO ₃	Carbon Cloth	Vulcan XC-72	PTFE solution (60 wt%, Aldrich)	2-propanol
96	Dry Powder	GDE study	N/A	N/A	Acetylene Black	PTFE suspension (Fluoroplast 4D)	N/A
97	Ink applied to carbon cloth	PEMFC	N/A	Hydrophobic Carbon Cloth	Vulcan XC-72	PTFE solution	2-propanol
98	Dry Pressing	Oxygen Electrode	N/A	Nickel Grid	Varied	4D-fluoroplastic (FT-4D)	Water

MPL Support

The only MPL support to date is carbon. Unfortunately, there were no studies on carbon type for GDEs used in CO₂ reduction. However, three studies were found that investigated the carbon used in GDL production for GDL used in other fields. Maja et al.¹⁷ studied the effect of carbon type on the performance of metal-air battery gas diffusion electrodes. Acetylene (Shawinigan Black AB50™) and two types of oil-furnace carbon (Vulcan XC72R™ and Black Pearls 3700™) were studied. They found that cathode performance decrease is caused by excessive electrode wettability. Additionally, they discovered that electrodes with oil-furnace blacks were the least stable due to the large wet pore volume in the active layer for their production method. Tomantschger et al.⁴ also determined acetylene black to be the material of choice for the diffusion layer of alkaline fuel cells after considering a furnace black (Vulcan XC-72R), acetylene black (Shawinigan SH100), oil flame black (Lampblack), and activated carbon (Black Pearls 2000). Kolyagin et al.²⁷ determined the best results for GDEs reacting oxygen to hydrogen peroxide composed of a 1:1 mixture of a hydrophobic acetylene black (A473-E) and a semi-hydrophobic furnace black (P702).

MPL Binder

Three studies were encountered that examined the PTFE content in a generic GDL. Kolyagin et al.²⁴ found that an increase in the PTFE content from 8 to 40 wt % increases the average diameter of hydrophilic pores and decreases the structure's surface area. Additionally, the whole carbon black surface is wetted by electrolyte with 8 - 20 wt % of PTFE. Similarly, Schulze et al.³ determined that a PTFE concentration of ~20 wt% marks the transition between hydrophilic and hydrophobic surfaces in their electrode structures. In addition to the permeability studies performed by Tseng et al.¹⁴ and Pozio et al.¹, Li et al.² found CO₂ permeability to be optimal when 30% PTFE is used in the GDL. Furthermore, they discovered that excess PTFE causes the carbon material to agglomerate too much, causing a blockage of pathways for CO₂ transport.

Solvent

Only one source was found that discusses the solvent in the formulation mixture of GDLs. Pozio et al.¹ studied using a water mixture with an alcohol (isopropanol or ethanol) and found that adding a 1:1 and 1:3 water/alcohol mixture to their 35 wt % PTFE solution turned the mixture into a gel. This mixture gelling allowed them to apply the GDL to the current collector better, resulting in a more homogeneous structure seen through surface continuity.

Pore Former

Pore formers can increase the porosity of the GDL structure, which can potentially increase the number of three-phase boundaries and enhance the performance of the overall electrode. However, the use of pore formers in producing GDLs is rare. Consequently, no studies were found that use pore formers in GDLs for CO₂ reduction. Only two studies were found that considered using pore formers in their GDL formulations for PEMFCs. Kong et al.¹⁹ varied amounts of LiCO₃ from 0 to 200 wt% relative to the carbon loading in the GDL. Their data

suggests using 58 wt% of pore former to create an optimal macropore volume of the GDL, which is desirable for PEMFCs. Zhao et al.²⁸ use several ammonium-based salts as pore formers. They found that the addition of NH_4CO_3 decreased the transport resistance of the structure and reduced the necessary catalyst loading while maintaining the same performance.

Current Collector

No sources were encountered that investigated the effects of varying the current collector on the performance of the GDL. This is most likely because it is not as crucial as the MPL in the function of the GDE. The current collector must only be conductive and not cause any preferential flow of reactant gas through sections of the structure. Furthermore, there is no way to modify the current collector itself. In all of the methods reviewed, only one method is used to attach the GDL to the current collector compared to the many techniques used to create and structure the GDL.

GDL Materials Outlook

It is challenging to draw conclusions about materials from combined data because each publication uses different GDL production methods. Furthermore, in most studies, only one material factor is varied, and the results are reported. This linear experimentation methodology neglects any interactions between factors that may affect the measured responses. For example, the optimal amount of PTFE can be determined for one carbon type but may be different for another carbon type. Similarly, one carbon type can be the best for a specific production method; however, another carbon type may be best for a different method. The variations in production methods are discussed next.

GDL Production Methods in Literature

The performance of different GDL production methods found for CO_2 reduction to formate reported in 5 various references is compared in Figure 2.4, while Figure 2.5 shows a block diagram of the steps used in the respective GDL production methods.

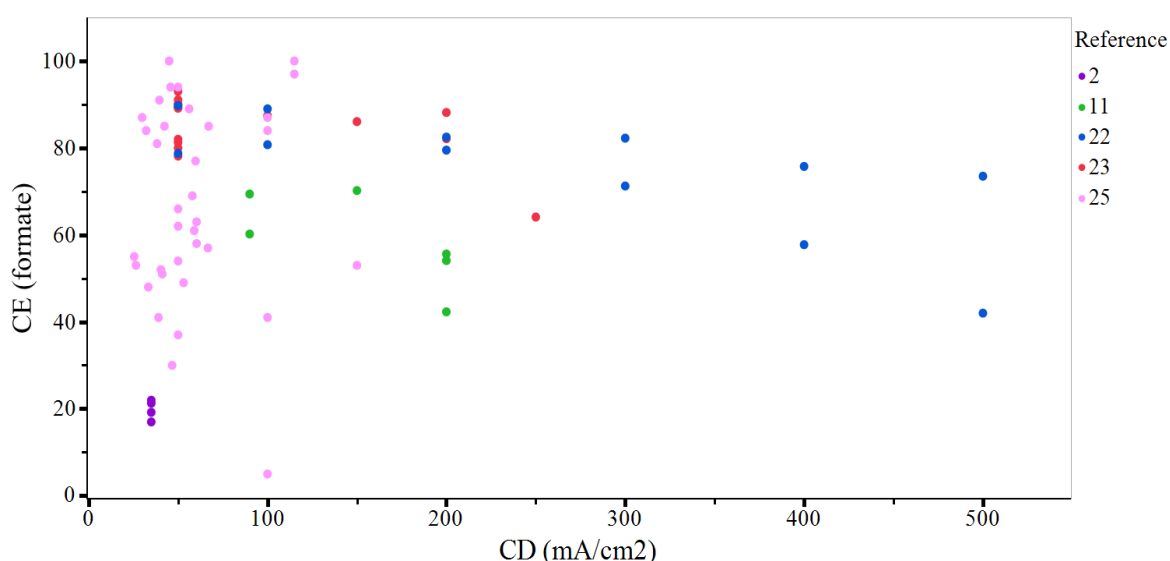
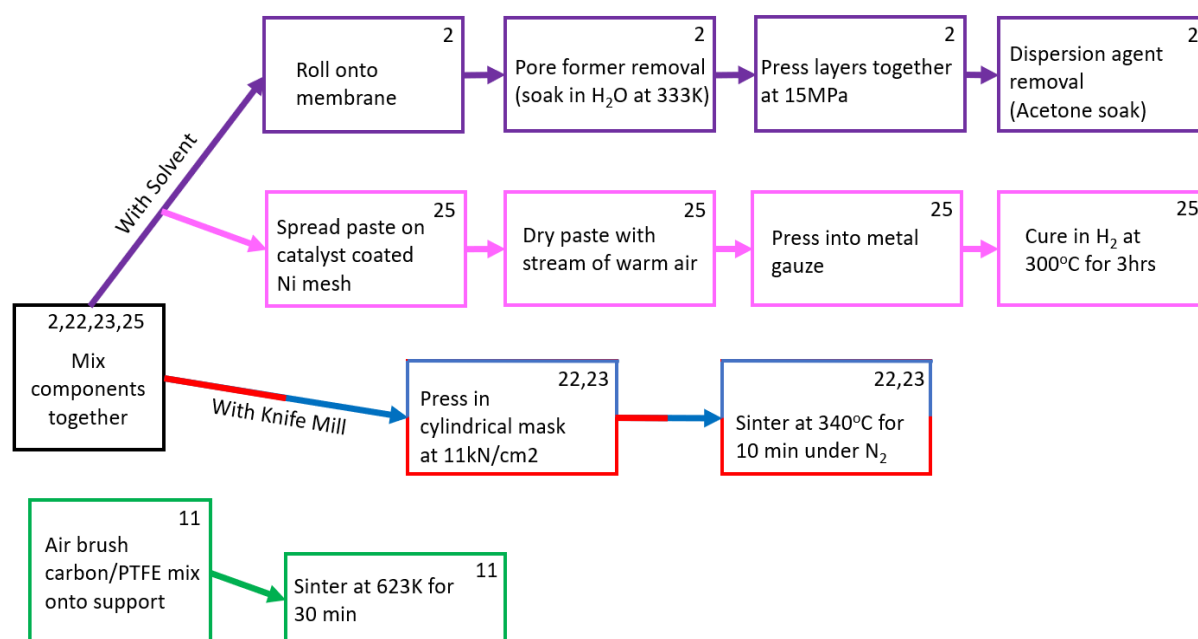


Figure 2.4. Performance of synthesized GDLs from literature.^{2,15,22,23,25}**Figure 2.5.** GDL production methods.^{2,15,22,23,25}

As seen in Figures 2.4 and 2.5, Mahmood et al.²⁵ achieve the highest current efficiency up to current densities near 100mA/cm² while using a wet method to produce GDLs. However, their performance seems to decline at 150mA/cm². Kopljar et al.^{22,23} demonstrate the highest current efficiencies at current densities beyond 100mA/cm² using a dry GDL production method.

Of course, other factors could be influencing the reported electrochemical performance. For example, the catalyst layer is different between these studies and will affect the electrochemical performance. However, there is still a lot of variance observed in data within individual studies and between studies that use the same catalyst.^{15,22,23,25} The lack of reproducibility of a GDL production method could be causing a lot of this variance; yet, no studies have been found that investigate the reproducibility of a production method. The reproducibility of a method can be advantageous to study as it will be necessary to understand when scaling up GDLs. With this in mind, we found two patents on methods to produce a GDL.

Patented GDL Production Methods

Gulla et al.²⁹ use a wet method to produce a GDL. They use acetylene black (Shawinigan Black™), a suspension of PTFE, and a 1:1 isopropanol (IPA):H₂O as the solvent. The formulation in this method is similar to other wet methods, and the solvent ratio used is in the same optimal range that Pozio et al.¹ found. This method uses calendaring followed by hot pressing to turn the dough mixture into a GDL. In one example given, they first extrude the dough to the desired thickness and then hot press it onto a silver mesh at 17.9 kPa and 120°C for 30 minutes. Then they increase the temperature and pressure to 335 °C and 44.8 kPa for 30 minutes before releasing the pressure and exposing the structure to ambient air for five minutes. The final step is to hot press again at 34.5 kPa at 335 °C for 30 minutes. This patent mentions advantages of this GDL, including its resistance to hydrostatic head, which allows for cheaper

cell designs that allow for lower cell potentials. In addition to the hydrostatic head characteristic, this patent characterizes the longitudinal elastic modulus of its structures, and they claim their GDLs have a longitudinal elastic modulus of at least 10,000 MPa.

The method used in this patent is very similar to the method Tomantschger et al.⁴ used earlier. Once they make the dough, it is pressed to a carbon cloth backing at 20 kg/cm². They heat their structure in three stages, starting at 100 °C for decomposition of ammonium bicarbonate (pore former). They then ramp up to 175 °C for the evaporation of their suspension agent. Finally, they sinter the structure at 320 °C for 20 min.

Another patent was found from Turek et al.³⁰, who started from a suspension to make GDLs. They make the suspension by mixing a silver catalyst, a PTFE suspension, a non-ionic surfactant, and hydroxyethyl methyl cellulose as a thickening agent. They disperse this mixture using a rotor-stator system in pulses to avoid excessive heating of the solution. They then spray this suspension several times onto nickel foam that is maintained at 100 °C. Once the desired loading is reached, they hot press the structure at 0.14 tonne/cm² and 130 °C before ramping to a sintering temperature of 340 °C for 15 minutes.

GDL Outlook

Patents do not discuss the scientific reasoning behind the material choice and the ratios that were used. Additionally, there is a lack of insight into the effect one step may have on the characteristics of the GDL structure. Understanding the production factors' influence on the characteristics of a GDL is critical for developing GDLs, and more focus should be given to this area in the future. Ideally, a method should be identified and developed to produce tunable GDLs. This would lay the groundwork for future studies to investigate GDL characteristics in more detail.

No studies were found that investigate how the catalyst layer characteristics can interact with the GDL characteristics to affect the electrochemical performance of the GDE. Including GDL characteristics with the optimization of the catalyst layer would be most beneficial as global, rather than local, optimums could be identified. Future research should strive to take this approach to optimize GDEs for this reaction. The catalyst layer is discussed next to better understand the key factors that should be included in studies that combine GDL and catalyst layer characteristics' influence on the GDE performance.

The Catalyst Layer

The catalyst layer consists of the electrocatalyst, usually immobilized on a supporting material that is applied to the GDL using various methods, with or without the use of a binder. Figure 2.6 shows factors of the catalyst layer that can influence the electrochemical performance of the GDE.

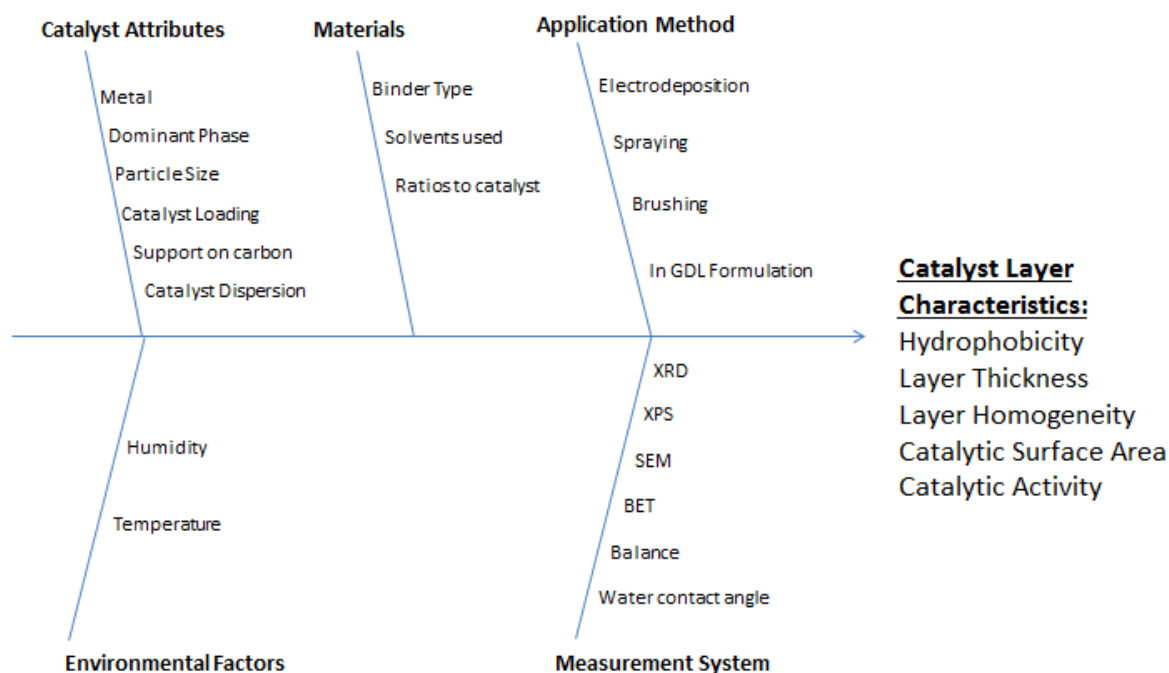


Figure 2.6. Fishbone diagram of factors influencing the catalyst layer.

The catalyst attributes, the materials used, and the application method can affect the characteristics of the catalyst layer. Similar to the GDL, the methods used to characterize the catalyst layer and environmental factors can influence the reported characteristics of this layer. There were 18 papers and one patent found that use a GDE for the electrochemical reduction of CO_2 to formate. Only a few of these studies explore the effect of characteristics of the catalyst layer on electrochemical performance. Out of all the factors shown in Figure 2.6, the effect of catalyst loading and catalyst particle size are the only factors that varied within a given study. However, there are different metal catalysts and binders, different application methods, varying particle sizes, and various catalyst loadings investigated between the studies. Therefore, only these five factors will be discussed in more detail.

Catalyst Metal

There were 11 metals used as a catalyst on a GDE from the 19 sources found reporting formate as a CO_2 reduction product. A summary of current efficiencies achieved for these metals is shown in Figure 2.7.

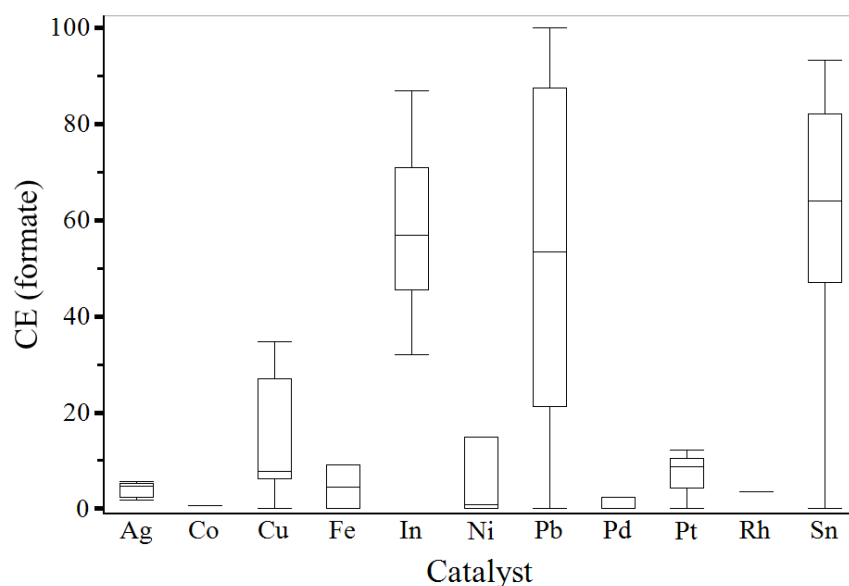


Figure 2.7. Current efficiency for formate vs catalyst metal.^{2,15,22,23,25,31–44}

Indium (In), lead (Pb), and tin (Sn) are the most studied metals on GDEs, and they are seen to achieve the highest CE for this reaction, with Pb showing the highest median and maximum CE for formate at 62% and 100% respectively.²⁵ For this reason, we will focus only on discussing the literature that uses these three catalysts in the following sections.

Application Method

Twelve of the 19 sources found use Pb, Sn, or In as a catalyst for CO₂ reduction to formate with a GDE. Seven catalyst application methods have been used across these 12 studies. These catalyst application methods are compared for the three catalysts in Figure 2.8.

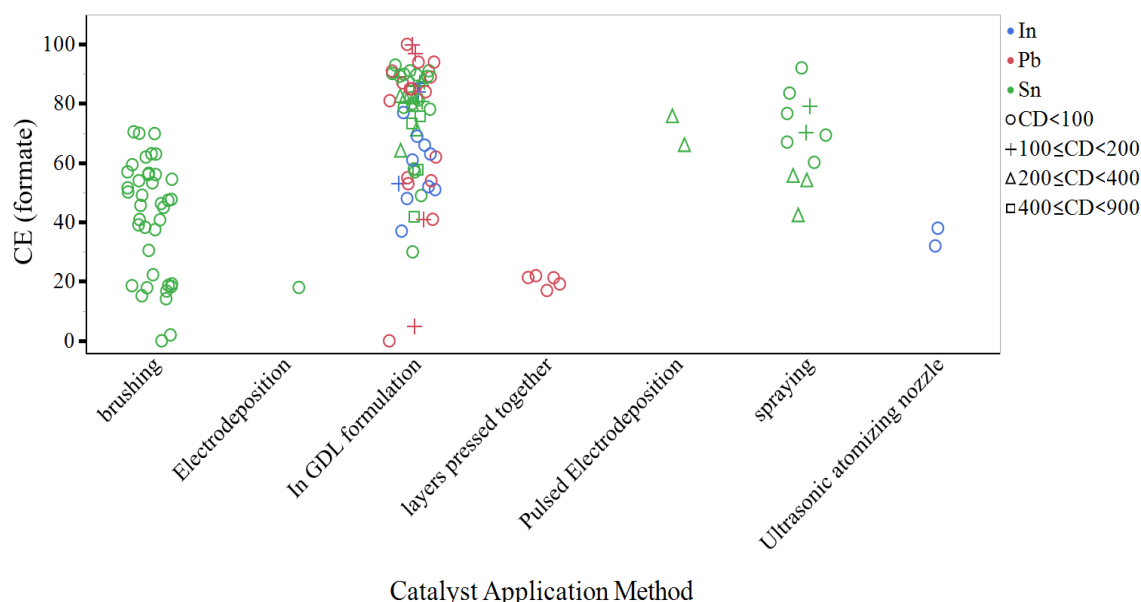


Figure 2.8. Current efficiency of CO₂ to formate for various catalysts and application methods.^{2,15,22,23,25,33,35,36,39–42}

The most frequent catalyst application method used included the catalyst in the initial GDL mixture. This could be advantageous by making operation more consistent as performance

would be more independent of electrode wettability, but consequently, this method would drastically increase the cost of these electrodes. This is due to the additional inactive catalyst in such a structure because it would be dispersed in places other than at the three-phase boundary. Although the common metals used for this reaction may be relatively cheap, the method to produce the catalyst can be expensive when considering the costs of other inputs (e.g., the cost of solvents, reducing agents, energy, and waste disposal). Therefore, this method is not as attractive from a cost perspective to scale up.

Brushing and spraying were the next most frequently used methods in applying a catalyst layer to the GDL. On average, spraying the catalyst has been shown to result in higher current efficiencies and operated current densities than brushing for the same metal catalyst. Both of these methods involve making a catalyst ink by dispersing catalyst particles in a solvent and either using a paint or airbrush to apply the catalyst ink to the GDL.^{15,33,36,40,42} These methods allow for more customization of the catalyst layer than other application methods, as the catalyst ink can be easily tuned.

The ultrasonic atomizing nozzle is similar to the spraying application method as a catalyst ink is used and applied as a fine droplet mist, which allows this method to achieve a homogeneous distribution of catalyst on the GDL.⁴¹ Electrodeposition involves reducing metallic ions on the GDL surface by applying a potential between the GDL and a counter electrode in a plating solution. This method is limited in the catalytic surface area it can produce compared to the other methods, as it typically generates a smooth, uniform layer on the plating substrate. Pulsed electrodeposition uses the same method as electrodeposition, except the current is pulsed during the deposition process. This method can lead to a highly dispersed and uniform catalyst nanoparticle layer.⁴⁰ These methods tested do not show high current efficiencies (Figure 2.8); however, there are not nearly as many studies performed on these methods (i.e., the sample size is too small for these methods to draw any conclusions). Pulsed electrodeposition especially seems promising as the only two points for which this method was applied operated at current densities $>200\text{mA/cm}^2$, while the majority of the points in Figure 2.8 result from experiments performed at lower current densities.

Catalyst Particle Size

Only eight of the studies found report the catalyst particle size used for Sn and In catalysts. Additionally, of those eight studies, only two vary the catalyst particle size. A summary of studies that report catalyst particle size and the current efficiency they achieve for In and Sn catalysts is shown in Figure 2.9. Particle size does not appear to affect the current efficiency towards formate formation below sizes of $20\text{ }\mu\text{m}$.

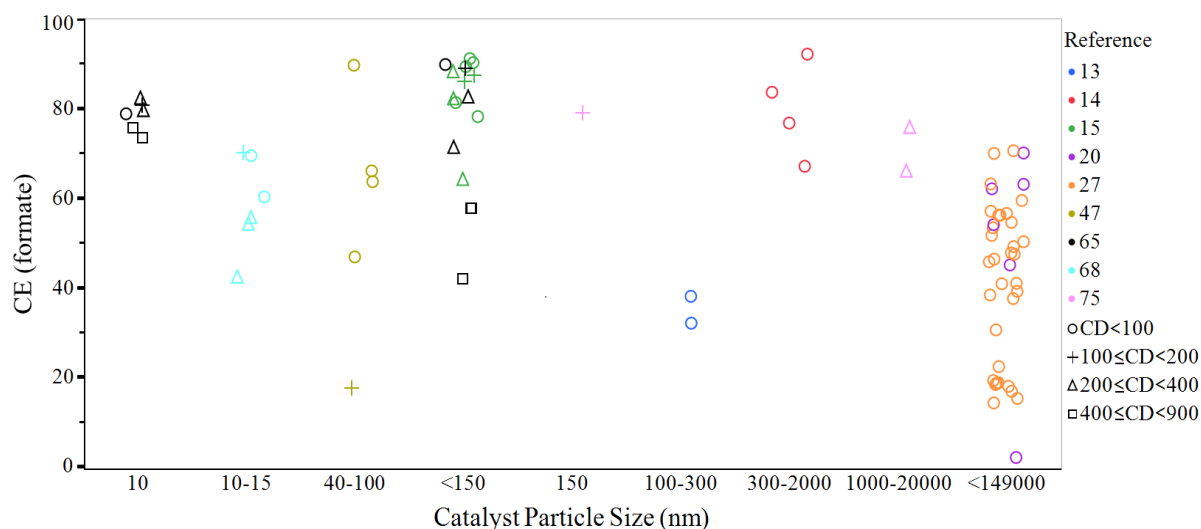


Figure 2.9. Current efficiency of formate vs catalyst particle size^{15,22,23,33,36,40–42,45}

Sen et al.⁴⁰ compared a pulsed electrodeposition method that produced 1-20 μm Sn particles to a commercially available 150 nm Sn catalyst. They found that the agglomerates could achieve 80% current efficiency at a current density of 388 mA/cm^2 , while the commercial catalyst achieved about 79% current efficiency below 150 mA/cm^2 . The loading of catalyst between the electrodes in this study also varies by about a factor of four, making it difficult to draw meaningful conclusions. Kopljär et al.²² studied $<150 \text{ nm}$ Sn powder and $\sim 10 \text{ nm}$ SnO_2 synthesized particles. They showed that the SnO_2 nanoparticles maintained a CE of about 75% as they increased the current density from $50\text{--}500 \text{ mA/cm}^2$, while the Sn powder showed better performance ($\sim 88\%$ CE) at lower current densities but decayed to below 50% CE at 500 mA/cm^2 .

Binder

The binder in the catalyst layer can modify the hydrophobicity of the layer and provide mechanical stability of the catalyst on the GDL. There were two types of binder found in the literature for this reaction: NafionTM and PTFE. There were also several studies that did not use any binder in the catalyst layer. A comparison of the CE for the binders used across the 12 studies is shown in Figure 2.10.

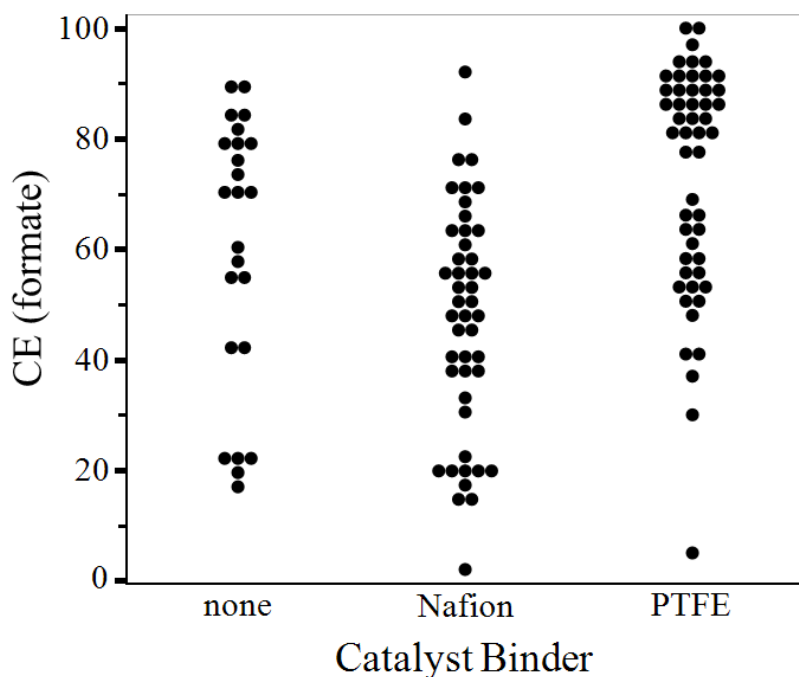


Figure 2.10. Current efficiency of formate vs catalyst binder.^{2,15,22,23,25,33,36,40–42}

It is difficult to draw conclusions from this data from multiple studies where many factors are different between them. However, the cluster of Nafion™ data appears to be weighted lower in current efficiency than PTFE or no binder. This may suggest that Nafion™ could hinder performance when used as a binder for this reaction. This should be a factor to investigate in future studies as a binder may become more important to use when electrode stability for this reaction is studied.

Catalyst Loading

Only four studies varied the catalyst loading of Sn, In, and Pb catalysts.^{23,25,36,42} Mahmood et al.²⁵ was the only study found that changed the loading of a Pb catalyst. A summary of the In and Sn catalyst loadings studied is shown in Figure 2.11.

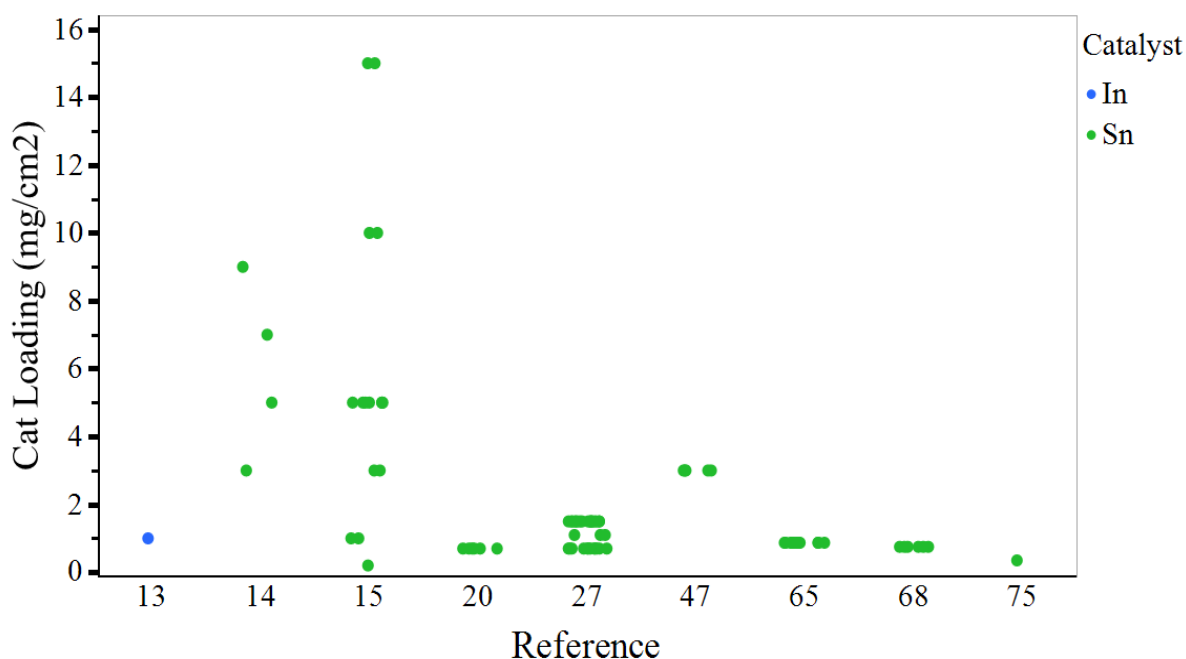


Figure 2.11. Catalyst loading studies for indium and tin ^{15,22,23,33,36,40–42,45}

Kopljar et al.²³ suggest that the metal loading changes the overpotential for the reaction at a given current density, and a shift in product distribution occurs (i.e., the current efficiency of CO increases while the efficiency for formate decreases). Understanding this observation further would be beneficial for developing the CO₂ to formate reaction. Furthermore, it would be beneficial to find a catalyst layer that functions through a wide range of operating current densities for a given loading to allow more flexibility in operation at a pilot or commercial scale.

Wang et al.⁴² studied the effect of catalyst and binder loading. They found an optimal tin loading of 5 mg/cm² with particle sizes between 300–2000 nm. They also claim that 50 wt% Nafion™ is the optimal amount. However, they study Nafion™ concentrations at one constant catalyst loading and then catalyst loading at a constant Nafion™ concentration. This method of experimentation does not allow interaction effects between the factors studied to be estimated. Therefore, there could be a better optimum in their experimental design space.

Mahmood et al.²⁵ used a Pb catalyst and varied loadings at two levels (50 and 100 mg/cm²). They do not report the size of their Pb catalyst particles on the GDE, and they do not see a significant change in electrode performance at low pH. However, the electrochemical cell that they use does not seem to allow for uniform current distributions to be achievable on the surface of their electrode. Their cell uses a plastic mesh as a separator, and the anode is perpendicular to the cathode rather than parallel. This could cause a bias in the results when working in electrolytes that are not very conductive.

Castillo et al.³⁶ performed a three-factor, full factorial design of experiments (DOE) and investigated the Sn catalyst loading, the flow rate of the catholyte standardized by cell area, and the current density. Unfortunately, the current density range studied was much lower than where a limitation should exist for GDEs in this reaction at 12–32 mA/cm², whereas current densities up to 400 mA/cm² have been reported for Sn GDEs.²² Nevertheless, they found that

the Sn loading in the GDE had the greatest main factor effect on the current efficiency, while the catholyte flow rate had little effect. This study supports the idea that the catalyst layer is more critical in overall cell performance than operational parameters such as electrolyte flow rate, pH, temperature, etc. This was the only study found that does not use a linear approach to investigate factors that affect cell performance. However, this study only looks at a total of three factors, and only one of them relates to a catalyst layer characteristic.

The other studies that have examined the catalyst layer are performed in a linear approach, which neglects any interactions that can exist. For example, the optimum catalyst loading can vary for different catalyst sizes and the amount supported on carbon, but these types of interactions have not been considered. As a result, these studies report local maximums in their experimental space rather than global maximums.

Outlook and Recommendations

In summary, the current density, current efficiency, and cell potential are the main KPIs for a given electrochemical reaction. Virtually all of the studies encountered for the electrochemical reduction of CO₂ to formate do not target to optimize the cell potential or report whole-cell potential data, so energy costs were not a valid comparison between studies. Future studies should report whole-cell and half-cell potential data to allow for energy assessments and further insights to be made. Many papers were investigated for this reaction, but not all reported enough information to compare the study to the rest. Future studies should report the KPIs discussed in Section 2 at the bare minimum (electrode size, current density, current efficiency, and cell potential).

GDEs are the most promising electrode type to pursue for the development of this reaction. GDEs consistently outperform 2D, 3D, and trickle flow electrode types as they are capable of operating at high efficiencies and higher current densities than these other electrode types. They can achieve this high performance by maintaining a three-phase boundary with the reacting gas, liquid electrolyte, and catalyst particles, which allows them to overcome mass transfer limitations that all other electrode types encounter at lower reaction rates. However, GDEs are complex, and there is still much more research that should be performed to further optimize GDEs for the commercialization of this reaction.

Overall, there are limited studies that correlate the formulation and production steps of a GDL to the characteristics of the structure. Additionally, only a few studies examine the effect that these structural characteristics have on the electrochemical performance of the electrode. No studies were found that examine the interaction effects of GDL formulation with variations in the production method. Future studies should aim to investigate these areas relating to the GDL in more detail by using a systematic approach, such as the design of experiments that can identify factor interactions.

Similarly, the catalyst layer is not well studied for this reaction; few publications study the effects of only one of the characteristics of the catalyst layer (such as loading) on the electrode performance. Furthermore, there is an inconsistency in the amount of data reported between

the studies. For example, 12 studies were found using tin, indium, or lead on a GDE for the electrochemical reduction of CO₂ to formate, but only eight of the 12 studies reported a catalyst particle size. Only one study was found that uses a design of experiment approach to assess the effects of three factors on the electrode performance. Although only one of the three factors studied was part of the catalyst layer, the study showed that the GDE characteristic parameters are more influential than cell operating parameters for this reaction. However, future studies should aim to be more consistent in reporting information such as catalyst particle size, loading, fraction supported, and ratios with a binder.

All of the GDL and catalyst layer studies use a linear experimentation methodology that neglects any interactions that may affect the measured response. This leads to a large risk of finding a local optimum and missing the global optimum that exists in the experimental parameter space. It would be highly beneficial for a study (or series of studies) to investigate the effect of the interaction between GDL characteristics with catalyst layer characteristics on the electrode's performance. This would allow for the optimum overall structure to be defined (i.e., the most conductive GDL structure that allows for the lowest catalyst loading to achieve a target current density and efficiency). Ultimately, this would result in high savings in production costs of the electrode and operating energy costs of the cells.

Finally, the operation of GDEs at a larger scale should be studied for longer times because there could be different implications to the scaling and lifetime compared to metal electrodes (e.g., the resistance of the electrode to hydrostatic head). As GDEs become larger, the pressure at the bottom/inlet of the cell will become more significant, which could cause flooding in lower sections of the structure. This is especially important because previous research has found that flooding (electrolyte wetting in the GDL) causes a decrease in the lifetime and performance of GDEs. Operating at longer times would allow more insights into the failure mechanisms of these structures for this reaction.

ACKNOWLEDGMENT/ Funding Sources

This work was supported by the European Commission under contract 722614 (Innovative training network Elcorel)

References

- (1) Pozio, A.; Cemmi, A.; Carewska, M.; Paoletti, C.; Zaza, F. Characterization of Gas Diffusion Electrodes for Polymer Electrolyte Fuel Cells. *J. Fuel Cell Sci. Technol.* **2010**, 7 (4), 041003, DOI 10.1115/1.3119061.
- (2) Li, A.; Wang, H.; Han, J.; Liu, L. Preparation of a Pb Loaded Gas Diffusion Electrode and Its Application to CO₂ Electroreduction. *Front. Chem. Sci. Eng.* **2012**, 6 (4), 381–388, DOI 10.1007/s11705-012-1216-2.
- (3) Schulze, M.; Lorenz, M.; Kaz, T. XPS Study of Electrodes Formed from a Mixture of Carbon Black and PTFE Powder. *Surf. Interface Anal.* **2002**, 34 (1), 646–651, DOI 10.1002/sia.1378.
- (4) Tomantschger, K.; Kordesch, K. V. Structural Analysis of Alkaline Fuel Cell Electrodes and Electrode Materials. *J. Power Sources* **1989**, 25 (3), 195–214, DOI 10.1016/0378-7753(89)80004-7.
- (5) Thompson, S. D.; Jordan, L. R.; Forsyth, M. Platinum Electrodeposition for Polymer Electrolyte Membrane Fuel Cells. *Electrochim. Acta* **2001**, 46 (10–11), 1657–1663, DOI 10.1016/S0013-4686(00)00767-2.
- (6) Dodds, W. S.; Stutzman, L. F.; Sollami, B. J. Carbon Dioxide Solubility in Water. *Ind. Eng. Chem. Chem. Eng. Data Ser.* **1956**, 1 (1), 92–95, DOI 10.1021/i460001a018.
- (7) Motoo, S.; Watanabe, M.; Furuya, N. Gas Diffusion Electrode of High Performance. *J. Electroanal. Chem. Interfacial Electrochem.* **1984**, 160 (1–2), 351–357, DOI 10.1016/S0022-0728(84)80139-4.
- (8) Wang, Q.; Dong, H.; Yu, H. Development of Rolling Tin Gas Diffusion Electrode for Carbon Dioxide Electrochemical Reduction to Produce Formate in Aqueous Electrolyte. *J. Power Sources* **2014**, 271, 278–284, DOI 10.1016/j.jpowsour.2014.08.017.
- (9) Şengül, E.; Erkan, S.; Eroğlu, İ.; Baç, N. Effect of Gas Diffusion Layer Characteristics and Pore-Forming Agents on the Performance of Polymer Electrolyte Membrane Fuel Cells. *Chem. Eng. Commun.* **2008**, 196 (1–2), 161–170, DOI 10.1080/00986440802293130.
- (10) Scheiba, F.; Kunz, U.; Butsch, H.; Zils, S.; Fuess, H.; Roth, C. Imaging the Electrode-GDL Interface by a Modified Wood's Intrusion Process; 2010; pp 85–92, DOI 10.1149/1.3496616.
- (11) Kenjo, T.; Kawatsu, K. Current-Limiting Factors and the Location of the Reaction Area in PTFE-Bonded Double-Layered Oxygen Electrodes. *Electrochim. Acta* **1985**, 30 (2), 229–233, DOI 10.1016/0013-4686(85)80087-6.
- (12) Lasia, A. Impedance of Porous Electrodes. In *ECS Transactions*; ECS, 2008; pp 1–18, DOI 10.1149/1.3004025.
- (13) Lee, H.-K.; Park, J.-H.; Kim, D.-Y.; Lee, T.-H. A Study on the Characteristics of the Diffusion Layer Thickness and Porosity of the PEMFC. *J. Power Sources* **2004**, 131 (1–2), 200–206, DOI 10.1016/j.jpowsour.2003.12.039.

- (14) Tseng, C.-J.; Lo, S.-K. Effects of Microstructure Characteristics of Gas Diffusion Layer and Microporous Layer on the Performance of PEMFC. *Energy Convers. Manag.* **2010**, *51* (4), 677–684, DOI 10.1016/j.enconman.2009.11.011.
- (15) Del Castillo, A.; Alvarez-Guerra, M.; Solla-Gullón, J.; Sáez, A.; Montiel, V.; Irabien, A. Sn Nanoparticles on Gas Diffusion Electrodes: Synthesis, Characterization and Use for Continuous CO₂ Electroreduction to Formate. *J. CO₂ Util.* **2017**, *18*, 222–228, DOI 10.1016/j.jcou.2017.01.021.
- (16) Moussallem, I.; Pinnow, S.; Wagner, N.; Turek, T. Development of High-Performance Silver-Based Gas-Diffusion Electrodes for Chlor-Alkali Electrolysis with Oxygen Depolarized Cathodes. *Chem. Eng. Process. Process Intensif.* **2012**, *52*, 125–131, DOI 10.1016/j.cep.2011.11.003.
- (17) Maja, M.; Orecchia, C.; Strano, M.; Tosco, P.; Vanni, M. Effect of Structure of the Electrical Performance of Gas Diffusion Electrodes for Metal Air Batteries. *Electrochim. Acta* **2000**, *46* (2–3), 423–432, DOI 10.1016/S0013-4686(00)00601-0.
- (18) Gülzow, E.; Schulze, M. Long-Term Operation of AFC Electrodes with CO₂ Containing Gases. *J. Power Sources* **2004**, *127* (1–2), 243–251, DOI 10.1016/j.jpowsour.2003.09.020.
- (19) Kong, C. S.; Kim, D.-Y.; Lee, H.-K.; Shul, Y.-G.; Lee, T.-H. Influence of Pore-Size Distribution of Diffusion Layer on Mass-Transport Problems of Proton Exchange Membrane Fuel Cells. *J. Power Sources* **2002**, *108* (1–2), 185–191, DOI 10.1016/S0378-7753(02)00028-9.
- (20) Uchida, M. Effects of Microstructure of Carbon Support in the Catalyst Layer on the Performance of Polymer-Electrolyte Fuel Cells. *J. Electrochem. Soc.* **1996**, *143* (7), 2245, DOI 10.1149/1.1836988.
- (21) Thompson, J. Design and Analysis in Chemical Research; Tranter, R. L., Ed.; 2000; pp 85–110.
- (22) Kopljär, D.; Wagner, N.; Klemm, E. Transferring Electrochemical CO₂ Reduction from Semi-Batch into Continuous Operation Mode Using Gas Diffusion Electrodes. *Chem. Eng. Technol.* **2016**, *39* (11), 2042–2050, DOI 10.1002/ceat.201600198.
- (23) Kopljär, D.; Inan, A.; Vindayer, P.; Wagner, N.; Klemm, E. Electrochemical Reduction of CO₂ to Formate at High Current Density Using Gas Diffusion Electrodes. *J. Appl. Electrochem.* **2014**, *44* (10), 1107–1116, DOI 10.1007/s10800-014-0731-x.
- (24) Kolyagin, G. A.; Kornienko, V. L. New Accelerated Method of Impregnation by Aqueous Electrolyte of Carbon Black Gas-Diffusion Electrodes to Study Their Structural and Electrochemical Characteristics. *Russ. J. Electrochem.* **2011**, *47* (11), 1268–1273, DOI 10.1134/S1023193511110115.

- (25) Mahmood, M. N.; Masheder, D.; Harty, C. J. Use of Gas-Diffusion Electrodes for High-Rate Electrochemical Reduction of Carbon Dioxide. I. Reduction at Lead, Indium- and Tin-Impregnated Electrodes. *J. Appl. Electrochem.* **1987**, *17* (6), 1159–1170, DOI 10.1007/BF01023599.
- (26) Kim, H.; Subramanian, N. P.; Popov, B. N. Preparation of PEM Fuel Cell Electrodes Using Pulse Electrodeposition. *J. Power Sources* **2004**, *138* (1–2), 14–24, DOI 10.1016/j.jpowsour.2004.06.012.
- (27) Kolyagin, G. A.; Vasil'eva, I. S.; Kornienko, V. L. Effect of the Composition of Gas-Diffusion Carbon Black Electrodes on Electrosynthesis of Hydrogen Peroxide from Atmospheric Oxygen. *Russ. J. Appl. Chem.* **2008**, *81* (6), 983–987, DOI 10.1134/S1070427208060116.
- (28) ZHAO, J.; HE, X.; WANG, L.; TIAN, J.; WAN, C.; JIANG, C. Addition of NH_4HCO_3 as Pore-Former in Membrane Electrode Assembly for PEMFC. *Int. J. Hydrogen Energy* **2007**, *32* (3), 380–384, DOI 10.1016/j.ijhydene.2006.06.057.
- (29) Gullá, A. F.; Krasovic, J. L. Gas-Diffusion Electrode. WO 2013/037902 A2, 2013.
- (30) Turek, T.; Moussallem, I.; Bulan, A.; Schmitz, N.; Weuta, P. Oxygen-Consuming Electrode with Multilayer Catalyst Coating and Process for the Production Thereof. US 9.243,337 B2, 2016.
- (31) Hara, K.; Sakata, T. Large Current Density CO_2 Reduction under High Pressure Using Gas Diffusion Electrodes. *Bull. Chem. Soc. Jpn.* **1997**, *70* (3), 571–576, DOI 10.1246/bcsj.70.571.
- (32) Hara, K. High Efficiency Electrochemical Reduction of Carbon Dioxide under High Pressure on a Gas Diffusion Electrode Containing Pt Catalysts. *J. Electrochem. Soc.* **1995**, *142* (4), L57, DOI 10.1149/1.2044182.
- (33) Prakash, G. K. S.; Viva, F. A.; Olah, G. A. Electrochemical Reduction of CO_2 over Sn-Nafion® Coated Electrode for a Fuel-Cell-like Device. *J. Power Sources* **2013**, *223*, 68–73, DOI 10.1016/j.jpowsour.2012.09.036.
- (34) Hara, K. Electrocatalytic Formation of CH_4 from CO_2 on a Pt Gas Diffusion Electrode. *J. Electrochem. Soc.* **1997**, *144* (2), 539, DOI 10.1149/1.1837445.
- (35) Machunda, R. L.; Ju, H.; Lee, J. Electrocatalytic Reduction of CO_2 Gas at Sn Based Gas Diffusion Electrode. *Curr. Appl. Phys.* **2011**, *11* (4), 986–988, DOI 10.1016/j.cap.2011.01.003.
- (36) Del Castillo, A.; Alvarez-Guerra, M.; Irabien, A. Continuous Electroreduction of CO_2 to Formate Using Sn Gas Diffusion Electrodes. *AIChE J.* **2014**, *60* (10), 3557–3564, DOI 10.1002/aic.14544.
- (37) Yamamoto, T.; Tryk, D. A.; Hashimoto, K.; Fujishima, A.; Okawa, M. Electrochemical Reduction of CO_2 in the Micropores of Activated Carbon Fibers. *J. Electrochem. Soc.* **2000**, *147* (9), 3393, DOI 10.1149/1.1393911.

- (38) Dufek, E. J.; Lister, T. E.; Stone, S. G.; McIlwain, M. E. Operation of a Pressurized System for Continuous Reduction of CO₂. *J. Electrochem. Soc.* **2012**, *159* (9), F514–F517, DOI 10.1149/2.011209jes.
- (39) Park, T. T.; Jeong, S. K.; Kim, H. J.; Kang, S. P.; Youn, M. H. Method and Apparatus for Preparing Reduction Product of Carbon Dioxide by Electrochemically Reducing Carbon Dioxide. US 2018 / 0202056 A1, 2018.
- (40) Sen, S.; Skinn, B.; Hall, T.; Inman, M.; Taylor, E. J.; Brushett, F. R. Pulsed Electrodeposition of Tin Electrocatalysts onto Gas Diffusion Layers for Carbon Dioxide Reduction to Formate. *MRS Adv.* **2017**, *2* (8), 451–458, DOI 10.1557/adv.2016.652.
- (41) Bitar, Z.; Fecant, A.; Trela-Baudot, E.; Chardon-Noblat, S.; Pasquier, D. Electrocatalytic Reduction of Carbon Dioxide on Indium Coated Gas Diffusion Electrodes—Comparison with Indium Foil. *Appl. Catal. B Environ.* **2016**, *189*, 172–180, DOI 10.1016/j.apcatb.2016.02.041.
- (42) Wang, Q.; Dong, H.; Yu, H. Fabrication of a Novel Tin Gas Diffusion Electrode for Electrochemical Reduction of Carbon Dioxide to Formic Acid. *RSC Adv.* **2014**, *4* (104), 59970–59976, DOI 10.1039/C4RA10775F.
- (43) Whipple, D. T.; Finke, E. C.; Kenis, P. J. A. Microfluidic Reactor for the Electrochemical Reduction of Carbon Dioxide: The Effect of PH. *Electrochem. Solid-State Lett.* **2010**, *13* (9), B109, DOI 10.1149/1.3456590.
- (44) Ikeda, S.; Ito, K.; Noda, H.; Rusop, M.; Soga, T. Electrochemical Reduction Of Carbon Dioxide Using Gas Diffusion Electrodes Loaded With Fine Catalysts. In *AIP Conference Proceedings*; AIP, 2009; pp 108–113, DOI 10.1063/1.3160110.
- (45) Lei, T.; Zhang, X.; Jung, J.; Cai, Y.; Hou, X.; Zhang, Q.; Qiao, J. Continuous Electroreduction of Carbon Dioxide to Formate on Tin Nanoelectrode Using Alkaline Membrane Cell Configuration in Aqueous Medium. *Catal. Today* **2018**, *318*, 32–38, DOI 10.1016/j.cattod.2017.10.003.

Chapter 3

Production of Gas Diffusion Layers with Tunable Characteristics³

³ This chapter is based on Philips, M. F.; Gruter, G.-J. M.; Koper, M. T. M.; Schouten, K. J. P. Production of Gas Diffusion Layers with Tunable Characteristics. ACS Omega 2022, 7 (27), 23041–23049, DOI 10.1021/acsomega.1c06977.

Introduction

Gas diffusion electrodes (GDEs) have found use in fuel cells, various electrolyzer applications, air batteries, and photocatalytic reactions.^{1–7} Gas diffusion electrodes (GDEs) enhance the mass transfer of gas reactants in electrochemical reactions by creating a three-phase boundary where the gaseous reactant contacts the electrolyte right at the catalyst interface. This enhancement of mass transfer allows for much higher reaction rates to be achieved than in other types of electrochemical technologies (e.g., 3D electrodes, trickle flow electrodes, etc.). A GDE consists of a gas diffusion layer (GDL) and a catalyst layer. Both layers can affect the overall performance of the GDE.^{3,8–11} Therefore, it is crucial to develop methods to produce GDLs with different characteristics so they can be screened with other catalyst layer factors.

A GDL typically consists of a microporous layer and a macroporous layer. The microporous layer is typically produced with some type of carbon and a hydrophobic binder such as PTFE.¹² Additionally, for wet methods, a solvent is employed. There are a few studies that we are aware of that investigate how different materials used in GDL production can affect a characteristic of the finished GDL. Schulze et al.¹³ found that using more carbon black in the initial powder mixture for their electrodes changed the hydrophobicity of the electrode from hydrophobic to hydrophilic. Kolyagin et al.¹⁴ similarly found that increasing the PTFE content in the GDL changes the hydrophobicity of the GDL from hydrophilic to hydrophobic. They also found that increasing the PTFE content decreases the surface area of the structure and increases the average diameter of hydrophilic pores. Maja et al.³ studied the effect of the carbon type used in their GDLs on the performance of their GDEs for metal-air batteries. They found that using oil-furnace carbons (Vulcan XC72RTM and Black Pearls 3700TM) rather than acetylene black resulted in larger wet pore volumes in their active layer and resulted in poorer electrode stability.

In terms of production process studies, we are only aware of one study that investigates in some detail how the production method for the GDL affects a characteristic of the GDL. Moussallem et al.¹⁵ found that increasing the applied pressure during their production process of GDLs for oxygen depolarized cathodes decreased the structures' porosity. Although these studies link one production factor to one characteristic, there are many other factors that can influence these characteristics, and there are other characteristics of a GDL that can influence the performance of a GDE. Other potential influential characteristics of GDLs that have been reported in studies include the conductivity and elasticity.^{3,10,21–25,11,13,15–20}

The GDL production method from this study is used to produce GDLs in Chapter 4 where we show 99% current efficiency at 400 mA/cm² for a two hour experiment.⁹ These GDLs contain a macroporous layer (woven carbon) and a microporous layer (acetylene black + PTFE), and are generally thicker than traditional GDLs. In this way, the GDL can be used in a configuration where it is directly in between a gas and a liquid phase. This thicker GDL allows us to maintain higher hydrostatic head pressures inside of an electrochemical cell and circumvents the need for additional inserts inside the cell (e.g., percolator) to avoid electrode

flooding. Consequently, some of the conclusions from this study may not be valid for thinner GDLs or GDLs produced from a different method.

In this study, GDLs are produced using a wet dough and a hot pressing method similar to the method of Tomantschger et al.¹⁹ We look at 11 factors in our GDL production method and measure six characteristics of the GDL. The goal of this study is to identify which factors in the GDL production method affect each characteristic of the GDL, and we achieve this through using a design of experiments (DOE). The results from this study provide a method to produce 26 GDLs with varying characteristics as well as lay the groundwork for future studies to focus on these factors and better explain how these factors are influential to the GDL characteristics.

Experimental

GDL Synthesis

The synthesis method used for all GDLs was adapted from a method developed earlier in our laboratory.²⁶ 15g of Soltex Acetylene black 75%-03 carbon was weighed and placed in a Bourguini (kitchen) mixer. The appropriate amount of PTFE dispersion 30 (average dispersion particle size of 0.220 μm) was added to 60mL of a 1:1 volume IPA /water mixture and stirred for 1 minute. The mixer was turned on at the lowest speed, and the PTFE mixture was slowly added to the mixer. 10mL of 1:1 volume IPA/water was used to rinse the beaker containing the initial PTFE mixture and added to the mixer. After 1 minute of mixing, a dough-like mixture was collected. The obtained dough was rolled with a marble rolling pin for about 10 minutes. This allows the material to become more workable to obtain a larger structure.

The dough was then rolled to the desired thickness using a cross rolling technique. The final dimensions of the rolled doughs were 200mm x 125mm. The dough rectangle was placed on aluminum foil on top of a flat steel compression plate. A paint roller was used to apply PTFE dispersion 30 diluted 50% with 1:1 volume IPA:H₂O to the back of the dough. Carbon fiber fabric (plain weave 3k) was used as the current collector and placed on top of the dough. Expanded metal mesh was placed on top of the current collector, then another layer of aluminum foil, and then a compression plate. A figure of the order of layers is shown in Appendix A (Figure A.1). The compression plates were then placed into a Carver heated press (Model number 4533) and pressed in three stages at various temperatures, pressures, and durations according to the DOE matrix. A figure plotting the temperature and pressure profile for GDL 17 is shown in Appendix A (Figure A.2). GDLs of 10 cm x 18 cm were cut from the end structure. A picture of what these structures typically look like with the layers labeled is shown in Figure 3.1. A schematic outlining the layers of the GDL is shown in Appendix A (Figure A.3)

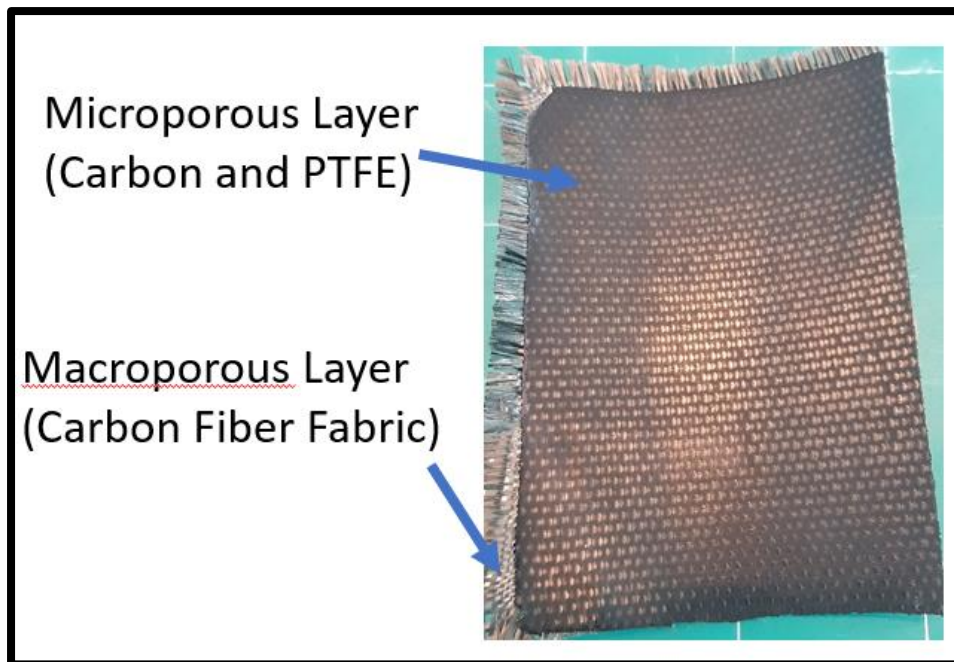


Figure 3.1. Picture of a GDL produced from the production process studied.

Design of Experiments

Eleven factors in the production method were considered for a DOE. We acknowledge that there are other factors that can be influencing the final characteristics of the GDL from this method (e.g., the type of binding agent, carbon type, solvents used, binder particle size, ratio of solvent to water, etc.); however, including additional factors in a DOE would substantially increase the number of experiments required to complete. The factors chosen for this study are: the temperature, pressure, and duration of each of the three steps in the pressing process, the PTFE content in the initial dough mixture, and the thickness the dough was rolled to before pressing. The software JMP was used to create a Definitive Screening Design (DSD) of Experiments. This is a small but efficient design used to identify the most influential factors on a response (characteristic) and thus can be used to reduce factors.²⁷ Each production factor was tested at three levels shown in the experimental matrix in Table 3.1.

Table 3.1. Levels of each production factor studied

Production Factor	Low Level	Center Level	High Level
PTFE wt%	20	35	50
Rolling Thickness Setting	4 (thinner setting)		2 (thicker setting)
Time Stage 1 (min)	5	32.5	60
Pressure Stage 1 (Ton)	0.5	10.25	20
Temperature Stage 1 (°C)	80	140	200
Time Stage 2 (min)	5	32.5	60
Pressure Stage 2 (Ton)	0.5	10.25	20
Temperature Stage 2 (°C)	280	307.5	335
Time Stage 3 (min)	5	32.5	60
Pressure Stage 3 (Ton)	1	13	25
Temperature Stage 3 (°C)	300	317.5	335

The factors were bounded from initial testing and development of this GDL method. 20 wt% PTFE content was chosen as the lower bound because the dough is more difficult to form with lower PTFE content. 50 wt% PTFE was chosen as the upper bound to try to keep the conductivity of the GDLs as high as possible. The time of each stage varied from 5 min to 60 min. These values were chosen to see how short a stage could last to decrease the overall production time. The first stage in the pressing process is designed to evaporate the IPA and H₂O in the structure. This can be done at a slow rate (80°C) or a fast rate (200°C). The second stage in the pressing process was designed to decompose the surfactant present in the PTFE dispersion and fluidize the PTFE in the structure. The third stage in the process is meant to further facilitate the fluidization of PTFE in the structure. The pressures of the stage varied from 0.5 Ton to 25 Ton, with the last stage having a slightly higher range in levels. This was done to observe the effect of higher pressures when the PTFE is more fluid.

The production conditions for each GDL are shown in Appendix A (Table A.1). Repeats were performed for three electrodes to validate the reproducibility of the method. The analyses of the repeats are shown in Appendix A (Figures A.4-A.18).

Resistance/Conductance Measurements

The surface and through-plane resistance of the GDL will directly affect the full cell potential. Contact resistance was used to measure the surface and through-plane resistance. Copper 101 alloy bars set in a plastic frame were used to make contact on the surfaces of the GDLs, and a PCE Instruments milliohm meter was used for the measurement. The plastic frame and GDLs were placed in a Carver Press AutoFour/3015-PL, H and pressed at a minimum pressure of 0.5 ton for 30 seconds before recording the resistance. This process was repeated on the opposite end of the GDL. 24.2 cm² of total contact area for through-plane measurements

was used. A separation of 1 cm was used for surface resistance measurements. Resistance and resistivity values were converted to conductance and conductivity values for analysis.

Elasticity and Thickness Measurements

The elasticity of the GDL can affect how the GDL bends during operation inside the cell, which can create non-uniform electrolyte flow over the electrode surface if the GDL is not stiff enough. Additionally, the thickness of the GDL can affect the design specifications for gasketing and sealing around the GDE inside the cell. For the elasticity, an Instron 5565 tension tester was used to measure the Young's Modulus of the GDLs. Six samples of 10 mm x 80 mm were cut from the 100 x 180 mm structure using a pre-made die. Three samples were cut from one corner, and another three samples were cut from the opposite corner of the 100 x 180 mm structure. A micrometer was used to measure the average thickness of each sample. The gauge length was 34mm, and the crosshead speed was set to 5mm/min.

Water Contact Angle Measurements

Although the hydrophobicity of the GDL is not measured during reacting conditions, this characteristic could still be useful in future developmental work. For example, the binding capabilities of various catalyst application methods could be affected by this characteristic. A microscope optical system with a backlight was used to picture three water droplets on each GDL. The target water droplet volume for each measurement was 50 μ L, and photos were taken within 20 seconds of droplet contact. The Drop Shape Analysis plugin for ImageJ was used to measure the water contact angle from the pictures.²⁸

Hg Porosimetry Measurements

The porosity of the GDL can influence how much gas dissolving area exists between the GDL and catalyst interface. This would directly impact the ability of a GDE to enhance the mass transfer of gaseous reactants. Hg Porosimetry analysis was outsourced to a 3rd party analytical lab. The sample mass for each measurement was about 0.25 g. The maximum test pressure was 400 MPa, and the increase and decrease speeds were set to 4 and 5 Pa, respectively. The mercury contact angle was 140.0 degrees. Each GDL was analyzed only once, so there is no data available for the method's reproducibility.

Workflow for Analysis

After all of the data for each characteristic was collected, the repeat runs were analyzed using a t-test to verify that the repeat and original GDLs were statistically the same. The stepwise platform in JMP was used for each characteristic to fit a model. All factors, interactions, and square terms were considered. Models were generated using the Bayesian Information Criterion (BIC) and Akaike Information Criterion (AIC) as stopping rules to help prevent overfitting.^{29,30} The models generated from both stopping rules for each characteristic are shown in Appendix A (Figures A.19-A.30). The models created were in the form of Equation 3.1:

$$y = b_1X_1 + b_2X_2 + b_3X_3 + \cdots + b_nX_n \quad (3.1)$$

where b_n is the model term coefficient, and X_n is the factor variable, which can be a multiplicative combination of two factors (two-factor interactions) or a squared factor (for modeling curvature). Interactions between two factors indicate that the trend of the response vs. one of the interacting factors can change from positive to less positive (or negative to less negative) with a change in the other interacting factor.

The term coefficients indicate the average change in response for every unit increase of the respective term. These coefficients, however, are affected by the scale of the factor (i.e., if one factor is in milli-units and the other is in kilo-units, there would be six orders of magnitude difference between the two predicted coefficients). Consequently, comparing these coefficients can lead to biased conclusions. However, fitting a model to scaled factors (making the range between the factors two and mean equal to zero) results in coefficients that can be equally compared and allows for concluding which factors are affecting the response the most.³¹

The model terms in the selected GDL characteristic models were sorted based on the coefficients of the scaled factors. This normalizes the factors so that the magnitude of the effects (coefficients) can be compared and thus shows which terms are influencing the response the greatest.³² It should be noted that the different models generated can have different magnitudes of scaled terms depending on the response that is modeled (i.e., Young's Modulus or GDL thickness). The scaled estimates are useful for standardizing the effect of factors for a given response. Additionally, t-tests were performed on the predicted model coefficients to determine with 95% confidence which coefficients were statistically significant. The null hypothesis of the t-tests performed is that the term coefficient is zero. P-values were calculated for each coefficient, and the null hypothesis was rejected when the p-value was less than 0.05 (95% confidence). In other words, when the p-value was below the threshold limit, the respective parameter coefficient was concluded with 95% confidence to be non-zero or statistically significant. All model's R^2 values, root mean square errors, coefficient estimates, and p-values for the coefficients are shown in Appendix A (Figures A.19, A.21, A.23, A.25, A.27, and A.29). Additionally, model profilers help visualize the models generated as they show a snapshot of the models. 2D plots of each model factor vs. the GDL characteristic modeled are shown. These model profilers are shown in Appendix A (Figures A.31-A.36). The top four most influential factors (based on the coefficient estimates for scaled factors) for each characteristic are discussed in more detail, even though there may be more than four statistically significant terms in the generated models.

Results and Discussion

The tabulated GDL characteristic data is shown in Appendix A (Table A.2).

Conductance Through and Surface Conductivity

Higher conductances through the structure and surface conductivities are desirable because they should lead to lower cell potentials and thus, lower energy costs. The model term coefficients for scaled factors for the conductance through the GDL are shown in Figure 3.2.

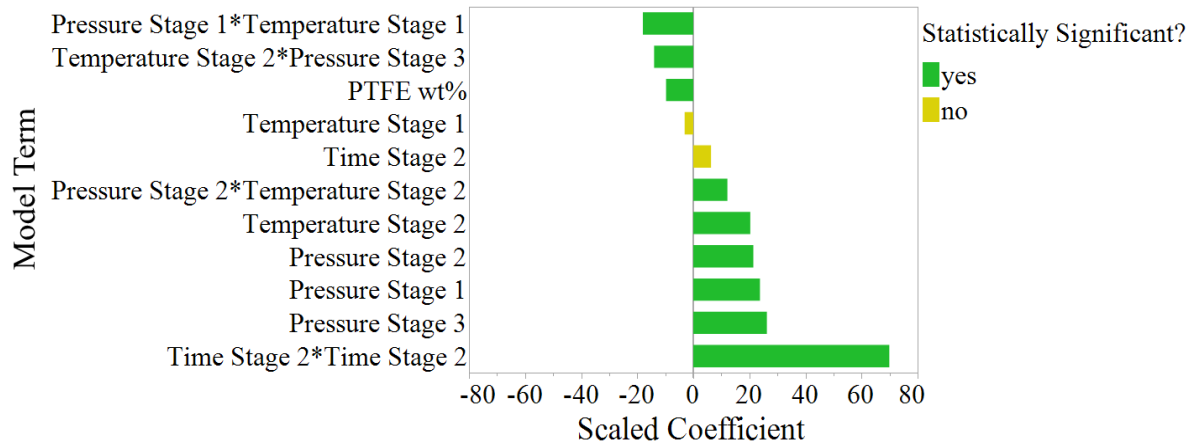


Figure 3.2. Model term coefficients for scaled factors for the conductance through the GDL model generated by using the AIC as the stopping rule. Terms with p-values less than 0.05 are shown as statistically significant.

The conductance through the GDL structures is highly affected by the pressures at each stage as well as the time and temperature of the second stage. The coefficient of the squared term of time of the second stage is the largest shown in Figure 3.2 and therefore affects the conductance through the structure the most. This signifies there is curvature in the data with respect to the time of the second stage. The pressures at each stage have positive coefficients, indicating that increasing pressure increases the conductance through the structure. Additionally, the pressures at each stage show nearly a 2x greater effect on the conductance through the GDL than the PTFE content in the starting mixture.

The model term coefficients for scaled factors for the surface conductivity of the GDL are shown in Figure 3.3.

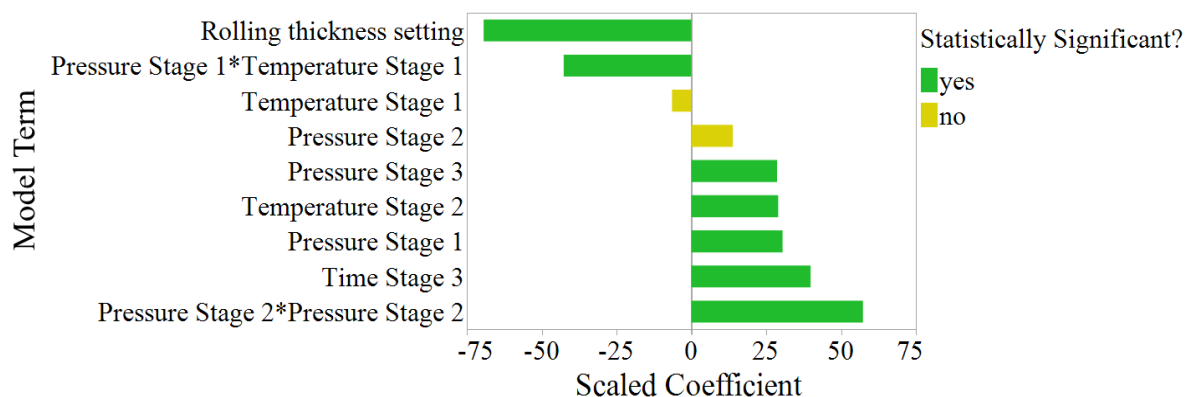


Figure 3.3. Model term coefficients for scaled factors for the surface conductivity of the GDL model generated by using the AIC as the stopping rule. Terms with p-values less than 0.05 are shown as statistically significant.

The surface conductivity is most affected by the thickness of the structure before pressing, the pressure of the second stage, the interaction between the pressure and temperature of the first stage, and the time of the third stage. The coefficient for the thickness of the structure before pressing is the largest in Figure 3.3, indicating that this factor affects the surface conductivity of the GDL the most. Similar to the conductance through the GDL, the pressures at each stage have positive coefficients, indicating higher pressures result in higher surface conductivities. The square term coefficient for the pressure of stage two (Pressure Stage 2*Pressure Stage 2) is the second largest coefficient and shows statistical significance, indicating there is a quadratic relationship between the surface conductivity and the pressure of stage 2.

Surprisingly, the pressures at each stage affect the surface conductivity and the conductance through the structure much more than the PTFE content. The positive coefficients for the pressures at each stage (Figures 3.2 & 3.3) signify that higher pressures lead to a higher conductance through the structure and a higher surface conductivity. Higher processing pressures can cause an increase in contact between the conductive acetylene black, resulting in a higher conducting structure. Additionally, this increased contact between carbon particles can offset the effect of higher PTFE concentrations in the structure, as seen when comparing the conductivities of GDL03 (low PTFE, low pressures) and GDL 08 (high PTFE, high pressures).

Young's Modulus

Some GDEs can bend outward during operation, touching the membrane and inhibiting the flow of the electrolyte. A higher Young's Modulus or stiffer structure is less prone to bending outward during operation. The model term coefficients for scaled factors for the Young's Modulus of the GDL are shown in Figure 3.4.

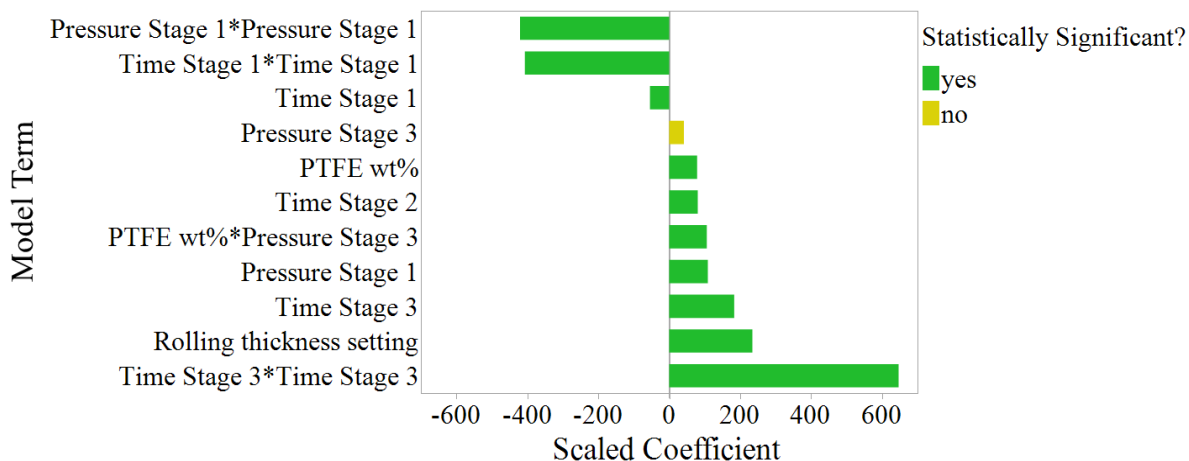


Figure 3.4. Model term coefficients for scaled factors for the Young's Modulus of the GDL model generated by using the AIC as the stopping rule. Terms with p-values less than 0.05 are shown as statistically significant.

The Young's Modulus of the GDL structures is highly influenced by the final and initial stage times, the pressure of the first stage, and the thickness of the structure before pressing. The time and pressure of the first stage and the time of the third stage show the highest scaled coefficients for their squared terms, indicating they affect the Young's Modulus of the GDL the most and that there is curvature in the data with respect to these factors. Maximum Young's

Modulus values are predicted near central values for the time and pressure of the first stage, while a minimum value is predicted near the center point for the time of the third stage. These results show that there are higher-order terms at play in influencing the stiffness of the GDL. More experiments are necessary to understand these higher-order relationships better. Nevertheless, the factor space for these experiments has been significantly narrowed down.

Structure Thickness

The model term coefficients for scaled factors for the thickness of the GDL are shown in Figure 3.5.

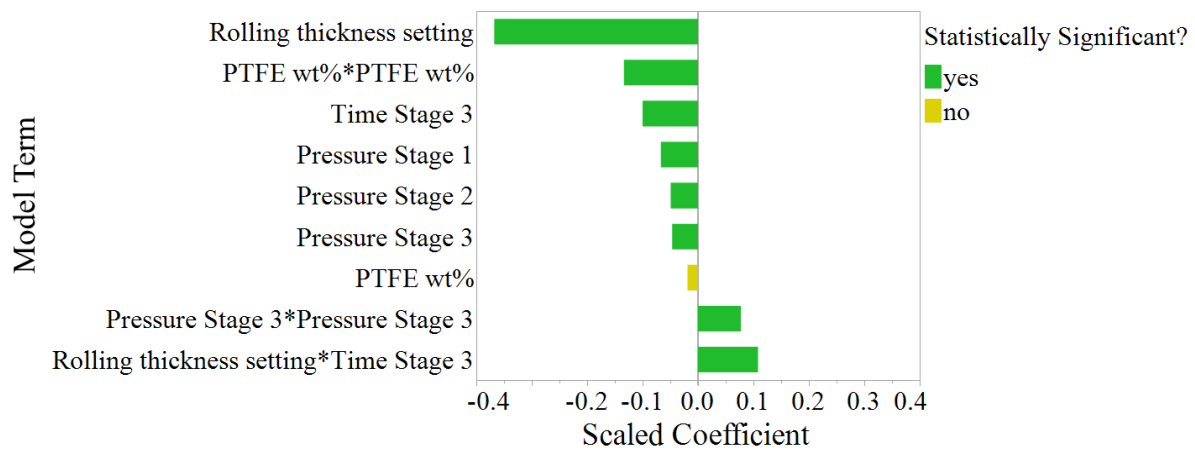


Figure 3.5. Model term coefficients for scaled factors for the thickness of the GDL model generated by using the AIC as the stopping rule. Terms with p-values less than 0.05 are shown as statistically significant.

As expected, the thickness of the dough before pressing influences the final structure's thickness the most out of all the factors. The PTFE content is the second most influential factor for the final structure thickness. Additionally, as expected, the pressures of each stage have a negative correlation with the thickness of the structure, indicating that as pressure increases, the structure becomes thinner.

The interaction between rolling thickness and time of the third stage shows that a thinner structure is achieved at longer times of the third stage only when the rolling thickness of the dough is set at 2 (thicker). However, when the rolling thickness of the dough is set at 4 (thinner), the time of the third stage is not predicted to affect the thickness of the structure (see Appendix A Figure A.34). The significance of this interaction is most likely explained by the difference in the amount of material between the two rolling thickness settings (e.g., the setting of 2 (thicker) will have more material in the press than a dough with a thickness setting of 4). More material can result in more time required to press the structure to become thinner. Additionally, higher pressures at all stages lead to thinner structures, as seen by their negative coefficients in Figure 3.5. However, this negative trend for the pressure at the third stage disappears at pressures greater than ten Ton, as seen in the model profiler (Figure A.34).

Water Contact Angle

The hydrophobicity of the GDL directly impacts how the GDE maintains a three-phase boundary. The greater the hydrophobicity of the GDL, the less likely it should be to flood and lose activity.³ The model term coefficients for scaled factors for the water contact angle of the GDL are shown in Figure 3.6.

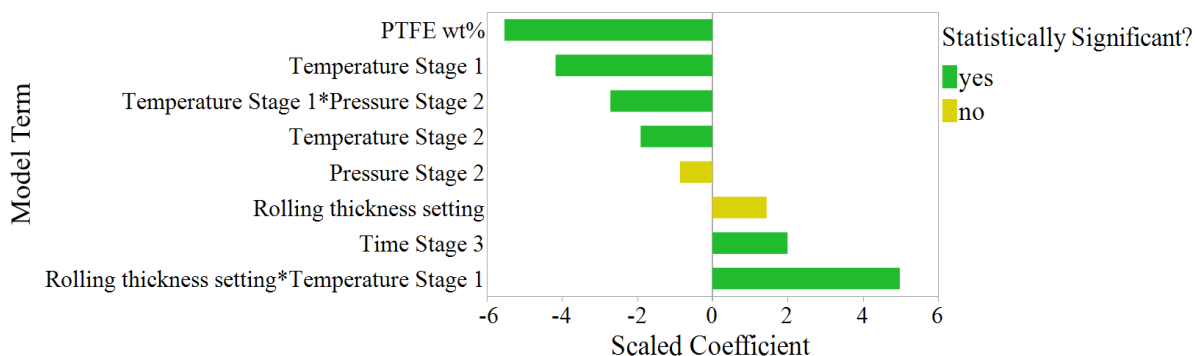


Figure 3.6. Model term coefficients for scaled factors for the water contact angle of the GDL model generated by using the AIC as the stopping rule. Terms with p-values less than 0.05 are shown as statistically significant

The water contact angle, or hydrophobicity, of the GDL structures is highly influenced by the PTFE content in the structure, the temperature of the first stage, and its interaction with the rolling thickness and the pressure of the second stage. The model profiler in Appendix A (Figure A.35) shows the behavior of these two interactions.

Unexpectedly, the PTFE content is negatively correlated with the hydrophobicity of the structure, suggesting that the more PTFE in the structure, the less hydrophobic it becomes. Analysis of the contact angle of PTFE and the acetylene black was performed to investigate this trend further. The PTFE had a contact angle of 108°, which agrees with other reported experiments.^{33–35} The water contact angle of acetylene black was measured to be 145° which shows that it is even more hydrophobic than PTFE. Furthermore, this trend with PTFE could be a result of changes in the surface roughness from varying porosities and pore sizes of the GDL. This ultrahydrophobicity phenomenon is known to occur with rough hydrophobic surfaces.^{36–38} The fact that the water contact angle appears to have a slight positive correlation with the structure's porosity (higher porosities also tend to have higher water contact angles) further supports this idea. Future work should strongly consider and measure the surface roughness of GDLs to identify if there is a correlation between the roughness and hydrophobicity of the layer.

Porosity

The porosity of the GDL will impact the gas-dissolving sites and thus, the mass transfer of the GDE. A more porous structure should lead to better mass transfer of gaseous reactant to the reacting sites of the GDE.³⁹ The model term coefficients for scaled factors for the porosity of the GDL are shown in Figure 3.7.

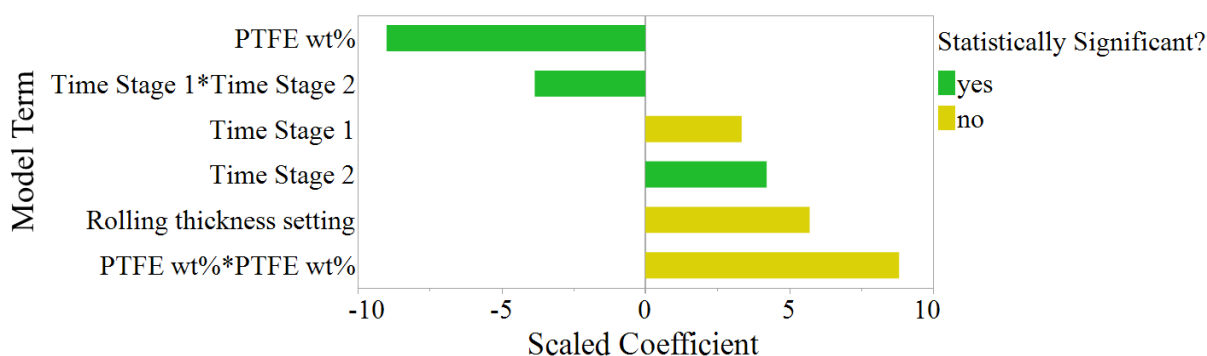


Figure 3.7. Model term coefficients for scaled factors for the porosity of the GDL model generated by using the AIC as the stopping rule. Terms with p-values less than 0.05 are shown as statistically significant

The PTFE content of the GDL, the times of stages 1 and 2, and the thickness of the structure before pressing affect the porosity of the GDL. The model profiler in Appendix A (Figure A.36) shows a negative correlation between the PTFE concentration and the porosity of the GDL. This correlation disappears at concentrations above 35 wt%. The PTFE concentration in the formulation has a quadratic relationship with the porosity as shown by the PTFE wt%*PTFE wt% term. The coefficient for this term, however, does not show statistical significance, indicating that this quadratic relationship should be further investigated for the porosity of the GDL. One explanation for this is that the quadratic relationship is shown to be more asymptotical rather than parabolic (see Figure A.36). This type of quadratic relationship (asymptotical vs. parabolic) reduces the observable difference between a quadratic fit and a linear fit (i.e., the R^2 for a linear fit on an asymptotic relationship will be higher).

The thickness of the structures before pressing is the second largest factor affecting the structure's porosity. The model profiler shows the thinner starting structures (setting 4) tend to lead to GDLs that are more porous. Additionally, the first and second stages' times and their interaction affect the GDL's porosity. At low times of stage one, increasing the time of stage 2 increases the porosity of the GDL. However, at high times of stage 1, increasing the time of stage 2 no longer has a large effect on the porosity (see Figure A.36). The significance of the initial structure thickness, the times of the first two stages, and the interaction suggests that solvent evaporation is crucial to creating a more porous structure.

Combined Characteristic Analysis

Table 3.3 shows a summary of the top four influential factors for each characteristic. This shows if there is a possibility of reducing the stages in the production method or what factors should be focused on in future work for developing GDLs with this method. Additionally, we explore if any of the characteristics measured are correlated with each other through the use of a scatterplot matrix shown in Figure 3.8.

Table 3.3 The top four influential factors in the GDL production method for each characteristic studied.

	Conductance (S)	Surface Conductivity (S/m)	Young's Modulus	Thickness (mm)	Water Contact Angle	Porosity (%)
PTFE content						
Rolling Thickness						
Pressure Stage 1						
Temperature Stage 1						
Time Stage 1						
Pressure Stage 2						
Temperature Stage 2						
Time Stage 2						
Pressure Stage 3						
Temperature Stage 3						
Time Stage 3						

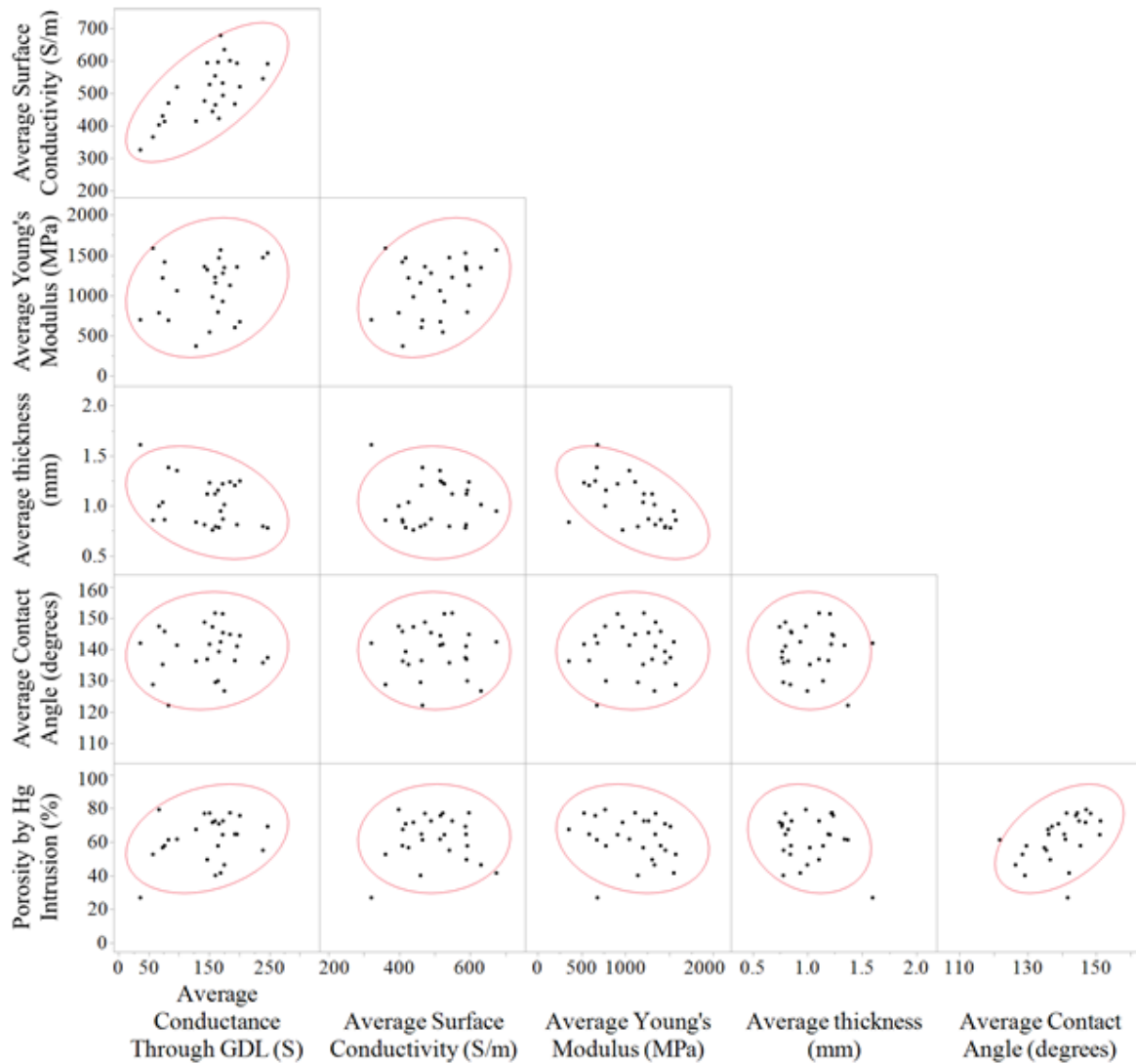


Figure 3.8. Scatterplot matrix of GDL characteristics

Overall, the temperatures of the second and third stages do not significantly impact any of the characteristics studied, as seen in Table 3.3. Additionally, the pressure of the third stage only affects two characteristics: the conductance through the GDL and the thickness of the final structure. Therefore, it could be possible to combine the second and third stages of this production process since the pressure of the third stage has the same (positive) correlation as the pressure of the second stage for the conductance through the GDL and the pressure of the second stage does not have a large effect on the thickness of the structure.

The density ellipses shown in Figure 3.8 help emphasize the characteristics that are slightly correlated with each other. The less circular (more elliptical) the red outline is, the more correlated the characteristics are with each other. A few characteristics appear to be slightly correlated with each other, showing that there are some limitations in the tunability of the GDLs produced from this method. The conductance through the GDL and Young's Modulus appears to be correlated with the structure's thickness. Additionally, there appears to be a slight correlation between the porosity and water contact angle of the GDL, as well as the surface conductivity and conductance through the GDL. The correlation between surface conductivity and conductance through the structure is expected since each GDL should have the same

skeletal structure of PTFE and carbon. Thus, as the conductance through the structure increases, so should the surface conductivity of the structure. As previously stated, the correlation between the porosity and contact angle of the GDLs can be explained by several studies that show rough surfaces lead to increased hydrophobicity.^{36–38} Hence, the more porous structures likely also have rougher surfaces from the pores, resulting in higher water contact angles.

Conclusions

The most influential factors in the GDL production process for six characteristics have been identified. However, not all of these characteristics appear to be completely independent of each other, and therefore, there may be some limitations on the tunability of these structures. The porosity of the GDL and the hydrophobicity do not appear to be completely independent characteristics, neither do the surface conductivity and the conductance through the GDL.

Correlation between the surface conductivity and through GDL conductance is expected to some degree since the core material (carbon + PTFE) is consistent throughout the structure. Therefore, an increase in conductivity through the GDL structure should indicate that the carbon plus PTFE layer (dough layer) in the structure is more conductive and, consequently, should result in an increase in conductance through the electrode. The porosity of the GDL seems to be positively correlated with the water contact angle of the GDL. This correlation has been observed in other fields where surface roughness has been shown to increase the hydrophobicity of the substrate.^{36–38}

Additionally, not all production factors appear to be highly influential in the characteristics of the GDL. The temperature of the third and second stages does not play a prominent role in influencing the characteristics of the GDL. It should be possible to tune GDLs using a method with a combined second and third stage, thus saving time and energy. The results from this study lay the groundwork for future studies to focus on these significant factors and better explain how they may be influencing the various characteristics. Work could be performed to better understand how the factors identified in this study affect the Young's Modulus, as it is not very clear why these factors are influential. Additionally, future research could investigate if the production method could be reduced to only two stages.

Finally, this study provides a method to produce 26 GDLs with varying characteristics. These results can be used in future studies to investigate the impact of a GDL on the performance of a catalyzed GDE. This also allows for interaction effects between the GDL and the catalyst layer to be studied, as we will show in Chapter 4. Future research on electrochemical reactions using GDEs can use these recipes to test GDLs with different characteristics and quantitatively understand what makes an ideal GDL.

Acknowledgements

This work was supported by the European Commission under contract 722614 (Innovative training network Elcorel)

References

- (1) Kolyagin, G. A.; Vasil'eva, I. S.; Kornienko, V. L. Effect of the Composition of Gas-Diffusion Carbon Black Electrodes on Electrosynthesis of Hydrogen Peroxide from Atmospheric Oxygen. *Russ. J. Appl. Chem.* **2008**, *81* (6), 983–987, DOI 10.1134/S1070427208060116.
- (2) Monteiro, M. C. O.; Philips, M. F.; Schouten, K. J. P.; Koper, M. T. M. Efficiency and Selectivity of CO₂ Reduction to CO on Gold Gas Diffusion Electrodes in Acidic Media. *Nat. Commun.* **2021**, *12* (1), 4943, DOI 10.1038/s41467-021-24936-6.
- (3) Maja, M.; Orecchia, C.; Strano, M.; Tosco, P.; Vanni, M. Effect of Structure of the Electrical Performance of Gas Diffusion Electrodes for Metal Air Batteries. *Electrochim. Acta* **2000**, *46* (2–3), 423–432, DOI 10.1016/S0013-4686(00)00601-0.
- (4) Wang, P.; Zhao, J.; Shi, R.; Zhang, X.; Guo, X.; Dai, Q.; Zhang, T. Efficient Photocatalytic Aerobic Oxidation of Bisphenol A via Gas-Liquid-Solid Triphase Interfaces. *Mater. Today Energy* **2022**, *23*, 100908, DOI 10.1016/j.mtener.2021.100908.
- (5) Shi, R.; Guo, J.; Zhang, X.; Waterhouse, G. I. N.; Han, Z.; Zhao, Y.; Shang, L.; Zhou, C.; Jiang, L.; Zhang, T. Efficient Wettability-Controlled Electroreduction of CO₂ to CO at Au/C Interfaces. *Nat. Commun.* **2020**, *11* (1), 3028, DOI 10.1038/s41467-020-16847-9.
- (6) Shi, R.; Wang, Z.; Zhao, Y.; Waterhouse, G. I. N.; Li, Z.; Zhang, B.; Sun, Z.; Xia, C.; Wang, H.; Zhang, T. Room-Temperature Electrochemical Acetylene Reduction to Ethylene with High Conversion and Selectivity. *Nat. Catal.* **2021**, *4* (7), 565–574, DOI 10.1038/s41929-021-00640-y.
- (7) Huang, H.; Shi, R.; Zhang, X.; Zhao, J.; Su, C.; Zhang, T. Photothermal-Assisted Triphase Photocatalysis Over a Multifunctional Bilayer Paper. *Angew. Chemie Int. Ed.* **2021**, *60* (42), 22963–22969, DOI 10.1002/anie.202110336.
- (8) Philips, M. F.; Gruter, G.-J. M.; Koper, M. T. M.; Schouten, K. J. P. Optimizing the Electrochemical Reduction of CO₂ to Formate: A State-of-the-Art Analysis. *ACS Sustain. Chem. Eng.* **2020**, DOI 10.1021/acssuschemeng.0c05215.
- (9) Philips, M. F.; Pavesi, D.; Wissink, T.; Figueiredo, M. C.; Gruter, G.-J. M.; Koper, M. T. M.; Schouten, K. J. P. Electrochemical CO₂ Reduction on Gas Diffusion Electrodes: Enhanced Selectivity of In–Bi Bimetallic Particles and Catalyst Layer Optimization through a Design of Experiment Approach. *ACS Appl. Energy Mater.* **2022**, acsaem.1c03156, DOI 10.1021/acsaem.1c03156.
- (10) Uchida, M. Effects of Microstructure of Carbon Support in the Catalyst Layer on the Performance of Polymer-Electrolyte Fuel Cells. *J. Electrochem. Soc.* **1996**, *143* (7), 2245, DOI 10.1149/1.1836988.

- (11) Kong, C. S.; Kim, D.-Y.; Lee, H.-K.; Shul, Y.-G.; Lee, T.-H. Influence of Pore-Size Distribution of Diffusion Layer on Mass-Transport Problems of Proton Exchange Membrane Fuel Cells. *J. Power Sources* **2002**, *108* (1–2), 185–191, DOI 10.1016/S0378-7753(02)00028-9.
- (12) Philips, M. F.; Gruter, G.-J. M.; Koper, M. T. M.; Schouten, K. J. P. Optimizing the Electrochemical Reduction of CO₂ to Formate: A State-of-the-Art Analysis. *ACS Sustain. Chem. Eng.* **2020**, *8* (41), 15430–15444, DOI 10.1021/acssuschemeng.0c05215.
- (13) Schulze, M.; Lorenz, M.; Kaz, T. XPS Study of Electrodes Formed from a Mixture of Carbon Black and PTFE Powder. *Surf. Interface Anal.* **2002**, *34* (1), 646–651, DOI 10.1002/sia.1378.
- (14) Kolyagin, G. A.; Kornienko, V. L. New Accelerated Method of Impregnation by Aqueous Electrolyte of Carbon Black Gas-Diffusion Electrodes to Study Their Structural and Electrochemical Characteristics. *Russ. J. Electrochem.* **2011**, *47* (11), 1268–1273, DOI 10.1134/S1023193511110115.
- (15) Moussallem, I.; Pinnow, S.; Wagner, N.; Turek, T. Development of High-Performance Silver-Based Gas-Diffusion Electrodes for Chlor-Alkali Electrolysis with Oxygen Depolarized Cathodes. *Chem. Eng. Process. Process Intensif.* **2012**, *52*, 125–131, DOI 10.1016/j.cep.2011.11.003.
- (16) Li, A.; Wang, H.; Han, J.; Liu, L. Preparation of a Pb Loaded Gas Diffusion Electrode and Its Application to CO₂ Electroreduction. *Front. Chem. Sci. Eng.* **2012**, *6* (4), 381–388, DOI 10.1007/s11705-012-1216-2.
- (17) Del Castillo, A.; Alvarez-Guerra, M.; Solla-Gullón, J.; Sáez, A.; Montiel, V.; Irabien, A. Sn Nanoparticles on Gas Diffusion Electrodes: Synthesis, Characterization and Use for Continuous CO₂ Electroreduction to Formate. *J. CO₂ Util.* **2017**, *18*, 222–228, DOI 10.1016/j.jcou.2017.01.021.
- (18) Pozio, A.; Cemmi, A.; Carewska, M.; Paoletti, C.; Zaza, F. Characterization of Gas Diffusion Electrodes for Polymer Electrolyte Fuel Cells. *J. Fuel Cell Sci. Technol.* **2010**, *7* (4), 041003, DOI 10.1115/1.3119061.
- (19) Tomantschger, K.; Kordesch, K. V. Structural Analysis of Alkaline Fuel Cell Electrodes and Electrode Materials. *J. Power Sources* **1989**, *25* (3), 195–214, DOI 10.1016/0378-7753(89)80004-7.
- (20) Kenjo, T.; Kawatsu, K. Current-Limiting Factors and the Location of the Reaction Area in PTFE-Bonded Double-Layered Oxygen Electrodes. *Electrochim. Acta* **1985**, *30* (2), 229–233, DOI 10.1016/0013-4686(85)80087-6.
- (21) Lasia, A. Impedance of Porous Electrodes. In *ECS Transactions*; ECS, 2008; pp 1–18, DOI 10.1149/1.3004025.
- (22) Lee, H.-K.; Park, J.-H.; Kim, D.-Y.; Lee, T.-H. A Study on the Characteristics of the Diffusion Layer Thickness and Porosity of the PEMFC. *J. Power Sources* **2004**, *131* (1–2), 200–206, DOI 10.1016/j.jpowsour.2003.12.039.

- (23) Tseng, C.-J.; Lo, S.-K. Effects of Microstructure Characteristics of Gas Diffusion Layer and Microporous Layer on the Performance of PEMFC. *Energy Convers. Manag.* **2010**, *51* (4), 677–684, DOI 10.1016/j.enconman.2009.11.011.
- (24) Gülzow, E.; Schulze, M. Long-Term Operation of AFC Electrodes with CO₂ Containing Gases. *J. Power Sources* **2004**, *127* (1–2), 243–251, DOI 10.1016/j.jpowsour.2003.09.020.
- (25) Gullá, A. F.; Krasovic, J. L. Gas-Diffusion Electrode. WO 2013/037902 A2, 2013.
- (26) Philips, M. F.; Ansovini, D.; Figueiredo, M. C. C.; Krasovic, J. Method for the Preparation of a Gas Diffusion Layer and a Gas Diffusion Layer Obtained or Obtainable by Such Method. WO2020165074A1, 2020.
- (27) SAS Institute Inc. *JMPTM 14 Design of Experiments Guide*; Cary, NC, 2018.
- (28) Stalder, A. F.; Kulik, G.; Sage, D.; Barbieri, L.; Hoffmann, P. A Snake-Based Approach to Accurate Determination of Both Contact Points and Contact Angles. *Colloids Surfaces A Physicochem. Eng. Asp.* **2006**, *286* (1–3), 92–103, DOI 10.1016/j.colsurfa.2006.03.008.
- (29) Claeskens, G.; Hjort, N. L. *Model Selection and Model Averaging*; 2006.
- (30) Klimberg, R.; McCullough, B. D. *Fundamentals of Predictive Analytics with JMP*; Cary, NC, 2013.
- (31) SAS Institute Inc. *JMPTM 14 Fitting Linear Models*; Cary, NC, 2018.
- (32) Thompson, J. Design and Analysis in Chemical Research; Tranter, R. L., Ed.; 2000; pp 85–110.
- (33) Włoch, J.; Terzyk, A. P.; Wiśniewski, M.; Kowalczyk, P. Nanoscale Water Contact Angle on Polytetrafluoroethylene Surfaces Characterized by Molecular Dynamics–Atomic Force Microscopy Imaging. *Langmuir* **2018**, *34* (15), 4526–4534, DOI 10.1021/acs.langmuir.8b00257.
- (34) Fox, H. .; Zisman, W. . The Spreading of Liquids on Low Energy Surfaces. I. Polytetrafluoroethylene. *J. Colloid Sci.* **1950**, *5* (6), 514–531, DOI 10.1016/0095-8522(50)90044-4.
- (35) Ellison, A. H.; Fox, H. W.; Zisman, W. A. Wetting of Fluorinated Solids by Hydrogen-Bonding Liquids. *J. Phys. Chem.* **1953**, *57* (7), 622–627, DOI 10.1021/j150508a004.
- (36) Extrand, C. W. Designing for Optimum Liquid Repellency. *Langmuir* **2006**, *22* (4), 1711–1714, DOI 10.1021/la052540l.
- (37) Quéré, D. Wetting and Roughness. *Annu. Rev. Mater. Res.* **2008**, *38* (1), 71–99, DOI 10.1146/annurev.matsci.38.060407.132434.
- (38) Marmur, A. From Hygrophilic to Superhydrophobic: Theoretical Conditions for Making High-Contact-Angle Surfaces from Low-Contact-Angle Materials. *Langmuir* **2008**, *24* (14), 7573–7579, DOI 10.1021/la800304r.

- (39) Motoo, S.; Watanabe, M.; Furuya, N. Gas Diffusion Electrode of High Performance. *J. Electroanal. Chem. Interfacial Electrochem.* **1984**, *160* (1–2), 351–357, DOI 10.1016/S0022-0728(84)80139-4.

Chapter 4

Electrochemical CO₂ Reduction on Gas Diffusion Electrodes: Catalyst Layer Optimization Through a Design of Experiment Approach⁴

⁴ This chapter is based on Philips, M. F., Pavesi, D., Wissink, T., Figueiredo, M. C., Gruter, G.-J. M., Koper, M. T. M. & Schouten, K. J. P. Electrochemical CO₂ Reduction on Gas Diffusion Electrodes: Enhanced Selectivity of In–Bi Bimetallic Particles and Catalyst Layer Optimization through a Design of Experiment Approach. *ACS Appl. Energy Mater.*, 2022, acsaem.1c03156 doi:10.1021/acsaem.1c03156.

Introduction

A GDE consists of a GDL and a catalyst layer. Both of these layers can affect the performance of the GDE and should be considered for the total optimization of the electrode. The effect of the GDL has been hardly studied in this reaction, while the catalyst layer characteristics have received the most attention. The type of binder used in the catalyst layer has been shown to give various performances of GDEs.¹ The catalyst loading has been shown to shift product distributions between formate and CO.² Yet, the amount of catalyst supported on carbon and the binder amount in the catalyst layer have also been scarcely studied for this reaction. Furthermore, most published results for this reaction have a run time of less than eight hours, and consequently, the stability of GDEs for this reaction has not been well assessed. The current state of the art in current density for this reaction appears to be the study by Löwe et al., where they achieve 1800 mA/cm² with 70% current efficiency toward formate for 45 minutes.³ Additionally, the longest operated GDE for this reaction we have found was from the paper by Yi et al., where the performance of a Bi GDE was monitored for 564 hours in a potentiostatic experiment with an average current density < 100 mA/cm².⁴

Chapter 3 showed how a gas diffusion layer (GDL) production method can be modified to change the characteristics of the GDL. Now, in this chapter, two GDLs with varying characteristics are tested with various catalyst layers to determine if any factors of the catalyst layer interact with the GDL and affect the performance of the gas diffusion electrode (GDE). Hg, Pb, Sn, In, and Bi have been typical electrocatalysts used for producing formate.⁵ These catalysts have been shown to produce formate at <90% current efficiency when used in a GDE. However, Avantium has discovered a catalyst that can achieve even higher current efficiencies at higher current densities.

Appendix B contains work included in the original paper that was performed in collaboration with Davide Pavesi, which compares Avantium's patented InBi electrocatalyst to pure In and Bi catalysts synthesized by the same method and provides a rationale for the enhanced performance of the InBi catalyst.⁶ We then use this superior catalyst in a Design of Experiments (DOE) to optimize a GDE. The DOE investigates the effect of the GDL type, catalyst loading, amount of catalyst supported on carbon, binder amount, binder type, and current density on the current efficiency toward formate, the cell potential, and the electrode stability. This is the first study of which we are aware that investigates possible interactions between catalyst layer characteristics and different GDL structures for the electrochemical conversion of CO₂ toward formate. Additionally, all of the studies that we have encountered for this reaction attempt to optimize the performance using one factor at a time approach, which can result in finding a local optimum rather than a global optimum. The DOE approach, instead, can help to find a global optimum by taking into account interactions between multiple factors.⁷ The goal of this study is to identify several factors and interactions between the factors investigated that are influencing the current efficiency toward formate and the cell potential. The significance of the interactions shows that several considerations should be made when comparing results between studies or designing future studies. A definitive explanation of the

reasons behind the significance of factors is beyond the scope of this study and should be the object of future investigations.

Experimental Methods

Materials and Chemicals

The materials and chemicals used in this chapter and the supplier they were purchased from are shown in Table C.1 in Appendix C.

Bimetallic Particle Production and Ink Formulation

The InBi catalysts (50% In, 50% Bi) were prepared with varying amounts supported on carbon (30, 60, or 90%) by a chemical reduction method described in the patent.⁶ 1.64 g of InCl_3 and 1.98 g of $\text{Bi}(\text{NO}_3)_3 \cdot 5\text{H}_2\text{O}$ were added to 250 mL of triethylene glycol. 1.14 g of trisodium citrate dihydrate was added to the mixture as a non-aggregation agent. The mixture was then heated to 60 °C under a nitrogen atmosphere while being stirred. Once all of the salts were dissolved, a calculated amount of Vulcan carbon was added to the mixture in accordance with the desired metal loading on carbon. This mixture was then stirred for approximately 15 hours (overnight) before being heated to 100 °C in an Argon atmosphere. Once at temperature, 4.5 mL of a 12.5 M NaBH_4 in water solution was injected into the reaction vessel in approximately 40 seconds. The mixture was then left to react for 15 minutes at 100 °C before cooling down to room temperature. A pressure filter was used to collect and rinse the catalyst with isopropanol and a 1:1 isopropanol/water mixture.

These catalysts were used in an ink formulation to apply to a gas diffusion layer by airbrushing. The ink formulation and airbrushing were performed by Davide Pavesi, and the method is described in Appendix B.

Gas Diffusion Layer Production

The synthesis method for the GDLs in this study was modified from a patented process.⁸ 8.92 mL of PTFE DISP 30 was added to 70 mL of a 1:1 volume IPA/water mixture and stirred for 1 minute before mixing with 15g of Soltex Acetylene black 75%-03 carbon in a Bourgini mixer. After 1 minute of mixing, a dough-like mixture was collected. A rolling pin was used to prepare the dough for a cross-rolling technique to obtain the desired thickness, where the thickness setting is a discrete numerical factor. A rectangle of about 250 cm² was cut from this structure, and a paint roller was used to apply PTFE DISP 30 diluted 50% with 1:1 volume IPA:H₂O to the back of the dough. Fibreglast™ 1k plain weave carbon fiber fabric was used as the current collector and placed on top of the PTFE applied layer. A Carver heated press (Model number 4533) was used to press the structure in three stages at various temperatures, pressures, and durations according to the two GDL methods tested shown in Table 4.1. GDLs of 4.4 cm x 4 cm were cut from the final structures. GDL synthesis methods 16 (GDL 1 in the DOE) and 23 (GDL 2 in the DOE) from Chapter 3 were used to explore the effect of the GDL

on the performance of the electrode. These two GDLs exhibit several differences in characteristics. This increases the chance of detecting the GDL type as having a significant effect on the electrode performance; however, it will not be clear as to which characteristic, or combination of characteristics, are mainly responsible for the effect of the GDL. A schematic of the GDLs synthesized from the above method and a picture of our GDL 2 structure (GDL 1 and GDL 2 look virtually identical on a macroscopic scale) are shown in Appendix C (Figures C.1 and C.2).

Table 4.1. GDL Production Conditions

Production Process Condition	GDL 1	GDL 2
PTFE wt%	35	35
Rolling Thickness Setting	4	4
Time Stage 1 (min)	60	32.5
Pressure Stage 1 (Ton)	20	10.25
Temp Stage 1 (°C)	200	140
Time Stage 2 (min)	60	32.5
Pressure Stage 2 (Ton)	20	10.25
Temp Stage 2 (°C)	335	307.5
Time Stage 3 (min)	60	32.5
Pressure Stage 3 (Ton)	25	13
Temp Stage 3 (°C)	335	317.5

Flow Cell Electrolysis

A commercial 10 cm² GDE cell from ElectroCell was used for all flow cell electrolysis experiments. The cathode and anode were separated by a NafionTM membrane (N-324). The cathode was a gas diffusion electrode that varied in formulation for the purpose of this study. The anode was a Ti current distributor coated with an Ir/Ru mixed metal oxide. The catholyte was 0.5M KHCO₃ and the anolyte was 0.5M H₂SO₄. The anodic reaction was the oxygen evolution reaction. Both electrolytes were recirculated through the cell at a flow rate of 50 mL/min. The CO₂ flow rate was dependent on the operating current density and was set to 50 - 100 mL/min. The cell was operated at constant current for two hours. The catholyte was neutralized with HCl and formate was quantified with a Perkin Elmer Lambda 35 UV-vis spectrometer. This UV method was developed separately at Avantium and validated by an ion chromatography method.

Design of Experiments for Catalyst Layer Optimization

The Custom Design Platform in JMP was used to generate a DOE for this study to investigate the effect of the following parameters on the cell potential, CE towards formate, and electrode stability: GDL, loading of the metal catalyst, amount of catalyst supported on carbon, the weight percentage of binder in the catalyst layer, binder type, and current density.⁹

The GDL and binder type were designated as categorical variables, while the others were continuous. All 2nd order interactions and quadratic terms were considered for a model. This resulted in a 32-run experimental matrix shown in the results section. Each GDE was operated for 120 minutes using the same conditions as mentioned above at the current density specified by the DOE. After the first 120 minutes, each GDE was operated at the other two current densities for 120 minutes each. Thus, each GDE was operated for a total of six hours at three current densities. Additionally, three runs were repeated to demonstrate the repeatability of the system. This data is shown in Appendix C (Figures C.3-C.6).

Assessing the Electrode Stability

Many of the GDEs were observed to have (bicarbonate) salt accumulate in the structure. This indicates that some structures are less stable than others. After each GDE was operated, the amount of salt accumulated in/on the structure was ranked on a scale of 1 to 5. Pictures demonstrating each level of salt accumulation can be found in Appendix C (Figure C.7). Analysis of the stability of the electrode was performed using the methods described in the next section and with this salt accumulation number as the response.

Extended operation experiments

Two experiments were performed as extended operation runs to determine the lifetime stability of these electrodes. The two electrodes used for experimental run 5 were used for these extended operation experiments. Therefore, each electrode for these experiments was operated for six hours in the DOE set prior to running the extended experiments. Each electrode was operated at a different constant current density until the current efficiency of formate decreased below 50%. Additionally, every 24 hours, the current to the electrochemical cell was set to zero, the cathode compartment was rinsed with deionized water, and air was passed through the cathode compartment for one hour to regenerate the electrode before restarting the cell at the operating current density.¹⁰

Design of Experiments Analysis Workflow

After all of the runs were performed and repeated experiments (i.e., separate electrodes were synthesized in the same specifications for the DOE experimental run) demonstrated repeatability, the stepwise platform in JMP was used to generate models for the current efficiency toward formate, the cell potential, and the electrode stability. All factors, two-way interactions, and square terms were considered for the model. Multiple linear regression was used to generate two models for each response, one using the Bayesian Information Criterion (BIC) and the other using the Akaike Information Criterion (AIC) as a stopping rule to help prevent overfitting.^{11,12} The models generated were in the form of Equation 4.1:

$$y = b_1X_1 + b_2X_2 + b_3X_3 + \cdots + b_nX_n \quad (4.1)$$

Where b_n is the model term coefficient, and X_n is the factor variable which can be a multiplicative combination of two factors (for interactions) or a squared factor (to model curvature).

The model that used the BIC stopping rule was chosen for the current efficiency towards formate, while both methods resulted in the same model for the cell potential. A comparison between the models generated from the two stopping rules and the reasoning for model selection can be found in Appendix C (Figures C.8-C.13). The model terms in the selected models were then sorted based on the coefficients of scaled model terms, which can be used to show which terms are affecting the response the greatest.⁷ Model terms with p values less than 0.01 (99% confidence) are discussed in more detail for each model.

Results

Design of Experiments

The tabulated DOE results are shown in Table 4.2.

Table 4.2. Experimental Design Matrix and Run Results

Run Number	GDL Method Number	Loading (mg/cm ²)	Catalyst on Carbon (wt%)	Current Density (mA/cm ²)	Binder in Catalyst Layer (wt%)	Binder Type	Cell Potential (V)	Formate Current Efficiency	Salt Accumulation Number
1	1	2	30	400	30	PVDF	10.18	68.50%	2.5
2	1	0.5	30	400	10	PVDF	10	93.50%	1
3	1	1.25	90	300	10	PVDF	8.45	69.90%	4
4	2	2	30	400	30	Nafion™	9.92	84.10%	4
5	1	2	60	400	20	PVDF	10.09	94.60%	1
6	1	0.5	30	400	20	Nafion™	9.43	83.50%	3
7	2	2	90	300	20	Nafion™	8.25	93.40%	1
8	1	2	90	400	10	Nafion	9.65	94.20%	1
9	1	2	60	200	30	Nafion™	6.84	82.40%	3
10	2	2	90	400	30	PVDF	8.35	28.20%	4
11	1	0.5	90	400	30	PVDF	11.46	23.40%	4
12	2	0.5	90	200	30	PVDF	6.4	86.30%	3
13	1	2	30	300	10	Nafion™	8.43	84.60%	2
14	2	1.25	60	400	10	Nafion™	8.29	77.20%	3.5
15	2	0.5	90	400	10	PVDF	9.25	60.00%	4
16	2	0.5	30	400	30	PVDF	9.12	93.10%	1
17	2	0.5	30	200	10	PVDF	6.74	90.30%	1
18	2	0.5	30	300	10	Nafion™	8.9	87.40%	4
19	2	0.5	30	200	30	Nafion™	6.9	79.70%	1
20	1	0.5	60	300	30	Nafion™	9.14	40.20%	3.5
21	2	2	90	200	10	PVDF	6.77	88.50%	4
22	1	2	90	200	30	PVDF	6.7	23.30%	3
23	2	2	30	200	30	PVDF	6.27	85.40%	2.5
24	1	0.5	90	200	10	Nafion™	7.14	95.40%	1
25	1	1.25	30	200	20	Nafion™	6.78	94.10%	2
26	2	1.25	90	200	30	Nafion™	6.84	70.30%	5
27	2	2	60	200	10	Nafion™	7	95.20%	3
28	1	0.5	30	200	30	PVDF	6.11	86.10%	4
29	1	2	30	200	10	PVDF	6.26	77.10%	2
30	2	0.5	90	400	20	Nafion™	8.12	99.40%	1
31	2	2	30	400	10	PVDF	9.39	63.40%	4
32	1	1.25	90	400	30	Nafion™	10.23	13.40%	3

Summaries of fit (including the R^2 values and root mean square error) and the coefficient estimates and p-values for the model terms are listed in order of statistical significance under the Sorted Parameter Estimates in Appendix C (Figures C.9 and C.11, and C.13). The null hypothesis of the t-test performed for each estimate is that the parameter's coefficient is zero. Therefore, when the p-value is low, the null hypothesis is rejected, and the model term is shown to have statistical significance. Furthermore, the lower the p-value, the higher the probability that the parameter is statistically significant.

Additionally, the three model profilers used for visualizing the respective equations are also shown in Appendix C (Figures C.14-C.16). The model profilers are only a snapshot of the whole model. The trend for each factor term in the model can be seen in these figures; however, these curves can change if there is a two-factor interaction in the model or can be shifted as other factors are changed.

The coefficients of the model terms indicate the average change in response for every unit increase in the factor term. Comparing these coefficients directly can lead to wrong conclusions as these coefficients are directly affected by the scale of the factor (i.e., current density measured in kA/m^2 vs. mA/cm^2 results in a two-order of magnitude difference in the numerical value and thus the coefficient for the single factor model term can vary by two orders of magnitude depending on which unit is used.) Therefore, scaling the factors such that the mean is zero and the range is two and then fitting a model with these scaled factors results in coefficients that can be impartially compared and allow for the determination of which factors are influencing the response the most.¹³ The model term coefficients for scaled factors for the current efficiency toward formate, cell potential, and salt accumulation number are shown in Figures 4.1 - 4.3.

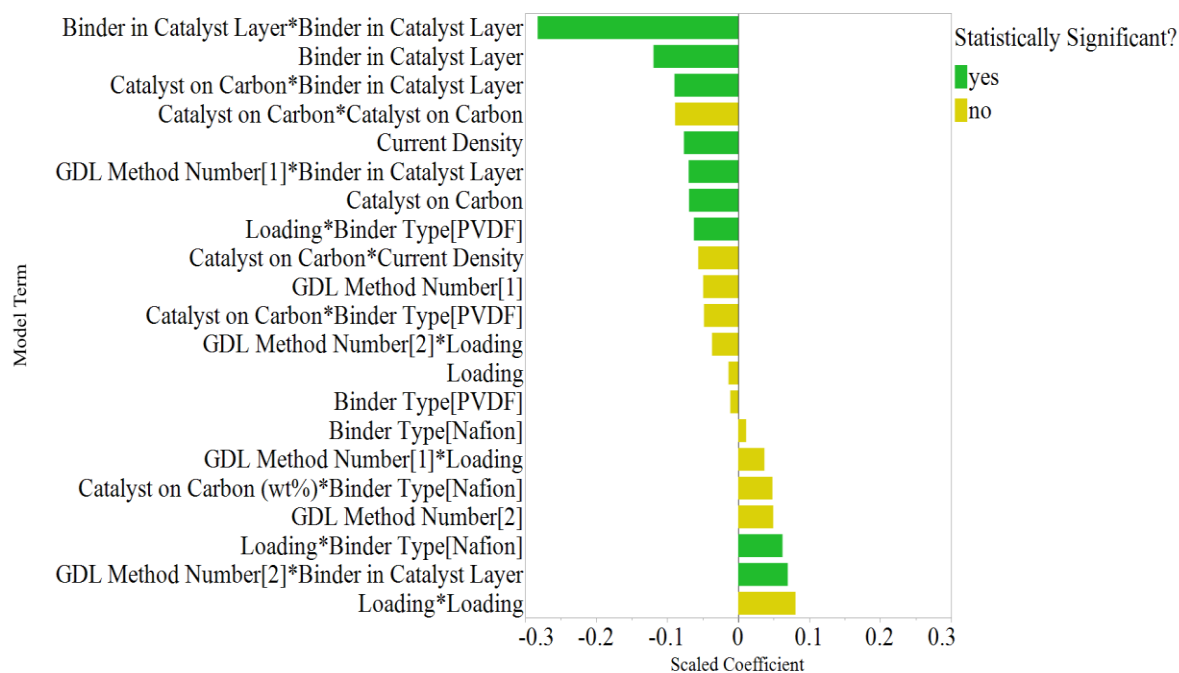


Figure 4.1. Model term coefficients for scaled factors for the current efficiency toward formate model generated by using the BIC as the stopping rule. Terms with p-values less than 0.01 are shown as statistically significant.

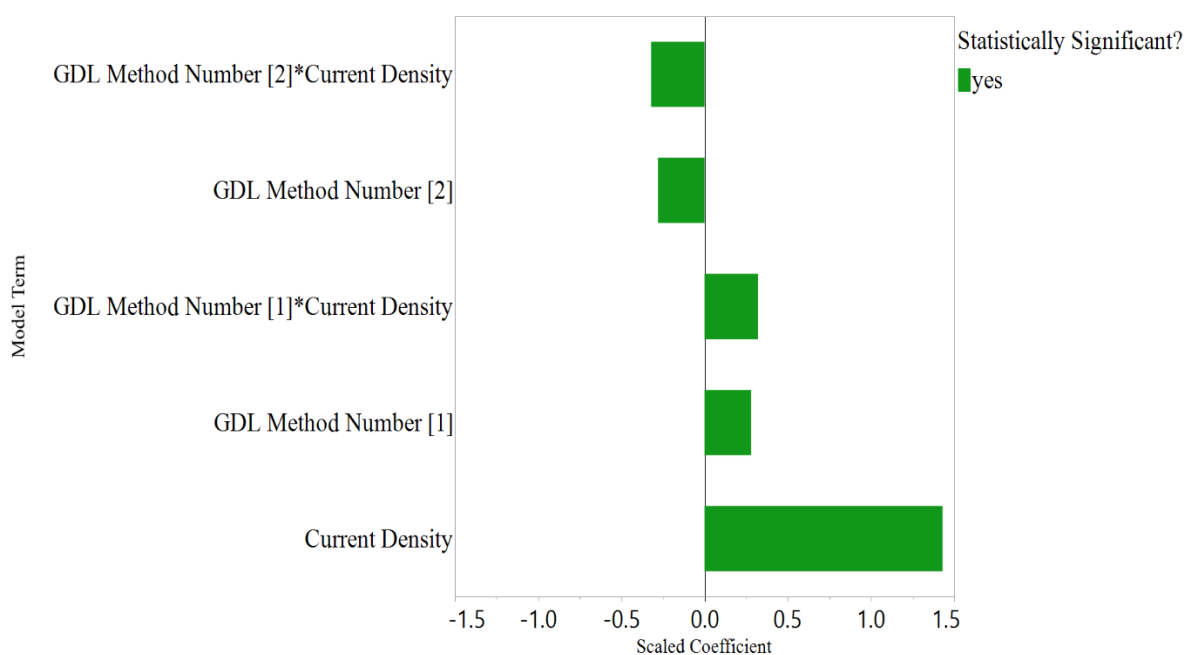


Figure 4.2. Model term coefficients for scaled factors for the cell potential model generated by using either the AIC or BIC as the stopping rule. Terms with p-values less than 0.01 are shown as statistically significant.

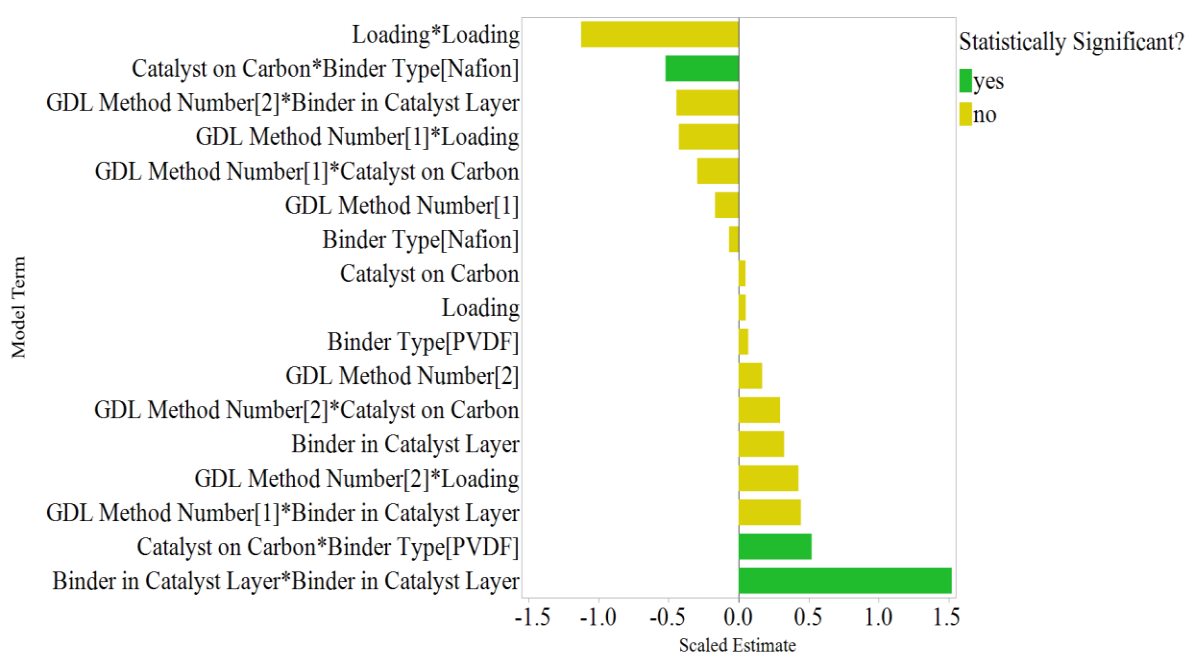


Figure 4.3. Model term coefficients for scaled factors for the salt accumulation number model generated by using the BIC as the stopping rule. Terms with p-values less than 0.01 are shown as statistically significant.

Extended operation experiments

These experiments were performed to demonstrate some level of stability with the electrodes synthesized in this study. Electrodes used from run number 5 (Table 4.2) were used for the extended operation experiments because of their high current efficiency toward formate and their low amount of salt accumulated in the structure. Furthermore, run number 5 was

included as a repeat in the DOE, so two of these electrodes were already synthesized and able to be used for a stability vs current density comparison. Each electrode used was run in the DOE for six hours before operating in the extended run experiments. Separate electrodes were operated at different current densities for these extended experiments. A plot of the current efficiency versus time for the two electrodes is shown in Figure 4.4.

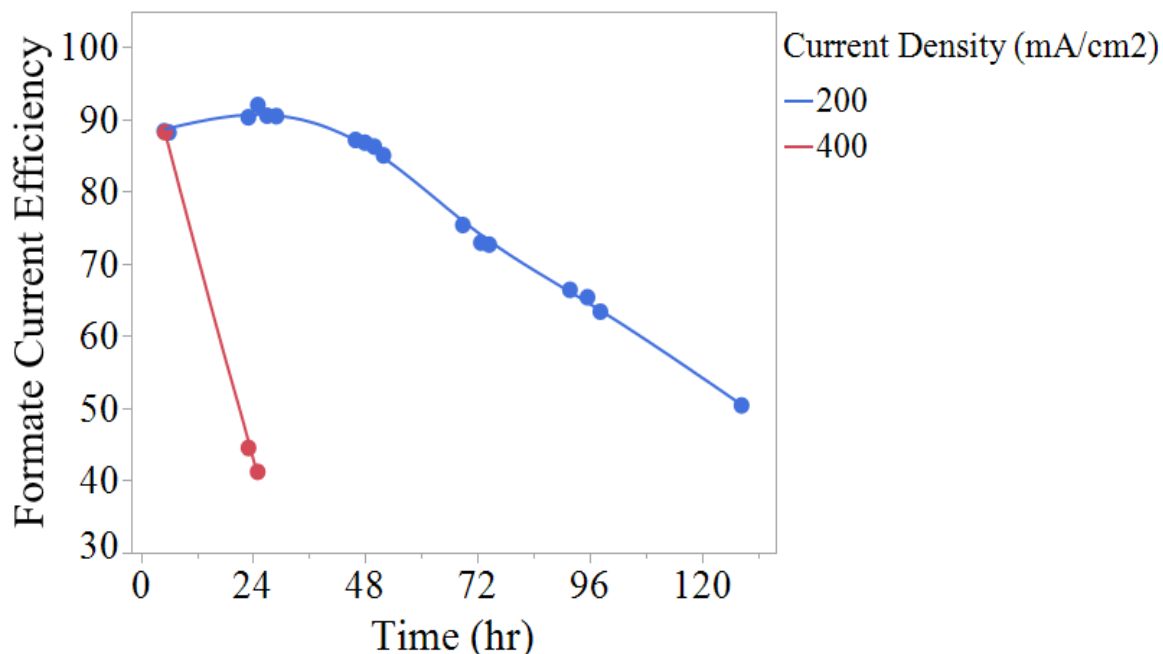


Figure 4.4. Current Efficiency toward formate vs time for two electrodes operated for extended hours. The electrodes used for these runs correspond to run number 5 in the DOE. In particular, the catalyst layer consisted of 60 wt% InBi/C with 20 wt% PVDF as a binder and a metal loading on the electrode of 2 mg/cm².

Discussion

Factors Influencing the Current Efficiency Toward Formate

The model for the formate current efficiency has an R^2 value of 0.901, indicating that 90.1% of the variation in the data is explained by this model. The best electrode at 400 mA/cm² is predicted to be with GDL method 2, 30 wt% catalyst on carbon, a loading of 0.5 mg/cm², 20 wt% PVDF. The significant factors and interactions in the model are explained in the next subsections.

Binder amount, catalyst on carbon, and the GDL Type

The amount of binder in the catalyst layer has the greatest influence on the CE toward formate. The square term for binder wt% indicates an optimal amount of binder to be used in the catalyst layer. Additionally, this optimum changes with varying amounts of catalyst supported on carbon and GDL type, as indicated by the significance of the interactions between these variables. Table 4.3 shows the predicted optimal binder for the range of catalysts on carbon and GDLs tested.

Table 4.3. Predicted optimal weight percentage of binder in the catalyst layer for different amounts of catalyst and GDL production methods

		GDL	
		1	2
Catalyst on carbon	90%	15.5 wt% binder	18.0 wt% binder
	30%	18.5 wt% binder	21.0 wt% binder

During the experiments, catalyst particles were physically observed in the catholyte of the first sample for GDEs that contained only 10 wt% binder, indicating that the catalyst was detaching from the surface. This low level of binder is therefore not enough to hold all of the catalyst onto the GDL. Conversely, when there is too much binder, the active catalytic area can be covered, and pores that are responsible for transporting CO₂ can become blocked and essentially rendered useless. This is supported by comparing the predicted optima in binder percentage. A lower optimum is predicted for higher amounts of catalyst on carbon. This is because a catalyst layer that is made with 90% catalyst supported on carbon should be thinner than a catalyst layer that is made with 30% catalyst supported on carbon for the same loading, and therefore, there is less material to bind to the GDL (i.e., the loading factor is defined as only the catalyst mass on the GDL). Decreasing the amount of catalyst supported on carbon is essentially diluting the catalyst in the solids that are applied to the GDL, and thus, more mass is needed to get to the same catalyst loading for lower percentages of catalyst supported on carbon. Additionally, using the same amount of binder in a thinner catalyst layer can result in the catalyst becoming covered more easily, resulting in a decrease in active catalytic surface area and a lower performance of the electrode.

A lower optimum is also predicted for GDL 1 than for GDL 2. These two GDLs have different characteristics; so, it is not clear which one, or combination, of GDL properties is influencing the performance of the GDE. This result shows that the choice of GDL is important for this reaction, and it is difficult to compare studies when different GDLs are used. Therefore, it is crucial to consider the GDL and how it interacts with the catalyst layer (mainly the amount of binder) when designing future studies.

It is surprising that the interaction between binder type and binder amount does not show statistical significance. This interaction would indicate that the optimum binder concentration is also dependent on the binder type used. The lack of statistical significance for this interaction suggests that the binder's role in the catalyst layer is primarily to bind the catalyst rather than provide ion conductivity. However, the fact that this interaction does not show significance in this study does not exclude that it could be relevant for other binders. These results only show that there is no significant difference in optimal binder amounts for Nafion™ and PVDF. Therefore, this interaction should still be considered with the use of a different binder.

Current density

As expected, the model shows a negative trend (designated by the negative coefficient) between the current density and the current efficiency toward formate. As the current density increases, the rate of CO₂ conversion also increases, which eventually cannot be sustained due to mass transfer limitations. This ultimately results in a decrease in the current efficiency toward formate. This mass transfer limitation can occur at one of several steps as discussed by Motoo et al.¹⁴ The limit can occur from: the supply of the reactant gas to the gas chamber side of GDL, the diffusion of the reactant gas through the GDL to the three-phase boundary and from the diffusion of dissolved gas at the three-phase boundary to the catalyst. Although the significance is not as high, the fact that the interaction between the catalyst on carbon and current density shows significance at $\alpha = 0.025$ (Figure C.9) suggests the limitation may be from a lack of accessible catalytic surface area. This interaction indicates that the lower percentage of catalyst supported on carbon performs better at the higher current densities tested (Figure C.14). This can be a result of a less dispersed catalyst on carbon and catalyst layer. SEM pictures (taken by Davide Pavesi) of the three catalysts tested are shown in Appendix B (Figure B.3). It seems that decreasing amounts of carbon cause an increase in the size of the particles obtained (i.e., the 90% catalyst supported on carbon contains much larger particles than either 60% or 30% catalyst supported on carbon). Additionally, the higher the amount of catalyst supported on carbon, the thinner the catalyst layer will be, and consequently, fewer layers will be sprayed onto the GDL in the spraying application process. This causes a less evenly dispersed catalyst across the geometrical area and can hinder mass transfer to the catalytic sites.

Loading of catalyst and binder type

The interaction between the catalyst loading and binder type is the last model term that shows significance for $\alpha = 0.01$. This interaction indicates that lower loadings of catalyst perform better with PVDF as a binder while higher loadings perform better with Nafion™ as a binder. There are several characteristics of the binder that could be contributing to this observation, such as the binder density and hydrophobicity. Additionally, Nafion™ has ion-conducting groups, which could be beneficial at higher loadings when there is more catalytic surface area. The significance of this effect shows the binder type used in the catalyst layer should not be overlooked when designing or comparing experiments for this reaction.

Factors influencing the cell potential

The cell potentials we observed may appear high because of the cell design that was used, non-optimized electrolyte feed concentrations, low product concentrations, and choice of the membrane. The model for the cell potential has an R^2 value of 0.88, indicating that 88% of the variation in the data is explained by this model with only two factors: the operating current density and the GDL type. These factors and interactions are discussed in the following subsections.

Current density and GDL production method

It is no surprise that the current density affects the cell potential the most out of all the factors. This is a consequence of the Butler-Volmer kinetics of the cathodic and anodic reactions as well as ohmic drop across the cell. The interaction between the GDL method and current density has the second largest effect on the cell potential. This interaction should be expected due to the different conductivities of the GDLs; however, the trend observed for the effect of the GDL on the cell potential is the opposite of what would be expected based solely on these characteristics. Table 4.4 shows the surface conductivity, conductance through, and porosity of the GDLs produced from methods 1 and 2.

Table 4.4. GDL Characteristic Data (from Chapter 3)

GDL	Surface Conductivity (S/m)	Conductance Through GDL (S)	Porosity by Hg Intrusion (%)	Average Cell Potential for all Runs with GDL Type (V)
1	591	249	69	8.56
2	365	59	53	7.91

The results from these experiments show that GDL 1 has a lower conductivity as the slope of the cell potential versus current density curve is seen to be larger in Figure C.15 for GDL 1. It is possible that the conductivity of the electrode changes depending on how wet it becomes during operation due to differences in the electrode's porosity or stability. Wetting of the electrode could occur more in GDL 1 due to it having a much higher porosity than GDL 2, as seen in Table 4.4. Additionally, some electrodes were observed to have a lot of salt accumulation on the back and in the pores of the GDL. In order for this salt accumulation to happen, some of the electrolyte had to penetrate the GDL during operation, which would directly affect the conductivity of the electrode and thus the cell potential. Analysis of this salt accumulation is discussed in more detail in the next section.

Factors Influencing the Salt Accumulation of the Electrode

The model generated for the salt accumulation number has a lower R^2 value than the other two responses investigated. This is a consequence of the admittedly rather subjective measurement accuracy and resolution, as only a scale of one to five was used to rank the salt accumulation in the electrode. The influential factors and interactions are discussed in the following subsections.

Binder amount, binder type, and catalyst on carbon

The binder amount influences the salt accumulation the most in the same way it affects the current efficiency of the cell. There are predicted optimum binder amounts between 15 and 20 wt% in the catalyst layer, while both the lower and higher amounts (10 and 30 wt%) show a higher salt accumulation. Additionally, 90 wt% catalyst on carbon performs with less salt accumulation than 30 wt% catalyst on carbon for Nafion™ binder electrodes, whereas the converse is true for PVDF binder electrodes. These factors were also highly influential for the

current efficiency of the electrode in the same type of trends (i.e., factor levels that show higher current efficiencies also show lower salt accumulation numbers). This makes the cause of the salt accumulation unclear and convoluted with the performance of the electrode. The salt accumulation could occur first and cause a decrease in the current efficiency of the cell, or the electrode could begin to lose activity which causes instability of the electrode and enables salt accumulation.

Extended stability experiments

The electrode that was operated at 200 mA/cm² (Figure 4.4) achieved 130.5 hours of total operation (including the hours of operation from the DOE experiment) above 50% current efficiency toward formate. Additionally, this electrode operated above 85% current efficiency toward formate for nearly 54 hours. On the other hand, the electrode that was run at 400 mA/cm² dropped drastically in current efficiency toward formate in less than 27 hours of total operation. This shows that the current density can extremely affect the lifetime of these electrodes. We suggest that the progressive deactivation of the catalyst can be due to a combination of factors. First, the fact that the activity can somewhat be extended by circulating clean water and exposing the electrode to air (as discussed in the experimental section) suggests that the accumulation of salt on the catalyst blinds active sites and the progressive loss of the metastable (hydr)oxides (the most active phase for CO₂ reduction) may play a role. Secondly, the highly alkaline environment reached during operation at high current density can contribute to the chemical degradation of the binder, decreasing its mechanical stability. Another DOE with the goal of determining which catalyst layer and GDL factors affect the electrode lifetime the most could lead to major insights into the cause of deactivation of these electrodes and/or the best formulation for long lifetime electrodes.

Conclusions

In conclusion, we took a holistic approach in optimizing a GDE for this reaction by using a DOE to identify crucial factors and interactions of a GDE that affect the current efficiency toward formate and cell potential. Nearly one-third of the GDEs produced for these experiments achieved over 90% current efficiency toward formate at current densities ≥ 200 mA/cm². The binder amount in the catalyst layer affects the current efficiency toward formate the most with the InBi catalyst. There appears to be an optimal binder amount that is dependent on the amount of catalyst supported on carbon and the GDL used. This is most likely due to a minimum amount of binder that is required to provide mechanical stability of the catalyst layer, while too much binder can reduce access to the catalyst and effectively reduce the total active surface area of the catalyst. Catalyst layers that use 30% catalyst supported on carbon will be thicker and have more particles to bind than a catalyst layer with 90% catalyst supported on carbon for the same catalyst loading in the layer. Therefore, it would be expected that the 30% catalyst supported on carbon requires more binder in the layer to physically bind all of the particles together than the 90% catalyst supported on carbon.

Although this optimal binder amount does not appear to depend on the binder type, only two binders were tested, so this interaction should not be overlooked when testing different binders in the future. For example, Wang et al. found an optimum PTFE concentration in the catalyst layer to be 11.1 wt% for a GDE converting CO₂ to formate. Their catalyst was not supported on carbon; however, the loading of the catalyst was 2.5x greater than the higher loadings in this study (5mg/cm² vs. 2mg/cm²). This optimal binder concentration is significantly less than the optimum concentrations found in this study for Nafion or PVDF.¹⁵

The 30 wt% catalyst supported on carbon was shown to perform better at higher current densities. This is expected to be due to the better dispersion of the catalyst on the carbon support (see Figure B3), leading to a more uniform distribution of catalyst across the geometrical area of the electrode, which further enhances the mass transfer of CO₂ to the catalyst surface. Additionally, Nafion™ is shown to be better than PVDF when higher loadings are used. This could be due to Nafion's™ ability to conduct cations, which will alter the local pH and environment of the electrode. The effect of the cation concentrations and pH on electrode performance has been studied and found to be significant for CO₂ electrocatalysts.^{16–20} This altered local environment could have a more significant effect for electrodes with higher loadings or more catalytic surface area. Alternatively, electrodes with a higher catalyst loading will have a thicker catalyst layer, which will increase the transport resistance of chemical species due to larger diffusion distances. This has been shown to hinder the performance of GDEs for CO production. Blake et al. found that although thinner catalyst layers had less reactive surface area, the benefit of shorter diffusion distances led to increased current efficiencies and higher CO current densities.²¹ On the other hand, an ion conductive binder (like Nafion) could help lower transport resistances in these thicker catalyst layers and thus improve the overall performance and durability of the electrode. For example, Nwabara et al. evaluated three types of binders in a GDE for CO production and found Nafion to be the most durable in terms of CO current efficiency for electrodes with a final loading of 1 mg/cm².²⁰

The current density and GDL are shown to affect the cell potential the most, as these two factors are able to explain over 88% of the variation in the data. The cell potentials reported in this study are high because electrolyte feeds, product concentrations, membrane used, and cell design were not optimized. These factors, along with the GDL, should be studied in a holistic approach to better optimize the cell potential.

The stability of the electrode was assessed by two methods: ranking the electrode structure post DOE run and operating two of the same electrodes at different current densities until the current efficiency toward formate decreased below 50%. The factors that were found to influence the salt accumulation on the electrode were similar to the factors affecting the current efficiency toward formate. This result shows the cause of the salt accumulation is convoluted with the current efficiency toward formate. The loss of activity of the electrode could cause electrode instability and lead to salt accumulation inside the structure, or the salt could inherently be accumulated in these electrodes, which could cause a decrease in the performance of the electrode. The latter is the more accepted hypothesis in literature.^{19,22–24} However, it is

still a question whether the salt is formed from electrode flooding and electrolyte drying, or if salt naturally precipitates in CO₂ GDEs throughout their operation.²²

Finally, the stability of the electrode was assessed by operating two of the same electrodes at different current densities until the current efficiency toward formate decreased below 50%. The two electrodes operated for extended hours were from experiment number five in the DOE. One electrode operated at 200mA/cm² above 50% current efficiency for a total of 130.5 hours. However, the other electrode ran for less than 24 additional hours before the current efficiency toward formate decreased to below 50%. This shows that the operating current density considerably affects the lifetime of the electrodes. Leonard et al. reported a similar trend in electrode lifetime vs current density when studying gas diffusion electrodes for CO₂ conversion to CO. They reported GDEs operating with high current efficiencies for 5 hours at current densities of 25mA/cm², while the same GDEs lasted for only 15 minutes when operated at 196 mA/cm².²³ A future study could look at several of the factors affecting stability outlined in this study and their effect on the lifetime of the electrodes to potentially find ways to operate for longer lifetimes at current densities greater than 200 mA/cm².

Acknowledgments

This work was supported by the European Commission under contract 722614 (Innovative training network Elcorel).

References

- (1) Philips, M. F.; Gruter, G.-J. M.; Koper, M. T. M.; Schouten, K. J. P. Optimizing the Electrochemical Reduction of CO₂ to Formate: A State-of-the-Art Analysis. *ACS Sustain. Chem. Eng.* **2020**, DOI 10.1021/acssuschemeng.0c05215.
- (2) Kopljär, D.; Inan, A.; Vindayer, P.; Wagner, N.; Klemm, E. Electrochemical Reduction of CO₂ to Formate at High Current Density Using Gas Diffusion Electrodes. *J. Appl. Electrochem.* **2014**, *44* (10), 1107–1116, DOI 10.1007/s10800-014-0731-x.
- (3) Löwe, A.; Schmidt, M.; Bienen, F.; Kopljär, D.; Wagner, N.; Klemm, E. Optimizing Reaction Conditions and Gas Diffusion Electrodes Applied in the CO₂ Reduction Reaction to Formate to Reach Current Densities up to 1.8 A Cm⁻². *ACS Sustain. Chem. Eng.* **2021**, *9* (11), 4213–4223, DOI 10.1021/acssuschemeng.1c00199.
- (4) Yi, L.; Chen, J.; Shao, P.; Huang, J.; Peng, X.; Li, J.; Wang, G.; Zhang, C.; Wen, Z. Molten-Salt-Assisted Synthesis of Bismuth Nanosheets for Long-term Continuous Electrocatalytic Conversion of CO₂ to Formate. *Angew. Chemie Int. Ed.* **2020**, *59* (45), 20112–20119, DOI 10.1002/anie.202008316.
- (5) Hori, Y. *Electrochemical CO₂ Reduction on Metal Electrodes, Modern Aspects of Electrochemistry*; Springer: New York, 2008.
- (6) Parajuli, R.; Ansovini, D.; Philips, M. F.; Schouten, K. J. P. Catalyst System for Catalyzed Electrochemical Reactions and Preparation Thereof, Applications and Uses Thereof. WO2019141827A1.
- (7) Thompson, J. Design and Analysis in Chemical Research; Tranter, R. L., Ed.; 2000; pp 85–110.
- (8) Philips, M. F.; Ansovini, D.; Figueiredo, M. C. C.; Krasovic, J. Method for the Preparation of a Gas Diffusion Layer and a Gas Diffusion Layer Obtained or Obtainable by Such Method. WO2020165074A1, 2020.
- (9) SAS Institute Inc. *JMPTM 14 Design of Experiments Guide*; Cary, NC, 2018.
- (10) Ansovini, D.; Philips, M. F.; Krasovic, J.; Figueiredo, M. C. C.; Schouten, K. J. Formation of Formic Acid with the Help of Indium-Containing Catalytic Electrode. WO2021122323, 2021.
- (11) Claeskens, G.; Hjort, N. L. *Model Selection and Model Averaging*; 2006.
- (12) Klimberg, R.; McCullough, B. D. *Fundamentals of Predictive Analytics with JMP*; Cary, NC, 2013.
- (13) SAS Institute Inc. *JMPTM 14 Fitting Linear Models*; Cary, NC, 2018.
- (14) Motoo, S.; Watanabe, M.; Furuya, N. Gas Diffusion Electrode of High Performance. *J. Electroanal. Chem. Interfacial Electrochem.* **1984**, *160* (1–2), 351–357, DOI 10.1016/S0022-0728(84)80139-4.

- (15) Wang, Q.; Dong, H.; Yu, H.; Yu, H. Enhanced Performance of Gas Diffusion Electrode for Electrochemical Reduction of Carbon Dioxide to Formate by Adding Polytetrafluoroethylene into Catalyst Layer. *J. Power Sources* **2015**, 279, 1–5, DOI 10.1016/j.jpowsour.2014.12.118.
- (16) Marcandalli, G.; Monteiro, M. C. O.; Goyal, A.; Koper, M. T. M. Electrolyte Effects on CO₂ Electrochemical Reduction to CO. *Acc. Chem. Res.* **2022**, 55 (14), 1900–1911, DOI 10.1021/acs.accounts.2c00080.
- (17) Wu, J.; Risalvato, F.; Zhou, X.-D. Effects of the Electrolyte on Electrochemical Reduction of CO₂ on Sn Electrode. *ECS Trans.* **2012**, 41 (33), 49–60, DOI 10.1149/1.3702412.
- (18) Moura de Salles Pupo, M.; Kortlever, R. Electrolyte Effects on the Electrochemical Reduction of CO₂. *ChemPhysChem* **2019**, 20 (22), 2926–2935, DOI 10.1002/cphc.201900680.
- (19) Endrődi, B.; Samu, A.; Kecsenovity, E.; Halmágyi, T.; Sebők, D.; Janáky, C. Operando Cathode Activation with Alkali Metal Cations for High Current Density Operation of Water-Fed Zero-Gap Carbon Dioxide Electrolysers. *Nat. Energy* **2021**, 6 (4), 439–448, DOI 10.1038/s41560-021-00813-w.
- (20) Nwabara, U. O.; Hernandez, A. D.; Henckel, D. A.; Chen, X.; Cofell, E. R.; De-Heer, M. P.; Verma, S.; Gewirth, A. A.; Kenis, P. J. A. Binder-Focused Approaches to Improve the Stability of Cathodes for CO₂ Electroreduction. *ACS Appl. Energy Mater.* **2021**, 4 (5), 5175–5186, DOI 10.1021/acsam.1c00715.
- (21) Blake, J. W.; Padding, J. T.; Haverkort, J. W. Analytical Modelling of CO₂ Reduction in Gas-Diffusion Electrode Catalyst Layers. *Electrochim. Acta* **2021**, 393, 138987, DOI 10.1016/j.electacta.2021.138987.
- (22) Sassenburg, M.; Kelly, M.; Subramanian, S.; Smith, W. A.; Burdyny, T. Zero-Gap Electrochemical CO₂ Reduction Cells: Challenges and Operational Strategies for Prevention of Salt Precipitation. *ACS Energy Lett.* **2023**, 8 (1), 321–331, DOI 10.1021/acsenergylett.2c01885.
- (23) Leonard, M. E.; Clarke, L. E.; Forner-Cuenca, A.; Brown, S. M.; Brushett, F. R. Investigating Electrode Flooding in a Flowing Electrolyte, Gas-Fed Carbon Dioxide Electrolyzer. *ChemSusChem* **2020**, 13 (2), 400–411, DOI 10.1002/cssc.201902547.
- (24) Xu, Y.; Edwards, J. P.; Liu, S.; Miao, R. K.; Huang, J. E.; Gabardo, C. M.; O'Brien, C. P.; Li, J.; Sargent, E. H.; Sinton, D. Self-Cleaning CO₂ Reduction Systems: Unsteady Electrochemical Forcing Enables Stability. *ACS Energy Lett.* **2021**, 6 (2), 809–815, DOI 10.1021/acsenergylett.0c02401.

Chapter 5

Custom Multipurpose Electrochemical Cell Design and Scale-Up

Introduction

Carbon Dioxide capture and utilization have been gaining attention as a way to combat climate change. There are several ways to convert carbon dioxide into higher-value chemicals. Electrochemical conversion has an advantage over traditional catalysis because it can occur at room temperature and ambient pressure. Additionally, formate has been identified in several studies as an attractive product to pursue from CO₂ electrochemically.^{1–5} However, currently, there are no commercial processes for this reaction.

There are several electrochemical configurations that can be used to produce formate from CO₂ (see Chapters 1 and 2 for a discussion and comparison). The current density, current efficiency, and cell potential are key metrics to compare when assessing the technologies. The current density directly affects the capital cost of the process, while the cell potential directly affects the energy costs, and the current efficiency affects both capital and energy costs. Conventional 3D electrodes, trickle flow configurations, and gas diffusion electrodes are the three main configurations researched for this reaction.⁶

3D electrodes have been thoroughly researched and have shown current efficiencies for formate up to 100% at current densities of 56 mA/cm².⁷ These electrodes convert CO₂ dissolved in an electrolyte, which causes a limitation in their maximum operable current density. This is seen by the current efficiency dropping to 63% at current densities of 95 mA/cm² for these electrodes. Trickle flow cell configurations use 3D electrodes but feed a gas-liquid mixture to the cathode. This CO₂ gas/electrolyte mixed feed slightly enhances the mass transfer of CO₂, resulting in current densities up to 294 mA/cm² and current efficiencies of 60% for this configuration.⁸ However, neither of these technologies can currently achieve as high efficiencies and current densities as gas diffusion electrodes (GDEs). GDEs are porous electrodes that create a three-phase boundary between the electrolyte, CO₂, and the catalyst. This three-phase boundary significantly enhances the mass transfer of CO₂ to the catalyst reaction sites on the electrode and allows for current efficiencies of 75% at current densities ranging from 390 to 500 mA/cm² to be achieved.^{9,10} For example, the work presented in Chapter 4 discovered a gas diffusion electrode that achieved 99.4% current efficiency at 400 mA/cm² for two hours. These are state-of-the-art results when compared to the literature reviewed in Chapter 1 (Figure 1.3).

GDEs are the most promising technology to pursue from a capital cost perspective.^{6,11} However, there is not much data published on cell potentials to thoroughly compare the technologies in terms of energy costs. Additionally, the cell potential is dependent on the electrolytes, the cell (current distribution and gap between electrodes), membrane, and anodic reaction, which further convolutes reported data. Furthermore, GDEs are more challenging to scale up as hydrostatic head can become a challenge to maintaining a three-phase boundary. Most reported research on GDEs for this reaction is at a scale of 10 cm² or less. This could be a consequence of a lack of commercially available GDE cells. However, larger-scale research is necessary to understand scaling challenges and eventually achieve a commercial process.¹² In this study, a multifunctional 200 cm² maximum area cell is designed for GDEs, conventional

3D electrodes, and trickle flow configurations for both the cathode and anode. Furthermore, we use this cell to scale up the best performing electrode formulation found in the set of DOE experiments in Chapter 4.

Experimental

Cell Design

A 200 cm² cell was designed in Solidworks for 3D or gas diffusion electrodes at the cathode and anode. The electrochemical cell design is significantly different for a GDE because an extra compartment is required for the gas feed to the GDE. This resulted in our designed cell having up to four compartments. The cell was constructed such that inserts could be used to adjust the active area to any desired size less than 200 cm², and flow distributions for each compartment are easily changeable and customizable. Comsol was used to screen flow distributor designs for uniform flow distribution inside the cell. Additionally, multiple cells could be pressed together into one assembly so that experimenting with cell stacks would be possible. A fully assembled cell view is shown in Figure 5.1 with its parts labeled and their material of construction listed in Table 5.1.

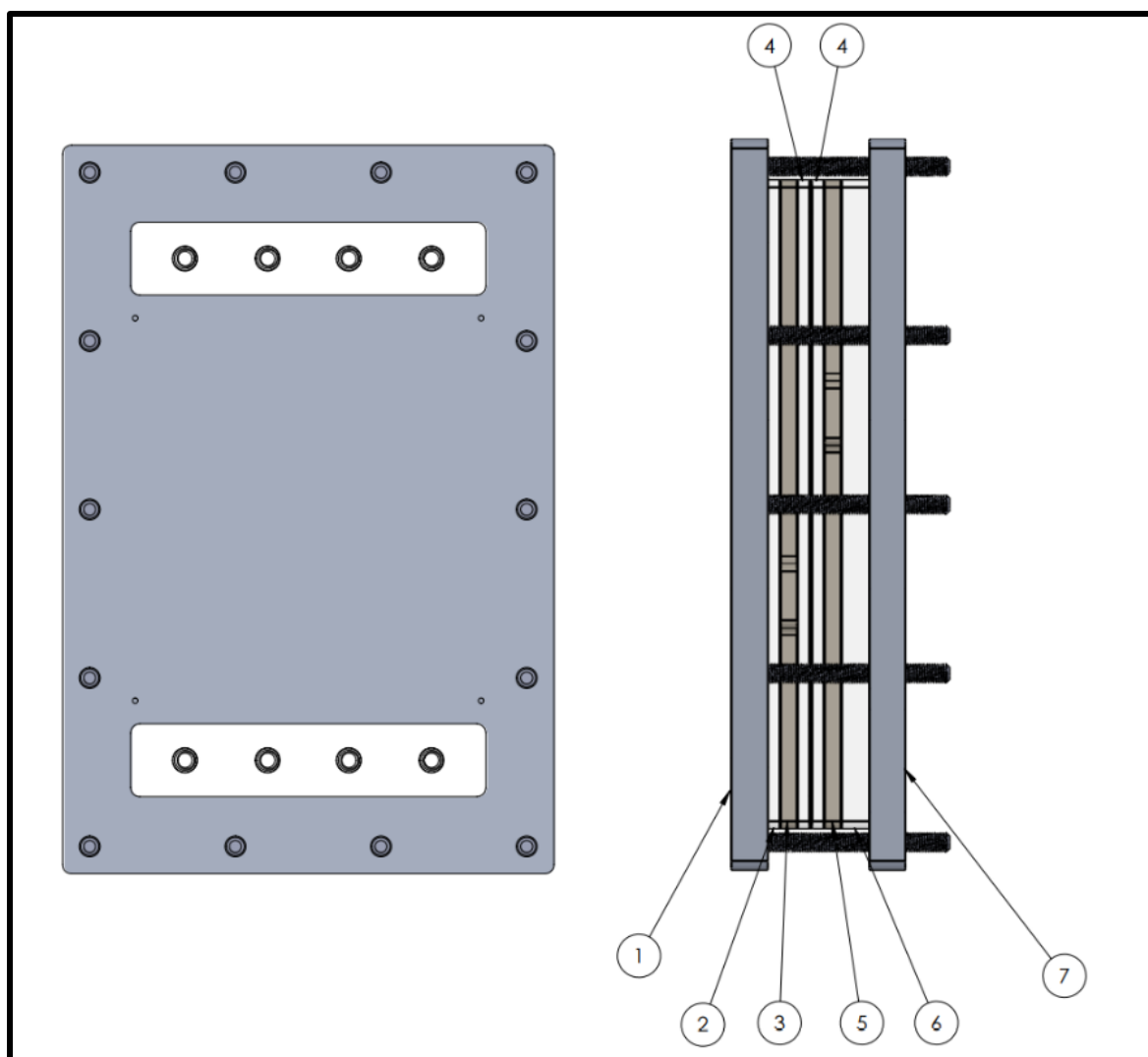


Figure 5.1. Whole-cell assembly with labeled parts description given in Table 5.1. The dimensions of the fully assembled cell are 27 cm x 40 cm x 12 cm. A GDE could fit in between rubber gaskets between parts 3 and 4 or 4 and 5. A membrane would fit between gaskets and the two chosen flow regions (4 and 4 for a two GDE setup, 3 and 4 or 4 and 5 for a single GDE setup, or 3 and 5 for a conventional 3D electrode flow through setup). The openings on the top compression plate are for clearance for NPT connections.

Table 5.1. Description of parts in Figure 1 and their material of construction.

Part Number	Description	Material
1	Base Compression Plate	Aluminum
2	Back Insulator Plate	PVC
3	Cathode Current Collector	Nickel
4	Flow Distributor	PVC
5	Anode Current Collector	Titanium
6	Feed Insulator Plate	PVC
7	Top Compression Plate	Aluminum

All flows are fed through the front of the cell, allowing multiple cells to be stacked in one assembly. Gaskets (not depicted) are employed in between each plate for sealing. This cell can run a GDE at the cathode and anode, resulting in a four-compartment design. This was to allow for the option of using a hydrogen anode with the cathodic reaction to reduce the cell potential significantly. If a conventional 3D anode is desired, one of the flow distributors (4) would be removed from the cell assembly. The flow distributor plate and customizations are displayed in Figure 5.2. Views A and B in Figure 2 show the core flow distributor plate of the cell. These plates are designed to be 6 mm thick so that testing various flow distributions would be easier (i.e., thinner flow inserts could deform more during operation and restrict flow in the cell). View C shows an example of flow distribution inserts (orange), while views D and E show inserts for reducing the cell's active area by half. This can be achieved such that the height of the cell is greater than the width of the cell (view D) or the width of the cell is greater than the height (views E & F). Inserts can be 3D printed using ABS filament allowing for fast and easy customization of these parts including customization of the cell area.

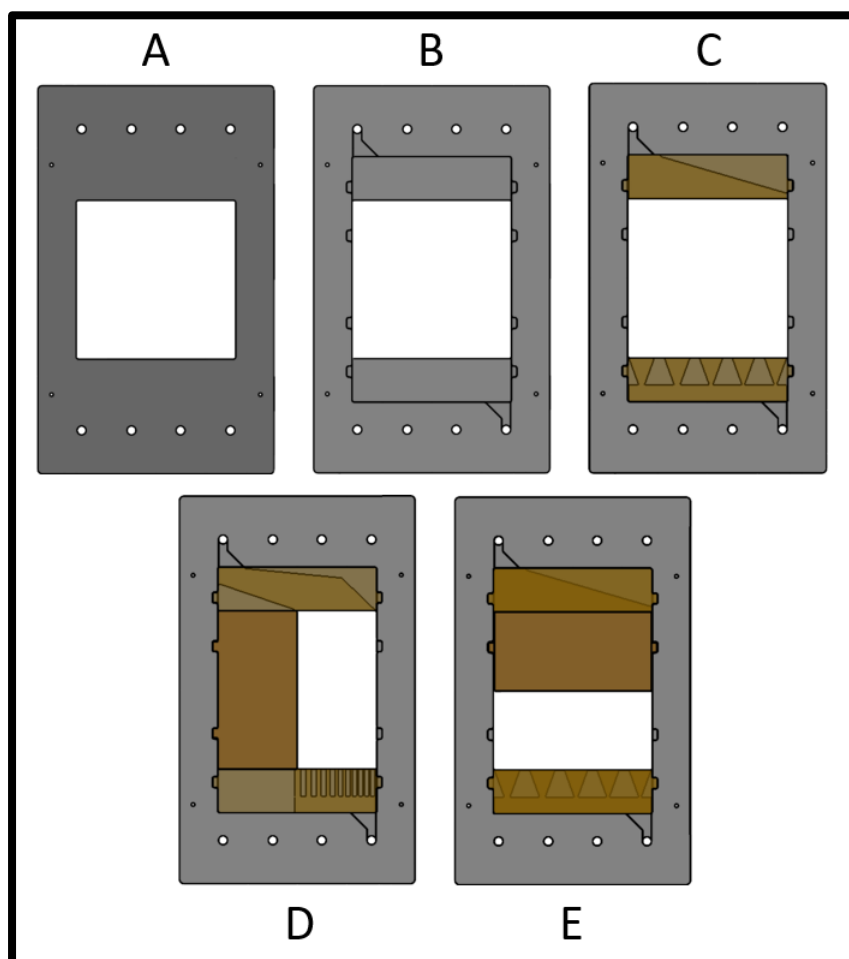


Figure 5.2. Configurations of the flow distributor plate with customizable inserts (orange). The insert shown in E is hollowed to allow flow behind it from the bottom to the top of the cell. A shows the front face of the flow distributor. B shows the back face of a flow distributor where connections with inserts are able to be made. C shows an example of two flow distribution inserts for a 200 cm² configuration. D shows two flow distribution inserts and a blinding/compression aid piece for a 100 cm² configuration where the electrode is taller than it is wide. E shows two flow distribution inserts and a blinding/compression aid piece for a 100 cm² configuration where the electrode is wider than it is tall.

Figure 5.3 displays the current collector plate and how it can be customized. Views A and B in Figure 5.3 show the core current collector plate. These plates are 10 mm thick. The anode is made from titanium, and the cathode is made from nickel. Additionally, the flow holes are lined with fluorinated ethylene propylene (FEP) to avoid shunt current losses. Similar to the flow distributor plate, inserts can be custom-designed for flow distribution on the backside of the current collector (view B). Views C and D show inserts for the current collector to modify the cell's active area by half, although adjusting the dimensions of this plate can change the active area to any value less than 200 cm². These inserts retain a recessed groove for a GDE to sit. A further open area of the plate allows for the placement of a conductive material (e.g., stainless steel mesh) to provide additional contact to the GDE on the backside. If a GDE is not desired, any 3D electrode can be placed in this open area on the current collector.

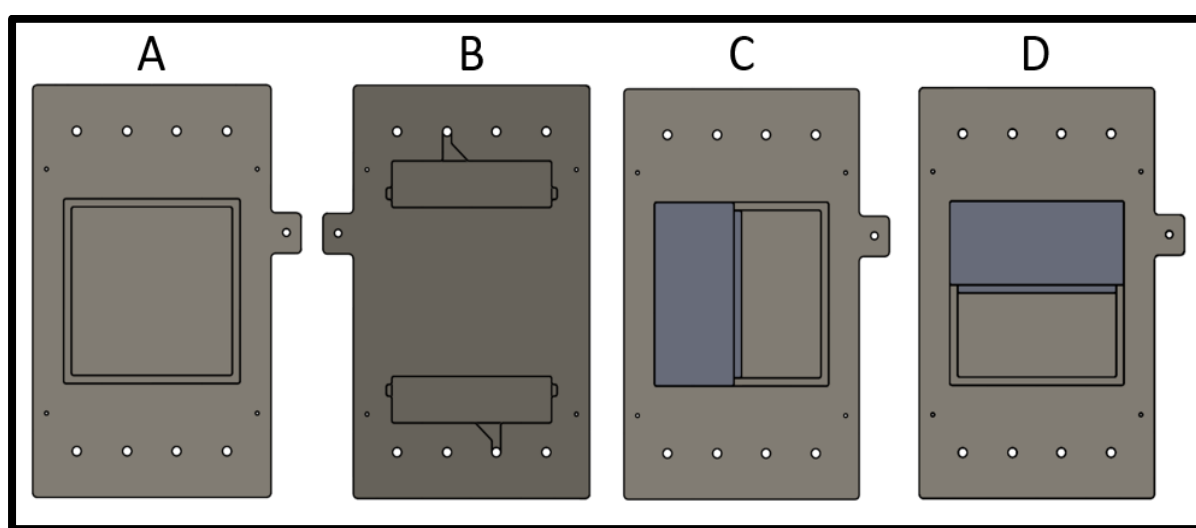


Figure 5.3. Current collector plate with customizable insert for cell area adjustment. The insert shown in D is hollowed to allow flow behind it from the bottom to the top of the cell. A shows the front face of the current collector. B shows the back face of a current collector where connections with inserts are able to be made. C shows a metallic insert that allows for a 100 cm² electrode to be used where the electrode is taller than it is wide. D shows a metallic insert that allows for a 100 cm² electrode to be used where the electrode is wider than it is tall.

Materials and Chemicals

The same materials used in Chapter 4 were used for the work performed in this chapter. Table C.1 summarizes the suppliers used for the materials and chemicals in this chapter.

Gas Diffusion Layer Explanation and Synthesis

Although Chapter 3 discussed the GDL production method could potentially be reduced to two heating regimes instead of three, we selected two methods from Chapter 3 with characteristics already measured (and vastly different in a few characteristics) to study the GDL with the catalyst layer in Chapter 4. This was done to demonstrate that the GDL can play a large role in the performance of the electrode and should be considered by researchers when performing their studies or comparing multiple studies. This chapter is now using a GDE recipe in Chapter 4 to demonstrate that the results at 10 cm² can scale to 200 cm². GDL formulation

23 from Chapter 3 was used to synthesize the GDL for the scale-up run in this chapter, which agrees with the formulation for the best performing electrode of the DOE in Chapter 4 (Run 30).

The synthesis method for the GDLs in this study was modified from a patented method.¹³ 8.92 mL of PTFE DISP 30 was added to 70 mL of a 1:1 volume IPA:water mixture and stirred for 1 minute before mixing with 15g of Soltex Acetylene black 75%-03 carbon in a Bourgini mixer. After 1 minute of mixing, a dough-like mixture was collected. A rolling pin was used to prepare the dough for a cross rolling technique to obtain the desired thickness where the thickness setting is a discrete numerical factor. A rectangle of about 250 cm² was cut from this structure and a paint roller was used to apply PTFE DISP 30 diluted 50% with 1:1 volume IPA:H₂O to the back of the dough. Fibreglast™ 1k plain weave carbon fiber fabric was used as the current collector and placed on top of the PTFE applied layer. A Carver heated press (Model number 4533) was used to press the structure at 140 °C and 10.25 Ton for 32.5 minutes. The temperature was then raised to 307.5 °C and held at 10.25 Ton for 32.5 minutes. Finally, the temperature was increased to 318 °C, and the pressure increased to 13 Ton for 32.5 minutes.

Catalyst Synthesis

The carbon-supported, bimetallic InBi catalyst (50:50 wt %, as in Chapter 4) was prepared in TEG *via* a chemical reduction method. 1.41 g of InCl₃ and 1.72 g of Bi(NO₃)₃·5H₂O were dissolved in 200 mL of triethylene glycol (TEG) along with 0.98 g of trisodium citrate dihydrate. The mixture was stirred and heated to 60 °C under a N₂ atmosphere until the salts were dissolved. 0.2 g of Vulcan carbon was added to achieve 90 wt% metal supported on carbon, and the mixture was stirred overnight. The resulting suspension was heated to 100 °C, and the N₂ atmosphere was switched to an Ar atmosphere. When the desired temperature was reached, 1.86 g NaBH₄ dissolved in 4 mL of water was added over 40 seconds to the reaction mixture. The mixture was left to react at temperature for 15 minutes before being cooled down, filtered, and washed several times with isopropanol and isopropanol/water mixtures.

GDE preparation

A die was used to cut the GDL to the shape required for the cell. The catalyst was sonicated in isopropanol before adding the Nafion™ binder. The amount of Nafion™ added to the ink was calculated based on the mass of catalyst used to make a 20 wt% Nafion™ solution. The ink was then airbrushed onto the GDL, targeting a theoretical metal loading of 0.5 mg_{metal}/cm².

Electrolysis

The electrolysis was carried out in the designed 200 cm² cell. The anode was a layered Ir/RuO₂ mesh contacted by a Ti backplate, and the cathode was a GDE formulated from our previous studies. A reinforced Nafion™ membrane N324 separated the cathode and anode. The anolyte was a 0.5M H₂SO₄ solution, and the catholyte was a 0.5M KHCO₃ solution. The anodic reaction was the oxygen evolution reaction (OER). The electrolyte solutions were circulated in the compartments at a flow rate of 1.2 L/min with a peristaltic pump, and CO₂

was fed through the GDE at a flow rate of 1 L/min. The cell was connected to a power supply and operated galvanostatically at a current density of 300 mA/cm². Catholyte samples were neutralized with HCl and analyzed for formate with a Perkin Elmer Lambda 35 UV-vis spectrometer.

Results and Discussion

Comsol was used to screen flow distribution designs for their ability to create uniform flow inside the cell. The modeled fluid velocity profile inside the cell with two flow distribution configurations is shown in Appendix D (Figures D.1-D.6). The flow velocity does not appear to be drastically different in the active area region of the cell for the inserts simulated. Therefore, experiments with various flow distribution inserts were not prioritized.

This cell was used to test a 200 cm² GDE synthesized from the abovementioned method. The 10 cm² GDE recipe that this experiment scaled up showed a current efficiency of 99.4% at a current density of 400 mA/cm² for 120 minutes of operation (Run 30 in Chapter 4). However, in a separate, unpublished experiment, when the current density was dropped to 300 mA/cm², this electrode achieved 92% current efficiency for 120 minutes. The first run of this scaled-up GDE only lasted for 15 minutes due to high heat generation from the cell, resulting in the electrolyte temperature rising to 55 °C. This first experiment only used 1.5 L of anolyte and catholyte. A second test was performed with the same electrode using eight liters of anolyte and catholyte contained in an ice bath. It resulted in two hours of additional operation time before the electrolyte temperature reached 55 °C. Figure 5.4 shows the current efficiency toward formate vs. the combined time of these two 200 cm² tests. The corresponding cell potential vs. time is shown in Figure 5.5. Furthermore, a plot of the current efficiency vs applied current, as shown in Chapter 1 (Figure 1.2), with the work contained in Chapters 4 and 5 in this thesis is shown in Figure 5.6.

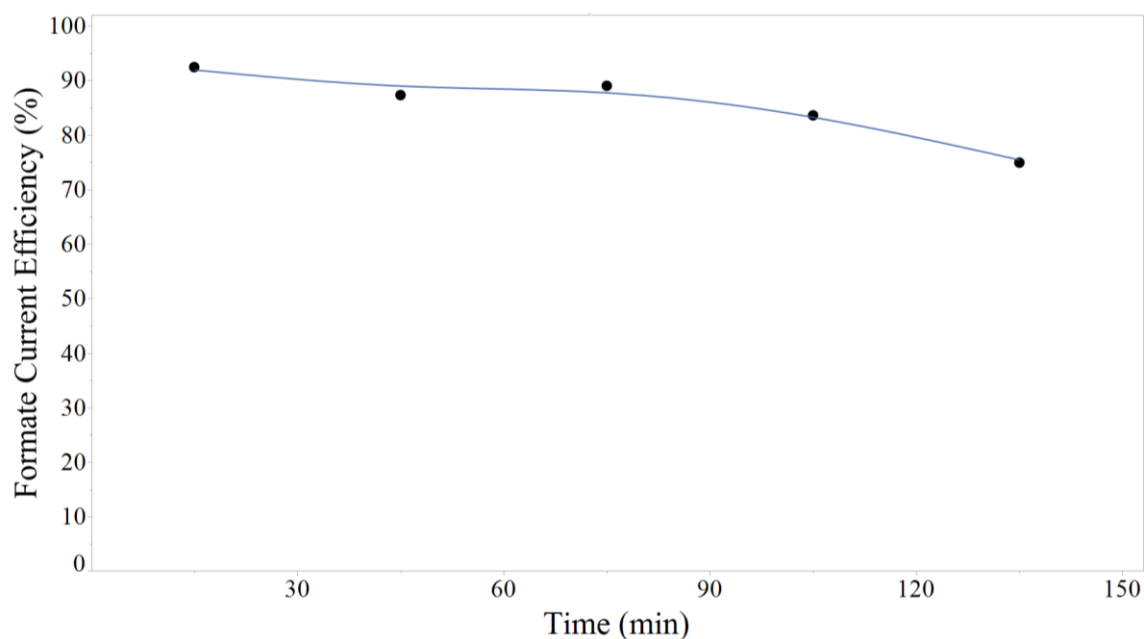


Figure 5.4. The current efficiency of formate vs. time for 200 cm² GDE at 300 mA/cm². The blue line is drawn to guide the eye.

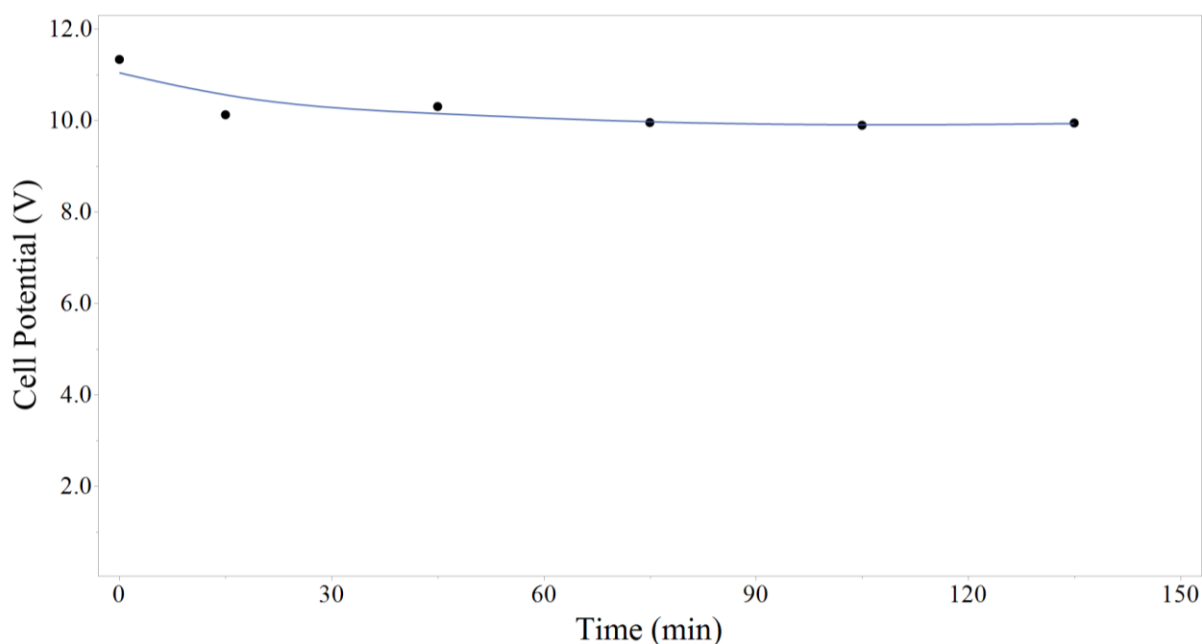


Figure 5.5. Cell potential vs. time for 200 cm² GDE at 300 mA/cm². The blue line is drawn to guide the eye.

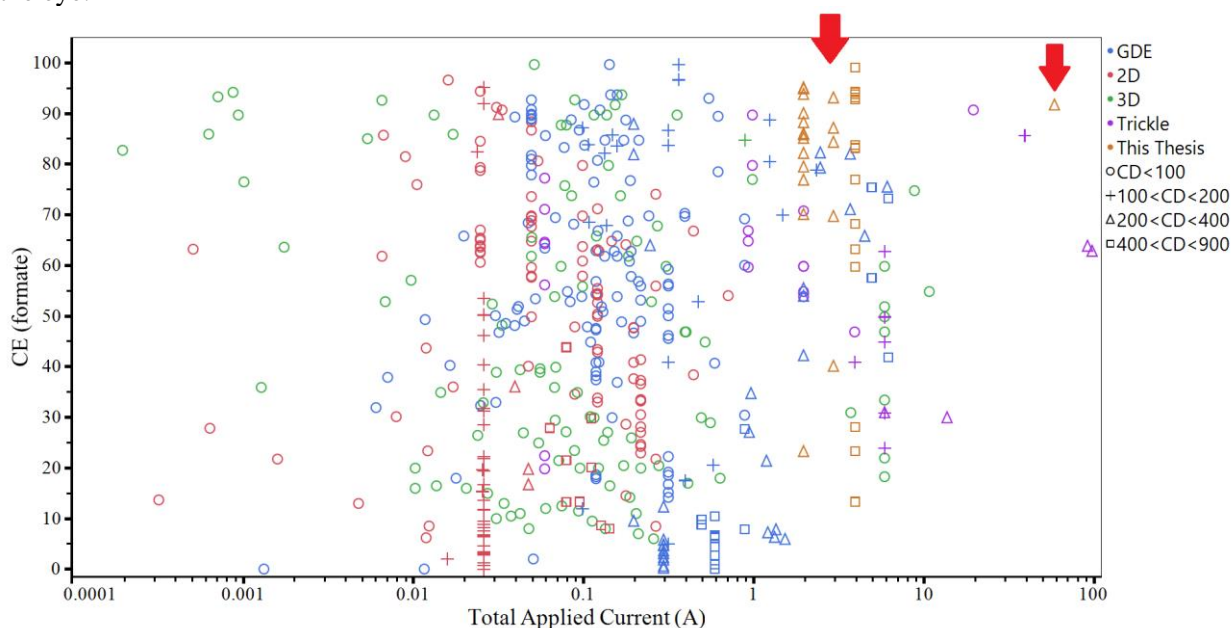


Figure 5.6. Current efficiency vs total applied current for experiments in this thesis overlaid with work reviewed in Chapter 1 (Figure 1.2). Data reported for this thesis at 60A of applied current is shown at the peak performance.

The 200 cm² GDE was not operated at 400 mA/cm² because the cell potential was nearly double that of the 10 cm² electrode. This increase in cell potential is attributed to the large gap of catholyte in the cell of about 9.5 mm, over a 2x increase in gap size from the 10 cm² cell (6.35 mm from the flow plate plus 3.15 mm from the gaskets). Consequently, the scaled electrode was only operated at 300 mA/cm². It ran at a current efficiency of 92.5% during the first 15-minute experiment. During the second experiment, this electrode achieved 89% current

efficiency for the first 60 minutes before dropping to 75% after a total of 135 minutes of operation.

The first 75 minutes of the scaled electrode operation show very similar current efficiencies to its 10 cm² counterpart with less than a 3% difference in current efficiency. However, the larger electrode did not show as good stability as the 10 cm² electrode, as seen by the drop in current efficiency at 105 minutes. This is most likely a consequence of the higher cell potential and the higher temperature at which this cell operated. Adapting the flow distributor plate to be about half of the current thickness and using thinner gaskets should help reduce the cell potential. Additionally, including a heat exchanger in the electrolyte tanks to control their temperatures would eliminate the possibility of electrode stability issues due to operating temperature. Nevertheless, this work successfully demonstrates that a GDE can be scaled up without a sacrifice in current efficiency, as seen in other electrolyzer technologies, as shown in Figure 5.6.

Conclusions

GDEs can be a challenge to scale up due to hydrostatic head pressure causing electrode flooding. Most published research on GDEs for CO₂ reduction toward formate is at a scale of 10 cm² or less; however, research at larger scales is necessary to understand scaling challenges and eventually achieve a commercial process. There is a lack of commercially available GDE cells for active areas greater than 10 cm². Therefore, it was necessary to custom design a cell for GDEs at a larger scale.

Our custom-designed cell featured four compartments, allowing for the possibility of using a hydrogen GDE anode to significantly reduce the cell potential. Additionally, the design allowed for multiple cells to be combined into one stack so that this type of configuration could be tested in the future. The cell's flow distribution and active area were customizable up to 200 cm². Although, the custom-designed flow distributions modeled in COMSOL did not appear to significantly change the velocity profile of the electrolyte in the active area of the cell.

The custom cell was used to scale the results from Chapter 4 at 10 cm² that showed 99% current efficiency at 400 mA/cm². The gap between the GDE and membrane of our 200 cm² cell was 9.5 mm, resulting in almost a 2x increase in cell potential from the smaller scale electrode. Consequently, the 200 cm² electrode was only operated at 300 mA/cm². However, it achieved a current efficiency of 89% for 75 minutes, similar to the performance of the 10 cm² electrode at 300 mA/cm² (92% current efficiency). Furthermore, the current efficiency of the 200 cm² electrode dropped to 75% after 135 minutes of operation, showing lower stability than at the smaller scale. This decrease in stability could be caused by the larger cell potential of the 200 cm² cell or the higher operating temperature of the electrolytes (55 °C). The InBi catalyst was characterized by Davide Pavesi in Appendix B using differential scanning calorimetry (DSC). Minor peaks associated with bimetallic phases at 66°C, 84 °C, and 107°C were observed on the first cycle (Figure B.5a). These peaks indicate the presence of In₂Bi, InBi, and the eutectic phase.¹⁴ However, during the second cycle (Figure B.5b), these peaks no longer appear. This shows that the InBi catalyst can be transformed when exposed to high

temperatures. Furthermore, the performance of either of the base metals in flow cell benchmarking experiments performed in Appendix B is not as good as the InBi alloy, as shown in Figure B.1. The fact that 1.5 L of electrolyte was heated to 55 °C in only 15 minutes in these large scale experiments indicates the electrode surface was at a significantly higher temperature than 55 °C. This elevated temperature could have been enough to cause a transformation of the catalyst, as observed from the DSC characterization work, resulting in a decrease in current efficiency, as seen in the benchmarking experiments in Appendix B.

Further research is required to understand why there was an observed decrease in electrode stability. The gap between the GDE and membrane in the cell can be reduced by using thinner gaskets and reducing the thickness of the flow distributor plate of the cell. Additionally, a better heat exchanger than an ice bath can be used to control the temperature of the electrolytes. Once the electrode stability is addressed, cell stacking should be investigated, as this can also be a challenge in managing pressures between CO₂ and catholyte compartments in the cell.

References

- (1) Durst, J.; Rudnev, A.; Dutta, A.; Fu, Y.; Herranz, J.; Kaliginedi, V.; Kuzume, A.; Permyakova, A. A.; Paratcha, Y.; Broekmann, P.; Schmidt, T. J. Electrochemical CO₂ Reduction – A Critical View on Fundamentals, Materials and Applications. *Chim. Int. J. Chem.* **2015**, *69* (12), 769–776, DOI 10.2533/chimia.2015.769.
- (2) Oloman, C.; Li, H. Electrochemical Processing of Carbon Dioxide. *ChemSusChem* **2008**, *1* (5), 385–391, DOI 10.1002/cssc.200800015.
- (3) Martín, A. J.; Larrazábal, G. O.; Pérez-Ramírez, J. Towards Sustainable Fuels and Chemicals through the Electrochemical Reduction of CO₂: Lessons from Water Electrolysis. *Green Chem.* **2015**, *17* (12), 5114–5130, DOI 10.1039/C5GC01893E.
- (4) Verma, S.; Kim, B.; Jhong, H.-R. “Molly”; Ma, S.; Kenis, P. J. A. A Gross-Margin Model for Defining Technoeconomic Benchmarks in the Electroreduction of CO₂. *ChemSusChem* **2016**, *9* (15), 1972–1979, DOI 10.1002/cssc.201600394.
- (5) Huang, Z.; Grim, R. G.; Schaidle, J. A.; Tao, L. The Economic Outlook for Converting CO₂ and Electrons to Molecules. *Energy Environ. Sci.* **2021**, *14* (7), 3664–3678, DOI 10.1039/D0EE03525D.
- (6) Philips, M. F.; Gruter, G.-J. M.; Koper, M. T. M.; Schouten, K. J. P. Optimizing the Electrochemical Reduction of CO₂ to Formate: A State-of-the-Art Analysis. *ACS Sustain. Chem. Eng.* **2020**, DOI 10.1021/acssuschemeng.0c05215.
- (7) Kaczur, J. J.; Kramer, T. J.; Keyshar, K.; Majsztrik, P.; Twardowski, Z. Process and High Surface Area Electrodes for the Electrochemical Reduction of Carbon Dioxide. US 8,858,777 B2, 2014.
- (8) Oloman, C.; Li, H. Continuous Co-Current Electrochemical Reduction of Carbon Dioxide. US 2016/0068974A1, 2016.
- (9) Sen, S.; Skinn, B.; Hall, T.; Inman, M.; Taylor, E. J.; Brushett, F. R. Pulsed Electrodeposition of Tin Electrocatalysts onto Gas Diffusion Layers for Carbon Dioxide Reduction to Formate. *MRS Adv.* **2017**, *2* (8), 451–458, DOI 10.1557/adv.2016.652.
- (10) Kopljär, D.; Wagner, N.; Klemm, E. Transferring Electrochemical CO₂ Reduction from Semi-Batch into Continuous Operation Mode Using Gas Diffusion Electrodes. *Chem. Eng. Technol.* **2016**, *39* (11), 2042–2050, DOI 10.1002/ceat.201600198.
- (11) Higgins, D.; Hahn, C.; Xiang, C.; Jaramillo, T. F.; Weber, A. Z. Gas-Diffusion Electrodes for Carbon Dioxide Reduction: A New Paradigm. *ACS Energy Lett.* **2019**, *4* (1), 317–324, DOI 10.1021/acsenenergylett.8b02035.
- (12) Burdyny, T.; Smith, W. A. CO₂ Reduction on Gas-Diffusion Electrodes and Why Catalytic Performance Must Be Assessed at Commercially-Relevant Conditions. *Energy Environ. Sci.* **2019**, *12* (5), 1442–1453, DOI 10.1039/C8EE03134G.
- (13) Philips, M. F.; Ansovini, D.; Figueiredo, M. C. C.; Krasovic, J. Method for the Preparation of a Gas Diffusion Layer and a Gas Diffusion Layer Obtained or Obtainable by Such Method. WO2020165074A1, 2020.

- (14) Okamoto, H.; Schlesinger, M. E.; Mueller, E. M. Bi (Bismuth) Binary Alloy Phase Diagrams. *Alloy Phase Diagrams*. ASM International April 2016, p 0, DOI 10.31399/asm.hb.v03.a0006150.

Chapter 6

A Density Functional Theory Study on Surface Poisoning of Indium-Bismuth Electrodes

Introduction

Climate change has become a highly discussed and important topic throughout the last decade. The effect of temperature rise is largely attributed to increased greenhouse gases in the atmosphere due to human activities.¹ Carbon dioxide (CO₂) is one of the most critical greenhouse gases to consider due to the tremendous rate at which it is generated and released into the atmosphere. In the coming decades, global emissions need to rapidly decline to reach net zero around 2050-2060. As zero emissions are virtually not possible, any remaining emissions (5-10 Gt/yr) need to be compensated by negative emissions to arrive at net zero. Consequently, the capture and conversion of CO₂ is a topic that is currently gaining significant attention. The low-temperature electrochemical conversion of CO₂ is advantageous over other conversion techniques because it can be performed at ambient temperature and pressure.^{2,3} Additionally, formate is one of the most economically viable products for electrochemical conversion of CO₂.⁴⁻⁷

Recently, the European Union has granted subsidies for projects such as OCEAN and RECODE for the electrochemical conversion of CO₂ to formate. One of the goals of these grants is to bring the technology from a technology readiness level (TRL) of 4/5 to 6.^{8,9} This includes using CO₂ from point sources rather than from a gas cylinder. Consequently, more impurities will be present in the CO₂ feed from these various sources than in a typical gas cylinder used in a research lab. Thus, it is essential to predict if any of these impurities can potentially poison the catalyst used for the electrochemical conversion and purify the CO₂ feed accordingly.

The work presented in this chapter was performed in collaboration with Federico Dattila and the Institut Català d'Investigació Química. In this chapter, we consider impurities found in the CO₂ feed used within the RECODE project and employ Density Functional Theory (DFT) to assess if any impurities could be poisons to Avantium's Indium Bismuth (InBi) alloy catalyst and Sn, another electrochemical catalyst known to convert CO₂ to formate efficiently.^{9,10} The background work presented in the "Electrochemical CO₂ Reduction to Formate" section, as well as the work presented correlating the partial charges of molecules with their adsorption energy, was performed in collaboration with Federico Dattila.

Results and Discussion

Computational Model

In and Sn are common catalysts used for electrochemical CO₂ reduction (eCO₂R) toward formate after a first observation by Hori *et al.*¹¹⁻¹³ However, the industrial exploitation of these materials is currently limited by their poor long-term stability.¹⁴ Remarkably, an InBi catalyst developed at Avantium has shown to be superior over pure Sn, In, or Bi for the electrochemical reduction of CO₂ to formate.¹⁰ Refer to Appendix B for the physical characterization of this InBi material.¹⁵ In the following, we do not focus on the specific formulation of Avantium's

catalyst, but we instead consider pure In, Bi, Sn, and different In-Bi alloys to pursue a more general density functional theory (DFT) model.

We modeled 4-layer thick slabs of In, In₅Bi₃, InBi, Bi, and Sn to account for pure metals and In-Bi intermetallic alloys with 37.5 and 50 atomic percent Bi content. We then examined different terminations of these slabs and computed their surface energies in vacuum, as reported in Table E.1. In(001), Bi(110), Sn(100), InBi(110)-Bi-terminated, and In₅Bi₃(010) resulted in the lowest surface energy configurations across the different terminations considered; thus, they are expected to be the most abundant for each as-synthesized material (without an applied electric potential).¹⁶ Consequently, we limited the investigation of eCO₂R performance and potential poisoning effects to these facets (Figure 6.1). As described in the Computational Methods section, we carried out the whole computational screening through the Vienna Ab Initio Simulation (VASP) package, employing the PBE density functional.^{17–19} To properly account for van der Waals interactions when assessing adsorption properties, we included dispersion coefficients through the D2 method.^{20–22} Lastly, we estimated stabilization effects on adsorption energies of intermediates due to the solvent medium through our in-house developed implicit VASP-MGCM model.^{23,24}

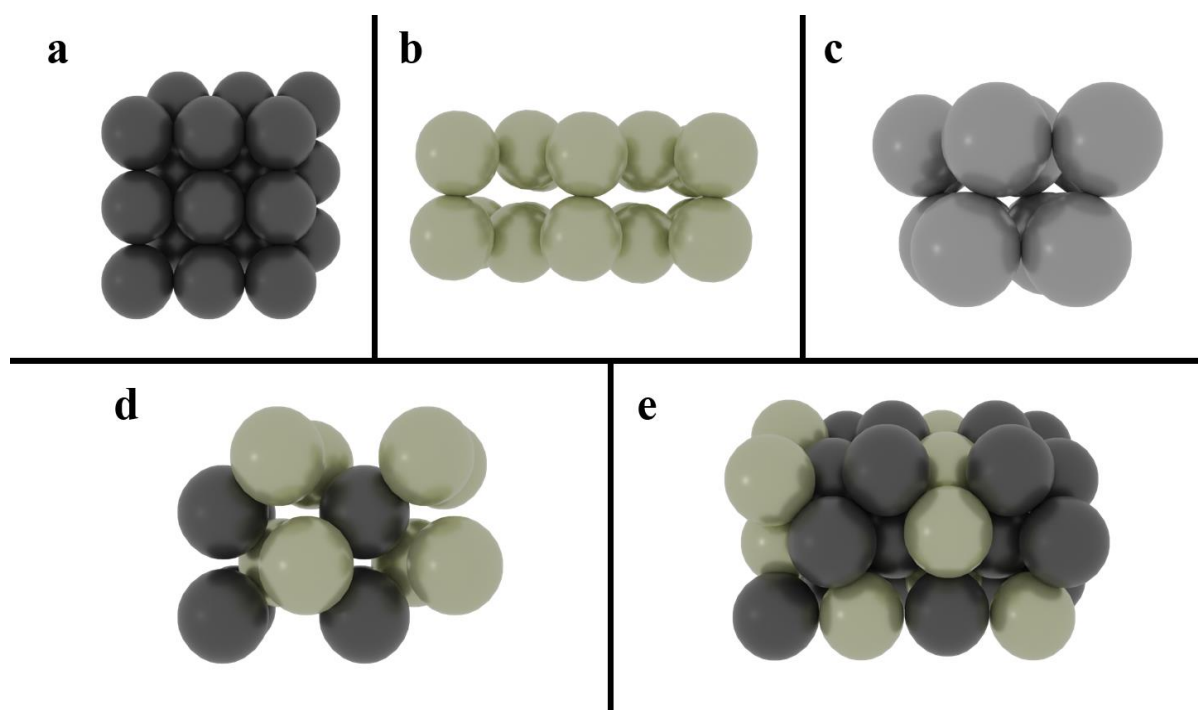


Figure 6.1. Density functional theory models for Bi, In, In-Bi, and Sn catalysts. Top view of the lowest surface energy terminations considered in this study: a) In(001), b) Bi(110), c) Sn(100), d) InBi(110)-Bi-terminated, and e) In₅Bi₃ (010). Other facets are reported in Table E.1

Electrochemical CO₂ Reduction to Formate

p-Block elements such as Sn and In are well-known to favor formate formation since the report by Hori *et al.*¹³ Recently, Bagger *et al.* attributed the enhanced formate yield for these elements to their endergonic hydrogen adsorption energy, as this limits the hydrogen evolution reaction (HER), thus favoring selective electroreduction of CO₂ to HCOO[−].²⁵ On Sn and In,

CO₂ reduction is expected to occur *via* adsorption of CO₂ as an *OCO⁻ intermediate (* = adsorbed species), facilitated by an electron transfer.²⁶ Thus, a $\eta_2(\text{O},\text{O})$ adsorption configuration (*i.e.*, two oxygens bound to the surface) is preferred to the CO-selective $\eta_2(\text{C},\text{O})$ (*i.e.*, carbon and one oxygen bound to the surface) due to the high oxygen affinity of Sn and In.²⁷ The *OCO⁻ specie then undergoes a proton transfer (PT) to form adsorbed *OCHO, which finally desorbs to yield formate. Alternatively, a proton-coupled electron transfer (PCET) route has been proposed as well on these materials, leading directly to the formation of the *OCHO intermediate from the CO₂ precursor.²⁸

According to the Computational Hydrogen Electrode (CHE), the Gibbs free energy of adsorption for species formed *via* proton-coupled electron transfers can be estimated at standard conditions by relating the chemical potential of the H⁺ + e⁻ pair to one-half of the hydrogen Gibbs free energy ($\frac{1}{2} G_{\text{H}_2}$).²⁹ This framework includes the effect of applied electric potential by lowering adsorption energies by $n|e^-|U$, where n is the number of proton-coupled electron transfers involved until that reaction step, and U is the electric potential vs. RHE. Thus, the Gibbs free energy of adsorption for *OCHO and *H intermediates can be calculated according to Equations 6.1 and 6.2, respectively, assuming for both species a single proton-coupled electron transfer, and CO₂ and H₂ as energy references.³⁰ In Equations 6.1 and 6.2, G^* represents the Gibbs free energy of the clean surface, while other parameters have been identified above. Since $\Delta G_{*\text{OCHO}}$ and $\Delta G_{*\text{H}}$ depend equally on electric potential U according to the CHE, these parameters can be compared to define the more favorable process.²⁹ Specifically, $\Delta G_{*\text{OCHO}} - \Delta G_{*\text{H}}$ can be employed as a suitable descriptor for formate selectivity on In, Sn, Bi, and In-Bi alloys (Figure 6.2). A negative value of this parameter implies more favorable *OCHO adsorption than *H, thus identifying HCOO⁻-selective catalysts. Instead, positive values of $\Delta G_{*\text{OCHO}} - \Delta G_{*\text{H}}$ lead to preferential *H adsorption and consequent HER.

$$\Delta G_{*\text{OCHO}} = G_{*\text{OCHO}} - G^* - G_{\text{CO}_2} - \frac{1}{2} G_{\text{H}_2} - |e^-|U \quad (6.1)$$

$$\Delta G_{*\text{H}} = G_{*\text{H}} - G^* - \frac{1}{2} G_{\text{H}_2} - |e^-|U \quad (6.2)$$

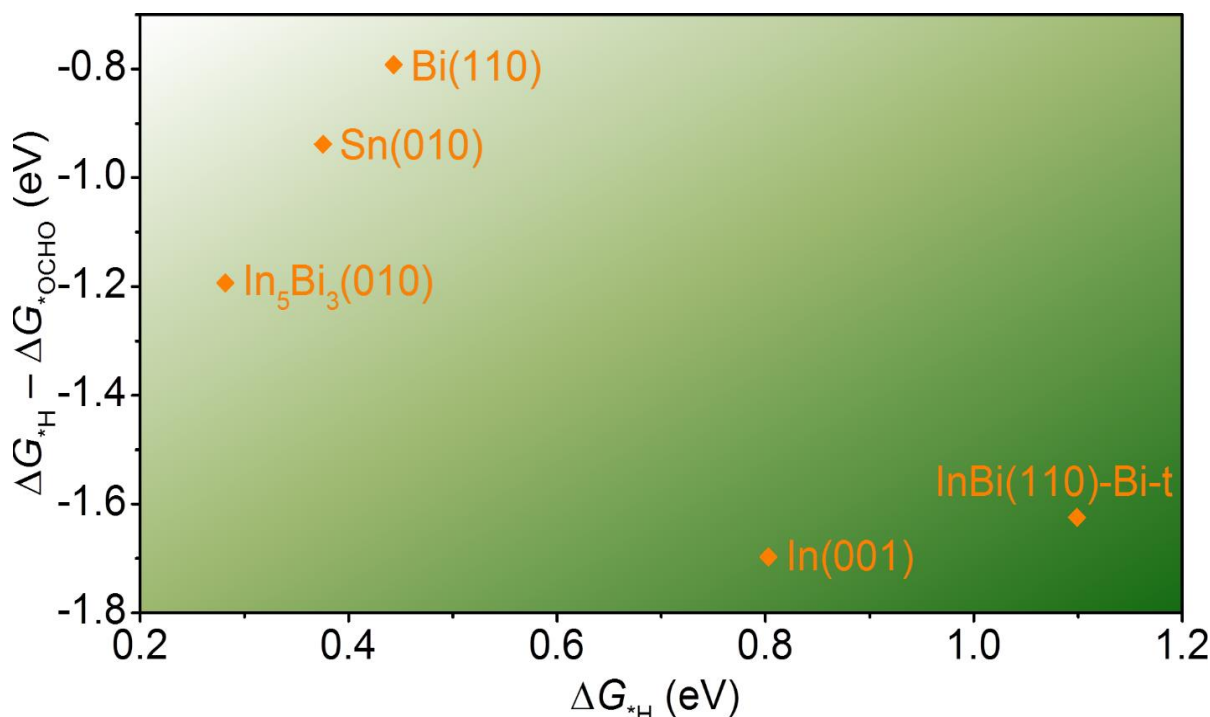


Figure 6.2. Competition between eCO₂R to formate and hydrogen evolution at $U = 0$ V vs. RHE. For all the investigated systems, Gibbs free energy for *H adsorption (x-axis, Equation 6.2) is endergonic, while *OCHO adsorption is exergonic and more favorable by at least -0.8 eV (y-axis, Equation 6.1). Most selective catalysts lie in the bottom right of the figure, highlighted by the darkest green shadow. Figure created by Federico Dattila.

According to the previous considerations, the element showing the most endergonic *H adsorption energy and the most exergonic *OCHO should be the best catalyst toward formate (*i.e.*, an ideal catalyst should lie in the bottom right of Figure 6.2). All the considered surfaces show a strong binding of the *OCHO intermediate rather than of *H, thus motivating their selectivity toward formate. Notably, In(001) and Bi-terminated In-Bi(110) hinder *H adsorption the most ($\Delta G_{*H} = +0.8$ and $+1.1$ eV, respectively), and their stark difference with Sn(100) ($\Delta G_{*H} = +0.4$ eV) motivates the higher formate yields reported experimentally for In.¹³ Furthermore, the In-Bi(110)-Bi-terminated alloy is expected to be the most selective toward formate because it prevents hydrogen adsorption even further. This evidence rationalizes its current use for industrial exploitation.

Assessment of Potential Surface Poisons

The potential poisoning of the catalytic surface by impurities can be assessed by estimating the thermodynamics of their adsorption. The impurities listed in the gas feed used in the RECODE project include CO, SO₂, N_xO_y, NH₃, HCl, and HF.⁹ Additionally, *CO₃ was considered because it typically forms under eCO₂R conditions due to chemical equilibrium reactions in the electrolyte and has been proposed as a poisoning agent.³¹ Energies of gas-phase molecules (see Computational Methods in Appendix E) and clean surfaces were used as energy references to estimate the Gibbs free energy of adsorption, which were corrected by entropic contributions. Energies of charged species such as NO₃⁻ and CO₃²⁻ were derived from the energies of their conjugated acids (HNO₃, H₂CO₃) by correcting for the pK_a of the acid/base

reaction (see Estimation of gas-phase energy in Appendix E) in line with our previous study.³² The Gibbs free energies of adsorption calculated in this chapter can be considered a first approximation to their potential poisoning of InBi catalysts because the references chosen for the calculation were energies of the gas-phase molecules. A more robust approach would be to use a solution phase reference as described by Granda-Marulanda et al.³³

Figure 6.3 shows the Gibbs free energy of adsorption for the listed impurities on each crystalline facet considered. Red quadrants display favorable adsorption (potential to poison the catalyst), while green quadrants highlight negligible interaction between catalyst and impurities (unlikely to poison the catalyst). We observe that oxygen-containing molecules have the highest binding energies ($\Delta E < -1.0$ eV) for any of the investigated catalysts, thus suggesting that $\ast\text{NO}$, $\ast\text{NO}_2$, and $\ast\text{NO}_3$ species may, in principle, poison the electrode during electrochemical CO_2 reduction to formate. Additionally, SO_2 may poison $\text{Sn}(100)$, $\text{In}_5\text{Bi}_3(010)$ or $\text{InBi}(110)$ and CO_3^{2-} may poison $\text{In}(001)$, $\text{In}_5\text{Bi}_3(010)$ and $\text{Sn}(010)$. Bi(110) exhibits the least poisoning of these catalysts, while $\text{Sn}(100)$ and $\text{In}(001)$ are the most affected. This may further motivate the employment of an InBi catalyst, which enables the best trade-off between long-term stability (negligible poisoning from Bi) and eCO_2R activity (from In).

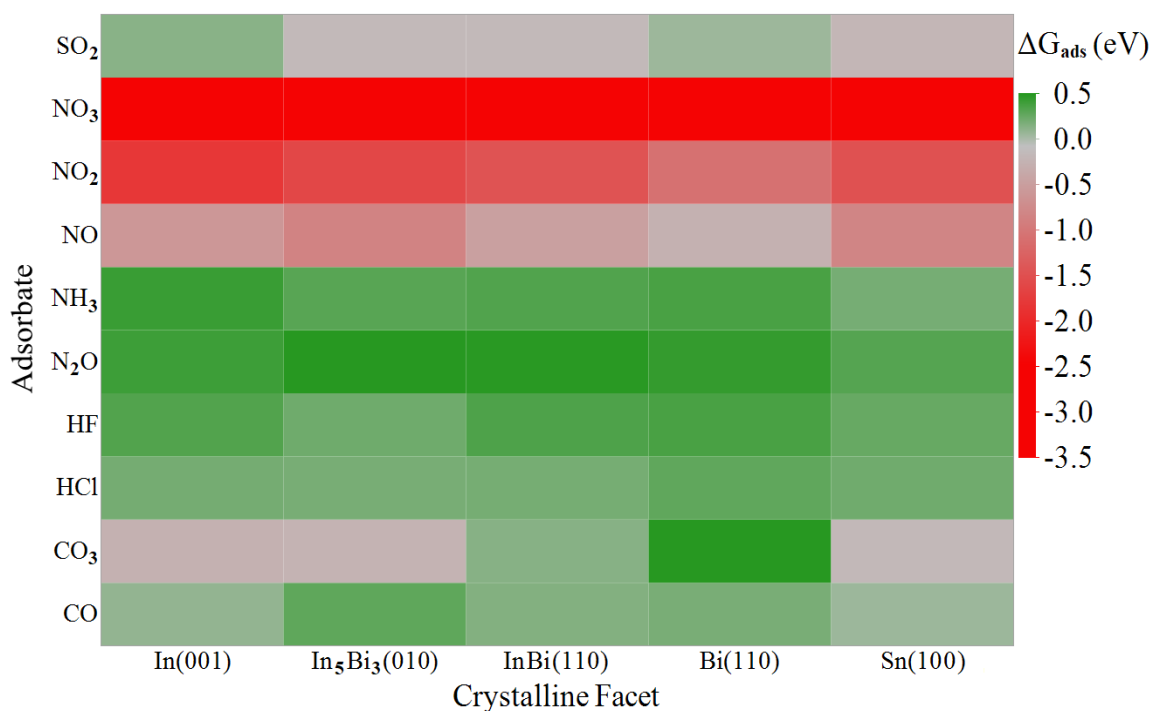


Figure 6.3. Gibbs free energies of adsorption for gas feed impurities (y-axis) versus Bi, In, In-Bi, and Sn catalysts (x-axis). Green colors indicate endergonic binding (negligible poisoning), while red colors designate stronger binding (potential poisoning). We used gas-phase molecules (CO , NO , NO_2 , N_2O , NH_3 , SO_2 , HCl , HF) and conjugated acids (HNO_3 , H_2CO_3) as the respective reference energy, as described in the section "Estimation of gas-phase energy," in Appendix E.

Impurities' partial charges tune the surface poisoning effect

Since oxygen-containing impurities strongly bind to the surface and the adsorption energy among the NO_x species increases following the number of oxygens for any catalyst (Figure

6.4), we hypothesize that electrostatic interactions between adsorbate and electrode rule the adsorbate's binding. Recent computational and experimental work from our groups highlighted the relevance of similar phenomena for electrochemical CO₂ reduction.^{34–36} Positively polarized In substituents on a Pd matrix destabilize C-adsorbed molecules such as CO and COOH due to electrostatic repulsion between the active site and the adsorbate, tuning CO poisoning on Pd and thus affecting CO selectivity on Pd-rich In catalysts.³⁶ Additionally, polarized Cu sites on oxide-derived copper (OD-Cu) exhibit stronger adsorption of O-terminated species and weaker binding of C-terminated species such as CO. Consequently, weakly bound CO can effectively couple to form C₂ products such as ethylene and ethanol on OD-Cu.³⁴ Extending this concept to electrolyte species, very recent robust experimental evidence demonstrated that a localized electrostatic interaction between positively charged metal cations and *CO₂[–] is critical to enable its reduction on gold, silver, and copper.³⁵

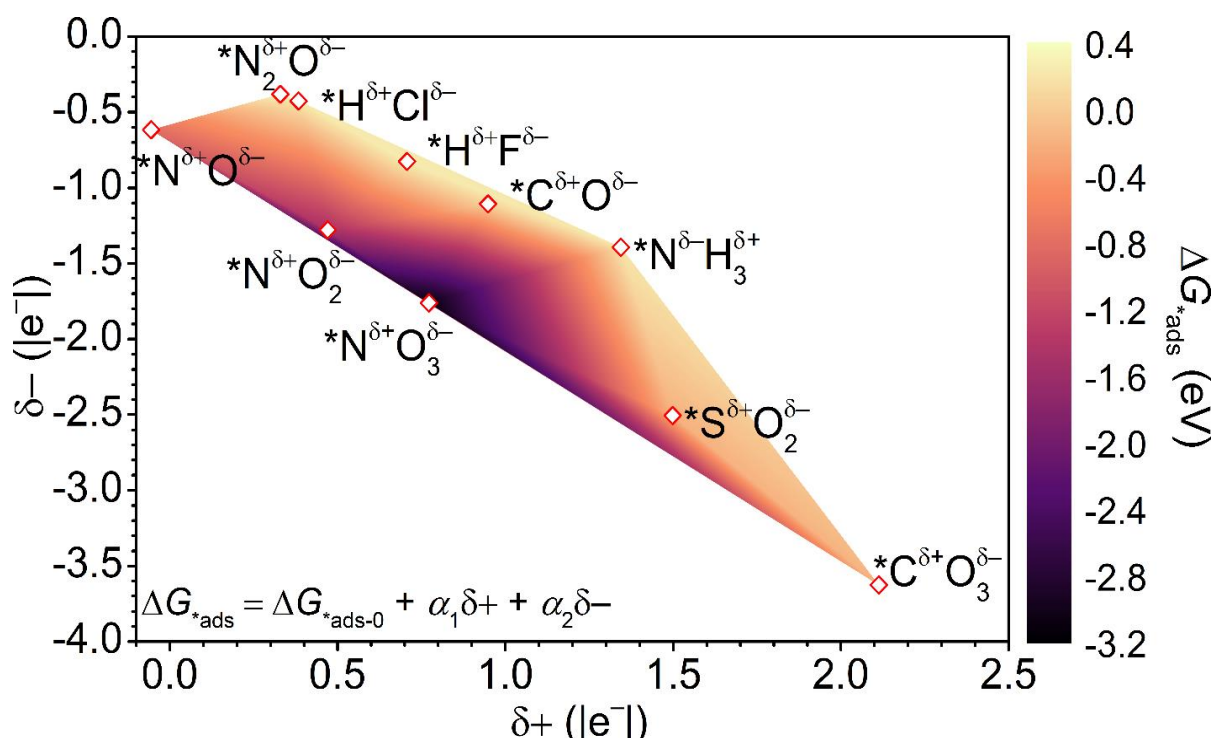


Figure 6.4. Adsorbates' partial charges describe the surface poisoning effect on Sn(100). The adsorption energy for the selected impurities depends on their partial charges (δ^+ , δ^-), estimated through Bader charge formalism.^{37–40} Figure created by Federico Dattila.

Due to the different electronegativity of their elemental components, all the considered impurities are polar, *i.e.*, electronic density is asymmetrically distributed throughout the molecule, leading to local partial charges. Thus, we propose that these molecules are attracted or repelled from the catalytic surface depending on their partial charges. To test our hypothesis for Sn(100), we computed the partial charges δ^+ and δ^- of the adsorbed impurities through the Bader formalism^{37–40} and plotted the Gibbs free energy of adsorption for the different species vs. these partial charges (Figure 6.4). The binding energy of the impurities correlates with partial charges δ^+ and δ^- following Equation 6.3, where ΔG_{*ads-0} is the Gibbs free energy of adsorption for a non-polar molecule.

$$\Delta G_{*ads} = \Delta G_{*ads-0} + \alpha_1 \delta^+ + \alpha_2 \delta^- \quad (6.3)$$

Both α_1 and α_2 are positive. Therefore, a positive partial charge causes a weakening of adsorption strength due to local repulsion with the electrode, while a negative partial charge leads to more exergonic adsorption energies due to the attraction between the surface and elements.

Since adsorption strength changes dramatically for $^*\text{NO}_2$ and $^*\text{NH}_3$, species with almost equivalent δ^- , but different δ^+ values (Figure 6.4), electrostatic repulsion between surface and positive partial charges affect adsorbates' binding properties to a larger extent than the attraction of elements with δ^- . Remarkably, $^*\text{NO}_x$ impurities sit at the top of the poisoning "volcano" due to their high δ^- and mild δ^+ . At the same time, $^*\text{S}$ - and $^*\text{C}$ -containing molecules interact less with the catalyst due to a trade-off between attraction and repulsion. Finally, N_2O does not adsorb on any of the considered catalysts (Figure 6.3) due to its low δ^- and δ^+ .

Conclusions

This work bridges the industrially relevant concept of surface poisoning and DFT-based fundamental studies using a very initial assessment. We have used DFT to calculate the Gibbs free energy of adsorption of impurities from industrial CO_2 streams on In(001), Bi(110), Sn(100), InBi(110)-Bi-terminated, and $\text{In}_5\text{Bi}_3(010)$ slabs. Except for N_2O , all oxygen-containing compounds considered showed an exergonic adsorption energy on some of the catalyst surfaces. NO_2 and NO_3 showed the strongest binding to all catalysts considered due to electrostatic interaction between their negative partial charges and the surface. Additionally, CO_3^{2-} and SO_2 adsorption is exergonic by 0.5 eV. Since NO_x species are expected to reduce under eCO_2R conditions, we suggest that CO_3^{2-} and SO_2 could potentially poison In, Sn, Bi, and In-Bi intermetallic catalysts.

Further experimental work using mock, poison-spiked CO_2 gas feeds would be valuable to validate these findings and determine the extent to which these impurities poison the catalyst. If there is substantial poisoning from a mock feed, pretreatment of the CO_2 stream may be necessary to remove SO_2 to guarantee long-term catalyst stability for CO_2 reduction to formate. From a more fundamental perspective, the computational framework developed here for predicting possible poisoning species and enabling longer catalyst lifetimes is easily transferable for assessing other impurities present in alternative CO_2 feed streams.

Acknowledgments

This work was supported by the European Commission under contract 722614 (Innovative training network Elcorel).

References

- (1) Rodhe, H. A Comparison of the Contribution of Various Gases to the Greenhouse Effect. *Science* (80-.). **1990**, *248* (4960), 1217–1219, DOI 10.1126/science.248.4960.1217.
- (2) Takht Ravanchi, M.; Sahebdehfar, S. Carbon Dioxide Capture and Utilization in Petrochemical Industry: Potentials and Challenges. *Appl. Petrochemical Res.* **2014**, *4* (1), 63–77, DOI 10.1007/s13203-014-0050-5.
- (3) Huang, Z.; Grim, R. G.; Schaidle, J. A.; Tao, L. The Economic Outlook for Converting CO₂ and Electrons to Molecules. *Energy Environ. Sci.* **2021**, *14* (7), 3664–3678, DOI 10.1039/D0EE03525D.
- (4) Durst, J.; Rudnev, A.; Dutta, A.; Fu, Y.; Herranz, J.; Kaliginedi, V.; Kuzume, A.; Permyakova, A. A.; Paratcha, Y.; Broekmann, P.; Schmidt, T. J. Electrochemical CO₂ Reduction – A Critical View on Fundamentals, Materials and Applications. *Chim. Int. J. Chem.* **2015**, *69* (12), 769–776, DOI 10.2533/chimia.2015.769.
- (5) Oloman, C.; Li, H. Electrochemical Processing of Carbon Dioxide. *ChemSusChem* **2008**, *1* (5), 385–391, DOI 10.1002/cssc.200800015.
- (6) Martín, A. J.; Larrazábal, G. O.; Pérez-Ramírez, J. Towards Sustainable Fuels and Chemicals through the Electrochemical Reduction of CO₂: Lessons from Water Electrolysis. *Green Chem.* **2015**, *17* (12), 5114–5130, DOI 10.1039/C5GC01893E.
- (7) Verma, S.; Kim, B.; Jhong, H.-R. “Molly”; Ma, S.; Kenis, P. J. A. A Gross-Margin Model for Defining Technoeconomic Benchmarks in the Electroreduction of CO₂. *ChemSusChem* **2016**, *9* (15), 1972–1979, DOI 10.1002/cssc.201600394.
- (8) Oxalic Acid from CO₂ using Electrochemistry at Demonstration Scale <https://www.spire2030.eu/ocean>.
- (9) Recycling Carbon Dioxide in the Cement Industry to Produce Added-Value Additives: A Step Towards a CO₂ Circular Economy <https://recodeh2020.eu/>.
- (10) Parajuli, R.; Ansovini, D.; Philips, M. F.; Schouten, K. J. P. Catalyst System for Catalyzed Electrochemical Reactions and Preparation Thereof, Applications and Uses Thereof. WO2019141827A1.
- (11) Philips, M. F.; Gruter, G.-J. M.; Koper, M. T. M.; Schouten, K. J. P. Optimizing the Electrochemical Reduction of CO₂ to Formate: A State-of-the-Art Analysis. *ACS Sustain. Chem. Eng.* **2020**, DOI 10.1021/acssuschemeng.0c05215.
- (12) Li, J.; Zhu, M.; Han, Y. F. Recent Advances in Electrochemical CO₂ Reduction on Indium-Based Catalysts. *ChemCatChem* **2021**, *13* (2), 514–531, DOI 10.1002/cctc.202001350.
- (13) Hori, Y.; Kikuchi, K.; Suzuki, S. Production of CO and CH₄ in Electrochemical Reduction of CO₂ At Metal Electrodes in Aqueous Hydrogencarbonate Solution. *Chem. Lett.* **1985**, *14* (11), 1695–1698, DOI 10.1246/cl.1985.1695.

- (14) Van Daele, K.; De Mot, B.; Pupo, M.; Daems, N.; Pant, D.; Kortlever, R.; Breugelmans, T. Sn-Based Electrocatalyst Stability: A Crucial Piece to the Puzzle for the Electrochemical CO₂ Reduction toward Formic Acid. *ACS Energy Lett.* **2021**, *6*, 4317–4327, DOI 10.1021/acsenergylett.1c02049.
- (15) Philips, M. F.; Pavesi, D.; Wissink, T.; Figueiredo, M. C.; Gruter, G.-J. M.; Koper, M. T. M.; Schouten, K. J. P. Electrochemical CO₂ Reduction on Gas Diffusion Electrodes: Enhanced Selectivity of In–Bi Bimetallic Particles and Catalyst Layer Optimization through a Design of Experiment Approach. *ACS Appl. Energy Mater.* **2022**, *acsaem.1c03156*, DOI 10.1021/acsaem.1c03156.
- (16) Wulff, G. Zur Frage Der Geschwindigkeit Des Wachstums Und Der Auflösung Der Krystallflächen. *Z. Krist.* **1901**, *34*, 449–530.
- (17) Perdew, J. P.; Burke, K.; Ernzerhof, M. Generalized Gradient Approximation Made Simple. *Phys. Rev. Lett.* **1996**, *77*, 3865–3868, DOI 10.1103/PhysRevLett.77.3865.
- (18) Kresse, G.; Furthmüller, J. Efficient Iterative Schemes for Ab Initio Total-Energy Calculations Using a Plane-Wave Basis Set. *Phys. Rev. B* **1996**, *54*, 11169–11186, DOI 10.1103/PhysRevB.54.11169.
- (19) Kresse, G.; Furthmüller, J. Efficiency of Ab-Initio Total Energy Calculations for Metals and Semiconductors Using a Plane-Wave Basis Set. *Comput. Mater. Sci.* **1996**, *6*, 15–50, DOI 10.1016/0927-0256(96)00008-0.
- (20) Grimme, S. Semiempirical GGA-Type Density Functional Constructed with a Long-Range Dispersion Correction. *J. Comput. Chem.* **2006**, *27*, 1787–1799, DOI 10.1002/jcc.
- (21) Bucko, T.; Hafner, J.; Lebègue, S.; Ángyán, J. G. Improved Description of the Structure of Molecular and Layered Crystals: Ab Initio DFT Calculations with van Der Waals Corrections. *J. Phys. Chem. A* **2010**, *114*, 11814–11824, DOI 10.1021/jp106469x.
- (22) Almora-Barrios, N.; Carchini, G.; Błoński, P.; López, N. Costless Derivation of Dispersion Coefficients for Metal Surfaces. *J. Chem. Theory Comput.* **2014**, *10*, 5002–5009, DOI 10.1021/ct5006467.
- (23) Garcia-Ratés, M.; López, N. Multigrid-Based Methodology for Implicit Solvation Models in Periodic DFT. *J. Chem. Theory Comput.* **2016**, *12*, 1331–1341, DOI 10.1021/acs.jctc.5b00949.
- (24) Garcia-Ratés, M.; García-Muelas, R.; López, N. Solvation Effects on Methanol Decomposition on Pd(111), Pt(111), and Ru(0001). *J. Phys. Chem. C* **2017**, *121*, 13803–13809, DOI 10.1021/acs.jpcc.7b05545.
- (25) Bagger, A.; Ju, W.; Varela, A. S.; Strasser, P.; Rossmeisl, J. Electrochemical CO₂ Reduction: A Classification Problem. *ChemPhysChem* **2017**, *18* (22), 3266–3273, DOI 10.1002/cphc.201700736.

- (26) Kortlever, R.; Shen, J.; Schouten, K. J. P.; Calle-Vallejo, F.; Koper, M. T. M. Catalysts and Reaction Pathways for the Electrochemical Reduction of Carbon Dioxide. *J. Phys. Chem. Lett.* **2015**, *6*, 4073–4082, DOI 10.1021/acs.jpcllett.5b01559.
- (27) Baruch, M. F.; Pander, J. E.; White, J. L.; Bocarsly, A. B. Mechanistic Insights into the Reduction of CO₂ on Tin Electrodes Using in Situ ATR-IR Spectroscopy. *ACS Catal.* **2015**, *5*, 3148–3156, DOI 10.1021/acscatal.5b00402.
- (28) Yoo, J. S.; Christensen, R.; Vegge, T.; Nørskov, J. K.; Studt, F. Theoretical Insight into the Trends That Guide the Electrochemical Reduction of Carbon Dioxide to Formic Acid. *ChemSusChem* **2016**, *9* (4), 358–363, DOI 10.1002/cssc.201501197.
- (29) Nørskov, J. K.; Rossmeisl, J.; Logadottir, A.; Lindqvist, L.; Kitchin, J. R.; Bligaard, T.; Jónsson, H. Origin of the Overpotential for Oxygen Reduction at a Fuel-Cell Cathode. *J. Phys. Chem. B* **2004**, *108*, 17886–17892, DOI 10.1021/jp047349j.
- (30) Yoo, J. S.; Christensen, R.; Vegge, T.; Nørskov, J. K.; Studt, F. Theoretical Insight into the Trends That Guide the Electrochemical Reduction of Carbon Dioxide to Formic Acid. *ChemSusChem* **2016**, *9*, 358–363, DOI 10.1002/CSSC.201501197.
- (31) Velasco-Vélez, J.-J.; Jones, T.; Gao, D.; Carbonio, E.; Arrigo, R.; Hsu, C.-J.; Huang, Y.-C.; Dong, C.-L.; Chen, J.-M.; Lee, J.-F.; Strasser, P.; Roldan Cuenya, B.; Schlögl, R.; Knop-Gericke, A.; Chuang, C. H. The Role of the Copper Oxidation State in the Electrocatalytic Reduction of CO₂ into Valuable Hydrocarbons. *ACS Sustain. Chem. Eng.* **2019**, *7*, 1485–1492, DOI 10.1021/acssuschemeng.8b05106.
- (32) García-Muelas, R.; Dattila, F.; Shinagawa, T.; Martín, A. J.; Pérez-Ramírez, J.; López, N. Origin of the Selective Electroreduction of Carbon Dioxide to Formate by Chalcogen Modified Copper. *J. Phys. Chem. Lett.* **2018**, *9*, 7153–7159, DOI 10.1021/acs.jpcllett.8b03212.
- (33) Granda-Marulanda, L. P.; McCrum, I. T.; Koper, M. T. M. A Simple Method to Calculate Solution-Phase Free Energies of Charged Species in Computational Electrocatalysis. *J. Phys. Condens. Matter* **2021**, *33* (20), 204001, DOI 10.1088/1361-648X/abf19d.
- (34) Dattila, F.; García-Muelas, R.; López, N. Active and Selective Ensembles in Oxide-Derived Copper Catalysts for CO₂ Reduction. *ACS Energy Lett.* **2020**, *5*, 3176–3184, DOI 10.1021/acsenerylett.0c01777.
- (35) Monteiro, M. C. O.; Dattila, F.; Hagedoorn, B.; García-Muelas, R.; López, N.; Koper, M. T. M. Absence of CO₂ Electroreduction on Copper, Gold and Silver Electrodes without Metal Cations in Solution. *Nat. Catal.* **2021**, *4*, 654–662, DOI 10.1038/s41929-021-00655-5.
- (36) Pavesi, D.; Dattila, F.; Van de Poll, R. C. J.; Anastasiadou, D.; García-Muelas, R.; Figueiredo, M.; Gruter, G.-J. M.; López, N.; Koper, M. T. M.; Jan Schouten, K. Modulation of the Selectivity of CO₂ to CO Electroreduction in Palladium Rich

- Palladium-Indium Nanoparticles. *J. Catal.* **2021**, *402*, 229–237, DOI 10.1016/j.jcat.2021.08.021.
- (37) Henkelman, G.; Arnaldsson, A.; Jónsson, H. A Fast and Robust Algorithm for Bader Decomposition of Charge Density. *Comput. Mater Sci.* **2006**, *36*, 354–360, DOI 10.1016/j.commatsci.2005.04.010.
- (38) Sanville, E.; Kenny, S. D.; Smith, R.; Henkelman, G. Improved Grid-Based Algorithm for Bader Charge Allocation. *J. Comput. Chem.* **2007**, *28*, 899–908, DOI 10.1002/jcc.
- (39) Tang, W.; Sanville, E.; Henkelman, G. A Grid-Based Bader Analysis Algorithm without Lattice Bias. *J. Phys. Condens. Matter* **2009**, *21*, 084204, DOI 10.1088/0953-8984/21/8/084204.
- (40) Yu, M.; Trinkle, D. R. Accurate and Efficient Algorithm for Bader Charge Integration. *J. Chem. Phys.* **2011**, *134*, 064111, DOI 10.1063/1.3553716.

Chapter 7

Outlook

Future Lab Scale Development

In Chapter 3, a GDL synthesis method was explored to determine how characteristics of the GDL can be tuned by production factors. This gave insights into how various GDLs can be produced with desired characteristics as more studies are completed in the future. In Chapter 4, five characteristics of the catalyst layer were studied with two GDLs to determine which factors and interactions between the factors investigated influence the current efficiency toward formate and the cell potential. The results showed the optimum amount of binder in the catalyst layer is dependent on the GDL that was used. This interaction could be an effect due to the average pore size on the surface of the GDL. Higher amounts of binder on a GDL with smaller pores at the surface could lead to clogging of the pores and hinder CO₂ transport to the catalyst layer. This interaction can be explored further in future studies using the results in Chapter 3 to determine which characteristics of the GDL cause a change in the optimum binder in the catalyst layer (e.g., porosity, water contact angle, etc.).

The results of Chapter 4 show that the binder amount and type play a significant role in affecting the current efficiency of the GDE. Therefore, other binders should be explored at various concentrations in the catalyst layer to optimize this GDE further. PVDF and Nafion showed similar optimum concentrations (~20%). However, a different binder type could have a much different optimum concentration. For example, Wang et al. found an optimum PTFE concentration in the catalyst layer to be 11.1 wt% for a GDE converting CO₂ to formate.¹ This is substantially lower than the optimal binder concentrations found in the results of Chapter 4.

Additionally, the binder type can interact with the loading of the catalyst on the electrode. Electrodes with a higher catalyst loading will have a thicker catalyst layer, which will increase the transport resistance of chemical species due to larger diffusion distances. This has been shown to hinder the performance of GDEs for CO production. Blake et al. found that although thinner catalyst layers had less reactive surface area, the benefit of shorter diffusion distances led to increased current efficiencies and higher CO current densities.² On the other hand, an ion conductive binder (like Nafion) could help lower transport resistances in these thicker catalyst layers and thus improve the overall performance and durability of the electrode. For example, Nwabara et al. evaluated three types of binders in a GDE for CO production and found Nafion to be the most durable in terms of CO current efficiency for electrodes with a final loading of 1 mg/cm².³

Furthermore, the binder concentration in the layer can interact with the amount of catalyst supported on carbon and the GDL type. This interaction is most likely due to the amount of material that is required to be bound to the GDL. Lower amounts of catalyst supported on carbon lead to a higher total mass of the catalyst layer for the same catalyst loading (i.e., more material to bind). Similarly, higher catalyst loadings lead to a higher total mass of the catalyst layer.

Therefore, in future studies, the binder concentration, the percent of catalyst supported on carbon, the loading of the catalyst on the GDL, and the GDL type should be explored together

with alternative binders. If a consistent GDL and current density are used in the exploration of alternative binders, then the DOE in Table 7.1 can be used to explore these interactions between the other three factors; however, these factors (particularly the binder wt%) would have to be re-bounded before performing the DOE shown in Table 7.1.

Table 7.1. DOE experimental matrix for exploring alternative binder types with a standard GDL and current density. The low value of the factor is designated by -1, the high value of the factor is designated by 1, and the center value of the factor is designated by 0.

Binder in Catalyst Layer (wt%)	Catalyst on Carbon (%)	Loading (mg/cm²)
1	1	1
0	1	1
-1	1	-1
1	1	-1
0	-1	1
0	1	-1
-1	1	1
1	-1	-1
-1	-1	1
0	0	0
1	-1	1
-1	-1	-1

Additionally, the results of Chapter 4 show that the stability of the GDEs developed is not where it needs to be for industrial exploitation. The salt accumulation on the back of the GDL is one of the challenges that need to be addressed to realize this technology in an industrial setting. Future studies should be performed to determine the root cause of the salt accumulation on the GDEs and if there is a cost-effective way to mitigate this issue.

Salt formation and accumulation in GDEs used for CO₂ reduction has been seen in many other groups in this field.^{3–11} Sassenburg et al. describe the mechanisms for salt precipitation and review recently reported strategies for preventing or reversing the formation of salt in CO₂ membrane electrode assembly electrolyzers.¹² They also acknowledge that it is unclear whether the salt formation occurs from electrode flooding, if salt precipitates naturally in CO₂ GDEs, or if it is a combination of both processes. Further optimization of the catalyst environment with respect to enhancing the mass transport of products and carbonate salts is crucial for realizing the technology at a commercial scale. For example, Nwabara et al. found that a combination of PTFE to Nafion in the catalyst layer eliminated carbonate formation typical of cathodes they tested with just Nafion.³

Future Scale-up Development

Minimizing the cell potential is one additional focus that future studies should achieve. As seen in Equation 1.2 and Figure 1.2, the cell potential directly impacts the energy costs of producing formate. Salvatore et al. studied energy losses in their flow cell design and found that the majority of the losses occurred from the catholyte and membrane.¹³ The cell design and configuration presented in Chapter 5 can be explored further to reduce the energy cost. A thinner version of the electrolyte flow distribution plates in the cell design presented in Chapter 5 should be made to reduce the ohmic losses in the cell. Additionally, alternative membranes can be explored to further reduce the cell potential.

Additionally, paired electrolysis should be explored to reduce the associated energy costs of producing formate.¹⁴ Na et al. performed process calculations to screen for the economic viability of 295 coproduction processes. They found that paired electrolysis with CO₂ reduction can significantly increase the economic viability of the process.¹⁵ The cell design in Chapter 5 can be used to quickly modify cell configurations to explore various paired electrolysis reactions. For example, because it has four compartments, a hydrogen anode configuration could be coupled with CO₂ reduction to significantly lower the cell potential. Alternatively, a third electrolyte compartment could be included for acidifying salts, or the cell design could be used as a standard, three compartment GDE cell with a dissolved reactant in the anolyte.

Going forward, I would recommend that the CO₂ electrolyzer developers, such as Avantium, continue to investigate ways to increase electrode lifetime by hindering, eliminating, or reversing salt accumulation in the GDE. I would recommend investigating alternative binders and mixtures of binders at various concentrations in the catalyst layer for eliminating or reducing salt accumulation in the GDE. I would also recommend that Avantium continue to develop its paired electrolysis technology of producing formate from glycerol at the anode. A next big step for Avantium would be to demonstrate this paired electrolysis at a scale of >100 cm² for the same duration/lifetime as their CO₂ GDE cell with the OER at the anode. Once the choice in chemistries of the electrochemical cell is made, I would recommend that Avantium focus on optimizing the cell potential by testing various alternative membranes, determining the optimum electrolyte compositions, and modifying cell designs to minimize electrolyte gaps in the cell.

References

- (1) Wang, Q.; Dong, H.; Yu, H.; Yu, H. Enhanced Performance of Gas Diffusion Electrode for Electrochemical Reduction of Carbon Dioxide to Formate by Adding Polytetrafluoroethylene into Catalyst Layer. *J. Power Sources* **2015**, 279, 1–5, DOI 10.1016/j.jpowsour.2014.12.118.
- (2) Blake, J. W.; Padding, J. T.; Haverkort, J. W. Analytical Modelling of CO₂ Reduction in Gas-Diffusion Electrode Catalyst Layers. *Electrochim. Acta* **2021**, 393, 138987, DOI 10.1016/j.electacta.2021.138987.
- (3) Nwabara, U. O.; Hernandez, A. D.; Henckel, D. A.; Chen, X.; Cofell, E. R.; De-Heer, M. P.; Verma, S.; Gewirth, A. A.; Kenis, P. J. A. Binder-Focused Approaches to Improve the Stability of Cathodes for CO₂ Electroreduction. *ACS Appl. Energy Mater.* **2021**, 4 (5), 5175–5186, DOI 10.1021/acsaem.1c00715.
- (4) de Jesus Gálvez-Vázquez, M.; Moreno-García, P.; Xu, H.; Hou, Y.; Hu, H.; Montiel, I. Z.; Rudnev, A. V.; Alinejad, S.; Grozovski, V.; Wiley, B. J.; Arenz, M.; Broekmann, P. Environment Matters: CO₂RR Electrocatalyst Performance Testing in a Gas-Fed Zero-Gap Electrolyzer. *ACS Catal.* **2020**, 10 (21), 13096–13108, DOI 10.1021/acscatal.0c03609.
- (5) Wheeler, D. G.; Mowbray, B. A. W.; Reyes, A.; Habibzadeh, F.; He, J.; Berlinguette, C. P. Quantification of Water Transport in a CO₂ Electrolyzer. *Energy Environ. Sci.* **2020**, 13 (12), 5126–5134, DOI 10.1039/D0EE02219E.
- (6) Endródi, B.; Samu, A.; Kecsenovity, E.; Halmágyi, T.; Sebők, D.; Janáky, C. Operando Cathode Activation with Alkali Metal Cations for High Current Density Operation of Water-Fed Zero-Gap Carbon Dioxide Electrolysers. *Nat. Energy* **2021**, 6 (4), 439–448, DOI 10.1038/s41560-021-00813-w.
- (7) Yang, K.; Li, M.; Subramanian, S.; Blommaert, M. A.; Smith, W. A.; Burdyny, T. Cation-Driven Increases of CO₂ Utilization in a Bipolar Membrane Electrode Assembly for CO₂ Electrolysis. *ACS Energy Lett.* **2021**, 6 (12), 4291–4298, DOI 10.1021/acsenenergylett.1c02058.
- (8) Pham, T. H. M.; Zhang, J.; Li, M.; Shen, T.; Ko, Y.; Tileli, V.; Luo, W.; Züttel, A. Enhanced Electrocatalytic CO₂ Reduction to C₂₊ Products by Adjusting the Local Reaction Environment with Polymer Binders. *Adv. Energy Mater.* **2022**, 12 (9), 2103663, DOI 10.1002/aenm.202103663.
- (9) Wachter, B. De. Wind farm with battery storage in Ireland <https://web.archive.org/web/20071102075502/http://www.leonardo-energy.org/drupal/node/959>.
- (10) Leonard, M. E.; Clarke, L. E.; Forner-Cuenca, A.; Brown, S. M.; Brushett, F. R. Investigating Electrode Flooding in a Flowing Electrolyte, Gas-Fed Carbon Dioxide Electrolyzer. *ChemSusChem* **2020**, 13 (2), 400–411, DOI 10.1002/cssc.201902547.

-
- (11) Xu, Y.; Edwards, J. P.; Liu, S.; Miao, R. K.; Huang, J. E.; Gabardo, C. M.; O'Brien, C. P.; Li, J.; Sargent, E. H.; Sinton, D. Self-Cleaning CO₂ Reduction Systems: Unsteady Electrochemical Forcing Enables Stability. *ACS Energy Lett.* **2021**, 6 (2), 809–815, DOI 10.1021/acsenerylett.0c02401.
- (12) Sassenburg, M.; Kelly, M.; Subramanian, S.; Smith, W. A.; Burdyny, T. Zero-Gap Electrochemical CO₂ Reduction Cells: Challenges and Operational Strategies for Prevention of Salt Precipitation. *ACS Energy Lett.* **2023**, 8 (1), 321–331, DOI 10.1021/acsenerylett.2c01885.
- (13) Salvatore, D.; Berlinguette, C. P. Voltage Matters When Reducing CO₂ in an Electrochemical Flow Cell. *ACS Energy Lett.* **2020**, 5 (1), 215–220, DOI 10.1021/acsenerylett.9b02356.
- (14) van den Bosch, B.; Rawls, B.; Brands, M. B.; Koopman, C.; Phillips, M. F.; Figueiredo, M. C.; Gruter, G. M. Formate Over-Oxidation Limits Industrialization of Glycerol Oxidation Paired with Carbon Dioxide Reduction to Formate. *Chempluschem* **2023**, 88 (4), DOI 10.1002/cplu.202300112.
- (15) Na, J.; Seo, B.; Kim, J.; Lee, C. W.; Lee, H.; Hwang, Y. J.; Min, B. K.; Lee, D. K.; Oh, H.-S.; Lee, U. General Technoeconomic Analysis for Electrochemical Coproduction Coupling Carbon Dioxide Reduction with Organic Oxidation. *Nat. Commun.* **2019**, 10 (1), 5193, DOI 10.1038/s41467-019-12744-y.

Appendix A

Supporting Information for Chapter 3

GDL Production Method and Layers

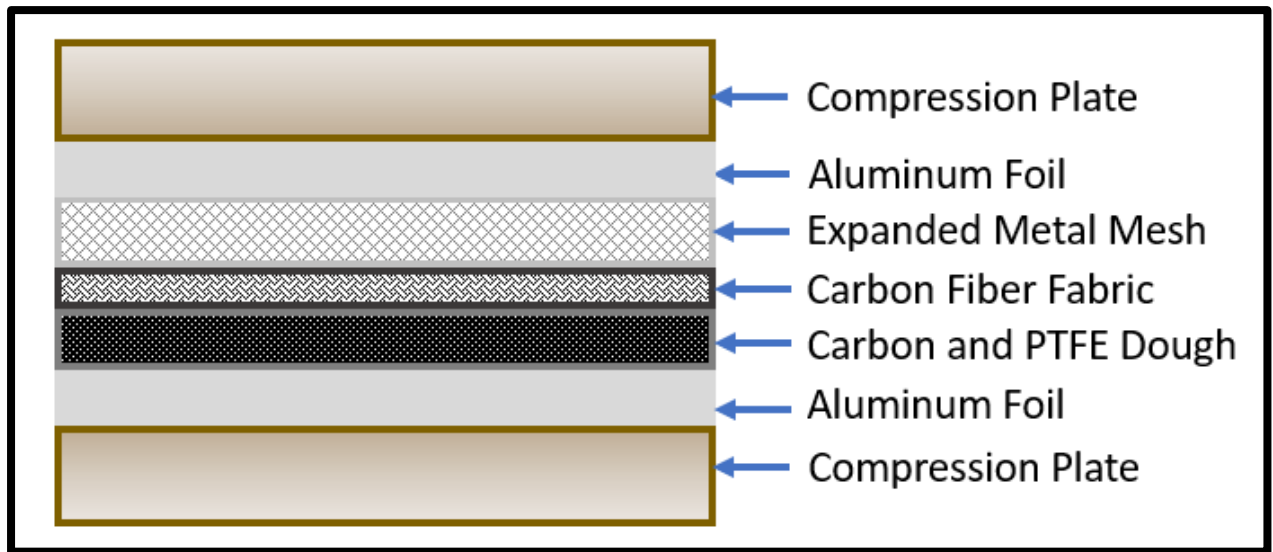


Figure A.1. Schematic of the GDL layers in the GDLs produced from this production method

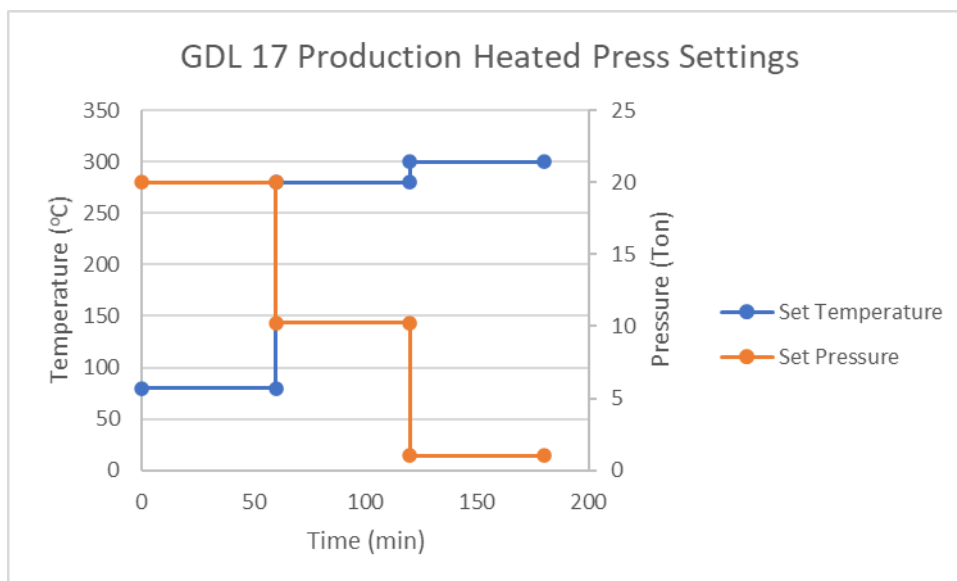


Figure A.2. Temperature and pressure set points for the heated press for GDL 17

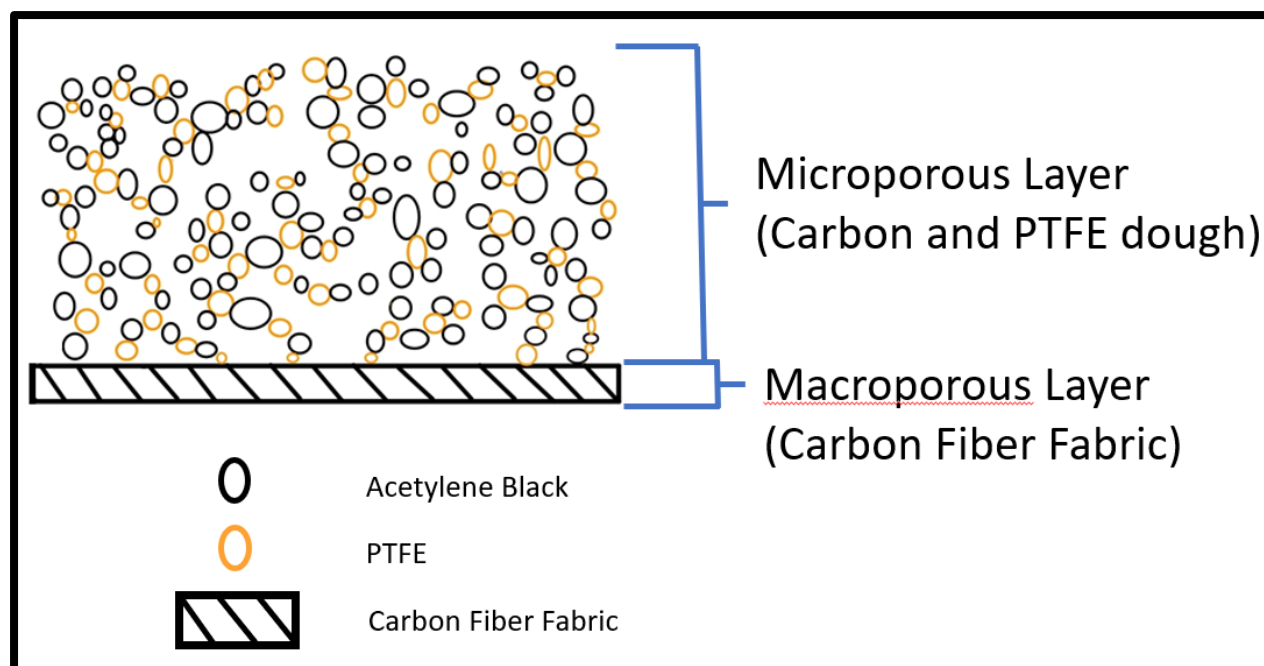


Figure A.3. Schematic of the GDL layers in the GDLs produced from this production method. Adapted with permission from Philips, M. F.; Pavesi, D.; Wissink, T.; Figueiredo, M. C.; Gruter, G.-J. M.; Koper, M. T. M.; Schouten, K. J. P. *Electrochemical CO₂ Reduction on Gas Diffusion Electrodes: Enhanced Selectivity of In–Bi Bimetallic Particles and Catalyst Layer Optimization through a Design of Experiment Approach*. Copyright 2022 ACS Applied Energy Materials

Table A.1. Experimental matrix for GDLs.

GDL Method Number	PTFE wt%	Rolliung Thickness Setting	Time Stage 1 (min)	Pressure Stage 1 (Ton)	Temp Stage 1 (°C)	Time Stage 2 (min)	Pressure Stage 2 (Ton)	Temp Stage 2 (°C)	Time Stage 3 (min)	Pressure Stage 3 (Ton)	Temp Stage 3 (°C)
GDL 1	20	4	5	20	140	5	20	280	5	1	335
GDL 2	50	4	5	20	200	60	0.5	280	5	25	300
GDL 3	20	4	60	0.5	200	32.5	0.5	335	5	1	300
GDL 4	20	2	5	0.5	80	60	20	335	5	25	317.5
GDL 5	20	2	5	20	200	60	0.5	335	32.5	1	335
GDL 6	20	2	32.5	0.5	200	5	0.5	280	60	25	335
GDL 7	50	2	60	20	80	5	0.5	335	5	13	335
GDL 8	50	2	5	20	80	32.5	20	280	60	25	335
GDL 9	50	4	60	0.5	80	5	20	280	32.5	25	300
GDL 10	20	2	60	20	200	5	20	307.5	5	25	300
GDL 11	20	4	5	0.5	200	60	20	280	60	13	300
GDL 12	50	4	60	20	200	5	0.5	280	60	1	317.5
GDL 13	50	4	32.5	20	80	60	20	335	5	1	300
GDL 14	50	4	5	0.5	200	5	10.25	335	5	25	335
GDL 15	50	2	60	0.5	200	60	20	280	5	1	335
GDL 16	35	4	60	20	200	60	20	335	60	25	335
GDL 17	20	2	60	20	80	60	10.25	280	60	1	300
GDL 18	20	2	60	0.5	80	5	20	335	60	1	335
GDL 19	20	4	60	10.25	80	60	0.5	280	5	25	335
GDL 20	35	2	5	0.5	80	5	0.5	280	5	1	300
GDL 21	35	2	32.5	10.25	140	32.5	10.25	307.5	32.5	13	317.5
GDL 22	50	2	60	0.5	140	60	0.5	335	60	25	300
GDL 23	35	4	32.5	10.25	140	32.5	10.25	307.5	32.5	13	317.5
GDL 24	50	4	5	0.5	80	60	0.5	307.5	60	1	335
GDL 25	20	4	5	20	80	5	0.5	335	60	25	300
GDL 26	50	2	5	10.25	200	5	20	335	60	1	300

Repeat GDL Analysis

GDL01

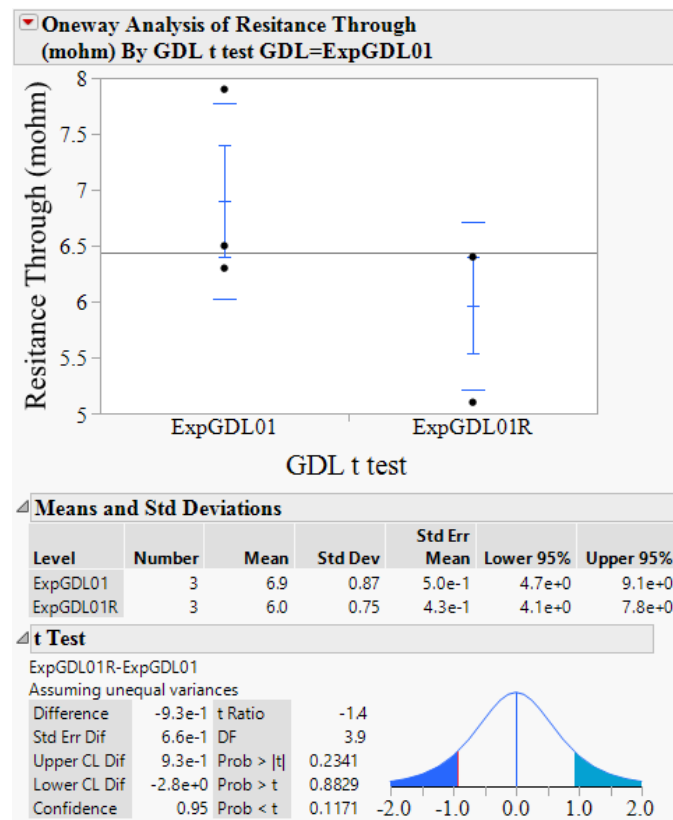


Figure A.4. Means, Standard Deviation, and t-test for resistance through of GDL01

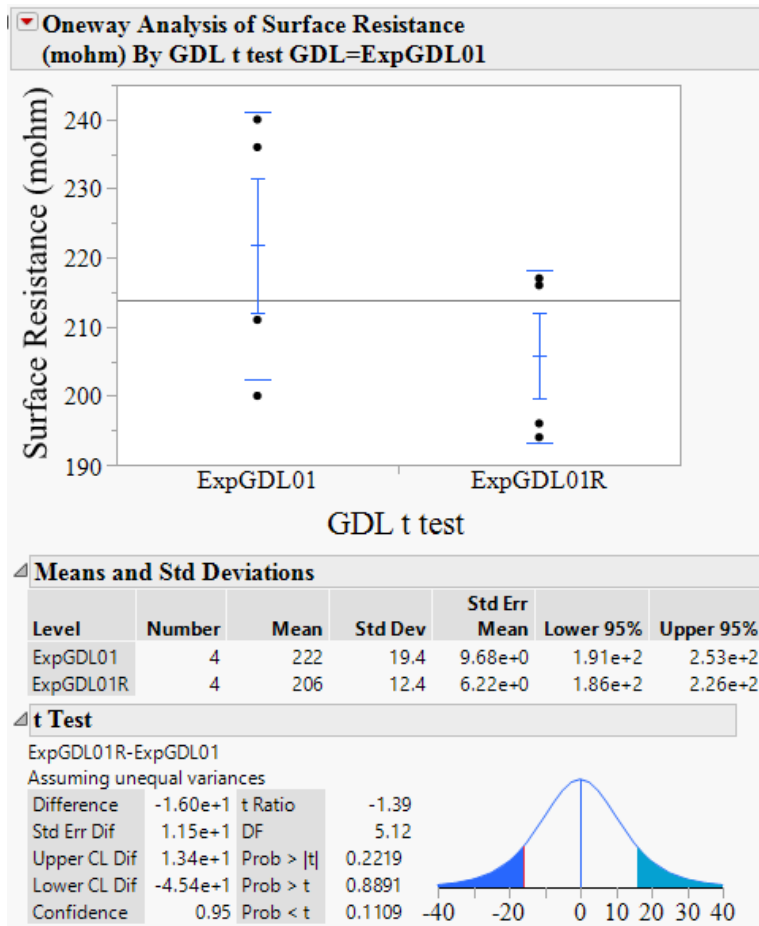


Figure A.5. Means, Standard Deviation, and t-test for surface resistance of GDL01

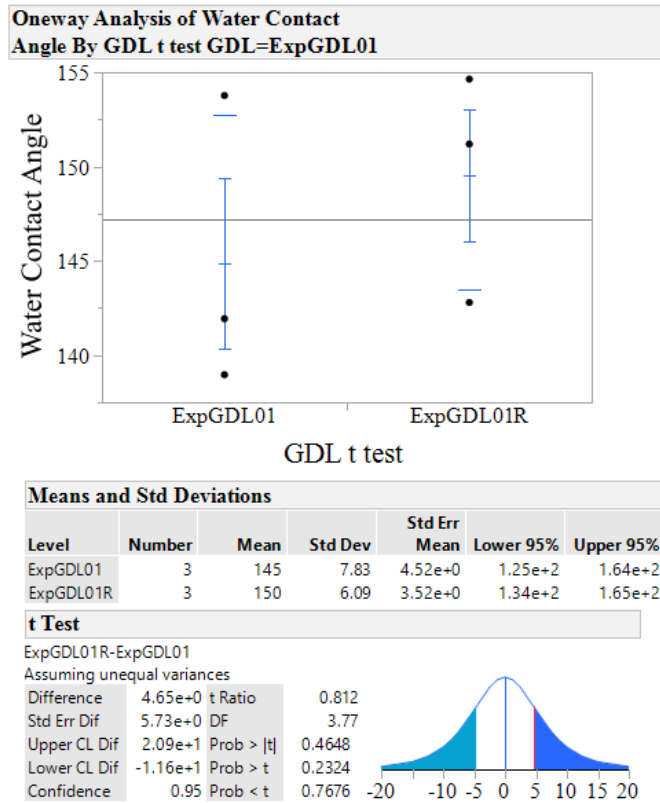


Figure A.6. Means, Standard Deviation, and t-test for water contact angle of GDL01

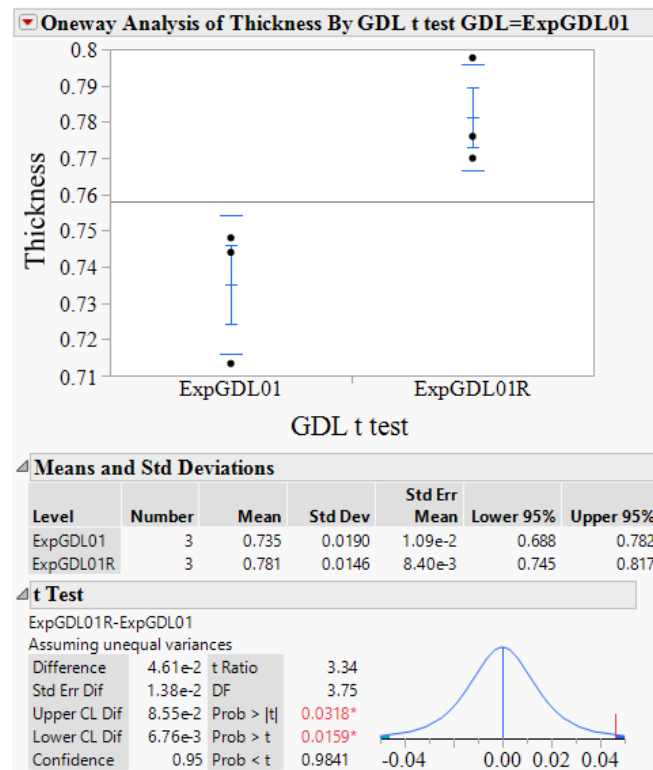


Figure A.7. Means, Standard Deviation, and t-test for thickness of GDL01

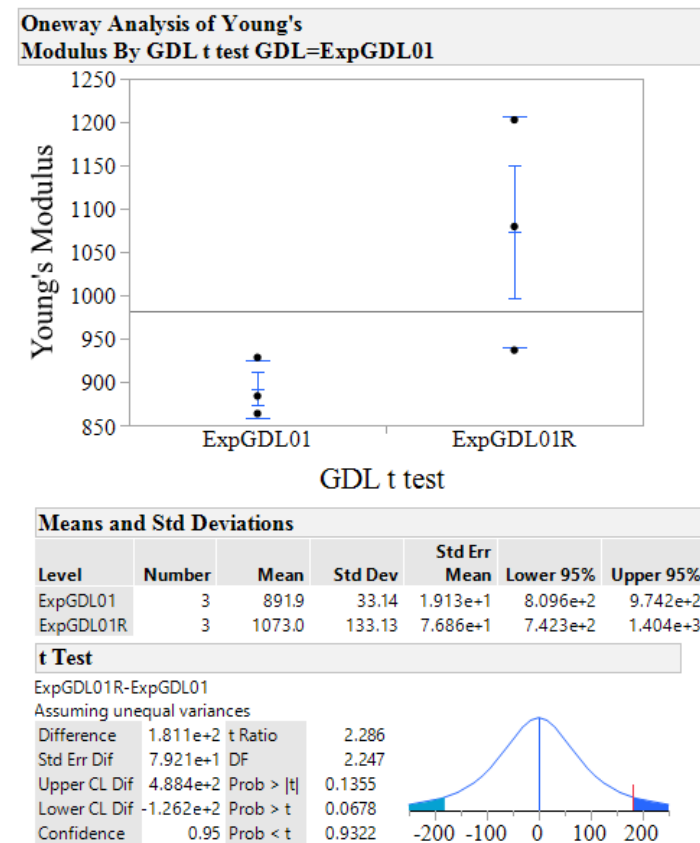


Figure A.8. Means, Standard Deviation, and t-test for the Young's Modulus of GDL01

GDL 12

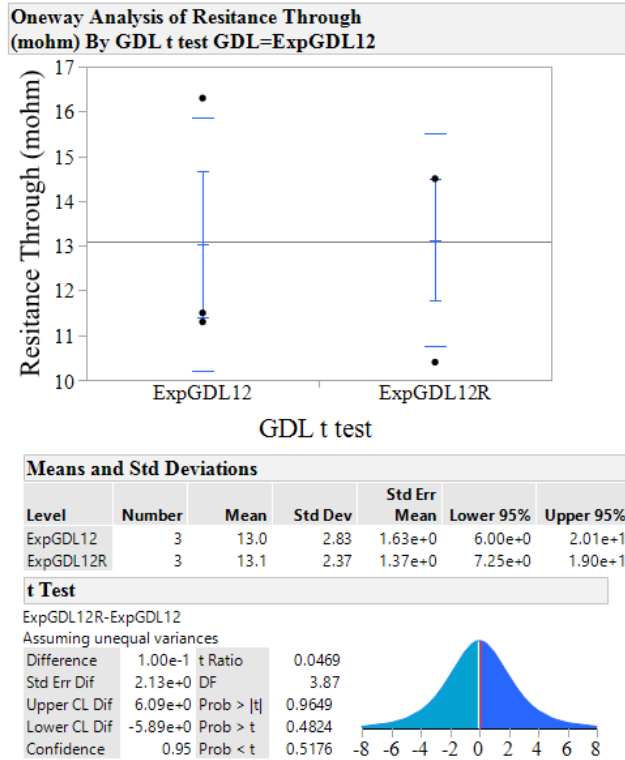


Figure A.9. Means, Standard Deviation, and t-test for the resistance through GDL12

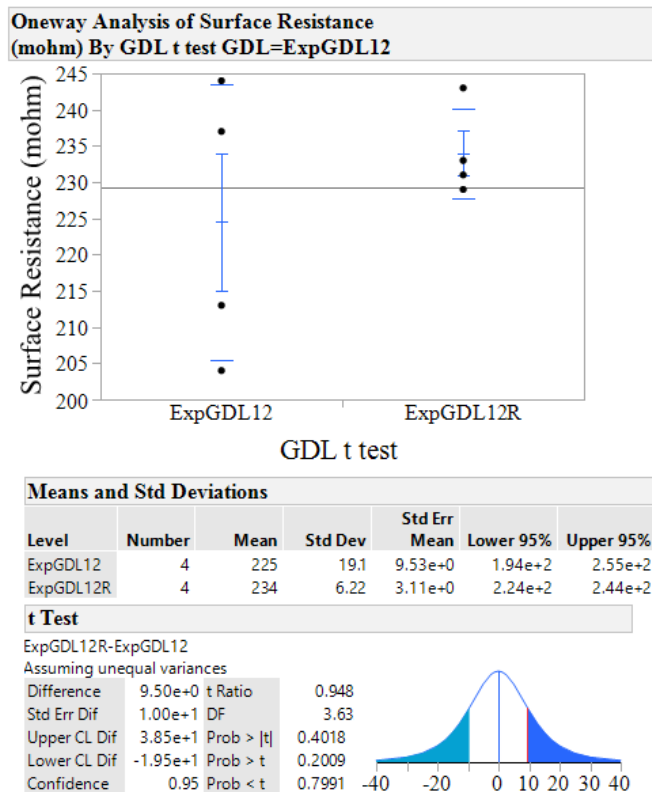


Figure A.10. Means, Standard Deviation, and t-test for the surface resistance of GDL12

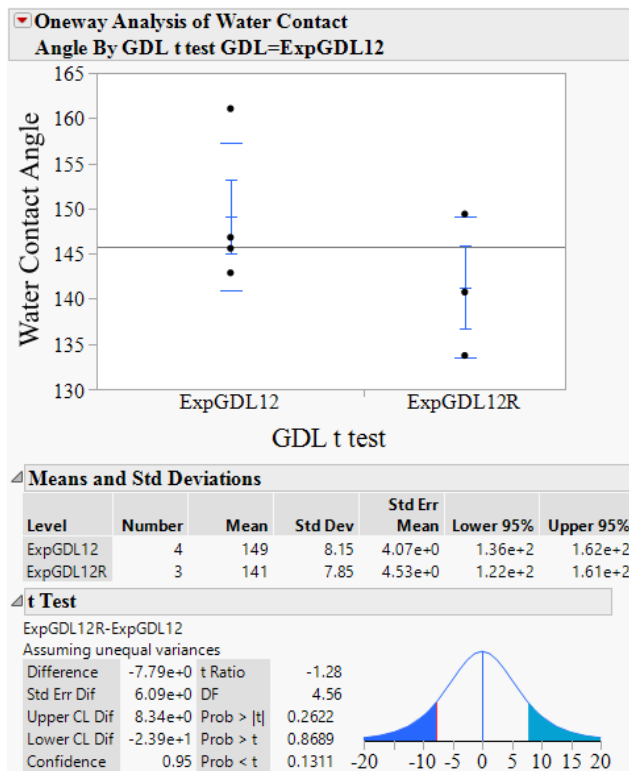


Figure A.11. Means, Standard Deviation, and t-test for the water contact angle of GDL12

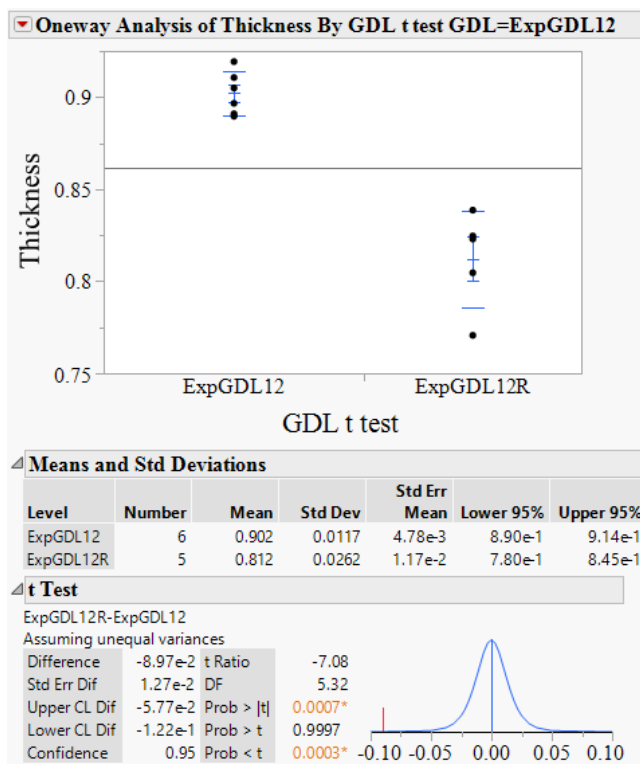


Figure A.12. Means, Standard Deviation, and t-test for the thickness of GDL12

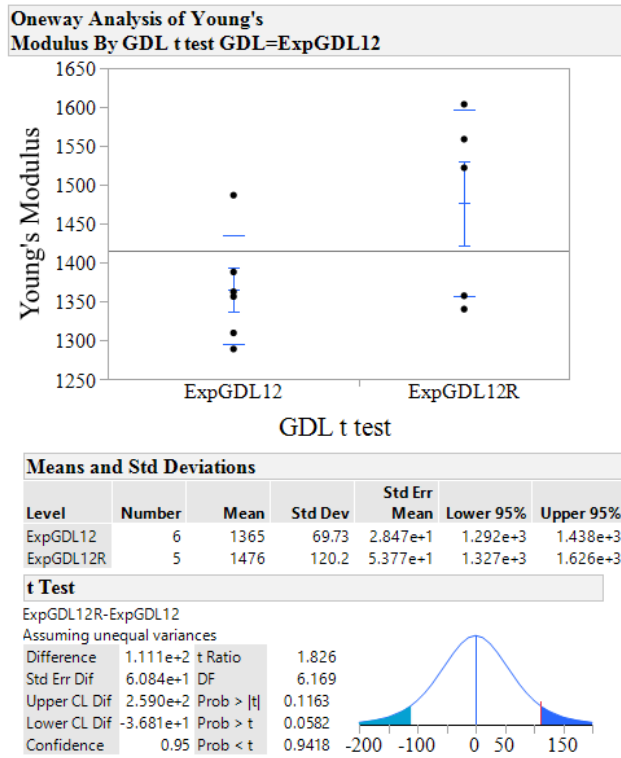


Figure A13. Means, Standard Deviation, and t-test for the Young's Modulus of GDL12

GDL 16

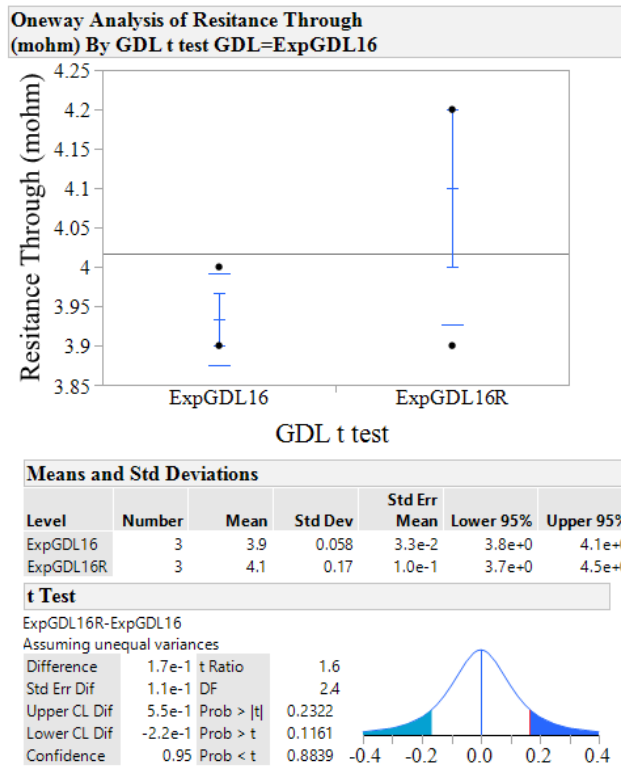


Figure A.14. Means, Standard Deviation, and t-test for the resistance through GDL16

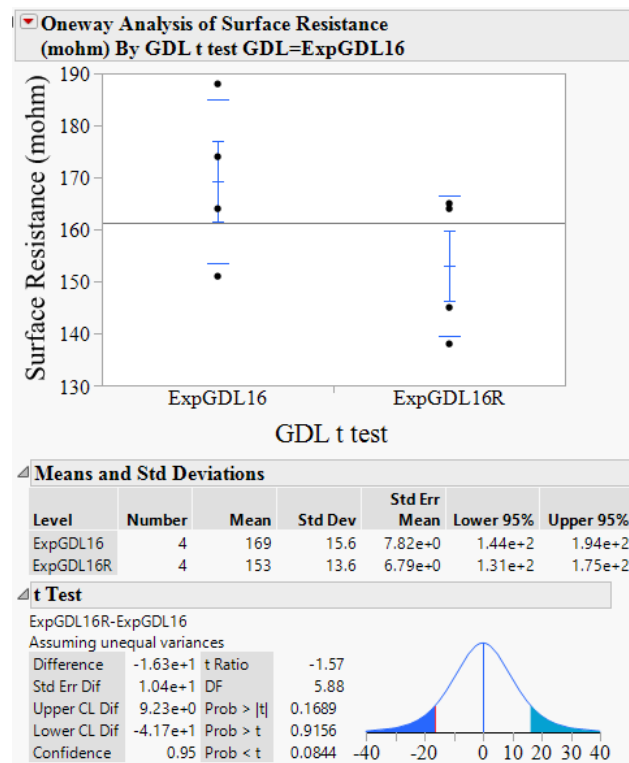


Figure A.15. Means, Standard Deviation, and t-test for the surface resistance of GDL16

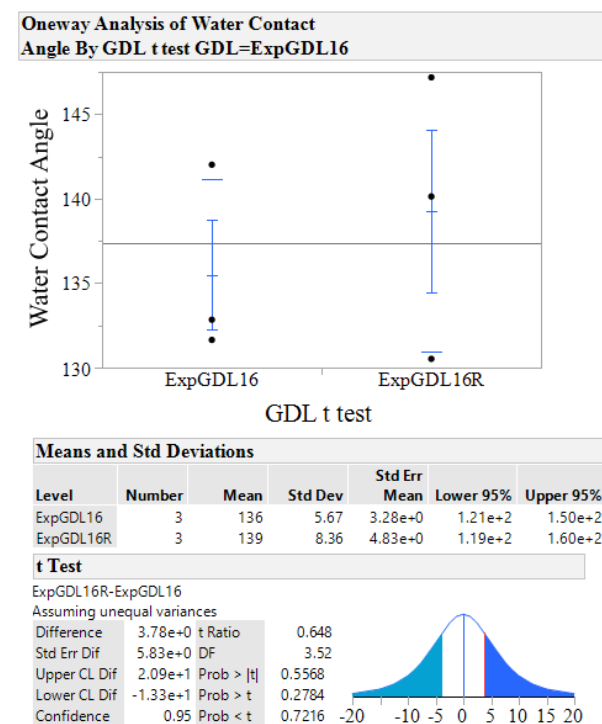


Figure A.16. Means, Standard Deviation, and t-test for the water contact angle of GDL16

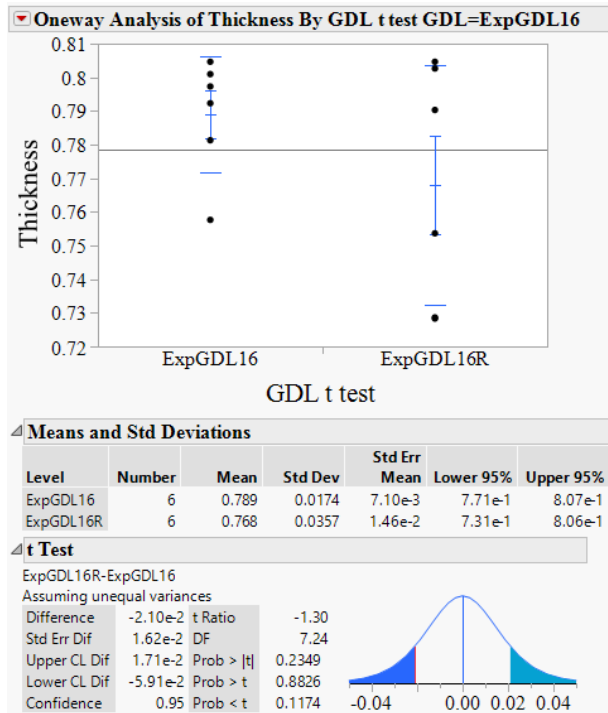


Figure A.17. Means, Standard Deviation, and t-test for the thickness of GDL16

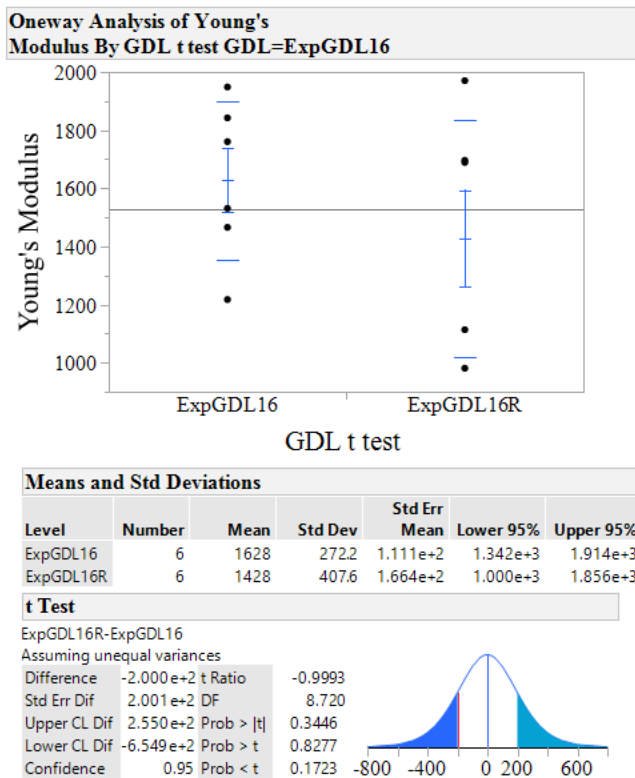


Figure A.18. Means, Standard Deviation, and t-test for the Young's Modulus of GDL16

Model Comparisons

Conductance Through Structure

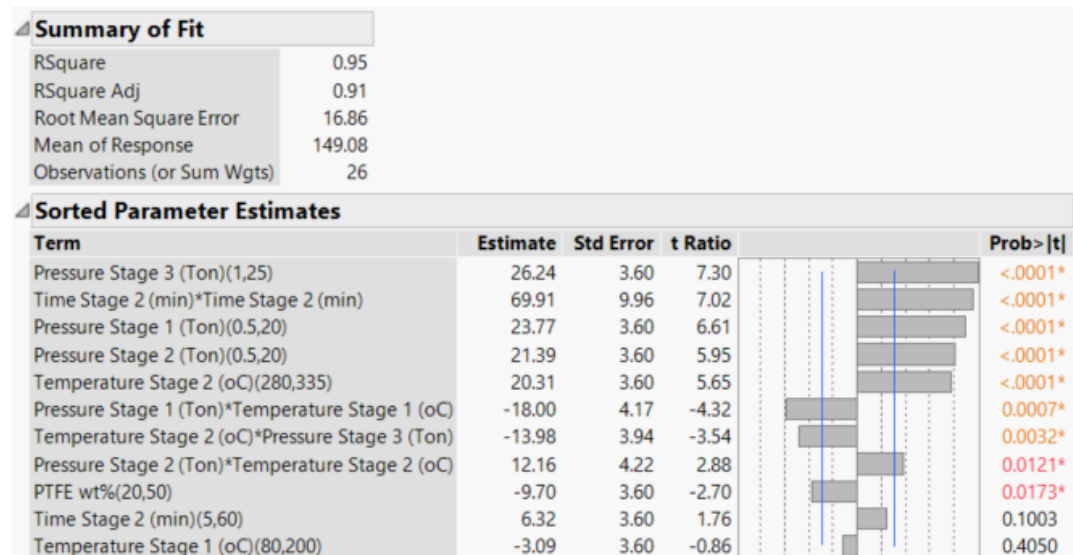


Figure A.19. Model summary and sorted parameter estimates of the model generated using the AIC as a stopping rule for the conductance through the GDL

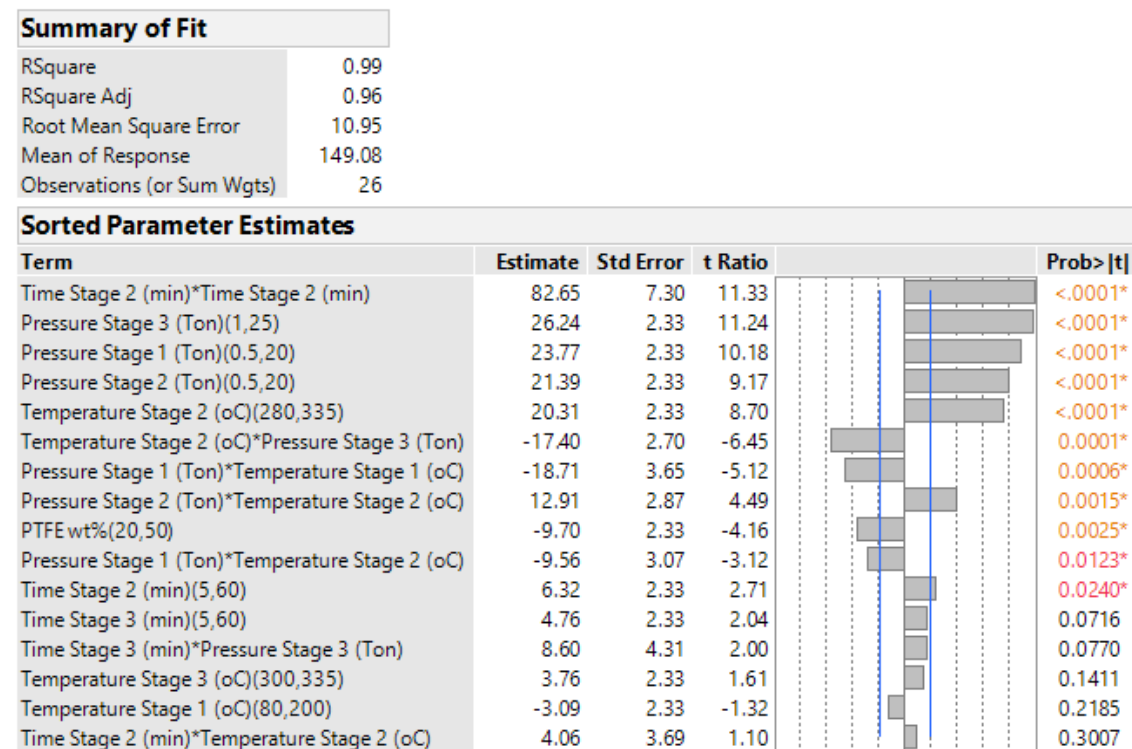


Figure A.20. Model summary and sorted parameter estimates of the model generated using the BIC as a stopping rule for the conductance through the GDL

Surface Conductivity

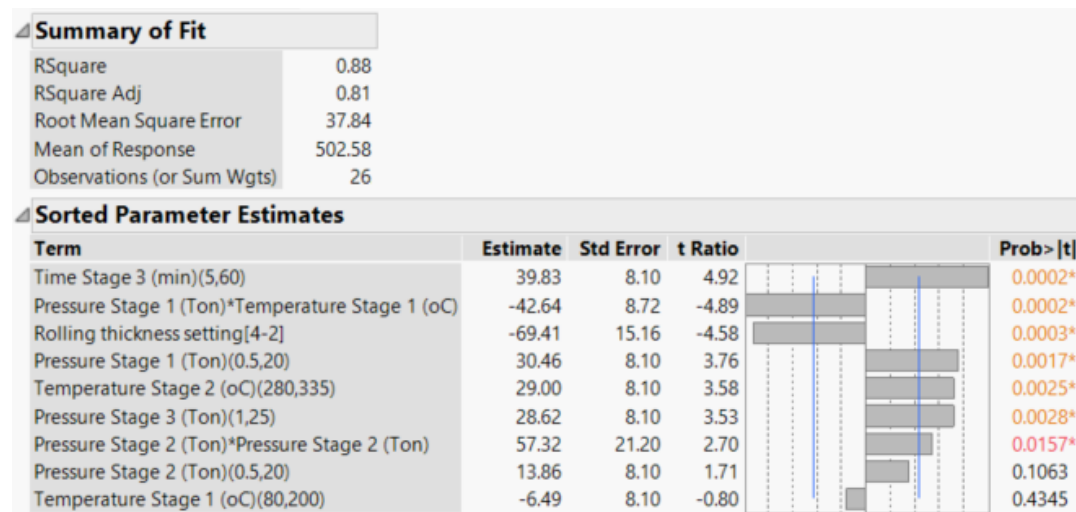


Figure A.21. Model summary and sorted parameter estimates of the model generated using the AIC as a stopping rule for the surface conductivity of the GDL

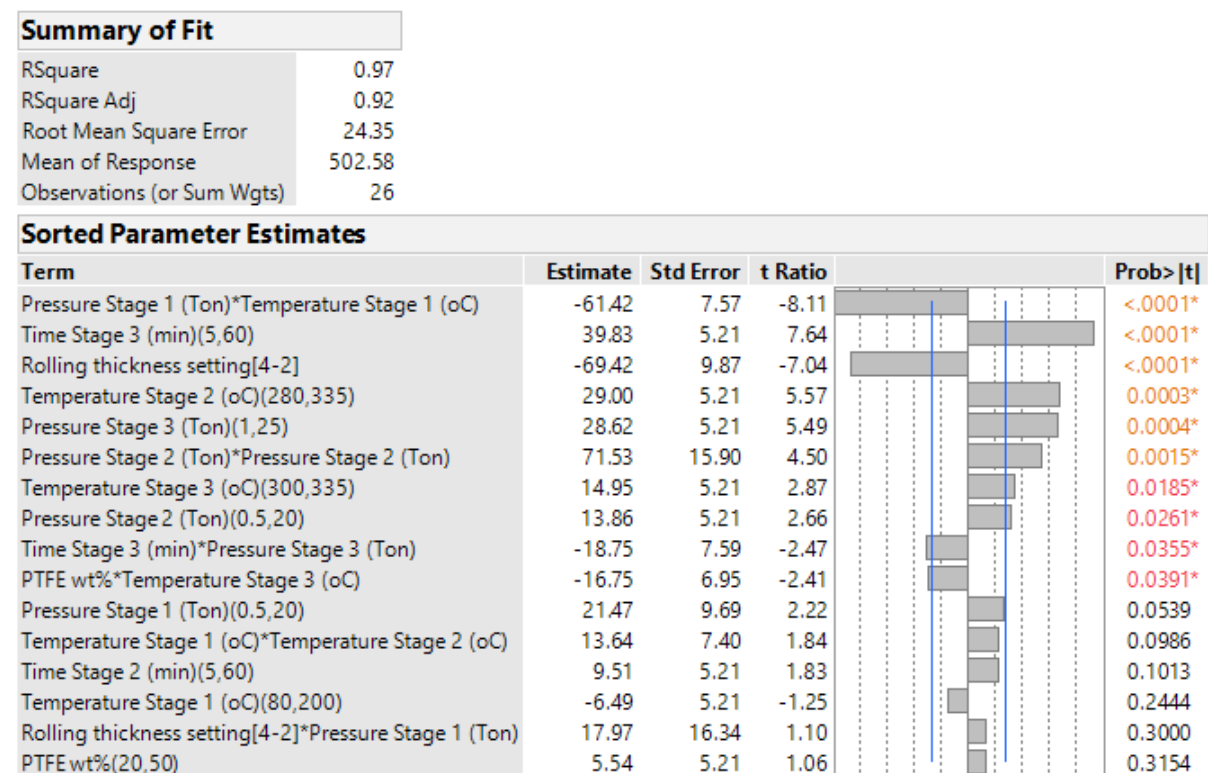


Figure A.22. Model summary and sorted parameter estimates of the model generated using the BIC as a stopping rule for the surface conductivity the GDL

Young's Modulus

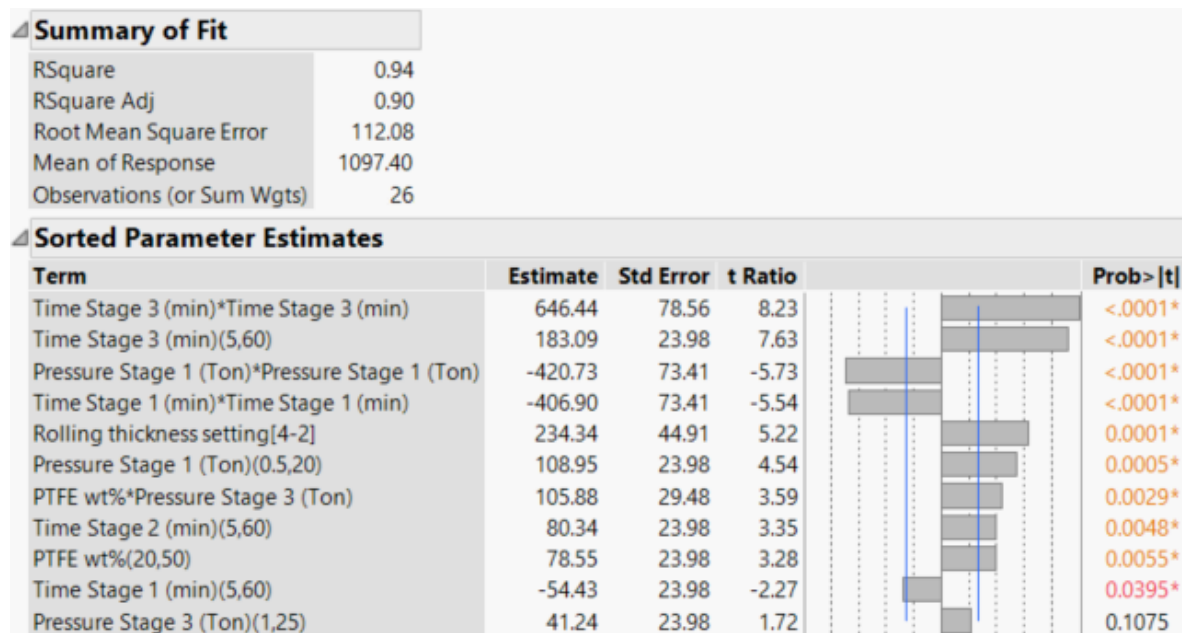


Figure A.23. Model summary and sorted parameter estimates of the model generated using the AIC as a stopping rule for the Young's Modulus of the GDL

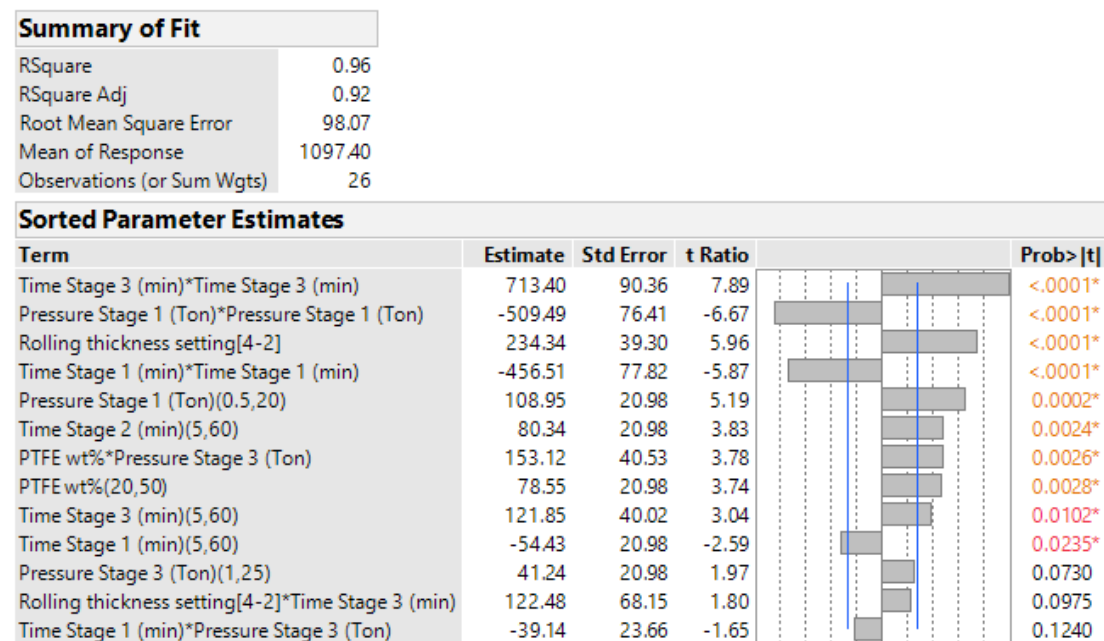


Figure A.24. Model summary and sorted parameter estimates of the model generated using the BIC as a stopping rule for the Young's Modulus of the GDL

Thickness

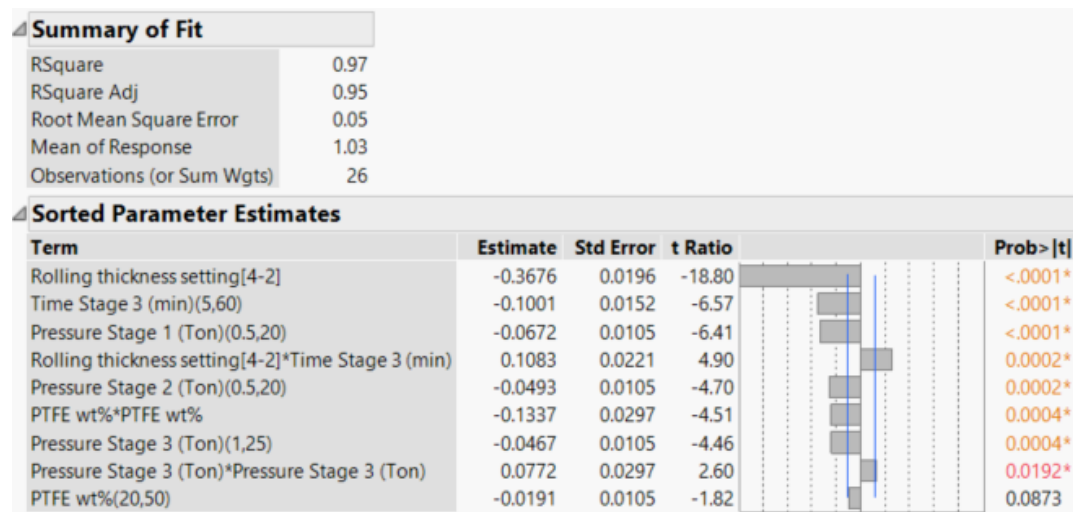


Figure A.25. Model summary and sorted parameter estimates of the model generated using the AIC as a stopping rule for the thickness of the GDL

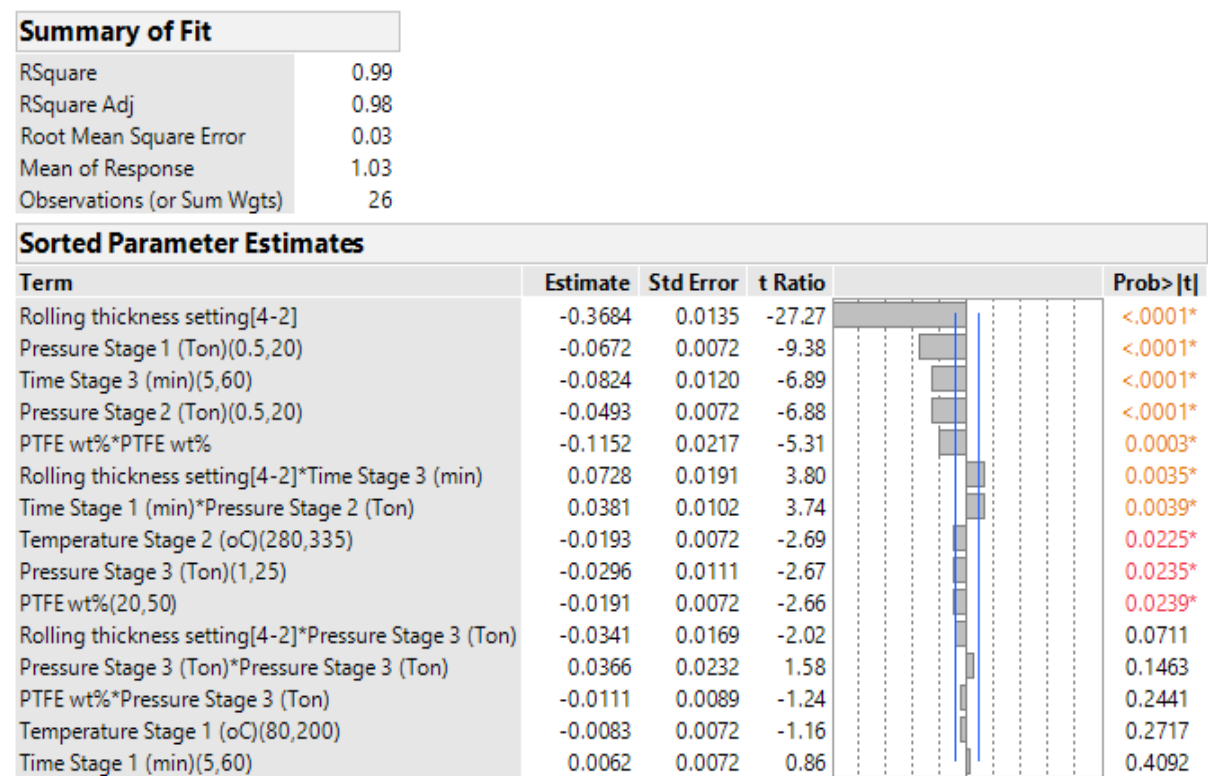


Figure A.26. Model summary and sorted parameter estimates of the model generated using the BIC as a stopping rule for the thickness of the GDL

Water Contact Angle

Summary of Fit	
RSquare	0.84
RSquare Adj	0.77
Root Mean Square Error	3.68
Mean of Response	139.58
Observations (or Sum Wgts)	26

Sorted Parameter Estimates					
Term	Estimate	Std Error	t Ratio		Prob> t
PTFE wt%(20,50)	-5.531	0.788	-7.02		<.0001*
Temperature Stage 1 (oC)(80,200)	-4.173	1.125	-3.71		0.0017*
Temperature Stage 1 (oC)*Pressure Stage 2 (Ton)	-2.716	0.839	-3.24		0.0048*
Rolling thickness setting[4-2]*Temperature Stage 1 (oC)	4.983	1.605	3.10		0.0065*
Time Stage 3 (min)(5,60)	1.997	0.788	2.53		0.0214*
Temperature Stage 2 (oC)(280,335)	-1.912	0.788	-2.43		0.0267*
Pressure Stage 2 (Ton)(0.5,20)	-0.865	0.788	-1.10		0.2878
Rolling thickness setting[4-2]	1.441	1.470	0.98		0.3408

Figure A.27. Model summary and sorted parameter estimates of the model generated using the AIC as a stopping rule for the water contact angle of the GDL

Summary of Fit	
RSquare	0.87
RSquare Adj	0.80
Root Mean Square Error	3.45
Mean of Response	139.58
Observations (or Sum Wgts)	26

Sorted Parameter Estimates					
Term	Estimate	Std Error	t Ratio		Prob> t
PTFE wt%(20,50)	-5.531	0.739	-7.49		<.0001*
Temperature Stage 1 (oC)(80,200)	-4.455	1.065	-4.18		0.0007*
Rolling thickness setting[4-2]*Temperature Stage 1 (oC)	5.547	1.536	3.61		0.0023*
Temperature Stage 1 (oC)*Pressure Stage 2 (Ton)	-2.660	0.787	-3.38		0.0038*
Time Stage 3 (min)(5,60)	1.997	0.739	2.70		0.0157*
Temperature Stage 2 (oC)(280,335)	-1.912	0.739	-2.59		0.0198*
Pressure Stage 2 (Ton)*Pressure Stage 2 (Ton)	3.506	1.915	1.83		0.0858
Pressure Stage 2 (Ton)(0.5,20)	-0.865	0.739	-1.17		0.2589
Rolling thickness setting[4-2]	1.441	1.378	1.05		0.3113

Figure A.28. Model summary and sorted parameter estimates of the model generated using the BIC as a stopping rule for the water contact angle of the GDL

Porosity by Hg Intrusion

Summary of Fit					
RSquare	0.74				
RSquare Adj	0.65				
Root Mean Square Error	7.83				
Mean of Response	62.01				
Observations (or Sum Wgts)	26				

Sorted Parameter Estimates					
Term	Estimate	Std Error	t Ratio		Prob> t
PTFE wt%(20,50)	-9.00	1.67	-5.37		<.0001*
Time Stage 2 (min)(5,60)	4.22	1.67	2.52		0.0210*
Time Stage 1 (min)*Time Stage 2 (min)	-3.85	1.80	-2.13		0.0463*
PTFE wt%*PTFE wt%	8.82	4.39	2.01		0.0588
Time Stage 1 (min)(5,60)	3.35	1.67	2.00		0.0601
Rolling thickness setting[4-2]	5.71	3.10	1.84		0.0814

Figure A.29. Model summary and sorted parameter estimates of the model generated using the AIC as a stopping rule for the porosity by Hg intrusion of the GDL

Summary of Fit					
RSquare	0.77				
RSquare Adj	0.68				
Root Mean Square Error	7.45				
Mean of Response	62.01				
Observations (or Sum Wgts)	26				

Sorted Parameter Estimates					
Term	Estimate	Std Error	t Ratio		Prob> t
PTFE wt%(20,50)	-8.98	1.59	-5.63		<.0001*
Time Stage 2 (min)(5,60)	4.23	1.59	2.66		0.0160*
Time Stage 1 (min)*Time Stage 2 (min)	-3.85	1.72	-2.24		0.0378*
PTFE wt%*PTFE wt%	8.82	4.17	2.11		0.0488*
Time Stage 1 (min)(5,60)	3.33	1.59	2.09		0.0512
Rolling thickness setting[4-2]	5.28	2.96	1.78		0.0918
Temperature Stage 1 (oC)(80,200)	2.76	1.59	1.73		0.1005

Figure A.30. Model summary and sorted parameter estimates of the model generated using the BIC as a stopping rule for the porosity by Hg intrusion of the GDL

Model Profilers

Conductance Through Structure

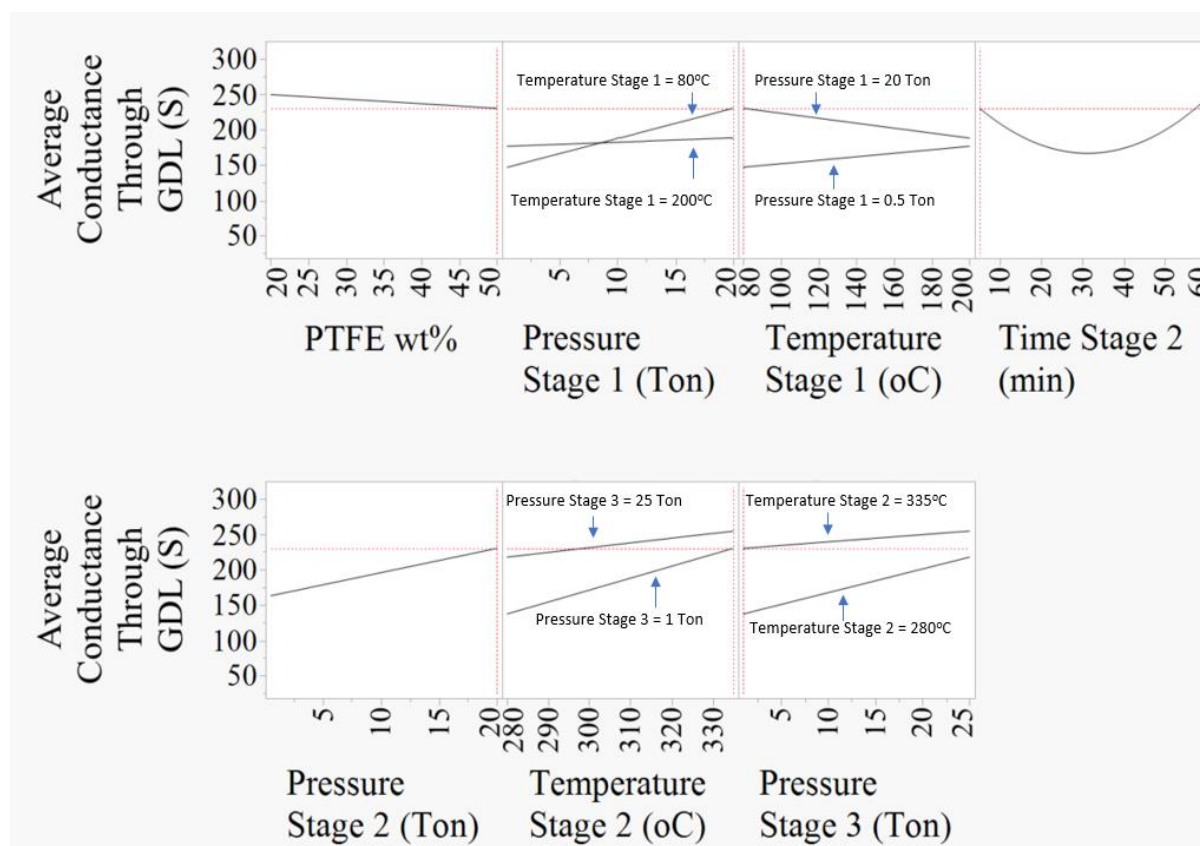


Figure A.31. Conductance through GDL model profiler

Surface Conductivity

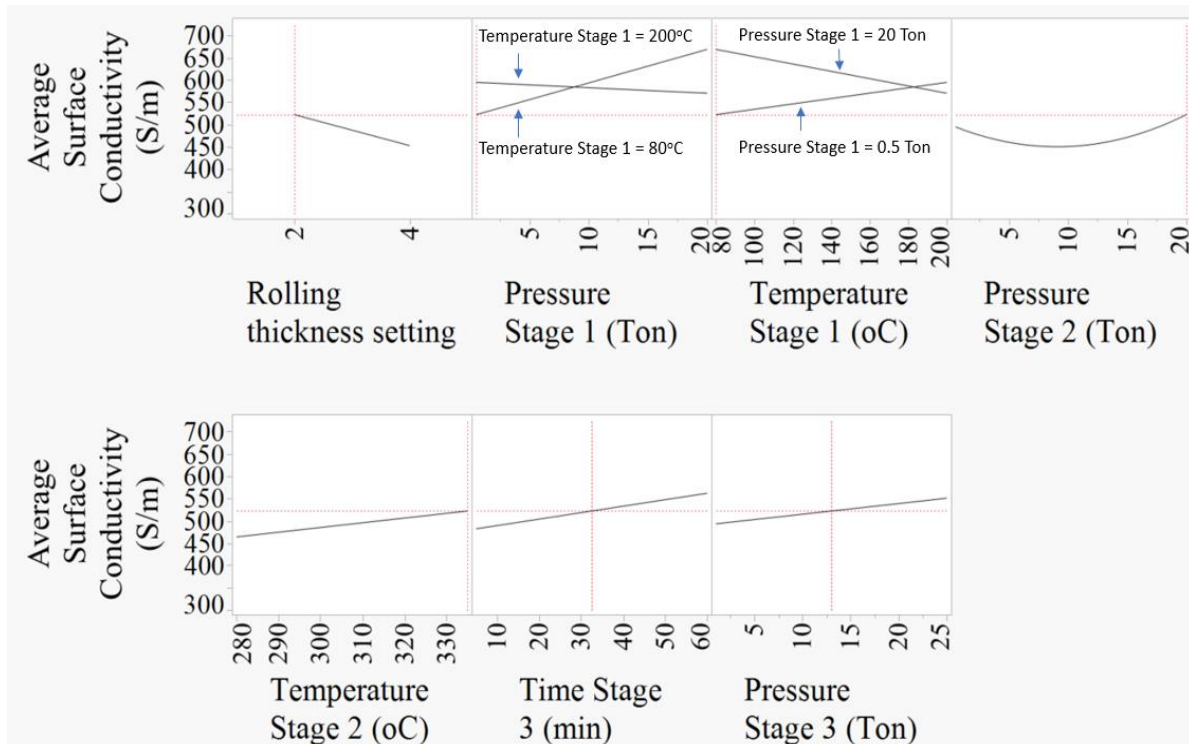


Figure A.32. GDL surface conductivity model profiler

Young's Modulus

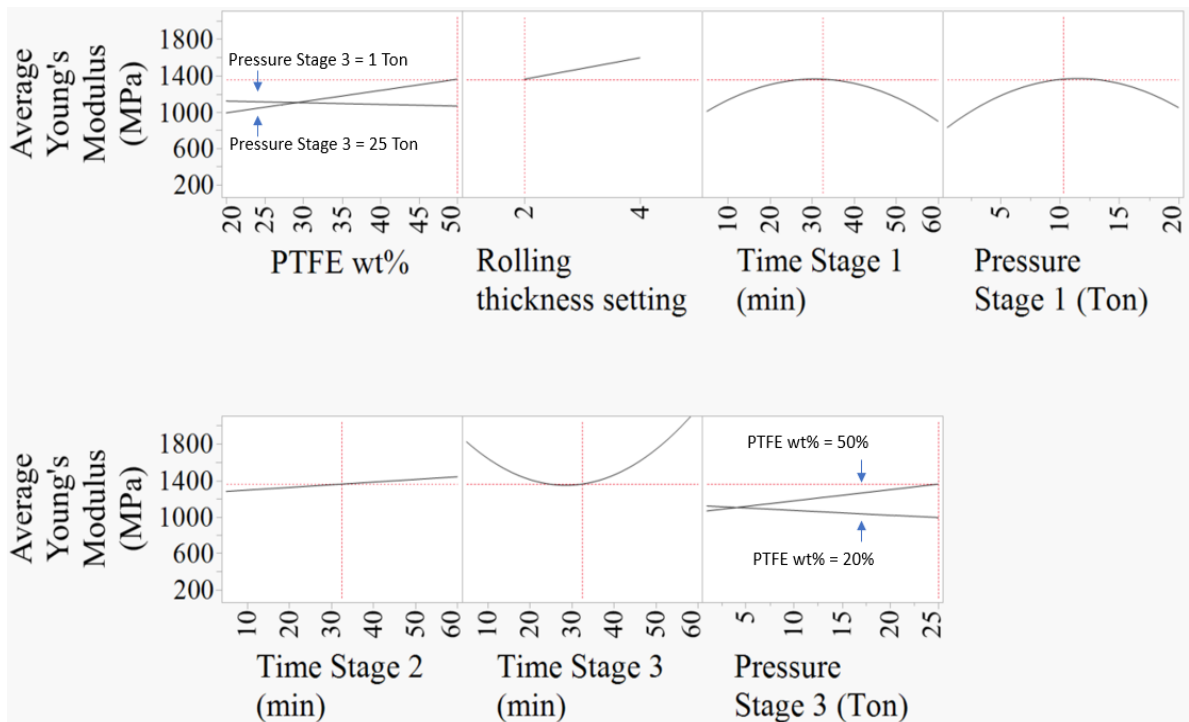


Figure A.33. Young's Modulus model profiler

Thickness

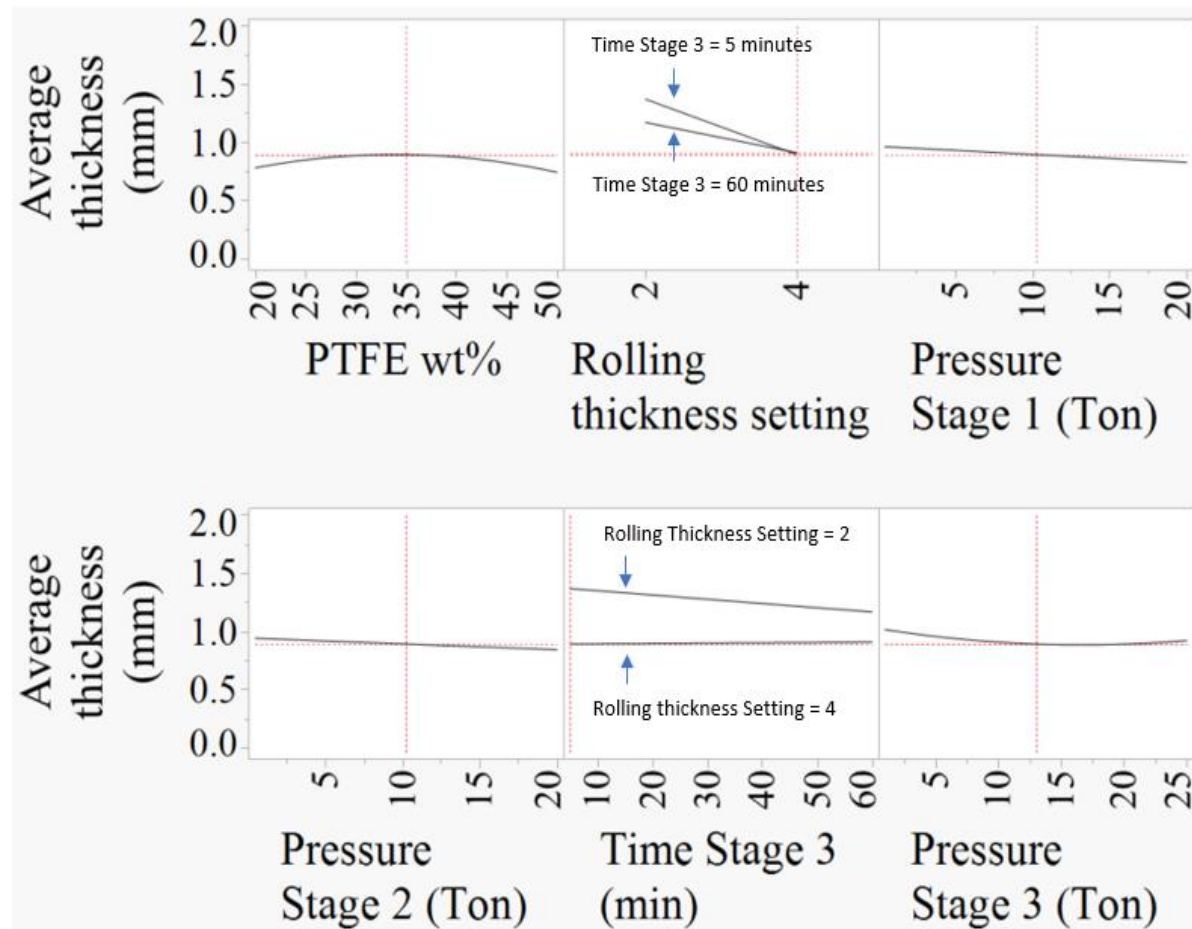


Figure A.34. GDL thickness model profiler

Water Contact Angle

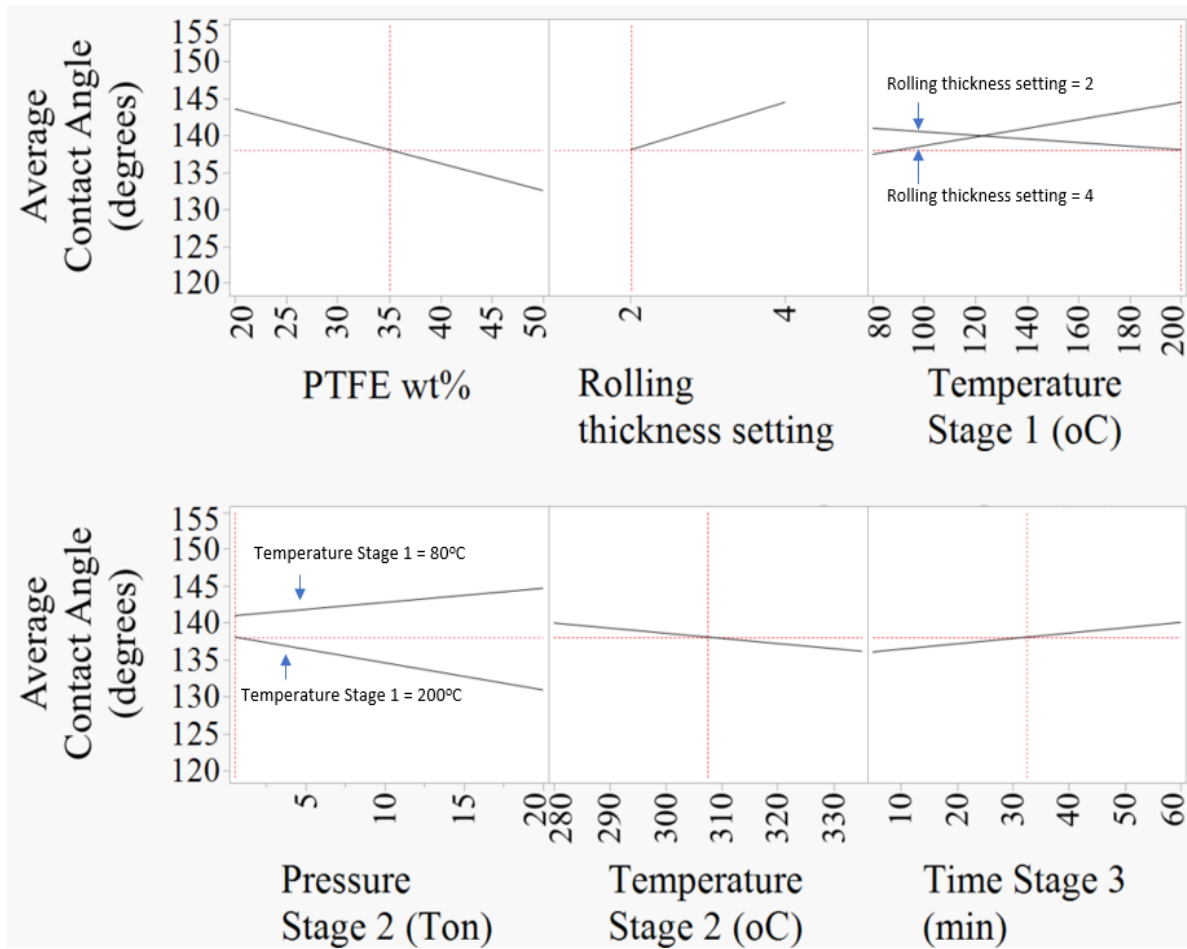


Figure A.35. Water contact angle model profiler

Porosity by Hg Intrusion

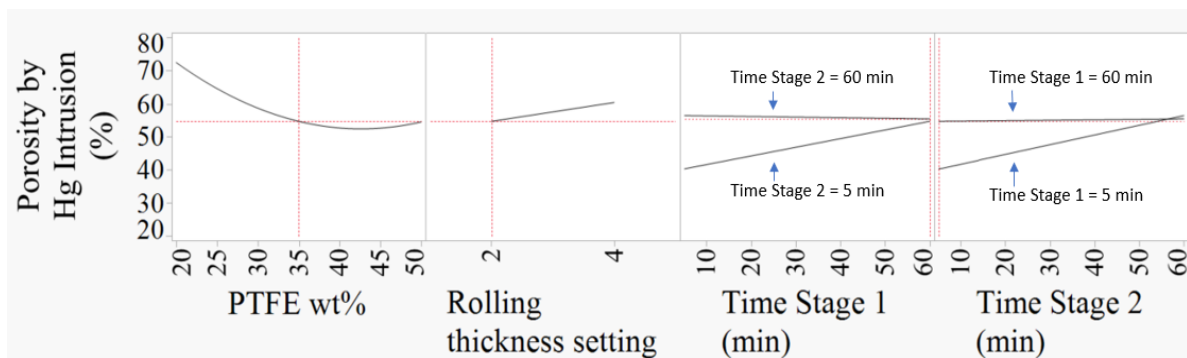


Figure A.36. Porosity by Hg intrusion model profiler

Tabulated Characteristic Data

Appendix A: Supporting Information for Chapter 3

Table A.2. Characteristic Data of 26 GDLs synthesized. Data for repeat GDLs is averaged with original data.

GDL Method Number	Average Conductance Through GDL (S)	StDev Conductance Through GDL (S)	Average Surface Conductivity (S/m)	StDev Surface Conductivity (S/m)	Average Young's Modulus (MPa)	StDev Young's Modulus (Mpa)	Average thickness (mm)	StDev Thickness (mm)	Average Contact Angle (degrees)	Std Dev Contact Angle (degrees)	Porosity from Hq Intrusion (%)
GDL 1*	158	22	444	35	982.4	131.8	0.8	0	147.2	6.8	71.65
GDL 2	169	8	422	22	1466.1	282.7	0.8	0	139.3	6.7	70.81
GDL 3	69	25	402	41	783.5	193.6	1	0	147.4	4.2	79.25
GDL 4	203	12	520	14	672	216.9	1.2	0	144.4	0.9	75.72
GDL 5	153	17	527	22	543.2	123.6	1.2	0	141.7	7.7	77.19
GDL 6	187	18	601	59	1125	202.5	1.2	0	144.8	2	77.36
GDL 7	167	27	596	24	792.6	54.7	1.2	0	129.9	9	57.75
GDL 8	171	37	678	23	1566.3	272.2	0.9	0	142.4	5.7	41.59
GDL 9	131	6	414	66	369.7	129.8	0.8	0	136.3	2.2	67.51
GDL 10	195	8	467	58	601.2	128.7	1.2	0	136.4	13.5	64.69
GDL 11	145	20	476	107	1358.6	136.2	0.8	0	148.7	4.6	76.99
GDL 12*	78	14	413	27	1415.7	107.6	0.9	0.1	145.7	8.4	57.86
GDL 13	242	30	545	39	1471	67	0.8	0	135.7	6.5	55.1
GDL 14	163	38	464	17	1157.5	168.7	0.8	0	129.5	10.5	40.14
GDL 15	85	2	469	44	689.5	123.1	1.4	0	122.1	8.9	61.32
GDL 16*	249	9	591	59	1527.9	346.6	0.8	0	137.4	6.7	69.26
GDL 17	162	0	553	42	1225.5	163.5	1.1	0.1	151.6	8.7	72.56
GDL 18	175	7	531	36	925.8	89.1	1.2	0	151.4	10.8	64.37
GDL 19	175	18	493	23	1277.6	239.7	0.9	0	145.3	2.4	72.55
GDL 20	38	11	325	33	696.3	88.1	1.6	0	142	4.6	26.9
GDL 21	99	6	519	19	1058.8	198.7	1.4	0.1	141.3	9.9	61.67
GDL 22	149	3	594	18	1320.1	49.6	1.1	0	136.9	5.4	49.55
GDL 23	59	14	365	37	1587.7	342.6	0.9	0.1	128.7	0.7	52.66
GDL 24	75	29	430	30	1217.5	203.6	1	0.1	135.2	7.8	56.68
GDL 25	199	0	592	38	1354.7	182.2	0.8	0	141	10.2	64.62
GDL 26	178	4	635	16	1346.1	142.9	1	0	126.7	7.5	46.44

*GDLs with repeat synthesis and analysis

Table A.3. Average and Median Pore Diameter of the 26 GDLs synthesized

	Average Pore Diameter (nm)	Median Pore Diameter (nm)
GDL01	90.32	335.43
GDL02	18.69	124.82
GDL03	120.55	489.74
GDL04	79.08	152.9
GDL05	98.16	298.93
GDL06	82.73	190.94
GDL07	68.15	119.43
GDL08	47.89	69.92
GDL09	94.46	275.55
GDL10	69.74	215.02
GDL11	110.08	471.17
GDL12	52.02	199.24
GDL13	48.1	343.9
GDL14	66.54	301.24
GDL15	64.58	134.55
GDL16	62.24	131.47
GDL17	83.83	241.42
GDL18	67.51	119.43
GDL19	35.84	124.19
GDL20	102.31	361.37
GDL21	52.96	106.13
GDL22	51.9	76.89
GDL23	66.25	139.86
GDL24	99.59	230.60
GDL25	66.36	154.39
GDL26	49.22	71.63

Appendix B

Comparison of Avantium's Patented InBi
Electrocatalyst to Pure In and Bi Catalysts and
Rationale for the Enhanced Performance of the
InBi Catalyst – Work Performed by Davide Pavesi

Experimental Methods

Indium and Bismuth Particle Production

For the single metals, the reaction was scaled down to 100 mL, and 1.1 g of InCl_3 were used for the In-only catalyst, while 2.4 g of $\text{Bi}(\text{NO}_3)_3 \cdot 5\text{H}_2\text{O}$ were used for the Bi-only catalyst. The amount of carbon was chosen so that the atomic % of metal on carbon rather than the weight % on carbon of the single metal catalyst would be similar to the 60 wt% InBi on carbon (53.7 wt% In on C and 67.9 wt% Bi on carbon). The InBi catalysts with different loadings on carbon were used for the Design of Experiments (DOE), while the single metal catalysts were compared to the InBi 60 wt% on carbon for the benchmarking and characterization.

Ink Formulation

Two types of binders were investigated in this study: PVDF and NafionTM. The inks were formulated according to the binder used. In the case of NafionTM, the catalysts were sonicated in isopropanol before the addition of the binder, while for PVDF, a mixture of isopropanol and acetone was used as a solvent to avoid the precipitation of the binder. Three different binder loadings were tested: 10, 20, and 30 wt% of dry binder in the catalyst layer. The amounts of binder added to the ink were chosen according to the catalyst weight in the ink.

The inks were airbrushed on homemade GDLs aiming to reach three different theoretical metal loadings: 0.5, 1.25, and 2 $\text{mg}_{\text{metal}} \text{cm}^{-2}$.

Electrochemical measurements

Cyclic voltammetry was carried out in a cell connected to a Bio-logic MPG2 potentiostat (with EC-lab software version 11.10). A leak-free Ag/AgCl electrode was used as the reference electrode, and the counter electrode was a Pt gauze. The working electrode was carbon cloth on which the catalytic ink was drop-casted. The electrolyte was a 0.5M KHCO_3 solution, saturated with either CO_2 or N_2 before running the experiments. The electrodes, with an exposed area of 1 cm^2 , were cycled at a scan rate of 50 mV/s with N_2 or CO_2 continuously purging the headspace of the cell.

Particle Characterization

X-ray diffraction patterns of the particles supported on carbon were obtained by a Philips X'pert equipped with X'lerator in a 2θ range from 20 to 80 degrees. SEM was performed on an Apreo SEM equipped with an energy dispersive X-ray (EDX) analyzer. X-ray photoelectron spectroscopy (XPS) measurements were performed on the catalyst powders with a Thermo Fisher K-alpha instrument. Differential scan calorimetry was performed on a Mettler Toled DSC 3+ Star^e System at a scan rate of 5 °C per minute between 25°C and 300°C for two times. The composition of the particles and the actual loading on the carbon support were investigated with inductively coupled plasma spectroscopy (ICP).

Results

Flow Cell Electrolysis: Benchmarking InBi Against Single Metals

The performance of the InBi catalyst was benchmarked against In and Bi single metal catalysts by comparing the current efficiency (CE) of the CO₂ electroreduction to formate at 200 mA cm⁻² for 4 hours. The catalyst layer was formulated with 20 wt% PVDF for these control experiments. The loading of catalyst applied to the GDL was chosen so that similar amounts (in mmol) of total metal would be present on the electrode in the case of InBi and the single metal catalysts. This was calculated according to the ICP results of metal loading on carbon and In:Bi ratio (see below) and corresponded to 2 mg_{InBi} cm⁻² for InBi, 1.4 mg_{In} cm⁻² for In and 2.8 mg_{Bi} cm⁻² for Bi. The results are summarized in Figure B.1. The InBi catalyst is the best performing one with a current efficiency of 96%, followed by 93% for In and 74% for Bi.

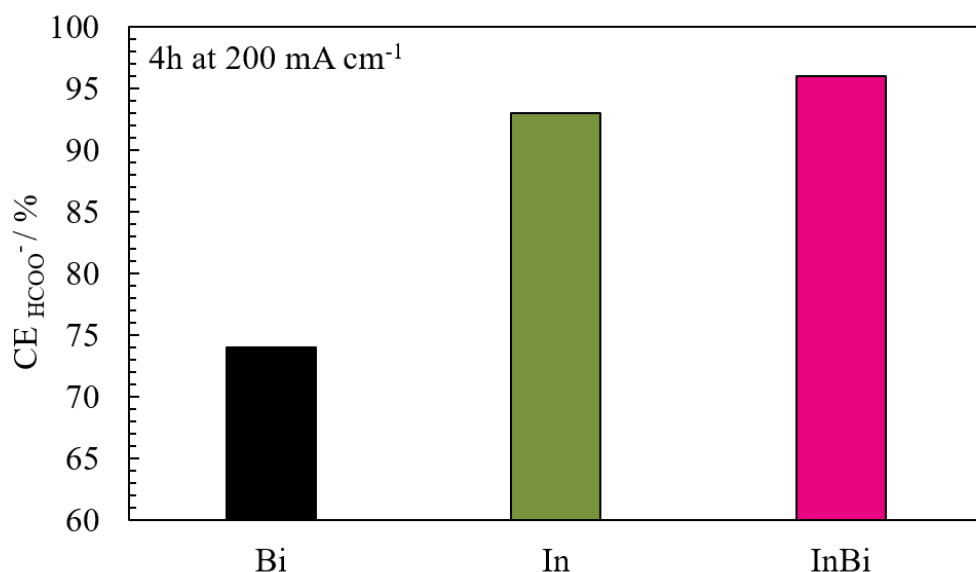


Figure B.1. Comparison of current efficiencies of the single metal catalysts compared to the bimetallic InBi catalyst during 4 hours of operation at 200 mA cm⁻².

Catalyst characterization

The physicochemical characteristics of the catalyst were investigated by means of several techniques.

SEM

The morphology and distribution of the particles on the carbon support were investigated with SEM. A comparison of the single metal catalysts and the InBi catalyst at a similar loading

on carbon as well as a comparison of InBi catalysts at different loadings on carbon are shown in Figures B.2 and B.3.

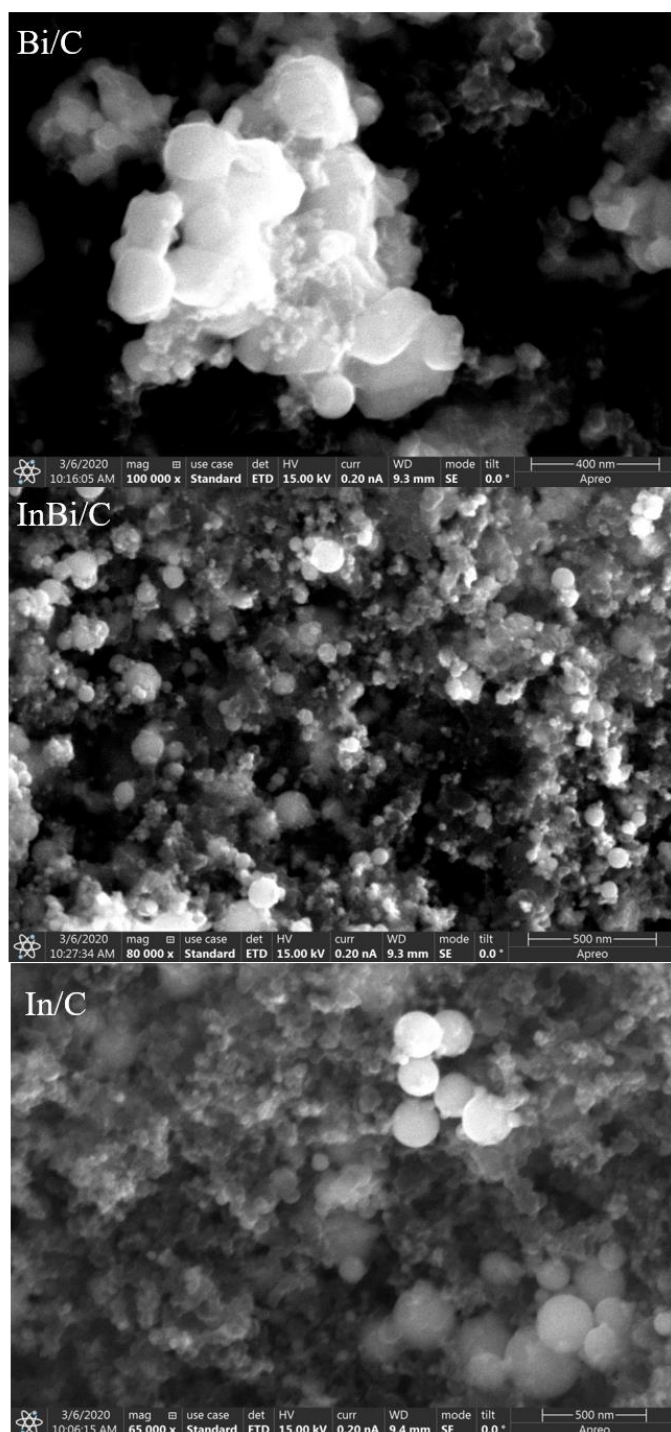


Figure B.2. Sample pictures of the Bi/C, In/C and InBi/C catalysts at the loading employed for the benchmarking and characterization.

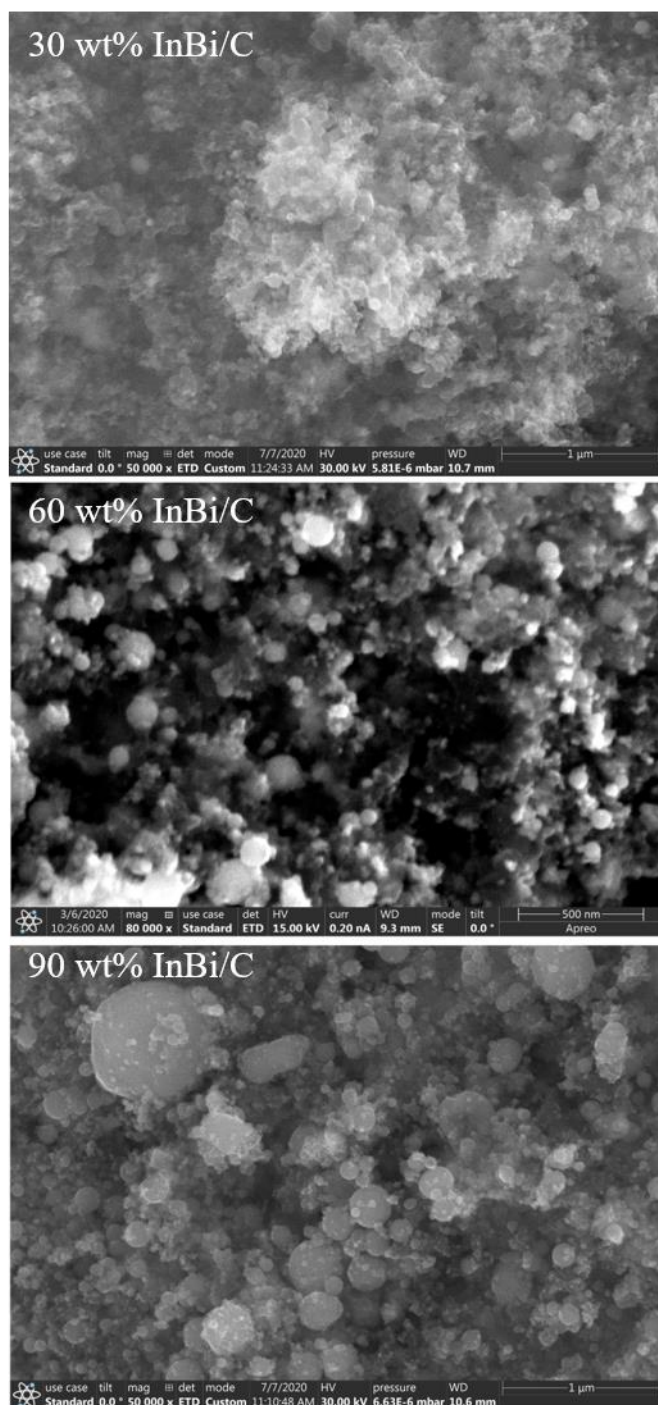


Figure B.3. Sample pictures of the InBi catalyst at the three different amounts of catalyst supported on carbon investigated. It is clear that while at 30 wt% supported the catalyst particles are well dispersed on the carbon support, decreasing the amount of carbon leads to bigger particles. This, however, does not necessarily have a negative impact on performance, as it can be seen from the results of the DOE in the main text.

In Figure B.3, it is possible to see that with the exception of the InBi 30 wt% on carbon, the synthesis yields big particles, in the range of hundreds of nanometers, embedded (rather than supported) on the carbon support due to the big size.

ICP

The elemental composition and loading on carbon were investigated by ICP. The results are shown in Figure B.4.

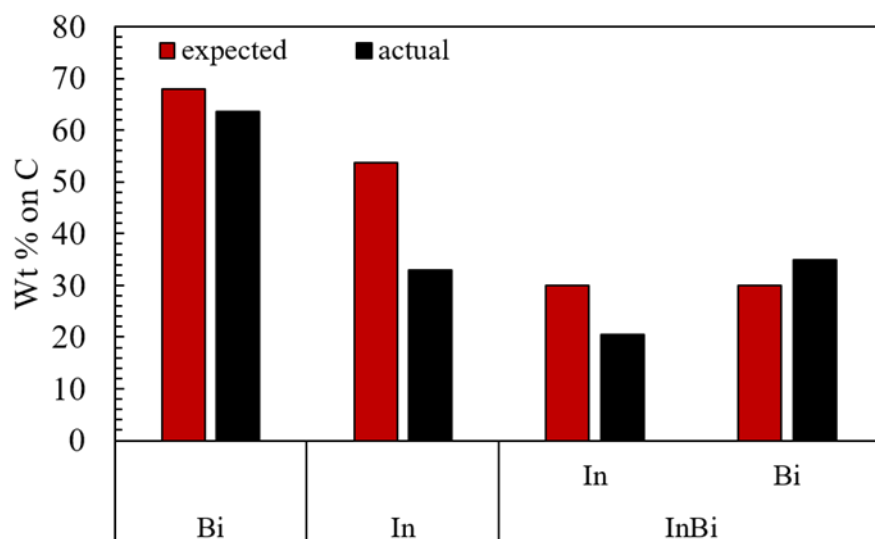


Figure B.4. Expected composition and actual composition from ICP analysis. While Bi concentration is consistent with the expected one, In is lower than expected.

While the amount of Bi on the carbon support is consistent with the expected one, In is lower in both the monometallic and bimetallic samples. During the washing cycles, a brown suspension was observed in the filtrate for the In and InBi catalysts, indicating that some of the metal was leached out. The actual loadings on carbon are 33% for In (53.7% expected), 63.6% for Bi (67.9% expected) and 55.4% for InBi (60% expected) with a weight ratio of In/Bi of 0.6 (expected ratio is 1). This gives a molar composition of approximately 50:50 In/Bi in the bimetallic catalyst (expected 65:35 In/Bi).

DSC

Figure B.5 shows the results of our DSC analysis of the three catalysts. With DSC, we can evaluate the bulk composition and the eventual presence of amorphous phases in our materials, making it a useful complement to such techniques as XPS and XRD. During the first cycle (Figure B.5a), In and Bi show the characteristic melting point of the metallic phases (156°C for In and 271 °C for Bi), while the only significant peak in the InBi sample is the one attributable to metallic Bi. InBi only shows minor peaks related to bimetallic phases at 66°C, 84 °C, and 107°C, which can respectively be attributed to the eutectic phase, the compound BiIn_2 , and the compound BiIn .¹ The melting points are slightly shifted to lower temperatures compared to the expected ones of 72°C, 88°C, and 109°C. This is possibly due to the existence of these compounds in very small crystalline domains, where the melting point depression effect starts to be significant.² A very small peak related to metallic indium (156 °C) is also visible.

During the second cycle (Figure B.5b) the DSC spectra are more flat and easily quantifiable, but, in the case of the InBi sample, all peaks related to InBi intermetallics and In have

disappeared, indicating that exposure to high temperatures can decompose the residual weak In-Bi bonds. The melting point of Bi is shifted to lower temperatures in the InBi catalyst compared to the pure Bi catalyst, and as In is not soluble in the Bi matrix, this is probably due to the existence of metallic Bi in small crystalline domains, rather than to the formation of solid solutions

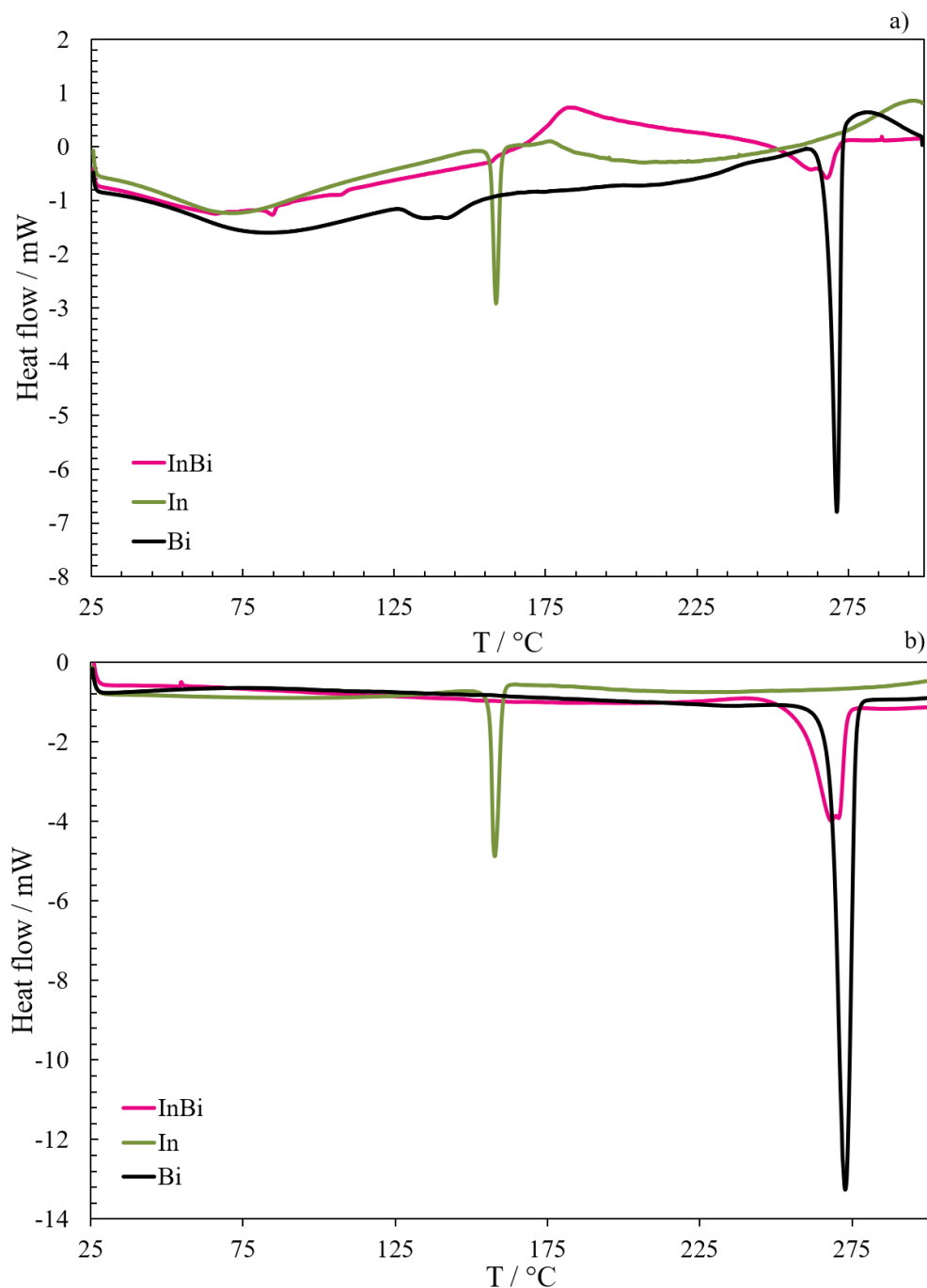


Figure B.5. Differential scanning calorimetry of pure In, pure Bi, and InBi particles supported on carbon. a) first cycle and b) second cycle.

XPS

The results of the XPS analysis are shown in Figure B.6.

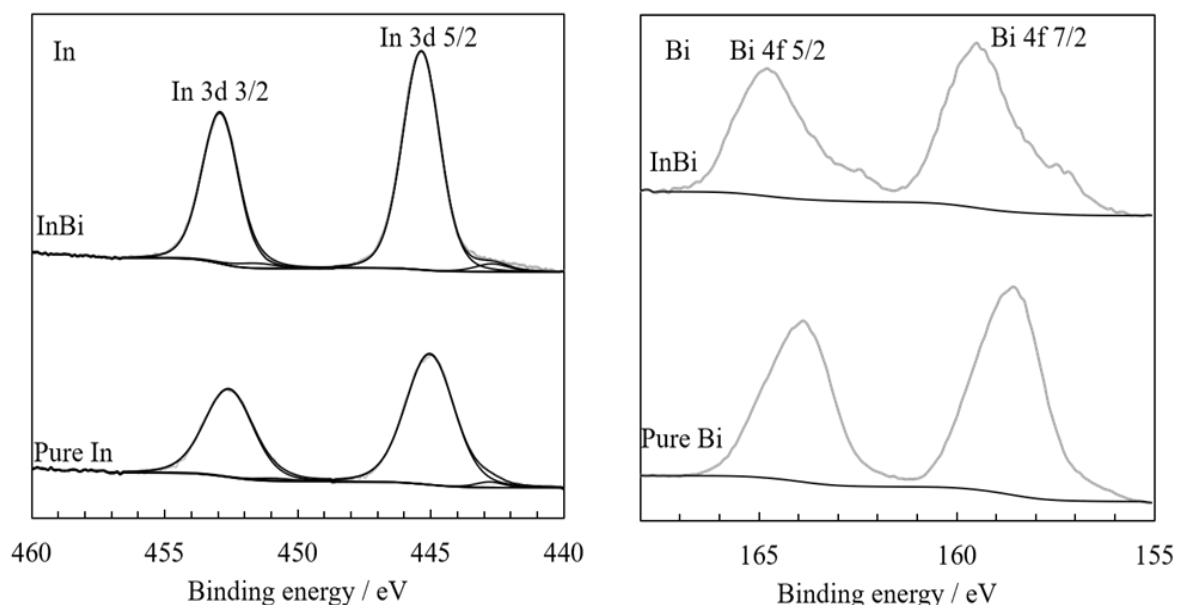


Figure B.6. XPS of In (left) and Bi (right) in pure metal particles (bottom line) and InBi particles (upper line). While the deconvolution into In³⁺ and In(0) is shown, the raw spectra are shown in the case of Bi, since only the peak area could be used for the atomic concentration calculations.

The species In³⁺ makes up 98-99% of observed In in the first layers of our In and InBi particles. XPS atomic ratios in InBi particles are 80.5% In and 19.5% Bi, indicating that the first few nanometers of the particles are indium-enriched. The In peaks in the InBi particles are shifted positively of 0.2 eV compared to those in the pure In particles, possibly due to the electron-withdrawing effect of the more electronegative Bi atoms, which in turn would increase the oxidizability of In.

XRD

The X-ray diffraction patterns of the three materials are shown in Figure B.7.

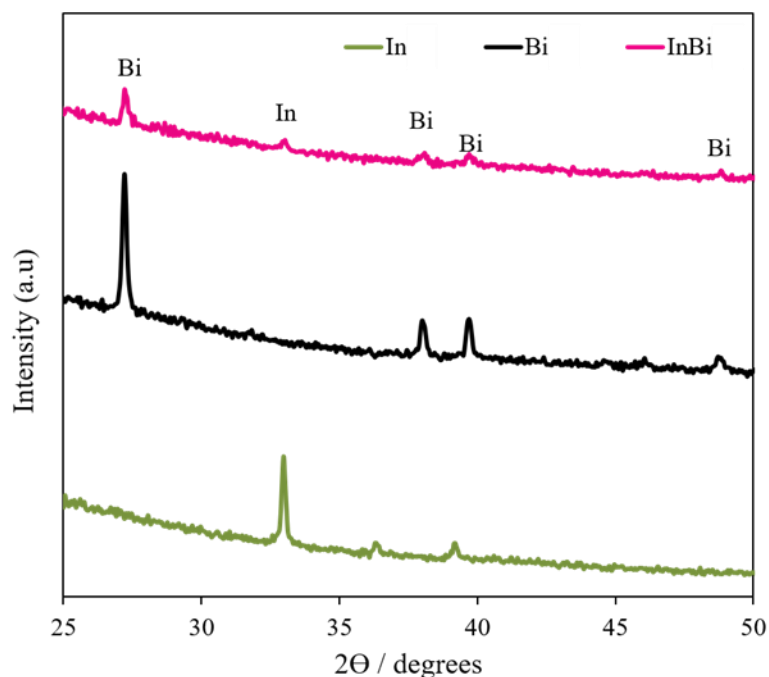


Figure B.7. X-ray diffraction patterns of the three investigated catalysts.

Only reflections relative to the elements in their metallic state can be seen in the diffraction patterns. A small reflection for metallic In is seen in the InBi particles, while all the other peaks can be assigned to metallic Bi, with no reflections assignable to the intermetallic phases.

Electrochemical measurements

A three-electrode setup was used to characterize our catalysts by cyclic voltammetry. The three catalysts were cycled several times in N_2 and CO_2 saturated 0.5M $KHCO_3$ at 50 mV/s. Figure B.8 shows the voltammograms while the comparison of the voltammetries of the three catalysts in N_2 and CO_2 saturated electrolyte is shown in Figure B.9.

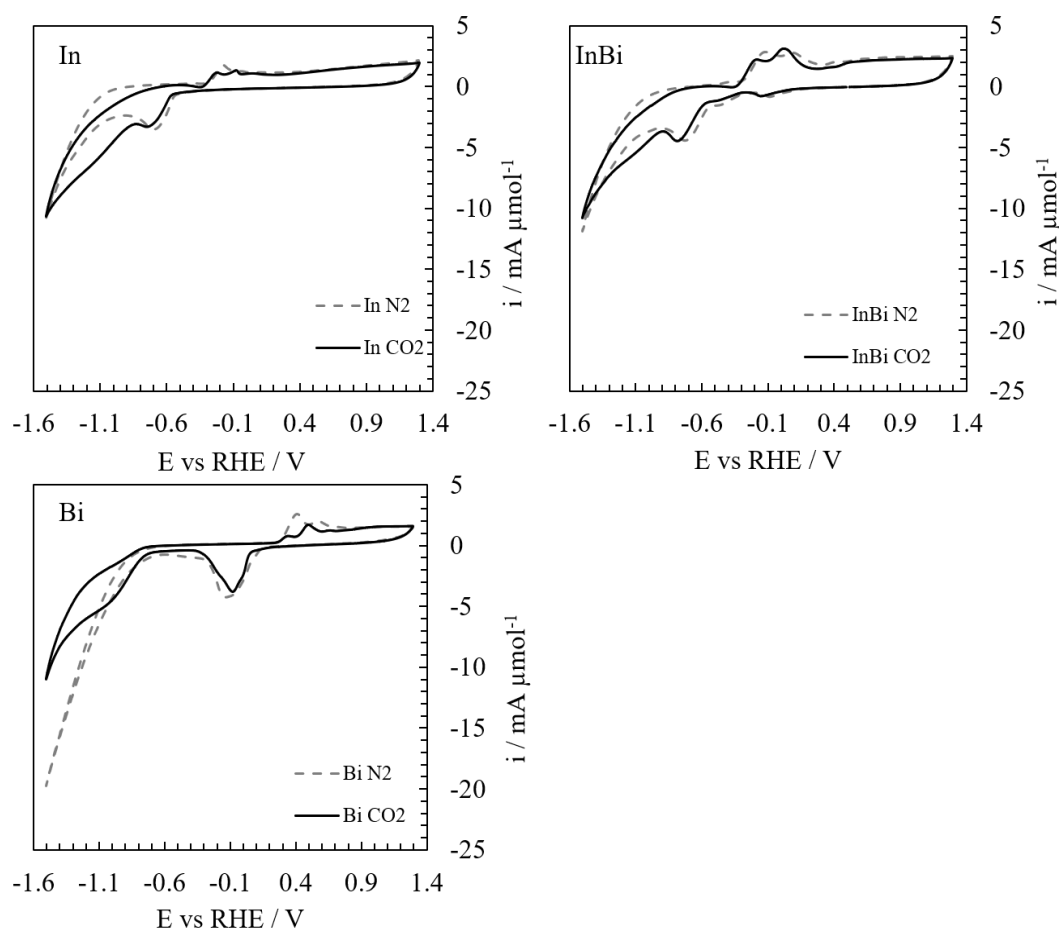


Figure B.8. Cyclic voltammograms of In, Bi and InBi in CO₂ saturated 0.5M KHCO₃ (solid black lines) and N₂ saturated 0.5M KHCO₃ (dashed gray lines).

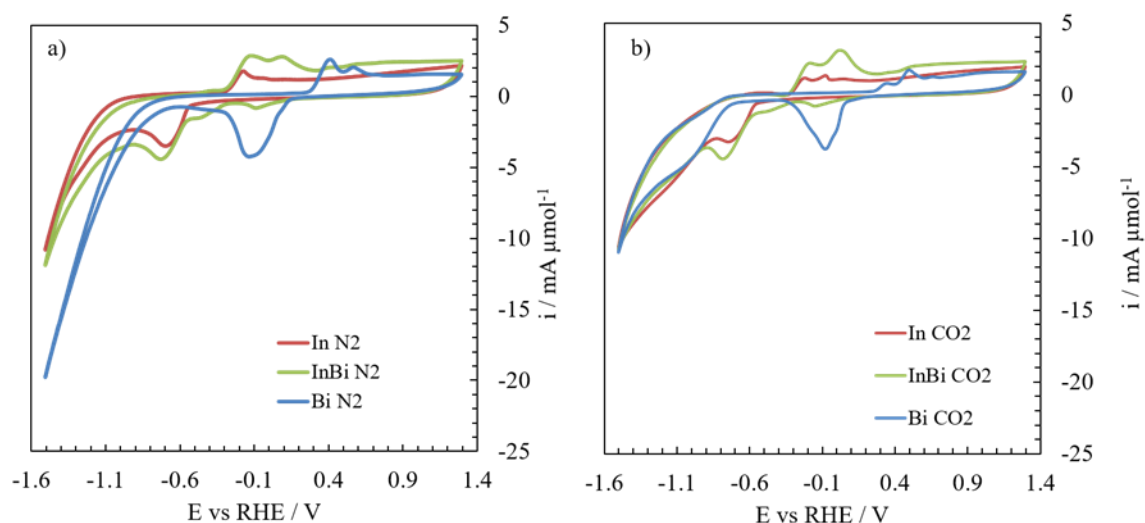


Figure B.9. Stable CVs of the three catalysts in N₂ and CO₂ saturated 0.5M KHCO₃. Bi has a lower hydrogen evolution overpotential than In. The InBi catalyst behaves like pure In in the HER region. The current density is given in mA μmol⁻¹. The indium reduction peaks around -0.7V vs RHE in In and InBi are in a similar range, suggesting that the surface areas of the two catalysts are similar.

Discussion

Catalyst Physicochemical Characterization

The enhanced performance of the InBi catalyst, as shown in Figure B.1, is in good agreement with the patented results³, which show that, in bulk metal electrodes, InBi is slightly more selective than an anodized In electrode (80% vs. 76% current efficiency) and significantly more selective than non-anodized In (64% current efficiency). In our case, In performs only slightly worse than the InBi catalyst. This may be caused by the fact that the particulate nature of the catalyst enhances the surface exposed, increasing the amount of oxide. The importance of metastable (hydr)oxides for the selectivity of In catalysts for CO₂ reduction to formate has been argued in previous studies.^{4,5} The overall enhancement of selectivity is probably attributable to the more favorable mass transport properties of the GDE configuration.

To understand the reasons behind this increase in selectivity, we characterized the catalyst by means of several techniques. In Figure B.5, we show our DSC analysis of the three catalysts. It is noticeable that, while in the single metal catalysts the melting of the pure metals is evident (peak at 156 °C for In and at 271 °C for Bi), in the InBi catalyst, only minor amounts of intermetallic compounds and metallic In are visible, and only the melting of metallic Bi is present, despite the ICP analysis showing an atomic In/Bi ratio of 50:50. The oxides of In and Bi are not visible in the investigated temperature range since their melting points are higher than 300 °C, so it is likely that the missing In peaks in the InBi particles are caused by a high fraction of this metal being in the oxidized state. By integrating the peak areas in Figure B.5 and knowing the heats of fusion (3.27 kJ mol⁻¹ for In and 11.3 kJ mol⁻¹ for Bi) and the total amounts of metal in the samples, we can estimate the amount of metal present in the metallic state, assuming that the remaining part will be in an oxidized state. The intermetallic compounds, not knowing the exact heats of fusion, are impossible to quantify, but the total amount of energy exchanged during their fusion is very small, indicating that only a minor amount of these compounds is present. During the first cycle, in the InBi sample, only 4% of the In is present in the metallic state. During the second cycle, the amount of metallic Bi is 60.9% in the pure Bi particles and 56.9% in the InBi particles. The amount of metallic In is 54.5% in the pure In particles and 0% in the InBi particles, indicating that all the In present is in the oxide form. Therefore, it seems that the presence of Bi can enhance the oxidizability of In rather than forming intermetallic compounds in our particles, at least after air exposure. This can be explained by the different electronegativity of In and Bi (1.78 vs. 2.02). Since Bi is a more noble metal, it could be favoring the oxidation of In in a galvanic corrosion process.

Our XPS analysis (Fig S14) shows that the surface of both In and InBi particles is predominantly oxidized and that the first layers in the InBi particles are enriched in In, with an atomic In/Bi ratio of 80.5:19.5, compared to 50:50 indicated by ICP. The behavior of the Bi XPS spectrum is somewhat more complex. The Bi peaks in the InBi catalyst are broadened and shifted to higher binding energy compared to the pure Bi catalyst, which would be counterintuitive if we expect the Bi atoms to simply bear the partial negative charge drawn

from the In. Such an effect could be caused, for example, by the dispersion of Bi in the In oxide matrix in the form of single atoms or small clusters, which would add layers of complexity to the overall photoemission behavior, compared to the bulk Bi to which it is compared. Similar shifts in XPS spectra with decreasing particle size have been observed before.⁵ As the Bi results may be difficult to deconvolute and interpret correctly, its XPS spectra were used only for the calculation of the atomic ratios.

In our cyclic voltammetry analysis (Figure B.8), it is easily noticeable that qualitatively speaking, the cyclic voltammogram of the InBi catalyst is very similar to the one of In. The redox features of Bi, and especially the reduction peak around -0.1V versus RHE, which is a prominent feature in the voltammetry of pure Bi, are barely noticeable. While the XPS shows that 80.5% of the metal atoms in the first few nanometers are indium atoms, with the cyclic voltammetry, we can see that the electroactive surface is likely even more enriched in In. Therefore, during CO₂ reduction, the catalytic surface is probably composed of a large amount of In, with a small number of Bi inclusions. Note that the current densities reported in the voltammograms are normalized by the amount of μmol s on the surface of the electrode. Since the currents registered for the redox peaks of In on In and InBi particles are similar, the particle size distribution of the two catalysts should be in a similar range, with the InBi particles possibly having a slightly larger surface area. This is clearer when comparing the In reduction peak around -0.7V versus RHE in Figure B.9 (for the In and InBi catalyst).

Aside from the features related to the metallic surface of the electrode, it is interesting to compare the behavior of the catalysts in the cathodic branch where hydrogen evolution and CO₂ reduction are expected to happen. The overlaid cyclic voltammeteries of the three catalysts in N₂ and CO₂ saturated electrolyte are shown in Figure B.9. It is clear that the behavior of the InBi catalyst in this cathodic region is very similar to the one of pure In, suggesting that In itself is the main contributor to the CO₂ reduction (or hydrogen evolution) behavior, while Bi seems to slightly enhance its performance in the case of CO₂ reduction.

While it is possible that during the synthesis of the particles some intermetallic compounds may be formed in accordance with the phase diagram of the In-Bi system,¹ it appears that exposure to the atmosphere will cause the In fraction of the particles to segregate on the surface. This is due to the extremely weak bonds formed between In and Bi, as shown by the only slightly exothermic enthalpies of formation of their intermetallic compounds,⁶ and by the larger tendency of In to be oxidized ($\Delta H_f^0 \text{Bi}_2\text{O}_3 = -573.9 \text{ kJ mol}^{-1}$ versus $\Delta H_f^0 \text{In}_2\text{O}_3 = -925.8 \text{ kJ mol}^{-1}$). Also, the percentage of In in its oxidized state is significantly higher in the InBi particles compared to the pure In particles, not only on the surface but also in the bulk, as shown by DSC. Interestingly, these oxides appear to be entirely amorphous, as they do not show in our XRD analysis (Figure B.7). The cyclic voltammetry of InBi shows predominantly features related to In, both in the metal redox peaks and in the cathodic branch, confirming that the electrochemically active surface area is predominantly composed of this element. At this stage, we cannot entirely exclude that the difference in selectivity between In and InBi can be caused by small differences in surface area. However, with the evidence presented above, and knowing that a similarly enhanced selectivity is observed also in bulk electrodes,³ we would like to

propose that the main active phase of our bimetallic catalyst is In, and the effect of the presence of Bi is similar to an anodization process, which has been shown in the literature to improve the selectivity of In catalysts.⁵ Moreover, it is possible that the electron-withdrawing effect of Bi on In could partially increase the stability of metastable In oxides, enhancing their presence on the surface and thereby slightly increasing the selectivity of this catalyst compared to a pure In one.

Conclusion

In conclusion, we have shown that InBi catalysts prepared with our method are slightly more selective than In catalysts and markedly more selective than Bi catalysts prepared with the same method. This effect seems to be due to the fact that Bi, in a process that may be similar to galvanic corrosion, increases the fraction of In in its oxidized state, a process that induces the segregation of this metal to the surface of the particles. The particles with a surface enriched in indium oxides, in turn, would increase the selectivity since this phase has been shown to be the most active for CO₂ reduction to formate.

References

- (1) Okamoto, H.; Schlesinger, M. E.; Mueller, E. M. Bi (Bismuth) Binary Alloy Phase Diagrams. *Alloy Phase Diagrams*. ASM International April 2016, p 0, DOI 10.31399/asm.hb.v03.a0006150.
- (2) Allen, G. L.; Bayles, R. A.; Gile, W. W.; Jesser, W. A. Small Particle Melting of Pure Metals. *Thin Solid Films* **1986**, *144* (2), 297–308, DOI 10.1016/0040-6090(86)90422-0.
- (3) Parajuli, R.; Ansovini, D.; Philips, M. F.; Schouten, K. J. P. Catalyst System for Catalyzed Electrochemical Reactions and Preparation Thereof, Applications and Uses Thereof. WO2019141827A1.
- (4) Pander, J. E.; Baruch, M. F.; Bocarsly, A. B. Probing the Mechanism of Aqueous CO₂ Reduction on Post-Transition-Metal Electrodes Using ATR-IR Spectroelectrochemistry. *ACS Catal.* **2016**, *6* (11), 7824–7833, DOI 10.1021/acscatal.6b01879.
- (5) Detweiler, Z. M.; White, J. L.; Bernasek, S. L.; Bocarsly, A. B. Anodized Indium Metal Electrodes for Enhanced Carbon Dioxide Reduction in Aqueous Electrolyte. *Langmuir* **2014**, *30* (25), 7593–7600, DOI 10.1021/la501245p.
- (6) Kulikova, T.; Mayorova, A.; Shubin, A.; Bykov, V.; Shunyaev, K. Bismuth-Indium System: Thermodynamic Properties of Liquid Alloys. *Kov. Mater.* **2015**, *53* (3), 133–137, DOI 10.4149/km-2015-3-133.

Appendix C

Supporting Information for Chapter 4

The Gas Diffusion Layer

A schematic of the gas diffusion layers produced in this study is shown in Figure C.1 while a picture of a synthesized GDL 2 is shown in Figure C.2.

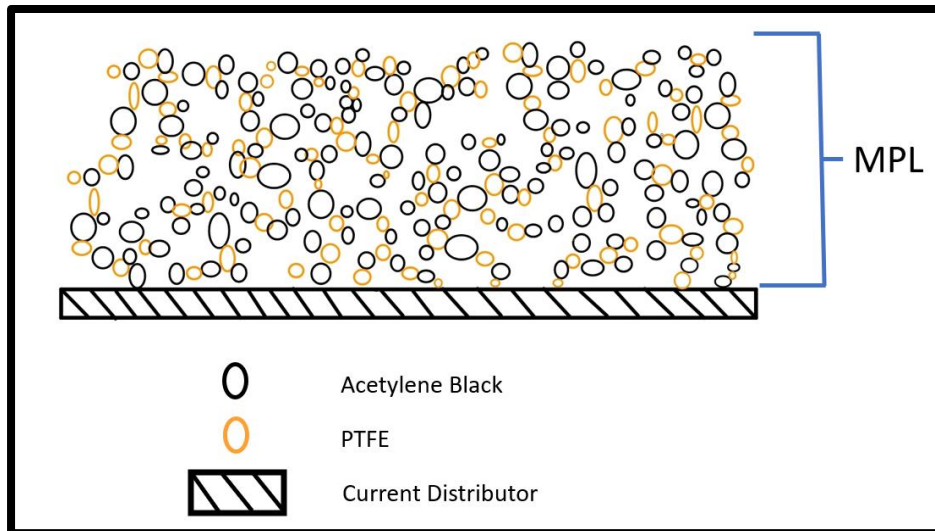


Figure C.1. Schematic of the GDLs produced for this study. MPL is microporous layer.

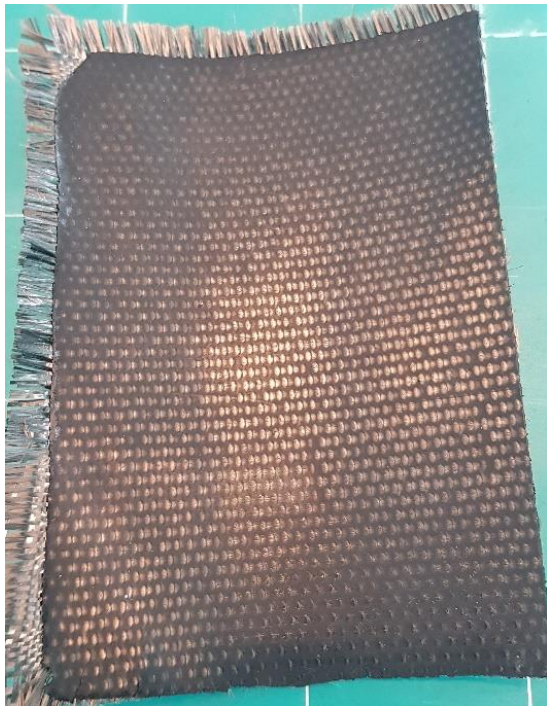


Figure C.2. Picture of a GDL 2 produced for this study. GDL 1 and 2 look virtually identical from a macroscopic scale. The microporous layer (MPL) is facing up and a graphitized carbon backing is used as a current distributor

Materials and Chemicals

Table C.1. Chemical and Material Suppliers Used in Chapter 4

Chemical or Material	Supplier
InCl ₃ 99.999%	Aldrich
Trisodium citrate dihydrate >99%	Aldrich
KHCO ₃ 99.5%	Acros Organics
H ₂ SO ₄ 95% solution in water	Acros Organics
NaBH ₄ 98+%	Acros Organics
Triethylene glycol (TEG) 99%	Alfa Aesar
Bi(NO ₃) ₃ ·5H ₂ O 98%	Alfa Aesar
Vulcan carbon (VXC72R)	Cabot Corp
60% Teflon treated carbon cloth	Fuel Cell Store
Nafion™ 5 wt% solution	Fuel Cell Store
Kynar flex 2801 (PVDF)	Arkema

Repeat Run Analysis

Figures C.3-C.5 show the comparison of the original and repeat runs performed in the DOE. In particular, runs 5, 7 and 10 were repeated to assess repeatability. The maximum difference between the repeat and original run was observed for run 10 at 5.5% difference as shown in Figure C.6. This is within the expected error of the quantification and sampling method. The means for these runs are used for the overall DOE analysis.

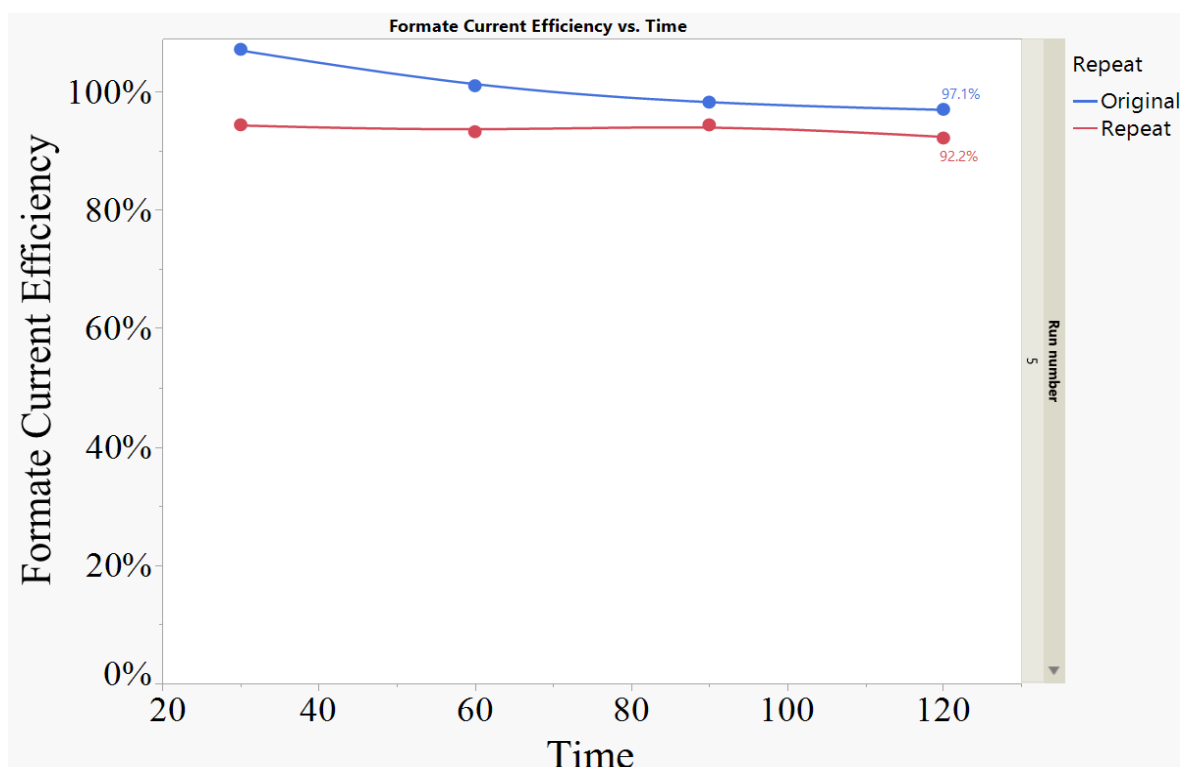


Figure C.3. Experimental run 5 original compared to repeat

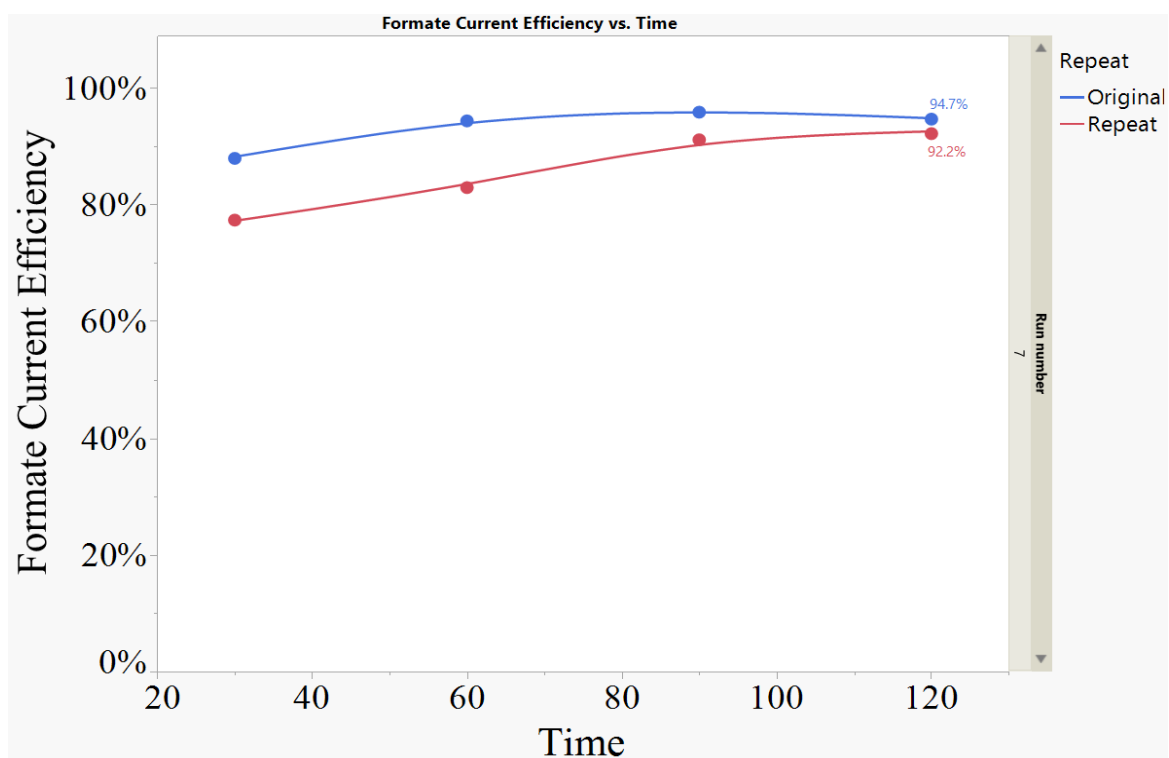


Figure C.4. Experimental run 7 original compared to repeat

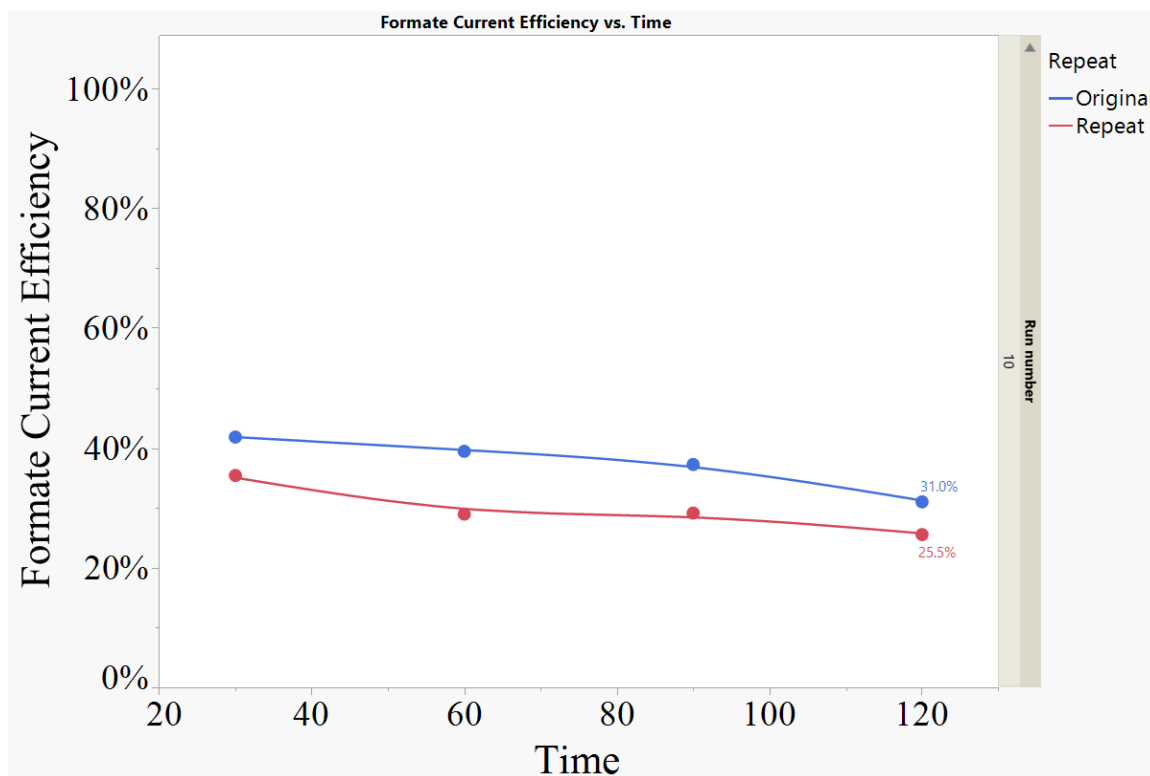
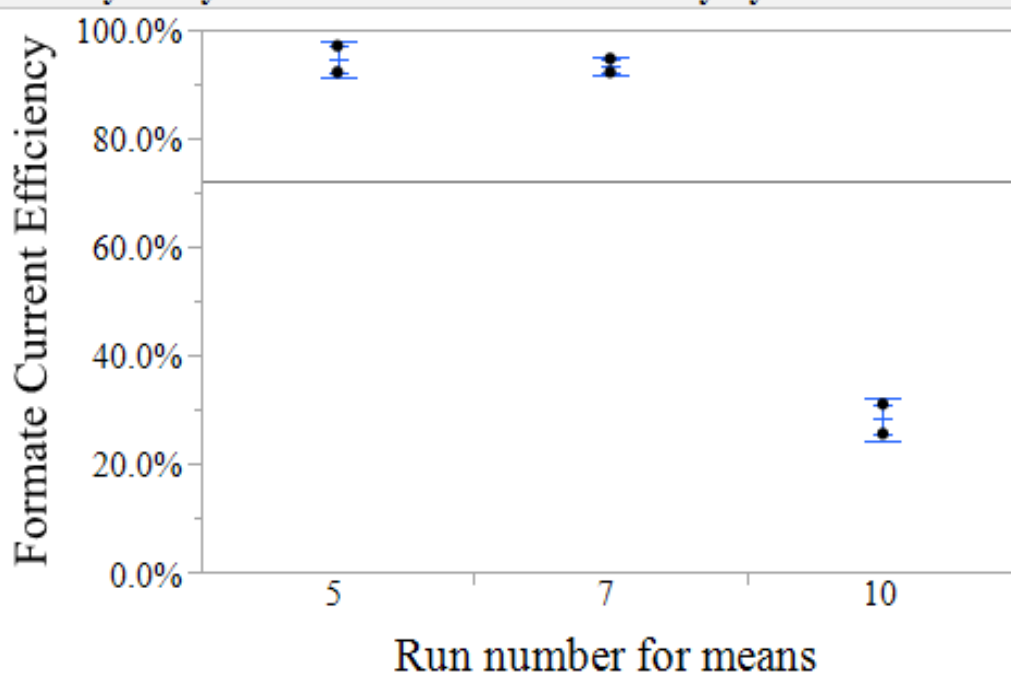


Figure C.5. Experimental run 10 original compared to repeat

Oneway Analysis of Formate Current Efficiency By Run number for means**Means and Std Deviations**

Level	Number	Mean	Std Dev	Std Err Mean	Lower 95%	Upper 95%
5	2	0.946	0.0343	0.0242	6.38e-1	1.25e+0
7	2	0.934	0.0175	0.0124	7.77e-1	1.09e+0
10	2	0.282	0.0387	0.0273	-6.50e-2	6.30e-1

Figure C.6. Repeat experimental runs means and standard deviations.

Salt Accumulation Scale











Description	Both Sides Look Like New	Catalyst Layer starting to look different and little to no salt on back	Distinct bumps forming in catalyst layer and little to no salt on back	Distinct bumps forming in catalyst layer and salt on back	Salt Formed a distinct pocket in the catalyst layer and completely covered the back
Front Photo					
Back Photo					
Rating	1 (Run5)	2 (Run23)	3 (Run22)	4 (Run3)	5 (Run26)

Figure C.7. Salt Accumulation Rating Number System

Model Selection

Figures C.8-C.13 show JMP screenshots of model terms for the models considered for selection. The model terms are listed in order of statistical significance under the Sorted Parameter Estimates. The null hypothesis of the t-test performed for each estimate is that the parameter's coefficient is zero. Therefore, when the p-value is low, the null hypothesis is rejected and the model term is shown to have statistical significance. Furthermore, the lower the p-value, the higher the probability that the parameter is statistically significant.

Formate Current Efficiency Models

The model generated using BIC as a stopping rule is used because it resulted in a better fitting model with more significant factors/interactions identified at 99% confidence ($\alpha = 0.01$). This was done so that no factor or interaction is overlooked.

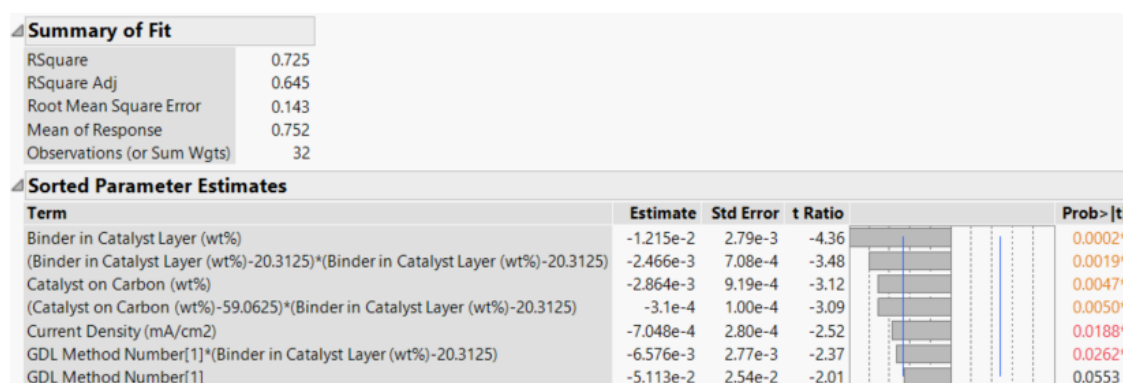


Figure C.8. AIC Model Summary and Sorted Parameter Estimates for the current efficiency toward formate

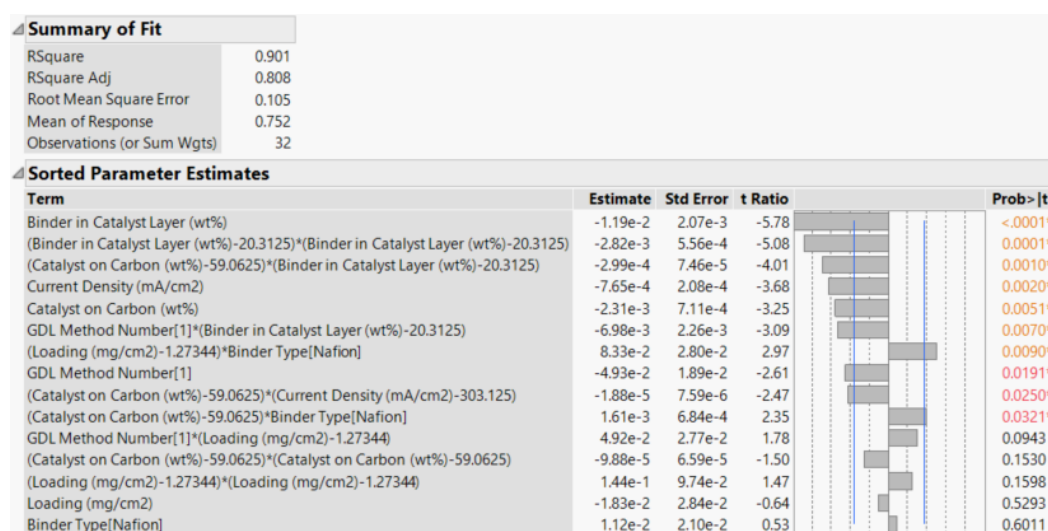


Figure C.9. BIC Model Summary and Sorted Parameter Estimates for the current efficiency toward formate

Cell Potential Models

Both AIC and BIC stopping rules resulted in the exact same model for the cell potential. However, an exceptional R^2 was maintained even when reducing the model to only the top three terms. Figure C.10 shows the model generated using the AIC or BIC as the stopping rule while Figure C.11 shows the model generated by only keeping the top three terms.

Summary of Fit					
RSquare	0.939				
RSquare Adj	0.918				
Root Mean Square Error	0.426				
Mean of Response	8.231				
Observations (or Sum Wgts)	32				
Sorted Parameter Estimates					
Term	Estimate	Std Error	t Ratio		Prob> t
Current Density (mA/cm2)	1.37e-2	8.39e-4	16.31		<.0001*
GDL Method Number[1]*(Current Density (mA/cm2)-303.125)	3.23e-3	8.25e-4	3.92		0.0007*
GDL Method Number[1]	2.59e-1	7.58e-2	3.42		0.0024*
GDL Method Number[1]*(Catalyst on Carbon (wt%)-59.0625)	8.11e-3	2.75e-3	2.95		0.0072*
(Current Density (mA/cm2)-303.125)*Binder Type[Nafion]	-2.40e-3	8.29e-4	-2.90		0.0080*
(Current Density (mA/cm2)-303.125)*(Current Density (mA/cm2)-303.125)	-4.66e-5	2.16e-5	-2.16		0.0415*
Binder Type[Nafion]	1.22e-2	7.82e-2	0.16		0.8776
Catalyst on Carbon (wt%)	3.51e-4	2.75e-3	0.13		0.8994

Figure C.10. AIC or BIC Model Summary and Sorted Parameter Estimates for the cell potential

Summary of Fit					
RSquare	0.881				
RSquare Adj	0.868				
Root Mean Square Error	0.540				
Mean of Response	8.231				
Observations (or Sum Wgts)	32				
Sorted Parameter Estimates					
Term	Estimate	Std Error	t Ratio		Prob> t
Current Density (mA/cm2)	1.43e-2	1.04e-3	13.73		<.0001*
GDL Method Number[1]*(Current Density (mA/cm2)-303.125)	3.21e-3	1.04e-3	3.08		0.0046*
GDL Method Number[1]	2.80e-1	9.55e-2	2.93		0.0067*

Figure C.11. Model Summary and Sorted Parameter Estimates for the cell potential with only the top three terms

Salt Accumulation Models

The AIC stopping rule resulted in a two-term model (Figure C.12) with a poor fit so the BIC model (Figure C.13) was chosen.

Response Salt Formation Number					
Whole Model					
Summary of Fit					
RSquare	0.168				
RSquare Adj	0.111				
Root Mean Square Error	1.196				
Mean of Response	2.688				
Observations (or Sum Wgts)	32				
Sorted Parameter Estimates					
Term	Estimate	Std Error	t Ratio		Prob> t
(Binder in Catalyst Layer (wt%)-20.3125)*(Binder in Catalyst Layer (wt%)-20.3125)	1.28e-2	5.82e-3	2.20		0.0360*
Binder in Catalyst Layer (wt%)	3.07e-2	2.33e-2	1.32		0.1978

Figure C.12. AIC Model Summary and Sorted Parameter Estimates for the salt accumulation number

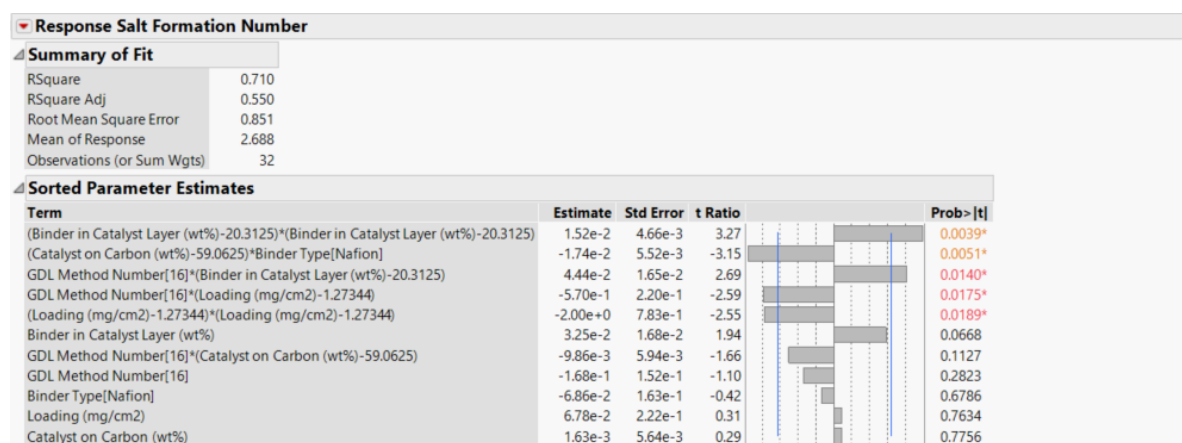


Figure C.13. BIC Model Summary and Sorted Parameter Estimates for the salt accumulation number

Model equations and profilers

Figures C.14-C.16 display a snapshot of the model profilers and equations for selected models. The trend for each factor term in the model can be seen in these figures however these curves can change if there is a two-factor interaction in the model, or can be shifted as other factors are changed.

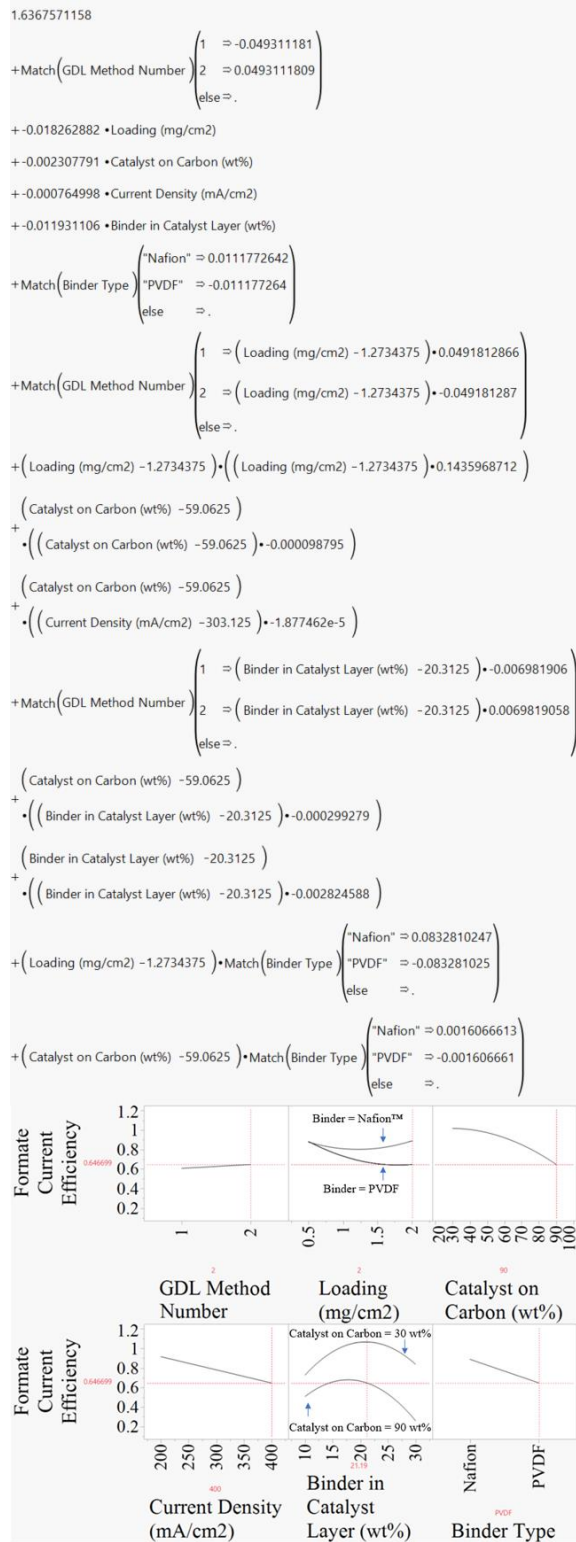


Figure C.14. Model equation and profiler for the formate current efficiency. Interaction trends are shown for the binder amount in the catalyst layer and catalyst supported on carbon as well as the loading of catalyst interaction with binder type.

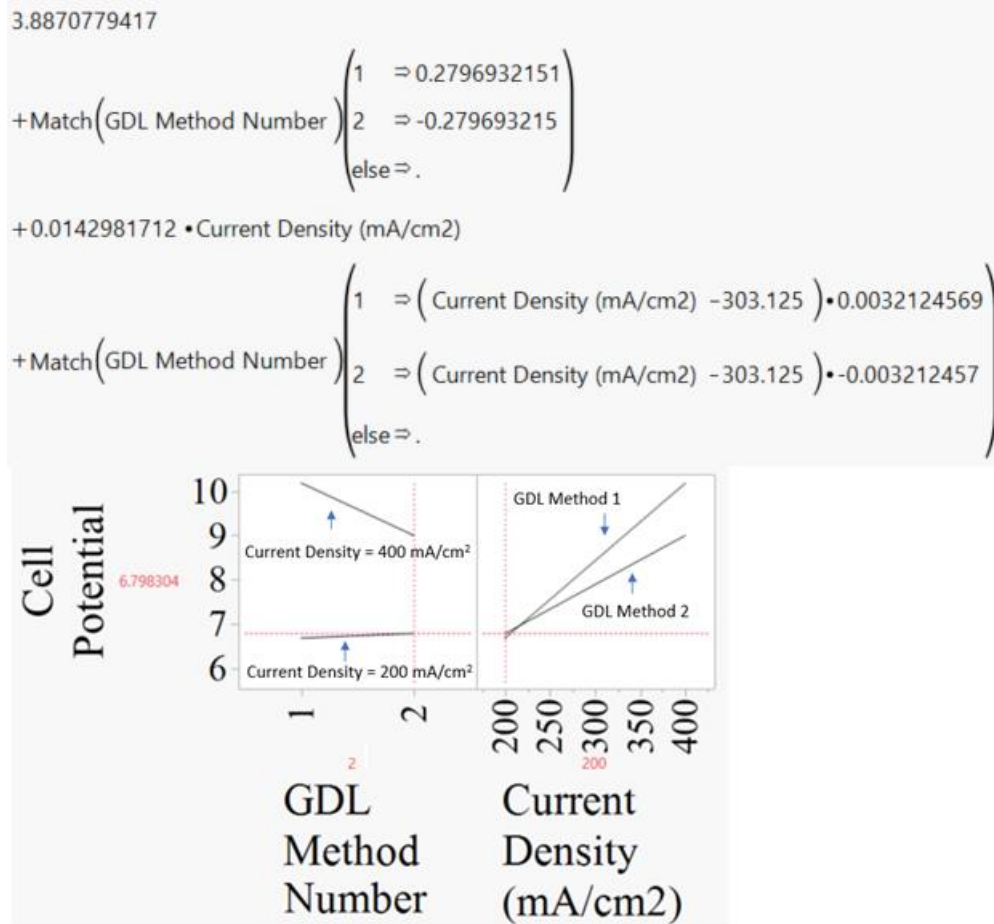


Figure C.15. Model equation and profiler for the cell potential

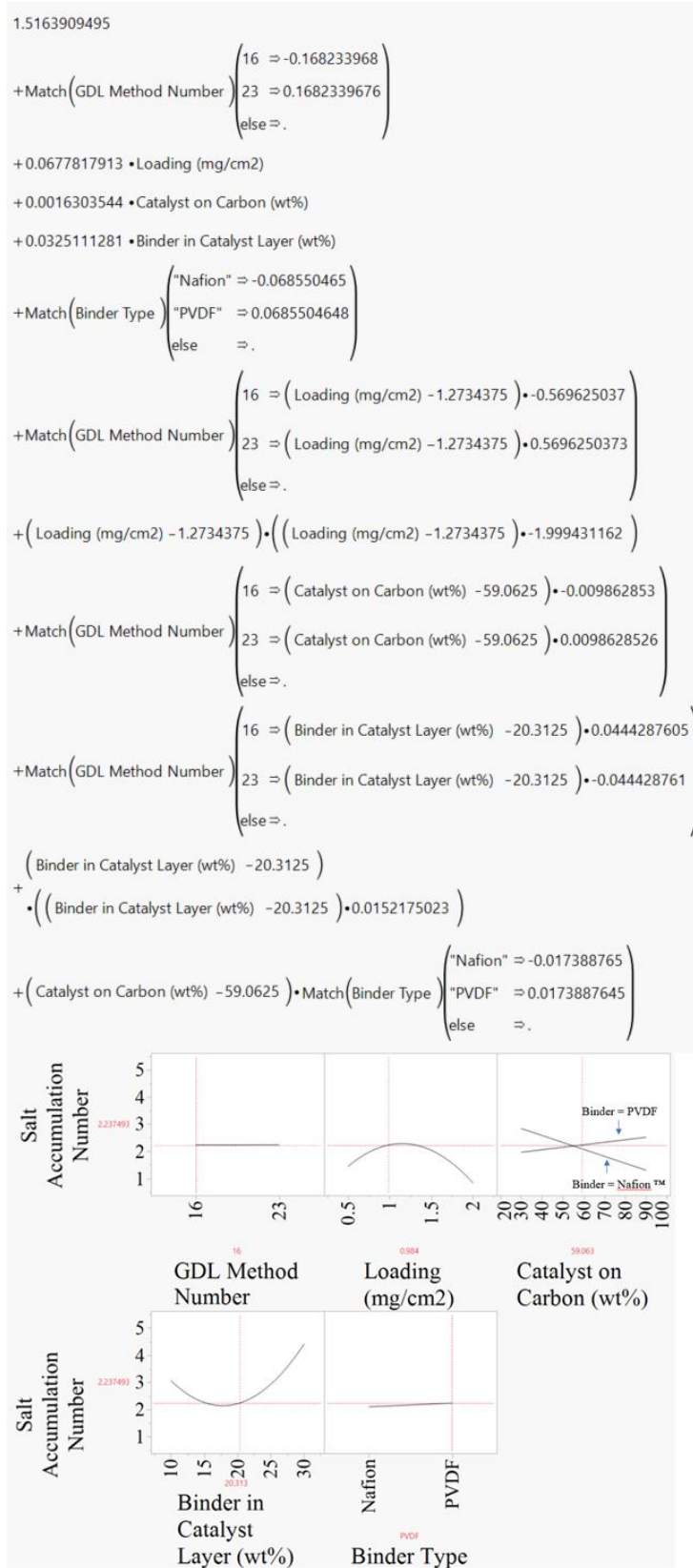


Figure C.16. Model profiler for the salt accumulation number

Appendix D

Supporting Information for Chapter 5

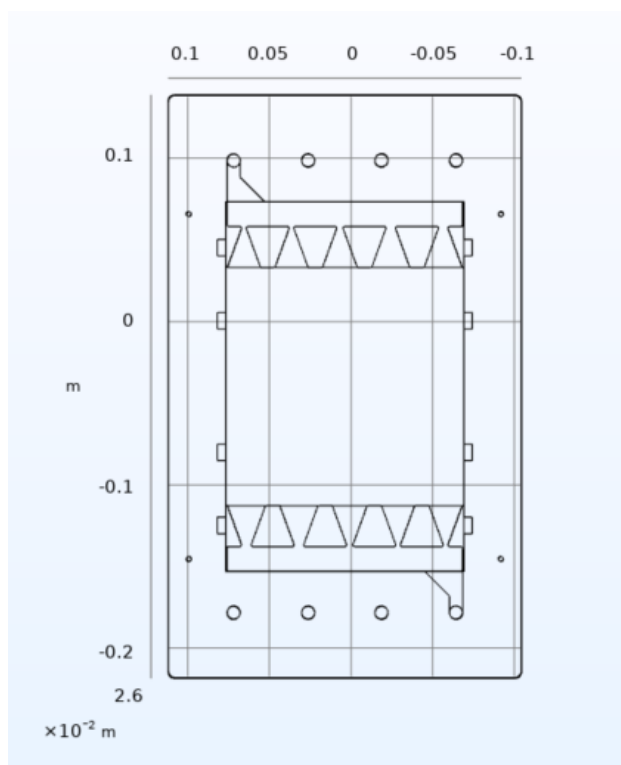


Figure D.1. First simulated design configuration for modeling flow velocity profiles. The flow inlet is on the bottom and the flow outlet is on top

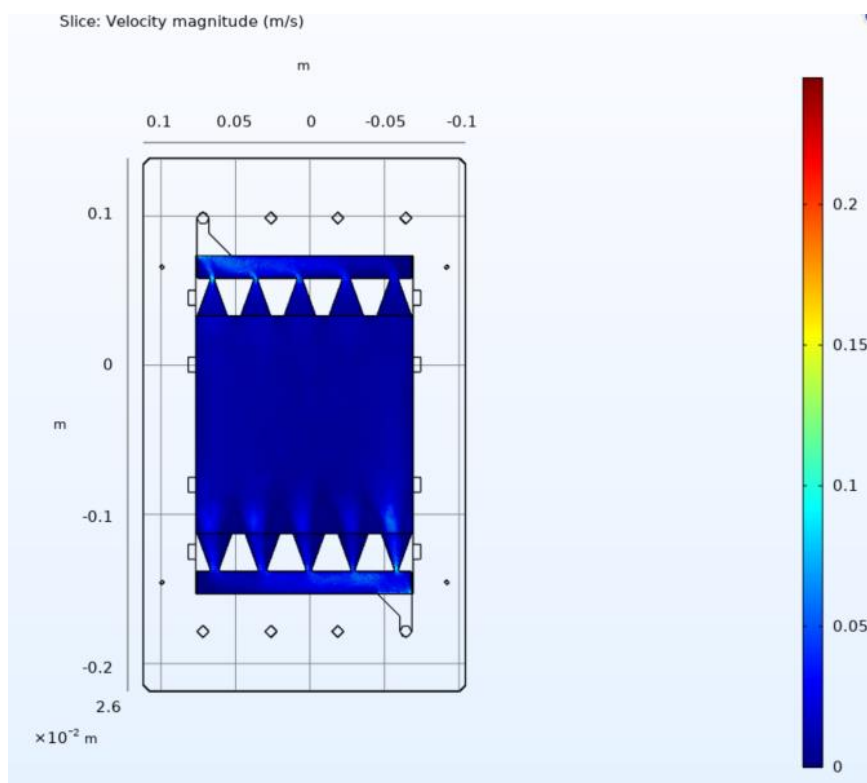


Figure D.2. Simulated fluid velocity profile for the first design configuration near the GDE or membrane surface. The flow inlet is on the bottom and the flow outlet is on top

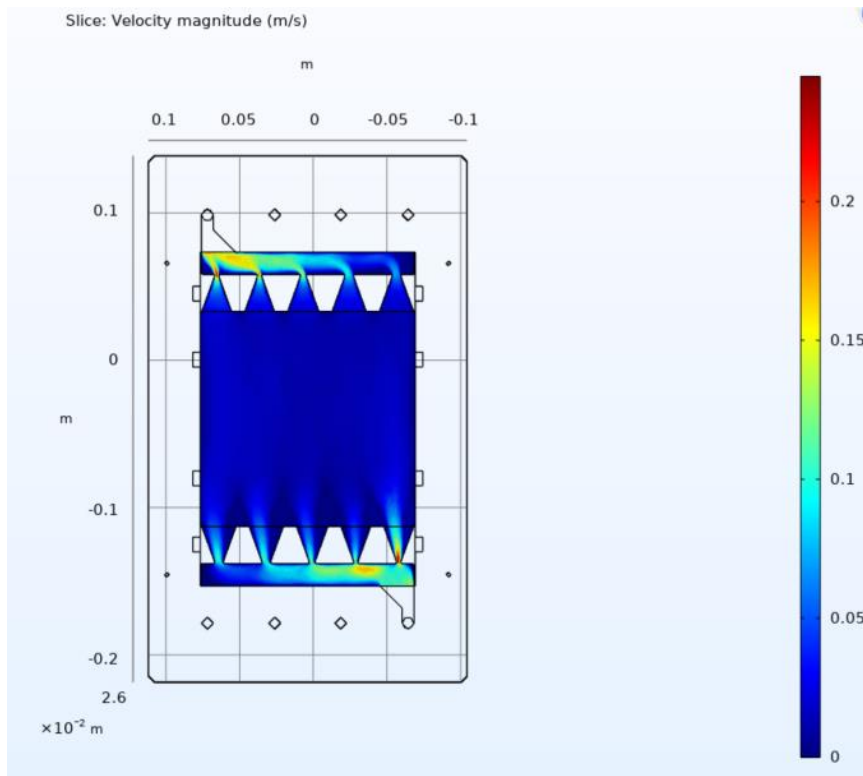


Figure D.3. Simulated fluid velocity profile for the first design configuration at the center of the flow distribution plate. The flow inlet is on the bottom and the flow outlet is on top

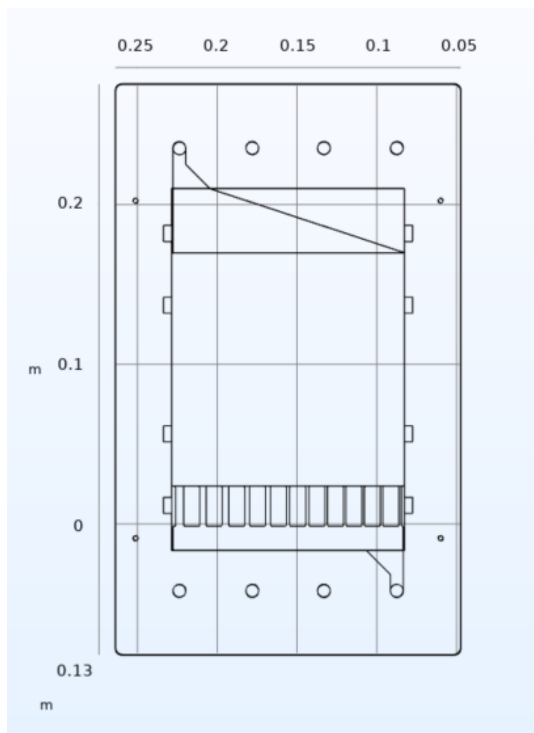


Figure D.4. Second simulated design configuration for modeling flow velocity profiles. The flow inlet is on the bottom and the flow outlet is on top

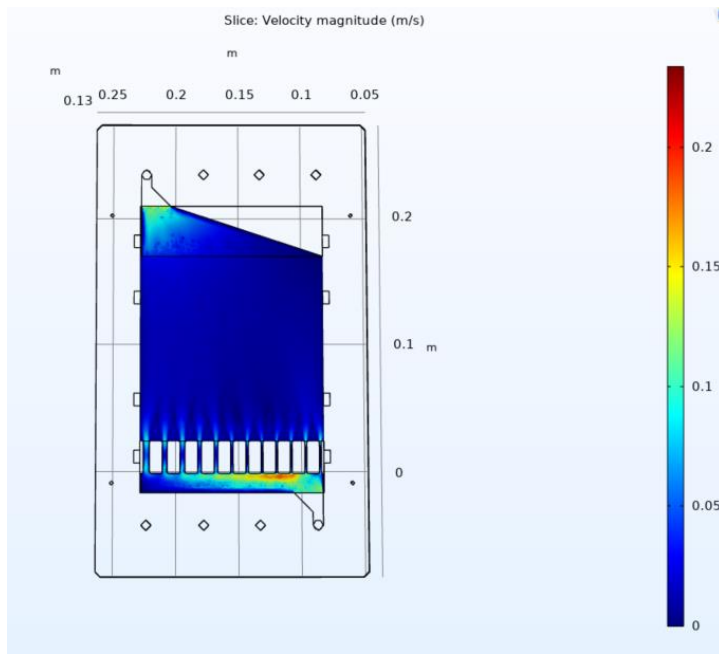


Figure D.5. Simulated fluid velocity profile for the second design configuration near the GDE or membrane surface. The flow inlet is on the bottom and the flow outlet is on top

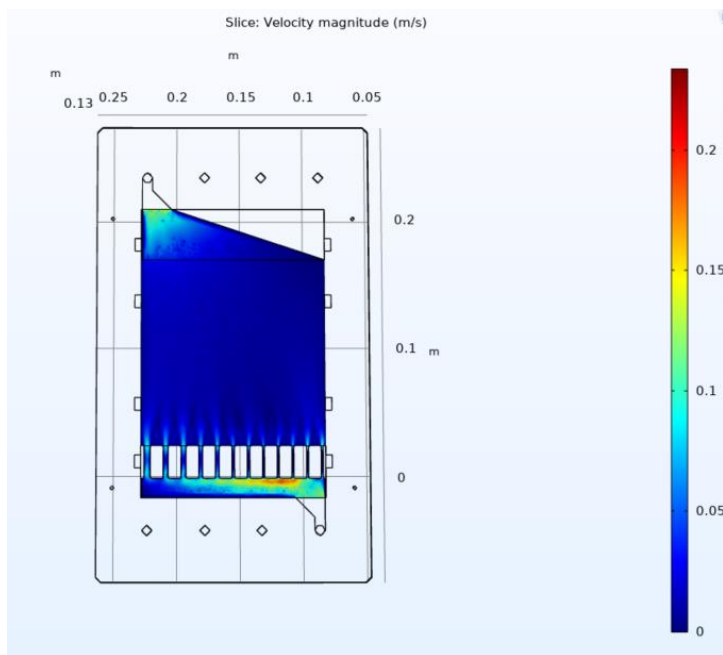


Figure D.6. Simulated fluid velocity profile for the second design configuration at the center of the flow distribution plate. The flow inlet is on the bottom and the flow outlet is on top

Appendix E

Supporting Information for Chapter 6

Computational Methods

The Density Functional Theory (DFT) calculations were done in VASP.^{1,2} We choose the PBE density functional³ including dispersion through the D2 method,^{4,5} with our reparameterization of C_6 coefficients for metals.⁶ Implicit solvation was included within the VASP-MGCM framework.^{7,8} Inner electrons were represented by PAW pseudopotentials^{9,10}, and the monoelectronic states for the valence electrons expanded as plane waves with a kinetic energy cutoff of 450 eV. The experimental system consists of an InBi catalyst employed in a Gas Diffusion Electrode configuration at Avantium.¹¹ On top of In-Bi alloys, we considered pure Sn and In metals since they are typically used for CO₂ reduction to formate.^{12,13}

We modeled three metal surfaces Sn(010), In(001), and Bi(110), and two intermetallic surfaces, In₅Bi₃(010) and InBi (110). These terminations exhibited the lowest surface energies among other facets considered (Table E.1); thus, they are expected to be the most abundant on the as-synthesized nanoparticles before electrocatalytic conditions, according to Wulff's theorem.¹⁴ The slabs contained at least four layers, where the two uppermost were fully relaxed and the rest fixed to the bulk distances. The vacuum between periodic slabs was larger than 10 Å. The Brillouin zone was sampled by a Γ -centered k-points mesh from the Monkhorst-Pack method,¹⁵ with a reciprocal grid size smaller than 0.03 Å⁻¹.

To assess adsorption energies for impurities and CO₂ reduction intermediates, we placed the adsorbates only on one side of the slab; thus, we introduced a dipole correction to remove spurious contributions arising from the asymmetric slab model.¹⁶ The surface coverage of the adsorbate ranged between 1/9 for In(001), 1/6 for In₅Bi₃(010) and Bi(110), and 1/4 for Sn(100) and InBi(110) Bi-terminated. All energies were reported using as references clean surfaces and gas-phase molecules as (i) CO₂, H₂ for the CO₂ reduction (CO₂R) and hydrogen evolution reactions (HER) study and (ii) CO, NO, NO₂, N₂O, NH₃, SO₂, HCl, HF for the surface poisoning study. The energy of the charged species NO₃⁻ and CO₃²⁻ was estimated from their corresponding conjugated acids, as reported in the Section “Estimation of gas-phase energy” and Table E.2. Gibbs free energy was estimated from DFT energies by including entropic contributions at $T = 298.15$ K.

Estimation of gas-phase energy

DFT energies for gas-phase molecules as H₂, HNO₃, and H₂CO₃ were calculated through VASP,^{1,2} employing the PBE density functional,³ and correcting for implicit solvation contributions within the VASP-MGCM framework.^{7,8} Gibbs free energies were calculated from Equation E.1.¹⁷ Internal energy E was calculated from DFT energy including rotational (E_{rot}) and translational (E_{trans}) energy computed through Gaussian (Ref.¹⁸) and contribution from vibrational frequencies, as in Equation E.2.¹⁷ Entropy S was estimated from rotational (S_{rot}) and translational (S_{trans}) entropy computed through Gaussian (Ref.¹⁸) and contribution from vibrational entropy, Equation E.3.¹⁷ k_B and h are Boltzmann and Planck constant,

respectively, T stands for temperature and ν_i is the wavenumber of the vibrational mode i of the given molecule.

$$G = E - TS + k_B T \quad (\text{E.1})$$

$$E = E_{\text{rot}} + E_{\text{trans}} + k_B \sum_i \left(\frac{1}{2} + \frac{1}{e^{h\nu_i/k_B T} - 1} \right) \quad (\text{E.2})$$

$$S = S_{\text{rot}} + S_{\text{trans}} + k_B \sum_i \left(\frac{h\nu_i/k_B T}{e^{h\nu_i/k_B T} - 1} - \ln(1 - e^{-h\nu_i/k_B T}) \right) \quad (\text{E.3})$$

The determination of Gibbs free energy for ions in solution has been carried out in the past by referring these species to non-charged precursors and then correcting for their equilibrium potential.^{19,20} For instance, the Computational Hydrogen Electrode (CHE) approach relates the energy of the $\text{H}^+ + \text{e}^-$ couple to the Gibbs free energy of H_2 ,²¹ while recently a similar framework has been extended to other ionic molecules relevant for electrocatalytic reactions.¹⁹ In line with one of our previous works, we determined the Gibbs free energy of NO_3^- and CO_3^{2-} from the energy of their conjugated acids (B), namely HNO_3 and H_2CO_3 , and the energy of a solvated proton, estimated as $\frac{1}{2} G_{\text{H}_2}$ in line with the CHE approach. When the pH of an aqueous solution is equal to the pKa of an acid-base reaction, acid and base are in equilibrium, Equation E.4. Thus, the Gibbs free energy for a given base can be estimated from Equation E.5, where pKa is respectively -1.4 , 6.3 , and 10.3 for $\text{HNO}_3/\text{NO}_3^-$, $\text{HCO}_3^-/\text{CO}_3^{2-}$, and $\text{H}_2\text{CO}_3/\text{HCO}_3^-$ acid-base reactions.



$$G_{B^-} = G_{\text{HB}} - \frac{1}{2} G_{\text{H}_2} - k_B T \ln(10)(\text{pH} - \text{pKa}) \quad (\text{E.5})$$

Supplementary tables

Table E.1. Surface energies γ (J m^{-2}) for selected facets of In, Sn, and In-Bi intermetallic alloys. The lowest energy configurations for a given system are highlighted in bold. For the In_5Bi_3 system, we selected the (010) facet since it is isoenergetic to (001)-Bi-t, but the surface stoichiometry contains both In and Bi.

Facet	$\gamma / \text{J m}^{-2}$
In(001)	0.28
In(010)	0.36
In(100)	0.36
In(110)	0.39
Sn(100)	0.35
Sn(110)	0.51
Bi(100)	0.40
Bi(110)	0.31
In_5Bi_3(001) Bi-terminated	0.28
In_5Bi_3 (001) In-terminated	0.31
In_5Bi_3(010)	0.29
In_5Bi_3 (110) Bi-rich	0.34
In_5Bi_3 (110) In-rich	0.32
InBi(100)	0.39
InBi(110) Bi-terminated	0.20
InBi(110) In-terminated	0.29

Table E.2. Gibbs free energies, solvation, rotational, and translational contributions for selected molecules.

	$\Delta G / \text{eV}$	$\Delta E_{\text{solv}} / \text{eV}$	$E_{\text{rot}} / \text{eV}$	$S_{\text{rot}} / \text{eV K}^{-1}$	$E_{\text{trans}} / \text{eV}$	$S_{\text{trans}} / \text{eV K}^{-1}$
H ₂	−6.71	−0.01	+0.03	+1.31E-04	+0.04	+1.21E-03
H ₂ O	−14.19	−0.40	+0.04	+4.50E-04	+0.04	+1.49E-03
CO	−15.06	−0.10	+0.03	+4.85E-04	+0.04	+1.54E-03
CO ₂	−23.38	−0.35	+0.03	+5.62E-04	+0.04	+1.60E-03
NO	−12.40	−0.04	+0.03	+4.95E-04	+0.04	+1.55E-03
NO ₂	−18.59	−0.15	+0.04	+8.45E-04	+0.04	+1.61E-03
HNO ₃	−25.74	−0.40	+0.04	+9.90E-04	+0.04	+1.65E-03
SO ₂	−18.14	−0.59	+0.04	+9.31E-04	+0.04	+1.65E-03
NH ₃	−19.37	−0.23	+0.04	+5.86E-04	+0.04	+1.48E-03
N ₂ O	−21.87	−0.19	+0.03	+6.15E-04	+0.04	+1.60E-03
H ₂ CO ₃	−37.30	−0.73	+0.04	+1.01E-03	+0.04	+1.65E-03
HF	−8.64	−0.48	+0.03	+2.82E-04	+0.04	+1.50E-03
HCl	−6.54	−0.14	+0.03	+3.40E-04	+0.04	+1.58E-03
NO ₃ [−]	−22.86	—	—	—	—	—
HCO ₃ [−]	−33.96	—	—	—	—	—
CO ₃ ^{2−}	−30.39	—	—	—	—	—

References

- (1) Kresse, G.; Furthmüller, J. Efficiency of Ab-Initio Total Energy Calculations for Metals and Semiconductors Using a Plane-Wave Basis Set. *Comput. Mater. Sci.* **1996**, *6*, 15–50, DOI 10.1016/0927-0256(96)00008-0.
- (2) Kresse, G.; Furthmüller, J. Efficient Iterative Schemes for Ab Initio Total-Energy Calculations Using a Plane-Wave Basis Set. *Phys. Rev. B* **1996**, *54*, 11169–11186, DOI 10.1103/PhysRevB.54.11169.
- (3) Perdew, J. P.; Burke, K.; Ernzerhof, M. Generalized Gradient Approximation Made Simple. *Phys. Rev. Lett.* **1996**, *77*, 3865–3868, DOI 10.1103/PhysRevLett.77.3865.
- (4) Grimme, S. Semiempirical GGA-Type Density Functional Constructed with a Long-Range Dispersion Correction. *J. Comput. Chem.* **2006**, *27*, 1787–1799, DOI 10.1002/jcc.
- (5) Bucko, T.; Hafner, J.; Lebègue, S.; Ángyán, J. G. Improved Description of the Structure of Molecular and Layered Crystals: Ab Initio DFT Calculations with van Der Waals Corrections. *J. Phys. Chem. A* **2010**, *114*, 11814–11824, DOI 10.1021/jp106469x.
- (6) Almora-Barrios, N.; Carchini, G.; Błoński, P.; López, N. Costless Derivation of Dispersion Coefficients for Metal Surfaces. *J. Chem. Theory Comput.* **2014**, *10*, 5002–5009, DOI 10.1021/ct5006467.
- (7) Garcia-Ratés, M.; López, N. Multigrid-Based Methodology for Implicit Solvation Models in Periodic DFT. *J. Chem. Theory Comput.* **2016**, *12*, 1331–1341, DOI 10.1021/acs.jctc.5b00949.
- (8) Garcia-Ratés, M.; García-Muelas, R.; López, N. Solvation Effects on Methanol Decomposition on Pd(111), Pt(111), and Ru(0001). *J. Phys. Chem. C* **2017**, *121*, 13803–13809, DOI 10.1021/acs.jpcc.7b05545.
- (9) Blöchl, P. E. Projector Augmented-Wave Method. *Phys. Rev. B* **1994**, *50*, 17953–17979, DOI 10.1103/PhysRevB.50.17953.
- (10) Kresse, G.; Joubert, D. From Ultrasoft Pseudopotentials to the Projector Augmented-Wave Method. *Phys. Rev. B* **1999**, *59*, 1758–1775, DOI 10.1103/PhysRevB.59.1758.
- (11) Philips, M. F.; Pavesi, D.; Wissink, T.; Figueiredo, M. C.; Gruter, G.-J. M.; Koper, M. T. M.; Schouten, K. J. P. Electrochemical CO₂ Reduction on Gas Diffusion Electrodes: Enhanced Selectivity of In–Bi Bimetallic Particles and Catalyst Layer Optimization through a Design of Experiment Approach. *ACS Appl. Energy Mater.* **2022**, aesaem.1c03156, DOI 10.1021/acsaelm.1c03156.
- (12) Hori, Y.; Kikuchi, K.; Suzuki, S. Production of CO and CH₄ in Electrochemical Reduction of CO₂ at Metal Electrodes in Aqueous Hydrogencarbonate Solution. *Chem. Lett.* **1985**, *14*, 1695–1698.
- (13) Bagger, A.; Ju, W.; Varela, A. S.; Strasser, P.; Rossmeisl, J. Electrochemical CO₂ Reduction: A Classification Problem. *ChemPhysChem* **2017**, *18* (22), 3266–3273, DOI 10.1002/cphc.201700736.

- (14) Wulff, G. Zur Frage Der Geschwindigkeit Des Wachstums Und Der Auflösung Der Krystallflächen. *Z. Krist.* **1901**, *34*, 449–530.
- (15) Monkhorst, H. J.; Pack, J. D. Special Points for Brillouin-Zone Integrations. *Phys. Rev. B* **1976**, *13*, 5188–5192, DOI 10.1103/PhysRevB.16.1748.
- (16) Makov, G.; Payne, M. Periodic Boundary Conditions in Ab Initio Calculations. *Phys. Rev. B* **1995**, *51*, 4014–4022, DOI 10.1103/PhysRevB.51.4014.
- (17) Ochterski, J. W. Thermochemistry in Gaussian. *Gaussian Inc* **2000**, *264*, 1–19, DOI 10.1016/j.ijms.2007.04.005.
- (18) Frisch, M. J.; Trucks, G. W.; Schlegel, H. B.; Scuseria, G. E.; Robb, M. A.; Cheeseman, J. R.; Scalmani, G.; Barone, V.; Mennucci, B.; Petersson, G. A.; Nakatsuji, H.; Caricato, M.; Li, X.; Hratchian, H. P.; Izmaylov, A. F.; Bloino, J.; Zheng, G.; Sonnenberg, J. L.; Hada, M.; Ehara, M.; Toyota, K.; Fukuda, R.; Hasegawa, J.; Ishida, M.; Nakajima, T.; Honda, Y.; Kitao, O.; Nakai, H.; Vreven, T.; Montgomery, J. A. J.; Peralta, J. E.; Ogliaro, F.; Bearpark, M.; Heyd, J. J.; Brothers, E.; Kudin, K. N.; Staroverov, V. N.; Kobayashi, R.; Normand, J.; Raghavachari, K.; Rendell, A.; Burant, J. C.; Iyengar, S. S.; Tomasi, J.; Cossi, M.; Rega, N.; Millam, J. M.; Klene, M.; Knox, J. E.; Cross, J. B.; Bakken, V.; Adamo, C.; Jaramillo, J.; Gomperts, R.; Stratmann, R. E.; Yazyev, O.; Austin, A. J.; Cammi, R.; Pomelli, C.; Ochterski, J. W.; Martin, R. L.; Morokuma, K.; Zakrzewski, V. G.; Voth, G. A.; Salvador, P.; Dannenberg, J. J.; Dapprich, S.; Daniels, A. D.; Farkas, O.; Foresman, J. B.; Ortiz, J. V.; Cioslowski, J.; Fox, D. J. Gaussian 09, Revision A.02. *Gaussian, Inc. Wallingford, CT* **2009**.
- (19) Granda-Marulanda, L. P.; McCrum, I. T.; Koper, M. T. M. A Simple Method to Calculate Solution-Phase Free Energies of Charged Species in Computational Electrocatalysis. *J. Phys. Condens. Matter* **2021**, *33*, 204001.
- (20) Abidi, N.; Lim, K. R. G.; Seh, Z. W.; Steinmann, S. N. Atomistic Modeling of Electrocatalysis: Are We There Yet? *WIREs Comput Mol Sci.* **2021**, *11*, e1499, DOI 10.1002/wcms.1499.
- (21) Nørskov, J. K.; Rossmeisl, J.; Logadottir, A.; Lindqvist, L.; Kitchin, J. R.; Bligaard, T.; Jónsson, H. Origin of the Overpotential for Oxygen Reduction at a Fuel-Cell Cathode. *J. Phys. Chem. B* **2004**, *108*, 17886–17892, DOI 10.1021/jp047349j.

Appendix F

DOE Reproducibility Analysis

Introduction

In this appendix, more background is provided to demonstrate how main factor effects in two-way factor interactions can be visualized and compared when analyzing data generated by a DOE. Furthermore, we demonstrate the robustness of the DOE methodology by simulating measurement error in a DOE generated to explore a four-factor system with a predefined relationship. The preset equation and description of how the simulations are generated are contained in the experimental section. Comparisons of the models generated are contained in the results section, while analysis of the results is contained in the discussion and conclusion sections.

DOE Data Analysis and Visualization

A DOE matrix is generated to explore how multiple factors and their interactions can affect a measured response. The factors are varied in the experimental set in an organized manner, which allows for the separation of parameter effects from each other and from noise. Analysis of data from a DOE aims to detect a correlation between a factor or interaction and the response (i.e., a slope greater than zero should exist between two levels of a factor if there is a correlation.).

Main effect plots and two-way factor interaction plots are useful for data exploration in DOE data sets. In these plots, the mean response for each level of a factor is plotted. This allows correlations to be visualized and compared across all factors. Interaction plots can also be generated by plotting the mean of the response for each factor level at different levels of another factor. When the slopes shown in these plots are drastically different, the interaction between the two factors is strong.

The main effect plots for the data collected in Chapter 4 are shown in Figures F.1, while two interaction plots are shown in Figures F.2 and F.4. Each point on the plots in Figures F.1 to F.3 are averages of several runs in the DOE. Large error bars observed in the main effect plot can be a sign of a two-factor interaction. A two-factor interaction occurs when the level of one factor affects the effect another factor has on the response. For example, splitting the data of current efficiency vs. binder wt% by catalyst supported on carbon (Figure 2), we see that 30 wt% catalyst on carbon achieves significantly higher current efficiencies at 30 wt% binder than 90 wt% catalyst supported on carbon. Additionally, by splitting the data of current efficiency vs binder wt% by the GDL method (Figure 3), we see that GDL 16 performed worse than GDL 23 at 30 wt% binder in the catalyst layer. These two interactions appear in the model selected in Chapter 4 and are determined to be statistically significant (Figure 4.1).

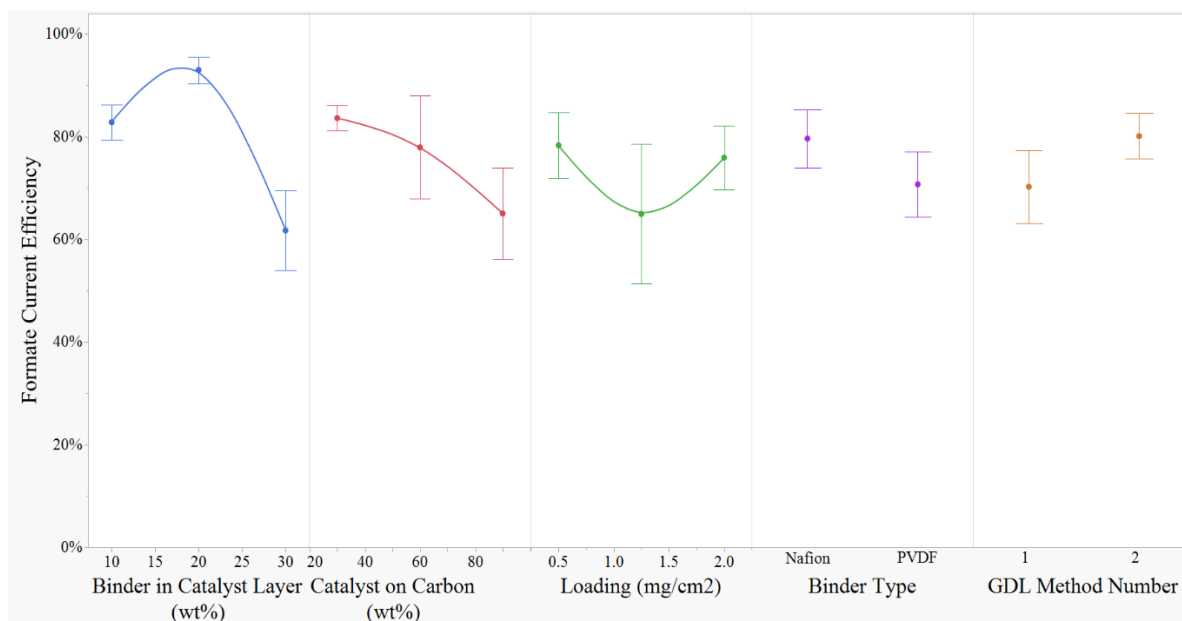


Figure F.1. Main Effect Plots for data collected in the DOE performed in Chapter 4. Each point is an average of all the experimental runs in the DOE matrix performed at that factor level. GDL Method 16 is GDL 1, and GDL Method 23 is GDL 2 in Chapter 4

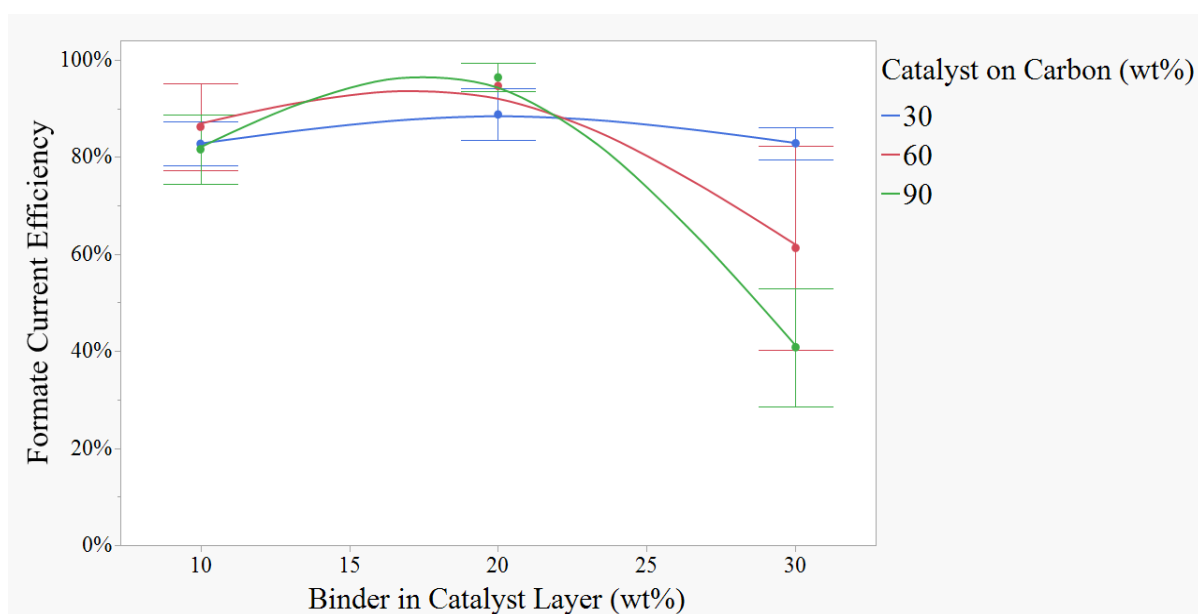


Figure F.2. Binder wt% by catalyst on carbon interaction plot for data collected in the DOE performed in Chapter 4. Each point is an average of all the experimental runs in the DOE matrix performed at the two-factor levels.

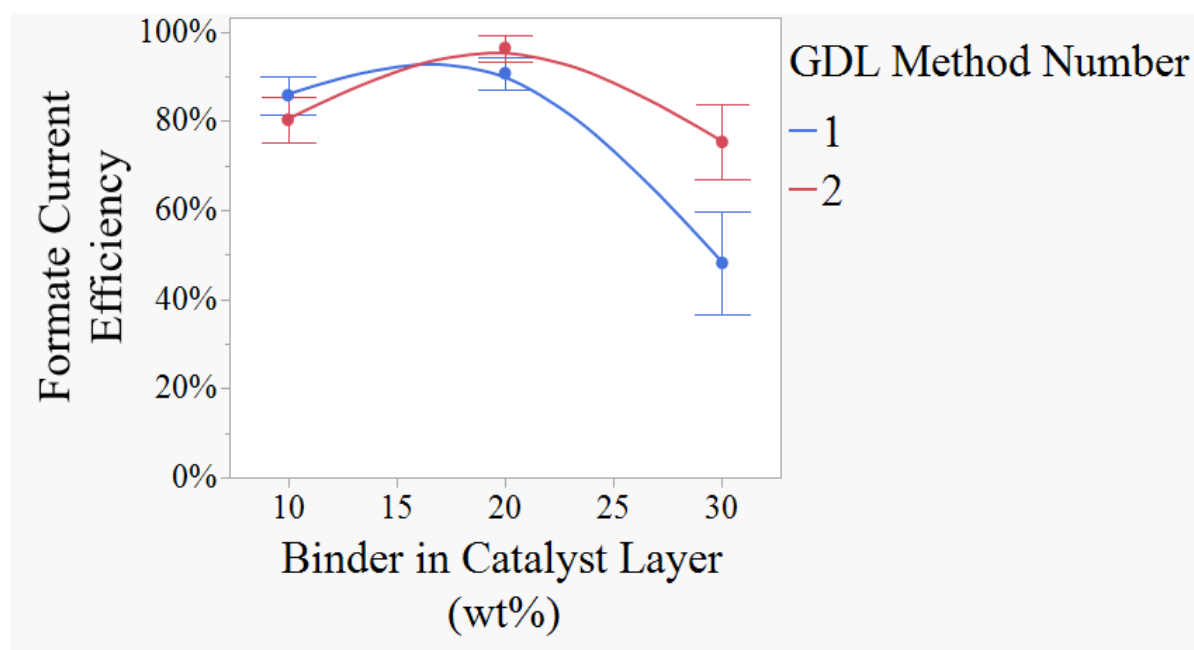


Figure F.3. Binder in catalyst layer by catalyst on carbon interaction plot for data collected in the DOE performed in Chapter 4.

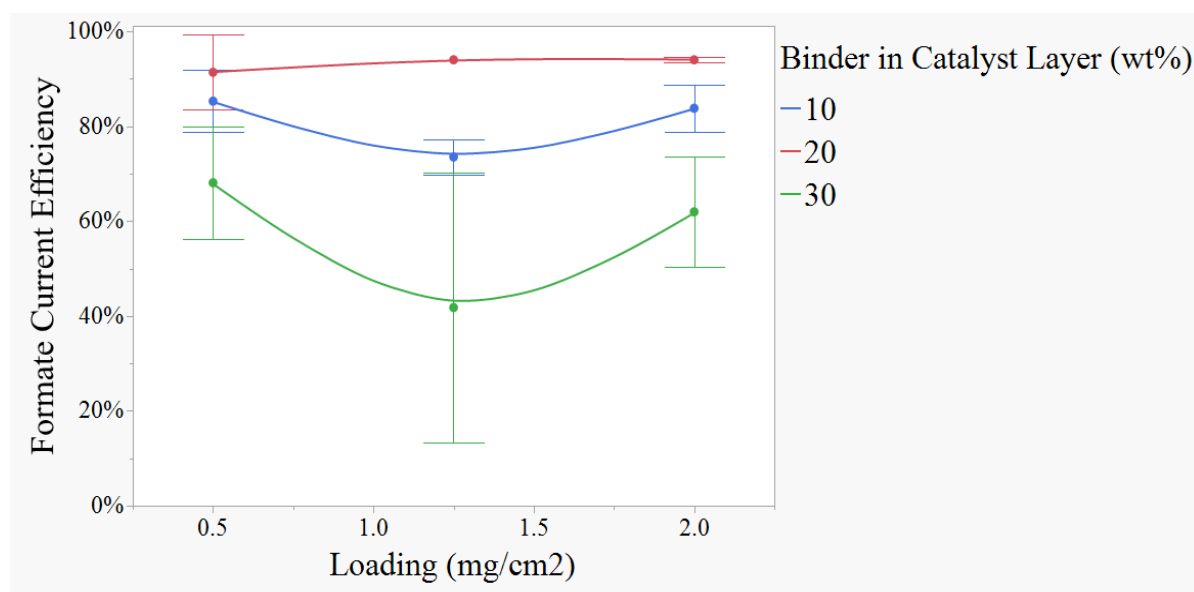


Figure F.4. Loading by binder wt% interaction plot for data collected in the DOE performed in Chapter 4. Each point is an average of all the experimental runs in the DOE matrix performed at the two-factor levels.

There is high error associated with the center values for the main effect of the loading of catalyst. Splitting this data of current efficiency vs loading by binder wt% (Figure 4) shows this large variation occurs with 30 wt% binder. One reason for the higher error is that there are only two runs in the DOE that are averaged at this level (loading = 1.25 and binder wt% = 30). It appears there may be curvature in the data for loading at 10 and 30 wt% binder in the catalyst layer, and the model in Chapter 4 includes the squared term of loading. However, this term is not shown to be statistically significant (Figure 4.1).

A DOE is designed such that main effects can be determined from the resulting data with no factor confounding (Factor confounding is when two factors are being changed in the same way together, so analysis would not be able to distinguish which factor is causing the measured effect). Each experimental run in a DOE experimental matrix is necessary to be performed for proper analysis of the data. This opens the question of what happens if there is noise or experimental error in the collected data? This question is addressed in the next section by simulating random error in the measured response in a DOE.

Experimental for Simulating Random Error

Four factors (X1, X2, X3, and X4) that can be influencing the response (Y_{actual}) were considered. JMP was used to create a DOE for four factors with the aim of finding which factors were the most influential for the response. Each factor was bounded between 1 and 10 for the DOE. The preset relationship between factors was set by Equation F.2. Table F.1 shows the experimental matrix for the created design and the actual value of the response (Y_{actual}).

$$Y_{\text{Actual}} = 10000 * X_1 + 1000 * X_2 + 100 * X_3 + 10 * X_4 + 400 * X_1 * X_1 + 300 * X_2 * X_3 \quad (\text{Eq F.2.})$$

Table F.1. Design matrix and actual value of the response for the generated DOE

Run Number	X1	X2	X3	X4	Y_{actual}
1	10	1	1	10	141500
2	5.5	10	1	1	80210
3	1	1	10	1	15410
4	10	1	10	10	145100
5	1	10	10	5.5	51455
6	1	10	5.5	1	37460
7	10	10	10	1	181010
8	1	1	10	10	15500
9	10	10	1	5.5	153155
10	1	1	1	1	11810
11	10	5.5	10	5.5	163055
12	1	1	1	10	11900
13	5.5	10	10	10	108200
14	10	1	1	1	141410
15	1	10	1	10	23600
16	10	5.5	5.5	1	155135
17	5.5	5.5	1	10	74450
18	10	10	5.5	10	167150
19	10	1	10	1	145010
20	5.5	1	5.5	5.5	70355

Once the “Actual” value of the response was calculated, Python was used to simulate variation in the data by multiplying each actual value in a data set by a random percentage in a chosen range (90% to 110%, 95% to 105%, and 97.5% to 102.5%). Twenty data sets were generated for the three chosen ranges of random error. Each data set is referred to as a simulation. The 20

sets of simulated responses for each variation range are shown in Tables F.8 – F.10 (a link to this data is provided at the beginning of the Results section). Models were fit to each simulated data set using the BIC and AIC as stopping rules. The AIC and BIC methods generated the same model for the “Actual” data set (control model). All simulated models for a simulated error range were compared by their model terms and the magnitude of their scaled coefficients.

Results

Note: the remaining Figures (F.4 to F.16) and Tables F.8 to F.10 can be found in a separate document [here](#).

An overview of the comparison of models for AIC and BIC models for 20% simulated variation (i.e., the simulated response was randomly between 90% to 110% of the actual response) is shown in Tables F.2 and F.3, respectively. Figure F.4 shows the summary of fit and scaled parameter estimates for the control model. Two examples of models for the 20 simulations generated by using the AIC as the stopping rule are shown in Figures F.5-F.6, while two examples of the models generated by using the BIC as the stopping rule are shown in Figures F.7 to F.8. The R^2 value shown is rounded to the 2nd decimal place. Therefore, an R^2 greater than 0.995 will appear as an R^2 of 1 in these Figures.

Table F.2. AIC model terms for 20 simulations of 20% variation in the measured response. Green cells indicate the term was included in the model, while the number refers to the magnitude of the scaled coefficient (1 designates the term has the highest magnitude of a scaled coefficient)

	Y _{actual}	sim1	sim2	sim3	sim4	sim5	sim6	sim7	sim8	sim9	sim10	sim11	sim12	sim13	sim14	sim15	sim16	sim17	sim18	sim19	sim20
X1	1	1	1	1	1	1	1	1	1	1	1	1	1	1	1	1	1	1	1	1	1
X2	2	2	2	2	3	2	3	2	2	2	3	3	2	3	2	2	2	2	3	2	2
X3	4	4	3	3	4	4	4	3	3	3	4	4	3	4	4	4	3	3	4	5	4
X4																					5
X1*X2																					
X1*X3																					
X1*X4																					6
X2*X3	5	5	4	6	6	3	5	4	4	4	5	5	4	5	5	5	4	4	5	4	3
X2*X4																					
X3*X4																					
X1*X1	3	3	5	4	5		2				2	2		2	3				2	3	
X2*X2				5	2																
X3*X3																3					
X4*X4																					

Table F.3. BIC model terms for 20 simulations of 20% variation in the measured response. Green cells indicate the term was included in the model, while the number refers to the magnitude of the scaled coefficient (1 designates the term has the highest magnitude of a scaled coefficient)

	Y _{actual}	sim1	sim2	sim3	sim4	sim5	sim6	sim7	sim8	sim9	sim10	sim11	sim12	sim13	sim14	sim15	sim16	sim17	sim18	sim19	sim20
X1	1	1	1	1	1	1	1	1	1	1	1	1	1	1	1	1	1	1	1	1	1
X2	2	2	2	2	3	2	4	2	2	2	3	3	2	3	2	2	2	2	3	2	2
X3	4	4	3	3	4	4	6	3	3	4	4	4	3	4	3	4	4	3	4	5	4
X4		10	9	12	10		9		8	7	9	9			8		14		9		8
X1*X2							8										13		11		10
X1*X3				8		5		7		6							12	5			11
X1*X4				11											7		9		8		9
X2*X3	5	7	4	9	6	3	7	6	6	5	7	6	4	5	5	6	3	4	7	4	3
X2*X4				10	9				9		8	8					11		10		
X3*X4		9	8												6		10				12
X1*X1	3	5	6	4	5		2	5	5	3	2	2		2	4	5	6		2	3	5
X2*X2		8	5	5	2												7				7
X3*X3		6		7	7		5	4	7		6	5				3	5		5		13
X4*X4		3	7	6	8		3		4		5	7					8		6		6

Two (Sim 1 and 14) out of 20 models generated by the AIC method in the simulated data set contained the exact same terms as in the control model (model generated from the actual data set). 11 (Sim 1,2,3,4,6,10,11,13,14,18 and 19) out of the 20 models generated by the AIC method in the simulated data set contained at least the same terms as the control model but contained some additional terms as well. None of the 20 models generated by the BIC method in the simulated data set contained the exact same terms as in the control model. 17 out of the 20 models (Sim 1,2,3,4,6,7,8,9,10,11,13,14,15,16,18,19,20) generated by the BIC method in the simulated data set contained at least the same terms as the control model but contained some additional terms as well.

An overview of the comparison of models for AIC and BIC models for 10% simulated variation (i.e., the simulated response was randomly between 95% to 105% of the actual response) is shown in Tables F.4 and F.5, respectively. Two examples of models for the 20 simulations generated by using the AIC as the stopping rule are shown in Figures F.9-F.10, while two examples of the models generated by using the BIC as the stopping rule are shown in Figures F.11 to F.12. The R^2 value shown is rounded to the 2nd decimal place. Therefore, an R^2 greater than 0.995 will appear as an R^2 of 1 in these Figures.

Table F.4. AIC model terms for 20 simulations of 10% variation in the measured response. Green cells indicate the term was included in the model, while the number refers to the magnitude of the scaled coefficient (1 designates the term has the highest magnitude of a scaled coefficient)

	Y _{actual}	sim1	sim2	sim3	sim4	sim5	sim6	sim7	sim8	sim9	sim10	sim11	sim12	sim13	sim14	sim15	sim16	sim17	sim18	sim19	sim20
X1	1	1	1	1	1	1	1	1	1	1	1	1	1	1	1	1	1	1	1	1	1
X2	2	2	2	2	2	2	2	2	2	2	2	2	2	2	2	2	2	2	2	2	2
X3	4	3	5	3	4	3	4	4	3	4	3	3	4	3	4	3	3	3	3	4	3
X4							7			6											
X1*X2					6																
X1*X3			7																6		
X1*X4							6														
X2*X3	5	5	4	5	5	5	5	5	4	5	5	5	5	5	5	5	5	5	5	5	5
X2*X4																					
X3*X4																					
X1*X1	3	4	3	4	3	4	3	3	5	3	4	4	3	4	3	4	4	4	4	3	4
X2*X2			6																		6
X3*X3																					
X4*X4																					

Table F.5. BIC model terms for 20 simulations of 10% variation in the measured response. Green cells indicate the term was included in the model, while the number refers to the magnitude of the scaled coefficient (1 designates the term has the highest magnitude of a scaled coefficient)

	Y _{actual}	sim1	sim2	sim3	sim4	sim5	sim6	sim7	sim8	sim9	sim10	sim11	sim12	sim13	sim14	sim15	sim16	sim17	sim18	sim19	sim20
X1	1	1	1	1	1	1	1	1	1	1	1	1	1	1	1	1	1	1	1	1	1
X2	2	2	2	2	2	2	2	2	2	2	2	2	2	2	2	2	2	2	2	2	2
X3	4	3	5	3	4	3	5	4	3	4	3	3	4	3	4	4	3	3	3	4	3
X4		8	8		11	7	7	8	9	6	12	9	11			11	11	10	9		8
X1*X2					9		12						9			8	9				
X1*X3			7				10				9	8			6	9			7		9
X1*X4			10				8			7									12		11
X2*X3	5	5	4	5	5	5	4	5	4	5	5	5	5	5	5	5	5	4	5	5	5
X2*X4						6		7	8		10		8			12		9	10		10
X3*X4			9		10		11				11		10			13	10		11		
X1*X1	3	4	3	4	3	4	3	3	5	3	4	4	3	4	3	3	4	5	4	3	4
X2*X2		6	6		7		6		6		8	6	7			6	7	7			6
X3*X3					8		9	6			6	7				10	6	6	8		7
X4*X4		7			6				7		7		6			7	8	8	6		

Four (Sim 7,12,14, and 19) out of 20 models generated by the AIC method in the simulated data set contained the exact same terms as in the control model (model generated from the actual data set). All of the 20 models generated by the AIC method in the simulated data set contained at least the same terms as the control model but contained some additional terms as well. One (Sim 19) out of 20 models generated by the BIC method in the simulated data set contained the exact same terms as in the control model. All of the 20 models generated by the BIC method in the simulated data set contained at least the same terms as the control model but contained some additional terms as well.

An overview of the comparison of models for AIC and BIC models for 5% simulated variation (i.e., the simulated response was randomly between 97.5% to 102.5% of the actual response) is shown in Tables F.6 and F.7, respectively. Two examples of models for the 20 simulations generated by using the AIC as the stopping rule are shown in Figures F.13-F.14, while two examples of the models generated by using the BIC as the stopping rule are shown in Figures F.15 to F.16. The R^2 value shown is rounded to the 2nd decimal place. Therefore, an R^2 greater than 0.995 will appear as an R^2 of 1 in these Figures.

Table F.6. AIC model terms for 20 simulations of 5% variation in the measured response. Green cells indicate the term was included in the model, while the number refers to the magnitude of the scaled coefficient (1 designates the term has the highest magnitude of a scaled coefficient)

X1	1	1	1	1	1	1	1	1	1	1	1	1	1	1	1	1	1	1	1	1
X2	2	2	2	2	2	2	2	2	2	2	2	2	2	2	2	2	2	2	2	2
X3	4	4	3	3	4	3	4	4	3	3	4	4	4	4	4	3	4	4	4	3
X4																				
X1*X2								6												
X1*X3							6		6											
X1*X4																				
X2*X3	5	5	5	5	5	5	5	5	5	5	5	5	5	5	5	5	5	5	5	5
X2*X4																				
X3*X4																				
X1*X1	3	3	4	4	3	4	3	3	4	4	3	3	3	3	3	4	3	3	3	4
X2*X2															6			6	6	
X3*X3															7					
X4*X4																				

Table F.7. BIC model terms for 20 simulations of 5% variation in the measured response. Green cells indicate the term was included in the model, while the number refers to the magnitude of the scaled coefficient (1 designates the term has the highest magnitude of a scaled coefficient)

	Y _{actual}	sim1	sim2	sim3	sim4	sim5	sim6	sim7	sim8	sim9	sim10	sim11	sim12	sim13	sim14	sim15	sim16	sim17	sim18	sim19	sim20
X1	1	1	1	1	1	1	1	1	1	1	1	1	1	1	1	1	1	1	1	1	1
X2	2	2	2	2	2	2	2	2	2	2	2	2	2	2	2	2	2	2	2	2	2
X3	4	4	3	4	4	3	4	4	3	4	4	4	4	4	4	3	4	4	4	4	4
X4		9	10		8			7		10	10	11		9	9	12	7	10	10	7	9
X1*X2		8	7					6		9	9			8	8	10			7		
X1*X3							7		7						10	11					
X1*X4			8							8		10			11	8	10		8		
X2*X3	5	5	5	5	5	5	5	5	5	5	5	5	5	5	5	5	5	5	5	5	5
X2*X4												8				9	8	9	9	6	
X3*X4		7	9		7					11	8	9		7		7	9	8			8
X1*X1	3	3	4	3	3	4	3	3	4	3	3	3	3	3	3	4	3	3	3	3	3
X2*X2		6	6		6							6		6	6	6		6	6		6
X3*X3							6		6	7	7				7						7
X4*X4										6	6	7					6	7			

Seven (Sim 1,4,10,11,12,13,16) out of 20 models generated by the AIC method in the simulated data set contained the exact same terms as in the control model (model generated from the actual data set). All of the 20 models generated by the AIC method in the simulated data set contained at least the same terms as the control model but contained some additional terms as well. One (Sim 3) of the 20 models generated by the BIC method in the simulated data set contained the exact same terms as in the control model. All of the 20 models generated by the BIC method in the simulated data set contained at least the same terms as the control model but contained some additional terms as well.

Discussion

When the simulated variation is 10% or less, all models generated by both methods contained all of the terms found in the control models. Additionally, when the simulated variation is 10% or less, the top five influential terms in all models matched the control model (although not always in order of the magnitude of the scaled coefficients). At 20% simulated variation, there becomes a risk of missing an influential variable or falsely detecting a highly influential effect. Nevertheless, these models still successfully identify a majority of highly influential factors (X1, X2, and X3 are always in the top 5 most influential factors for the AIC method and 19/20 times for the BIC method).

Additionally, although X4 is included in Equation 1, it is not included in the control model. This is because its effect is much smaller than any other factor effect. Additionally, it would only account for a small percent of the total response in the range the factor was tested (i.e., it ultimately is not responsible within its bounds for explaining enough variation in the data for it to be considered in the model). This is also reflected by the R^2 value of the control model being greater than 0.995.

Conclusion

DOE methodology with using either AIC or BIC for penalizing the number of parameters in a model is a robust methodology that can tolerate variation due to measurement error. At 10% simulated variation and lower, we show that the top five influential terms in the 80 simulated models are the same five terms that appear in the control model. Even at 20% simulated variation in the response, we observe a majority of highly influential factors correctly identified.

In Chapters 4 and 5, we observe < 20% variation in the data sets based on the repeat runs (See Appendix A and C). Additionally, the AIC method is used for all models in Chapter 4 (higher variation in data than in Chapter 5). Although the BIC method is used in Chapter 5, the repeat runs showed low variation. Additionally, all model terms in the AIC method models are included as the top terms in the BIC method model.

Summary

Carbon dioxide capture and utilization technologies are necessary to create a truly circular economy. The electrochemical reduction of carbon dioxide to formate is an appealing carbon utilization method as it can be performed at room temperature and pressure, it only requires two electrons, and it has a high atom efficiency. This reaction has been known and studied for decades, but no commercial process is currently practiced. In Chapter 1, we explain why formate is one of the best products to pursue for electrochemical CO₂ reduction (ECCR), why a gas diffusion electrode is the best technology to use for this reaction, and why the design of experiments (DOE) methodology and density functional theory (DFT) are powerful tools that can be used to optimize this reaction.

Chapter 2 explores the theory of a gas diffusion electrode (GDE). GDEs allow electrochemical reactions to occur at higher rates by enhancing the mass transport of gaseous reactants to the catalyst. These electrodes are made of two layers: the catalyst layer and the gas diffusion layer (GDL). Work performed on GDEs for the ECCR towards formate is reviewed in this chapter. The gas diffusion layer and catalyst layer can affect the electrode's performance and should be considered together for the optimization of the reaction. However, no studies have investigated possible interaction effects that may be present between these two layers. Exploring these potential interactions between layers is one goal of this thesis, and Chapters 3 and 4 focus on this topic.

In order to investigate potential interactions between the two layers of a GDE for the ECCR towards formate, access to a variety of GDLs with varying characteristics is necessary. A design of experiments is used in Chapter 3 to understand how multiple factors in a production method for GDLs can be adjusted to tune the characteristics of the GDL. The conductance through the GDL, surface conductivity, thickness, elasticity, hydrophobicity, and porosity are measured for the 26 synthesized electrodes, and the top influential production factors are identified for each characteristic. This sets the groundwork for eventually having the capability of producing GDLs with prespecified characteristics and allows for more definitive studies focusing on both layers of the GDE to be performed. Two GDLs were selected from this work to study potential interaction effects with the catalyst layer.

In Chapter 4, catalyst layer characteristics are studied with the GDL to determine how these factors affect the overall performance of the electrode. A DOE is used to investigate how the binder type and concentration in the catalyst layer, the amount of catalyst supported on carbon, and its loading on the GDL, as well as the GDL type and operating current density, affect the current efficiency towards formate and cell potential. This is the first study we are aware of that explores how the GDL can interact with different characteristics of the catalyst layer and affect the cell's performance. The binder concentration in the catalyst layer is found to be substantially influential for the performance of the electrode. Furthermore, interactions between the GDL and several catalyst layer factors are found to influence the performance. The best-performing electrodes screened in this study show nearly 100% current efficiency at current densities of up to 400 mA/cm² for two hours. Additionally, one electrode operated at a

current density of 200 mA/cm² for 48 hours at a current efficiency of 85% and remained working with a current efficiency above 50% for 124 hours.

The experiments in Chapter 4 are performed at a 10 cm² scale. The scale-up of these electrodes to 200 cm² is another goal of this thesis and is the focus of Chapter 5. In this chapter, a custom-designed multifunctional 200 cm² maximum area cell is reviewed and used to demonstrate the scale-up of results reported in Chapter 4. The 200 cm² electrode achieved a current efficiency of 92.5% during the first 15-minute experiment and then a current efficiency of 89% for an additional 60 minutes. This result is similar to the performance of the 10 cm² electrode at 300 mA/cm² (92% current efficiency).

A key step for commercializing a chemical technology is demonstrating process robustness using real chemical feeds. The European subsidy RECODE targets to electrochemically convert CO₂ produced from cement manufacturing into formic acid and other products. This stream of CO₂ will have additional (and higher concentrations of) impurities compared to CO₂ coming from a cylinder in a research lab. In Chapter 6, the impurities found in the flue gas from the cement factory were identified, and DFT was used to investigate the potential of these impurities to poison catalysts known to produce formate and the catalyst used in Chapters 4 and 5. Nearly all oxygen-containing impurities showed an exergonic adsorption energy. Since NO_x species are expected to reduce under CO₂ reduction conditions, carbonate and SO₂ in the flue gas could potentially poison the catalysts.

Chapter 7 concludes this thesis with an outlook on how this research can be used in future studies. Future lab scale development ideas are explored, focusing on additional GDL development and catalyst layer binder exploration. Finally, future scale-up development is discussed, focusing on ways to minimize the operating cell potential.

Samenvatting

Technologieën voor het opvangen en benutten van kooldioxide zijn noodzakelijk om een werkelijk circulaire economie te creëren. De elektrochemische reductie van koolstofdioxide tot formiaat is een aantrekkelijke methode voor koolstofgebruik, omdat deze kan worden uitgevoerd bij kamertemperatuur en druk, er slechts twee elektronen voor nodig zijn en de atomefficiëntie hoog is. Deze reactie is al tientallen jaren bekend en bestudeerd, maar er wordt momenteel geen commercieel proces toegepast. In Hoofdstuk 1 leggen we uit waarom formiaat een van de beste producten is om na te streven voor elektrochemische CO₂-reductie (ECCR), waarom een gasdiffusie-elektrode de beste technologie is om voor deze reactie te gebruiken, en waarom de Design of Experiments (DOE) methodologie en dichtheidsfunctionaaltheorie (DFT) zijn krachtige hulpmiddelen die kunnen worden gebruikt om deze reactie te optimaliseren.

Hoofdstuk 2 onderzoekt de theorie van een gasdiffusie-elektrode (GDE). GDE's maken het mogelijk dat elektrochemische reacties met hogere snelheden plaatsvinden door het massatransport van gasvormige reactanten naar de katalysator te verbeteren. Deze elektroden zijn gemaakt uit twee lagen: de katalysatorlaag en de gasdiffusie laag (GDL). Het werk dat is verricht aan GDE's voor de ECCR richting formate wordt in dit hoofdstuk besproken. De gasdiffusielaag en de katalysatorlaag kunnen de prestaties van de elektrode beïnvloeden en moeten samen worden overwogen voor de optimalisatie van de reactie. Er zijn echter geen studies die mogelijke interactie-effecten tussen deze twee lagen hebben onderzocht. Het onderzoeken van deze potentiële interacties tussen lagen is één doel van dit proefschrift, en de hoofdstukken 3 en 4 richten zich op dit onderwerp.

Toegang tot een verscheidenheid aan GDL's met verschillende kenmerken is noodzakelijk om potentiële interacties tussen de twee lagen van een GDE voor de ECCR naar formiaat te onderzoeken. In hoofdstuk 3 wordt een ontwerp van experimenten gebruikt om te begrijpen hoe meerdere factoren in een productiemethode voor GDL's kunnen worden aangepast om de kenmerken van de GDL af te stemmen. De geleiding door de GDL, oppervlaktegeleiding, dikte, elasticiteit, hydrofobiciteit en porositeit worden gemeten voor de 26 gesynthetiseerde elektroden, en de belangrijkste invloedrijke productiefactoren worden voor elk kenmerk geïdentificeerd. Dit legt de basis voor het uiteindelijk kunnen produceren van GDL's met vooraf gespecificeerde kenmerken en maakt het mogelijk om meer definitieve onderzoeken uit te voeren die zich op beide lagen van de GDE richten. Uit dit werk werden twee GDL's geselecteerd om potentiële interactie-effecten met de katalysatorlaag te bestuderen.

In Hoofdstuk 4 wordt de GDL bestudeerd met de eigenschappen van de katalysatorlaag om te bepalen hoe deze factoren de algehele prestaties van de elektrode beïnvloeden. Een DOE wordt gebruikt om te onderzoeken hoe het bindmiddeltype en de concentratie in de katalysatorlaag, de hoeveelheid katalysator die op koolstof wordt gedragen, en de belasting ervan op de GDL, evenals het GDL-type en de bedrijfsstroombichtheid, de stroomefficiëntie richting formiaat en het cel potentieel. Dit is de eerste studie waarvan we op de hoogte zijn en die onderzoekt hoe de GDL kan interageren met verschillende kenmerken van de

katalysatorlaag en de prestaties van de cel kan beïnvloeden. De bindmiddelconcentratie in de katalysatorlaag blijkt substantieel van invloed te zijn op de prestatie van de elektrode. Bovendien blijkt dat interacties tussen de GDL en verschillende katalysatorlaagfactoren de prestaties. De best presterende elektroden die in dit onderzoek zijn onderzocht, vertonen een stroomefficiëntie van bijna 100% bij stroomdichtheden tot 400 mA/cm^2 gedurende twee uur. Bovendien werkte één elektrode gedurende 48 uur bij een stroomdichtheid van 200 mA/cm^2 met een stroomefficiëntie van 85% en bleef gedurende 124 uur werken met een stroomefficiëntie van meer dan 50%.

De experimenten in Hoofdstuk 4 worden uitgevoerd op een schaal van 10 cm^2 . Het opschalen van deze elektroden naar 200 cm^2 is een ander doel van dit proefschrift en is ook het doel van Hoofdstuk 5. In dit hoofdstuk wordt een op maat ontworpen multifunctionele cel met een maximale oppervlakte van 200 cm^2 beoordeeld en gebruikt om de opschaling van de resultaten gerapporteerd in hoofdstuk 4. De elektrode van 200 cm^2 bereikte een stroomrendement van 92,5% tijdens het eerste experiment van 15 minuten en daarna een stroomrendement van 89% gedurende nog eens 60 minuten. Dit resultaat is vergelijkbaar met de prestatie van de 10 cm^2 elektrode bij 300 mA/cm^2 (92% stroomefficiëntie).

Een belangrijke stap bij het commercialiseren van een chemische technologie is het aantonen van procesrobuustheid met behulp van echte chemische grondstoffen. De Europese subsidie RECODE heeft tot doel CO_2 , geproduceerd bij de cementproductie, elektrochemisch om te zetten in mierenzuur en andere producten. Deze stroom CO_2 zal extra (en hogere concentraties) onzuiverheden bevatten vergeleken met CO_2 dat uit een cilinder in een onderzoekslaboratorium komt. In hoofdstuk 6 werden de onzuiverheden gevonden in het rookgas van de cementfabriek geïdentificeerd, en DFT werd gebruikt om het potentieel van deze onzuiverheden te onderzoeken om katalysatoren te vergiften waarvan bekend is dat ze formiaat produceren en de katalysator die in de hoofdstukken 4 en 5 werd gebruikt. Bijna alle zuurstofhoudende onzuiverheden vertoonden een exergonische adsorptie-energie. Carbonaat en SO_2 werden geïdentificeerd als potentiële vergiften voor de katalysatoren, omdat verwacht wordt dat NO_x -soorten zullen worden geconsumeerd onder CO_2 -reductieomstandigheden.

Hoofdstuk 7 sluit dit proefschrift af met een vooruitblik op hoe dit onderzoek in toekomstige studies kan worden gebruikt. Toekomstige ontwikkelingsideeën op laboratoriumschaal worden onderzocht, waarbij de nadruk ligt op aanvullende GDL-ontwikkeling en verkenning van katalysatorlaagbinders. Ten slotte wordt toekomstig opschalingswerk besproken, waarbij de nadruk ligt op manieren om het potentieel van de elektrochemische cel te minimaliseren.

Curriculum Vitae

Matthew Philips was born on June 24th, 1990, in the town of Mount Holly, New Jersey, in the United States of America. He went to Bishop Eustace Preparatory High School in Pennsauken, New Jersey, where he pursued college-level chemistry and mathematics courses. He enjoyed these courses and knew he wanted to ultimately end up in a career focused on renewable resources or energy. He was accepted to attend the Georgia Institute of Technology (Georgia Tech) in 2008 and chose to major in chemical engineering.

During his studies at Georgia Tech, he performed undergraduate research for fuel cells and characterized membranes by their electro-osmotic drag coefficient. In 2012, Matt graduated from Georgia Tech with a BS in chemical engineering with highest honor. Shortly after graduating, he worked for LithChem, a startup battery company in Philadelphia. In 2013, Matt joined Liquid Light, a startup company spun out of Princeton University that focused on converting carbon dioxide (CO₂) into higher-value chemicals. Here, he gained extensive knowledge and experience in the design of experiments (DOE) methodology, electrochemical cell optimization, test station design and fabrication, and process engineering separations.

In 2016, Liquid Light went out of business, and Matt and his colleagues were told on a Monday that their last day would be Friday. Over the following weekend, the previous CEO of Liquid Light reached out to Matt and five other colleagues to assemble a team to try to sell Liquid Light's intellectual property and assets to other companies. In the summer of 2016, Matt was first introduced to Dr. Gert-Jan Gruter and Frank Roerink, the CTO and CFO of Avantium, respectively. By October 2016, Matt was planning to move to the Netherlands as part of Avantium's acquisition of Liquid Light.

Matt started working for Avantium on a one-year contract in January 2017 as a senior process engineer. He was responsible for demonstrating three of Liquid Light's core unit operations at Avantium within the year. In September 2017, Matt was offered the opportunity to continue working at Avantium as a senior process engineer and become a PhD student in the International Training Network ELCOREL. Matt eagerly took up this opportunity and studied under the guidance of Professor Marc Koper, Professor Gert-Jan Gruter, and Dr. Klaas Jan Schouten.

Matt's studies were focused on optimizing the gas diffusion electrode (GDE) for the electrochemical conversion of CO₂ to formate. During his time in ELCOREL, he gained vast knowledge of the current state of the art for CO₂ reduction towards formate and published a literature review of relevant work in ACS Sustainable Chemistry and Engineering. He continued studying the gas diffusion layer and found ways to make these layers with varying characteristics. He then worked with Davide Pavesi to investigate how the catalyst layer can interact with the gas diffusion layer to affect the performance of the electrode. He spent three months in a virtual secondment at the Institut Català d'Investigació Química under the supervision of Professor Noria Lopez and Federico Dattila. Here, he studied the potential that various impurities in industrial CO₂ streams had to poison typical catalysts used for the electrochemical reduction of CO₂ to formate.

In 2021, Matt returned to the United States to be with his fiancé (now wife) and continued to work on his thesis writing. While working on the writing of his thesis, he began working as the director of manufacturing for TreadStone, a coatings company that provides conductive, corrosion-resistant coatings for electrochemical industries. Currently, he has found a new role in the field of CO₂ reduction as a principal electrochemical engineer at OCOchem in Washington state.

List of Publications:

Chapter 1 and 2

Philips, M. F.; Gruter, G.-J. M.; Koper, M. T. M.; Schouten, K. J. P. Optimizing the Electrochemical Reduction of CO₂ to Formate: A State-of-the-Art Analysis. *ACS Sustain. Chem. Eng.* 2020, 8 (41), 15430–15444, DOI 10.1021/acssuschemeng.0c05215.

Chapter 3

Philips, M. F.; Gruter, G.-J. M.; Koper, M. T. M.; Schouten, K. J. P. Production of Gas Diffusion Layers with Tunable Characteristics. *ACS Omega* 2022, 7 (27), 23041–23049, DOI 10.1021/acsomega.1c06977.

Chapter 4

Philips, M. F.,* Pavesi, D.,* Wissink, T., Figueiredo, M. C., Gruter, G.-J. M., Koper, M. T. M. & Schouten, K. J. P. Electrochemical CO₂ Reduction on Gas Diffusion Electrodes: Enhanced Selectivity of In–Bi Bimetallic Particles and Catalyst Layer Optimization through a Design of Experiment Approach. *ACS Appl. Energy Mater.*, 2022, acsaem.1c03156 doi:10.1021/acsaem.1c03156.

*Both authors contributed equally

Other Publications:

Monteiro, M. C. O.; Philips, M. F.; Schouten, K. J. P.; Koper, M. T. M. Efficiency and Selectivity of CO₂ Reduction to CO on Gold Gas Diffusion Electrodes in Acidic Media. *Nat. Commun.* 2021, 12 (1), 4943, DOI 10.1038/s41467-021-24936-6.

Shih, A. J.; Monteiro, M. C. O.; Dattila, F.; Pavesi, D.; Philips, M.; da Silva, A. H. M.; Vos, R. E.; Ojha, K.; Park, S.; van der Heijden, O.; Marcandalli, G.; Goyal, A.; Villalba, M.; Chen, X.; Gunasooriya, G. T. K. K.; McCrum, I.; Mom, R.; López, N.; Koper, M. T. M. Water Electrolysis. *Nat. Rev. Methods Prim.* 2022, 2 (1), 84, DOI 10.1038/s43586-022-00164-0.

Acknowledgments

The journey of my PhD research was intense, laborious, and, at times, frustrating. I would like to take some space in this dissertation to thank the people who have helped me through this time. I would like to extend my deepest appreciation toward my promotor, Prof. Marc Koper, and co-promotors Prof. Gert-Jan Gruter and Dr. Klaas Jan Schouten for all of the extensive feedback on my chapters and publications, and for making the revisions requested from peer reviewers so much less stressful.

I would also like to extend my sincere thanks to Prof. Nuria Lopez for allowing me the opportunity to spend some time working on DFT simulations at the Institute of Chemical Research of Catalonia (ICIQ). I am also extremely grateful to Federico Dattila for teaching me everything practical on performing basic DFT simulations and expanding my knowledge on the subject. I would have been lost in the DFT world without you.

Prior to joining Avantium, I spent three and a half years working for Liquid Light, a startup electrochemical company that spun out of Princeton University. I want to thank everyone I had the pleasure of working with at Liquid Light. I learned so much from my experiences in electrochemistry and process engineering and am very grateful to have been a part of such an awesome group. In particular, thank you, Alex Bauer, for teaching me electrochemistry fundamentals and being such a joy to work with in the labs.

My time during my PhD was spent working at Avantium, and I would like to sincerely thank the Volta team for being such a great group to work with. I have so many fond memories with you all. I am extremely grateful to Julia Krasovic for teaching me so much of what I know and understand about electrochemistry, starting from the Liquid Light days. I want to thank Bart van den Bosch for all of the mentally stimulating conversations about anode electrochemistry at the coffee machine and for appreciating arts and crafts as much as I do.

I did not know anyone when I moved to the Netherlands on December 22, 2016. I want to thank several people who helped me transition to living in the Netherlands in my first year abroad. I would like to extend my gratitude to Martijn Zieverink for hosting me at his family's Christmas dinner that year. I am also grateful to Bart Berenbak for inviting me to a New Year's Eve party to ring in 2017. I would also like to thank Bart van Den Bosch for showing me some of the coolest places in Amsterdam throughout my time in the Netherlands.

I made several great friends during my time in the Netherlands who could always reduce any stress I faced. Thank you, Davide Pavesi, for the numerous memories we shared in exploring Europe and the Netherlands. I still laugh out loud when I think back to many experiences we shared. Thank you, Julia Krasovic, Mariana Paredinha Araujo, Gil Felgueiras, and Marta Costa-Figueiredo, for always being down for a beer festival and hosting dinner get-togethers. Thank you, Lotte Metz, for all of your enthusiasm to tour the breweries of the Netherlands.

I am extremely grateful to my parents and sister for all of their love and unwavering support throughout this adventure. I would like to thank my friends in the US who visited me while I was staying in the Netherlands. Thank you, Todd Selby, Sam Fala, Ronak Ravani, Jarred

Acknowledgments

Cannon, Will Maher, and Emily Spitzer. It was awesome exploring Amsterdam with you. I would also like to thank my best friends, Adam Grobelny and Mike Piccininni. You both have unique views of this world that inspire creativity.

When I moved to the Netherlands, I was only supposed to stay for a year, which is what I told my girlfriend at the time. I am forever grateful to my (now) wife, Denise Dometita Philips, for putting up with a long-distance relationship for an extended period, and for all of your love and support in this journey.